Technical Design Report for:

The Central Tracking System of

$\overline{\text{P}}$ANDA Experiment

(AntiProton Annihilations at Darmstadt)

Strong Interaction Studies with Antiprotons

$\overline{\text{P}}$ANDA Collaboration

August 29, 2011

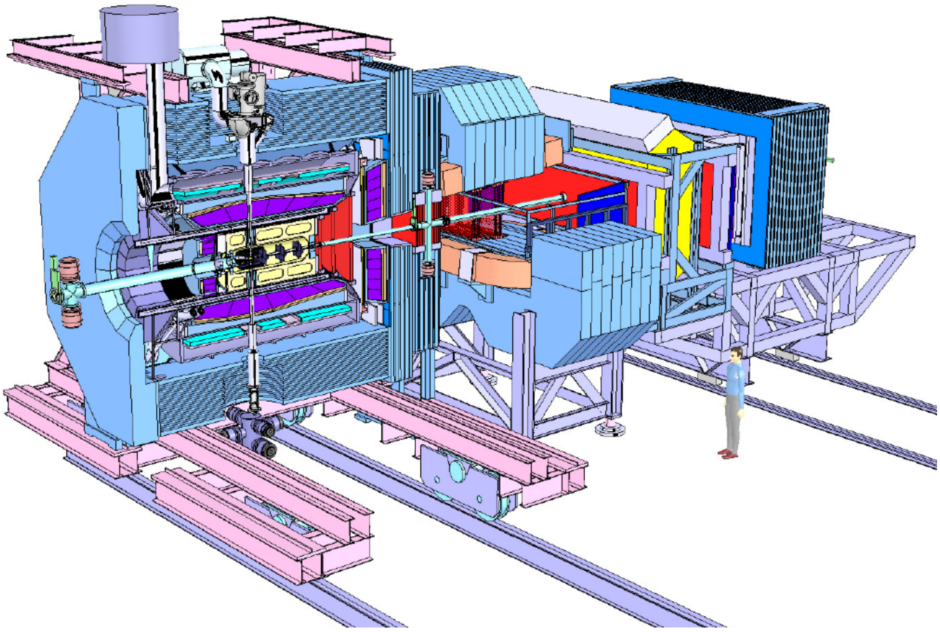

The $\overline{\mathrm{P}}$ANDA Collaboration

Universität **Basel**, Switzerland
W. Erni, I. Keshelashvili, B. Krusche, M. Steinacher

Institute of High Energy Physics, Chinese Academy of Sciences, **Beijing**, China
Y. Heng, Z. Liu, H. Liu, X. Shen, Q. Wang, H. Xu

Universität **Bochum**, I. Institut für Experimentalphysik, Germany
M. Albrecht, J. Becker, K. Eickel, F. Feldbauer, M. Fink, P. Friedel, F.-H. Heinsius, T. Held, H. Koch, B. Kopf, M. Leyhe, C. Motzko, M. Pelizäus, J. Pychy, B. Roth, T. Schröder, J. Schulze, M. Steinke, T. Trifterer, U. Wiedner, J. Zhong

Rheinische Friedrich-Wilhelms-Universität **Bonn**, Germany
R. Beck, M. Becker, S. Bianco, K.-T. Brinkmann, C. Hammann, F. Hinterberger, D. Kaiser, R. Kliemt, K. Koop, C. Schmidt, R. Schnell, U. Thoma, P. Vlasov, D. Walther, C. Wendel, T. Würschig, H.-G. Zaunick, R. Zimmermann

Università di **Brescia**, Italy
A. Bianconi

Institutul National de C&D pentru Fizica si Inginerie Nucleara ”Horia Hulubei”, **Bukarest-Magurele**, Romania
M. Bragadireanu, M. Caprini, C. Ciortea, M. Ciubancan, D. Pantea, D. Pantelica, P.D. Tarta

IIT, Illinois Institute of Technology, **Chicago**, U.S.A.
D. Kaplan

AGH, University of Science and Technology, **Cracow**, Poland
T. Fiutowski, M. Idzik, B. Mindur, D. Przyborowski, K. Swientek

IFJ, Institute of Nuclear Physics PAN, **Cracow**, Poland
E. Bialkowski, A. Budzanowski, B. Czech, S. Kliczewski, A. Kozela, P. Kulessa, P. Lebiedowicz, M. Kistryn, K. Pysz, W. Schäfer, R. Siudak, A. Szczurek

Instytut Fizyki, Uniwersytet Jagiellonski, **Cracow**, Poland
S. Jowzaee, M. Kajetanowicz, B. Kamys, S. Kistryn, G. Korcyl, K. Korcyl, W. Krzemien, A. Magiera, P. Moskal, Z. Rudy, P. Salabura, J. Smyrski, A. Wroñska

Gesellschaft für Schwerionenforschung GmbH, **Darmstadt**, Germany
M. Al-Turany, R. Arora, I. Augustin, H. Deppe, H. Flemming, A. Gerhardt, K. Götzen, G. Hohler, A.-F. Jordi, G. Kalicy, R. Karabowicz, D. Lehmann, B. Lewandowski, J. Lühning, F. Maas, H. Orth, M. Patsyuk, K. Peters, T. Saito, G. Schepers, C.J. Schmidt, L. Schmitt, C. Schwarz, J.Schwiening, B. Voss, P. Wieczorek, A. Wilms

Veksler-Baldin Laboratory of High Energies (VBLHE), Joint Institute for Nuclear Research. **Dubna**, Russia
V.M. Abazov, G. Alexeev, A. Arefiev, V.I. Astakhov, M.Yu. Barabanov, B.V. Batyunya, Yu.I. Davydov, V.Kh. Dodokhov, A.A. Efremov, A.G. Fedunov, A.A. Feshchenko, A.S. Galoyan, S. Grigoryan, A. Karmokov, E.K. Koshurnikov, V.I. Lobanov, Yu.Yu. Lobanov, A.F. Makarov, L.V. Malinina, V.L. Malyshev, G.A. Mustafaev, A. Olshevski, M.A. Pasyuk, E.A. Perevalova, A.A. Piskun, T.A. Pocheptsov, G. Pontecorvo, V.K. Rodionov, Yu.N. Rogov, R.A. Salmin, A.G. Samartsev, M.G. Sapozhnikov, G.S. Shabratova, A.N. Skachkova, N.B. Skachkov, E.A. Strokovsky, M.K. Suleimanov, R.Sh. Teshev, V.V. Tokmenin, V.V. Uzhinsky A.S. Vodopyanov, S.A. Zaporozhets, N.I. Zhuravlev, A.G. Zorin

University of **Edinburgh**, United Kingdom
D. Branford, D. Glazier, D. Watts, P. Woods

Friedrich Alexander Universität **Erlangen-Nürnberg**, Germany

A. Britting, W. Eyrich, A. Lehmann, F. Uhlig

Northwestern University, **Evanston**, U.S.A.
S. Dobbs, Z. Metreveli, K. Seth, X. Ting, A. Tomaradze

Università di Ferrara and INFN Sezione di Ferrara, **Ferrara**, Italy
D. Bettoni, V. Carassiti, P. Dalpiaz, A. Drago, E. Fioravanti, I. Garzia, M. Negrini, M. Savriè, G. Stancari

INFN Laboratori Nazionali di **Frascati**, Italy
N. Bianchi, B. Dulach, P. Gianotti, C. Guaraldo, V. Lucherini, E. Pace

INFN Sezione di **Genova**, Italy
A. Bersani, G. Bracco, M. Macri, R.F. Parodi

Justus Liebig-Universität **Gießen**, II. Physikalisches Institut, Germany
D. Bremer, V. Dormenev, P. Drexler, M. Düren, T. Eissner, K. Föhl M. Galuska, T. Gessler, A. Hayrapetyan, P. Koch, B. Kröck, W. Kühn, S. Lange, Y. Liang, M. Liu, O. Merle, V. Metag, M. Moritz, D. Münchow, M. Nanova, R. Novotny, B. Spruck, H. Stenzel, M. Thiel, T. Ulrich, M. Werner

University of **Glasgow**, United Kingdom
J. Annand, T. Clarkson, C. Euan, D. Hamilton, M. Hoek, D. Ireland, T. Keri, I. Lehmann, K. Livingston, S. Lumsden, D. MacGregor, B. McKinnon, R. Montgomery, M. Murray, D. Protopopescu, G. Rosner, B. Seitz, G. Yang

Kernfysisch Versneller Instituut, University of **Groningen**, Netherlands
M. Babai, A. Glazenborg-Kluttig, E. Guliyev, V.S. Jothi, M. Kavatsyuk, P. Lemmens, H. Löhner, H. Moeini, J. Messchendorp, T. Poelman, H. Smit, G. Tambave, J.C. van der Weele

Forschungszentrum Jülich, Institut für Kernphysik, **Jülich**, Germany
M. Büscher, R. Dosdall, R. Dzhygadlo, S. Esch, A. Gillitzer, F. Goldenbaum, D. Grunwald, G. Kemmerling, H. Kleines, A. Lehrach, R. Maier, M. Mertens, H. Ohm, D. Prasuhn, T. Randriamalala, J. Ritman, M. Roeder, V. Serdyuk, G. Sterzenbach, T. Stockmanns, P. Wintz, P. Wüstner, H. Xu

University of Silesia, **Katowice**, Poland
J. Kisiel

Chinese Academy of Science, Institute of Modern Physics, **Lanzhou**, China
S. Li, Z. Li, Z. Sun, H. Xu

Lunds Universitet, Department of Physics, **Lund**, Sweden
S. Fissum, K. Hansen, L. Isaksson, M. Lundin, B. Schröder

Johannes Gutenberg-Universität, Institut für Kernphysik, **Mainz**, Germany
P. Achenbach, S. Bleser, A. Denig, M. Distler, M. Fritsch, D. Kangh, W. Lauth, H. Merkel, M. Michel, M.C. Mora Espi, U. Müller, E. Panzenboeck, J. Pochodzalla, S. Sanchez, A. Sanchez-Lorente C. Sfienti

Research Institute for Nuclear Problems, Belarus State University, **Minsk**, Belarus
V.I. Dormenev, A.A. Fedorov, M.V. Korzhik, O.V. Missevitch

Institute for Theoretical and Experimental Physics, **Moscow**, Russia
V. Balanutsa, V. Chernetsky, A. Demekhin, A. Dolgolenko, P. Fedorets, A. Gerasimov, V. Goryachev, V. Varentsov

Moscow Power Engineering Institute, **Moscow**, Russia
A. Boukharov, O. Malyshev, I. Marishev, A. Semenov

Technische Universität **München**, Germany
F. Böhmer, S. Dørheim, C. Höppner, B. Ketzer, I. Konorov, A. Mann, S. Neubert, S. Paul

Westfälische Wilhelms-Universität **Münster**, Germany
A.-K. Hergemöller, A. Khoukaz, E. Köhler, A. Täschner, J. Wessels

IIT Bombay, Department of Physics, **Mumbai**, India
R. Varma

Budker Institute of Nuclear Physics, **Novosibirsk**, Russia

E. Baldin, K. Kotov, S. Peleganchuk, Yu. Tikhonov

Institut de Physique Nucléaire, **Orsay**, France
T. Hennino, R. Kunne, C. Le Galliard, D. Marchand, A. Maroni, S. Ong, J. Pouthas, B. Ramstein, P. Rosier, M. Sudol, E. Tomasi-Gustafsson, J. Van de Wiele, T. Zerguerras

Dipartimento di Fisica Nucleare e Teorica, Università di Pavia, INFN Sezione di Pavia, **Pavia**, Italy
G. Boca, A. Braghieri, S. Costanza, A. Fontana, P. Genova, L. Lavezzi, P. Montagna, A. Rotondi

Institute for High Energy Physics, **Protvino**, Russia
V. Abramov, N. Belikov, A. Davidenko, A. Derevschikov, Y. Goncharenko, V. Grishin, V. Kachanov, D. Konstantinov, V. Kormilitsin, Y. Melnik A. Meschanin, N. Minaev, V. Mochalov, D. Morozov, L. Nogach, S. Nurushev, A. Ryazantsev, S. Ryzhikov, P. Semenov, L. Soloviev, A. Uzunian, A. Vasiliev, A. Yakutin

Kungliga Tekniska Högskolan, **Stockholm**, Sweden
T. Bäck, B. Cederwall

Stockholms Universitet, **Stockholm**, Sweden
L. Gerén, P.E. Tegnér, P. Thörngren, K.M. von Würtemberg

Petersburg Nuclear Physics Institute of Academy of Science, Gatchina, **St. Petersburg**, Russia
S. Belostotski, G. Gavrilov, A. Itzotov, A. Kashchuk, A. Kisselev, P. Kravchenko, O. Levitskaya, S. Manaenkov, O. Miklukho, Y. Naryshkin, D. Veretennikov, V. Vikhrov, A. Zhadanov

Università di Torino and INFN Sezione di Torino, **Torino**, Italy
D. Alberto, A. Amoroso, M.P. Bussa, L. Busso, F. De Mori, M. Destefanis, L. Fava, L. Ferrero, M. Greco, T. Kugathasan, M. Maggiora, S. Marcello, S. Sosio, S. Spataro, L. Zotti

INFN Sezione di Torino, **Torino**, Italy
D. Calvo, S. Coli, P. De Remigis, A. Filippi, G. Giraudo, S. Lusso, G. Mazza, O. Morra, A. Rivetti, R. Wheadon

Politecnico di Torino and INFN Sezione di Torino,**Torino**, Italy
F. Iazzi, Y. Hannas, A. Lavagno, P. Quarati

Università di Trieste and INFN Sezione di Trieste, **Trieste**, Italy
F. Bradamante, A. Bressan, A. Martin

Universität Tübingen, **Tübingen**, Germany
H. Clement

The Svedberg Laboratory, **Uppsala**, Sweden
B. Galander

Uppsala Universitet, Institutionen för Strålningsvetenskap, **Uppsala**, Sweden
L. Caldeira Balkestal, H. Calén, K. Fransson, T. Johansson, A. Kupsc, P. Marciniewski, E. Thomé, M. Wolke, J. Zlomanczuk

Universitat de **Valencia**, Dpto. de Física Atómica, Molecular y Nuclear, Spain
J. Díaz, A. Ortiz

University of Technology, Institute of Atomic Energy Otwock-Swierk, **Warsaw**, Poland
K. Dmowski, R. Korzeniewski, P. Duda, B. Slowinski

Soltan Institute for Nuclear Studies, **Warsaw**, Poland
S. Borsuk, A. Chlopik, Z. Guzik, J. Kopec, T. Kozlowski, D. Melnychuk, M. Plominski, J. Szewinski, K. Traczyk, B. Zwieglinski

Österreichische Akademie der Wissenschaften, Stefan Meyer Institut für Subatomare Physik, **Wien**, Austria
P. Bühler, A. Gruber, O. Hartman, P. Kienle, J. Marton, K. Suzuki, E. Widmann, J. Zmeskal

The GEM-TPC Collaboration

Technische Universität **München**, Germany
F. Böhmer, S. Dørheim, C. Höppner, B. Ketzer, I. Konorov, S. Neubert, S. Paul, J. Rauch, S. Uhl, M. Vandenbroucke

Excellence Cluster “Universe”, TU **München**, Germany
M. Berger, J.-C. Chen, F. Cusanno, L. Fabbietti, R. Münzer

GSI Helmholtzzentrum für Schwerionenforschung GmbH, **Darmstadt**, Germany
R. Arora, J. Frühauf, M. Kiš, Y. Leifels, V. Kleipa, J. Hehner, J. Kunkel, N. Kurz, H. Risch, C. Schmidt, S. Schwab, D. Soyk, B. Voss, J. Voss, J. Weinert

Helmholtz-Institut für Strahlen- und Kernphysik, **Bonn**, Germany
R. Beck, D. Kaiser, M. Lang, R. Schmitz, D. Walther

Stefan Meyer Institut für Subatomare Physik, **Vienna**, Austria
P. Müllner, K. Suzuki, J. Zmeskal

Universität **Heidelberg**, Germany
N. Hermann

Editors:	Paola Gianotti	Email: `gianotti@lnf.infn.it`
	Peter Wintz	Email: `p.wintz@fz-juelich.de`
	Bernhard Ketzer	Email: `Bernhard.Ketzer@tum.de`
	Laura Fabbietti	Email: `Laura.Fabbietti@tum.de`
Technical Coordinator:	Lars Schmitt	Email: `l.schmitt@gsi.de`
Deputy:	Bernd Lewandowski	Email: `b.lewandowski@gsi.de`
Physics Coordinator:	Diego Bettoni	Email: `diego.bettoni@fe.infn.it`
Deputy:	Albrecht Gillitzer	Email: `a.gillitzer@fz-juelich.de`
Computing coordinator:	Johan Messchendorp	Email: `messchendorp@kvi.nl`
Deputy:	Stefano Spataro	Email: `stefano.spataro@to.infn.it`
Spokesperson:	Ulrich Wiedner	Email: `ulrich.wiedner@ruhr-uni-bochum.de`
Deputy:	Paola Gianotti	Email: `paola.gianotti@lnf.infn.it`

Preface

This document illustrates the technical layout and the expected performance of the charged particle tracking system of the $\overline{\mathsf{P}}$ANDA experiment. This is a composite system that includes different sub-detectors in the Target and in the Forward spectrometer, with the aim of reconstructing the trajectories of all the charged particles emitted following antiproton's annihilation. This document is organized in 6 volumes each one dedicated to a particular sub-system.

Contents

1 Introduction

After the shutdown of the LEAR machine at CERN, and the closure of the fixed target program at Fermilab, The $\overline{\mathsf{P}}$ANDA experiment at FAIR represents a new and unique opportunity for the world-wide hadron physics community to come back to study QCD in the non perturbative regime with antiprotons. In the past, experiments like Crystal Barrel and OBELIX at CERN, E760 and E835 at Fermilab have shown how powerful are antiproton beams to explore strong interaction, determining a significant progress in our understanding of QCD spectrum. Nowadays these studies are carried out mainly at electron machines that offer the advantage of a clean environment, but at the price of a reduced set of final states and reduced cross-sections.

The antiproton beam foreseen for the HESR represent a step forward with respect to the previously mentioned facilities: up to 10^{11} antiprotons will be stored into the machine, with the possibility to reduce the momentum spread of the beam down to 10^{-5}. These are goals never achieved, that would be possible thanks to the complex FAIR aragement of storage rings equipped with stochastic and electron cooling systems.

The construction of the LHC detectors and of the B-factory experiments has also determined a significant progress in the detector technology, optimazing or introducing new concepts and instruments.

Today the $\overline{\mathsf{P}}$ANDA collaboration is in the ideal situation to be able to combine the unique characteristics of the best ever available high-resolution high-intensity antiproton beam with a hermetic detector for charged and neutral particles in the energy range between 10 MeV and 10 GeV to address the aforementioned fundamental questions. Clearly the design choices for the detector should represent a compromise between physics needs and available resources, nevertheless $\overline{\mathsf{P}}$ANDA represents for the hadronic physics community a unique opportunity. No other detector is foreseen for the HESR which is beeing designed with a single interaction point, and no other similar antiproton beam will be available elsewhere.

$\overline{\mathsf{P}}$ANDA should be sufficiently robust and resistant to radiation damage for an operation of many years. Furthermore, a high modularity would be necessary in order to allow different and complementary measurements from nuclear to particle physics.

The rate of antiproton annihilations, $2{\cdot}10^7$ per second, represents a challenge for the detector components, the trigger and the data acquisition systems impose to use all the most performant and up-to-date newfound of information technology.

1.1 The $\overline{\mathsf{P}}$ANDA experiment

The physics program of the FAIR facility covers a wide range of topics that address central issues of strong interactions and QCD. The antiproton beam of unprecedented quality in the momentum range from 1.5 GeV/c to 15 GeV/c will allow to make high precision, high statistics measurements, from charmonium spectroscopy to the search for exotic hadrons and the study of nucleon structure, from the study of in-medium modifications of hadron masses to the physics of hypernuclei.

To explore these items the $\overline{\mathsf{P}}$ANDA collaboration wants to build a state-of-the-art general purpose detector to study $\bar{\mathrm{p}}\mathrm{p}$, $\bar{\mathrm{p}}\mathrm{A}$ annihilations. This will consists in a set of systems surrounding an internal proton or nuclear target placed in one of the two straight sections of the High Energy Storage Ring (HESR) foreseen for FAIR. Fig. 1.1 shows the layout of the $\overline{\mathsf{P}}$ANDA detector. It consist of a 4m long 2T superconducting solenoid instrumented to detect both charged and neutral particles emitted at large and backward angles (Target Spectrometer, TS) and of a 2Tm resistive dipole magnetic spectrometer to detect charged and neutral particles emitted at angles between 0 an 20 degrees (Forward Spectrometer, FS).

$\overline{\mathsf{P}}$ANDA will take advantage of the latest detector technologies to achieve good particle identification with an almost complete solid angle combined with excellent mass, momentum and spatial resolution. A silicon vertex detector sorrounds the interaction point, while both the TS and the FS are equippped with different sub-systems meant for charged particle tracking, electromagnetic calorimetry, cherenkov light detection, muon identification. This complex detector arrangement is necessary in order to reconstruct the complete set of final states relevant to achieve the proposed physics goals. The main aspects of the $\overline{\mathsf{P}}$ANDA scientific program are described in the following section.

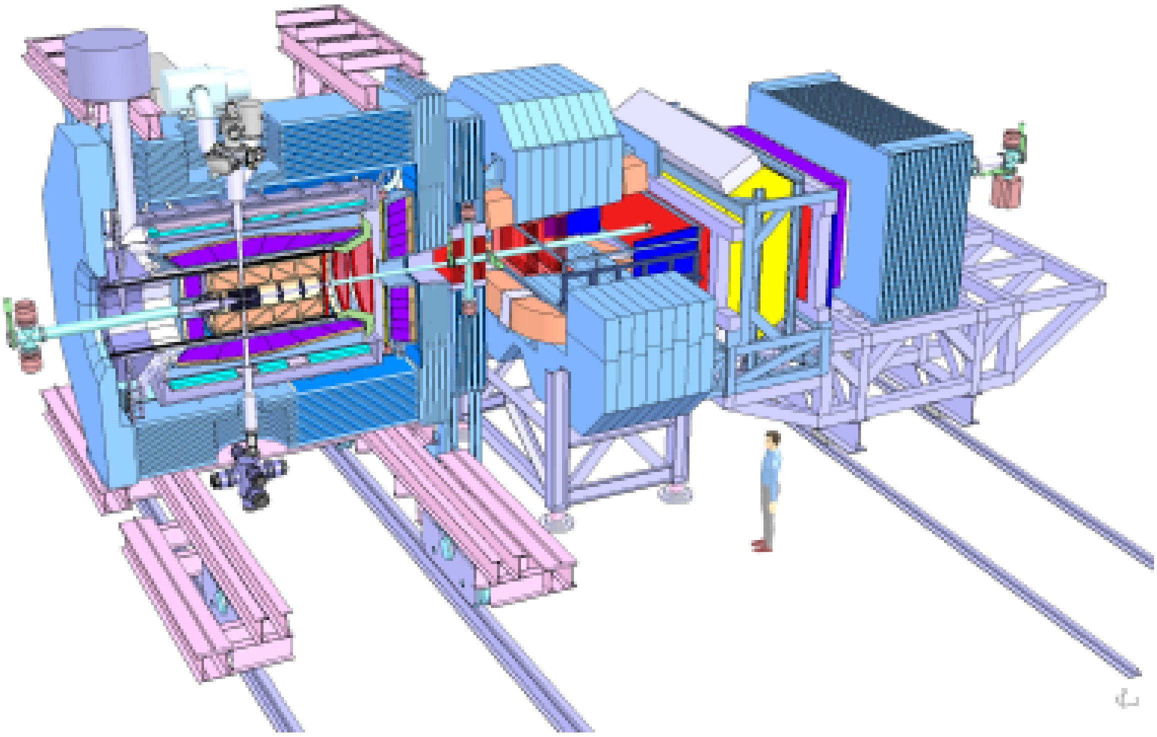

Figure 1.1: Layout of the $\overline{\text{P}}$ANDA detector consisting of a Target Spectrometer, surrounding the interaction region, and a Forward Spectrometer to detect particles emitted in the forward region. The HESR antiproton beam enters the apparatus from the left side.

1.2 The scientific program

One of the most challenging and fascinating goals of modern physics is the achievement of a fully quantitative understanding of the strong interaction, which is the subject of hadron physics. Significant progress has been achieved over the past few years thanks to considerable advances in experiment and theory. New experimental results have stimulated a very intense theoretical activity and a refinement of the theoretical tools.

Still there are many fundamental questions which remain basically unanswered. Phenomena such as the confinement of quarks, the existence of glueballs and hybrids, the origin of the masses of hadrons in the context of the breaking of chiral symmetry are long-standing puzzles and represent the intellectual challenge in our attempt to understand the nature of the strong interaction and of hadronic matter.

Experimentally, studies of hadron structure can be performed with different probes such electrons, pions, kaons, protons or antiprotons. In antiproton-proton annihilation particles with gluonic degrees of freedom as well as particle-antiparticle pairs are copiously produced, allowing spectroscopic studies with very high statistics and precision. Therefore, antiprotons are an excellent tool to address the open problems.

The FAIR facility will provide antiproton beams of the highest quality in terms of intensity and resolution, which will provide an excellent tool to answer these fundamental questions.

The $\overline{\text{P}}$ANDA experiment will use the antiproton beam from the HESR colliding with an internal proton target and a general purpose spectrometer to carry out a rich and diversified hadron physics program.

The experiment is being designed to fully exploit the extraordinary physics potential arising from the availability of high-intensity, cooled antiproton beams. The aim of the rich experimental program is to improve our knowledge of the strong interaction and of hadron structure. Significant progress beyond the present understanding of the field is expected thanks to improvements in statistics and precision of the data.

Many experiments are foreseen in $\overline{\text{P}}$ANDA.

- Charmonium spectroscopy. The $c\bar{c}$ spectrum can be computed within the framework of non-relativistic potential models and, more recently, in Lattice QCD. A precise measurement of all states below and above open charm threshold is of fundamental importance for a better understanding of QCD. All charmonium states can be formed directly in $\bar{\mathrm{p}}\mathrm{p}$ annihilation.

  At full luminosity $\overline{\mathsf{P}}$ANDA will be able to collect several thousand $c\bar{c}$ states per day. By means of fine scans it will be possible to measure masses with accuracies of the order of 100 keV and widths to 10% or better. The entire energy region below and above open charm threshold will be explored.

- Search for gluonic excitations (hybrids and glueballs). One of the main challenges of hadron physics is the search for gluonic excitations, i.e. hadrons in which the gluons can act as principal components. These gluonic hadrons fall into two main categories: glueballs, i.e. states of pure glue, and hybrids, which consist of a $q\bar{q}$ pair and excited glue. The additional degrees of freedom carried by gluons allow these hybrids and glueballs to have J^{PC} exotic quantum numbers: in this case mixing effects with nearby $q\bar{q}$ states are excluded and this makes their experimental identification easier. The properties of glueballs and hybrids are determined by the long-distance features of QCD and their study will yield fundamental insight into the structure of the QCD vacuum.

  Antiproton-proton annihilations provide a very favourable environment in which to look for gluonic hadrons.

- Study of hadrons in nuclear matter. The study of medium modifications of hadrons embedded in hadronic matter is aimed at understanding the origin of hadron masses in the context of spontaneous chiral symmetry breaking in QCD and its partial restoration in a hadronic environment. So far experiments have been focussed on the light quark sector. The high-intensity $\bar{\mathrm{p}}$ beam of up to 15 GeV/c will allow an extension of this program to the charm sector both for hadrons with hidden and open charm. The in-medium masses of these states are expected to be affected primarily by the gluon condensate.

  Another study which can be carried out in $\overline{\mathsf{P}}$ANDA is the measurement of J/ψ and D meson production cross sections in $\bar{\mathrm{p}}$ annihilation on a series of nuclear targets. The comparison of the resonant J/ψ yield obtained from $\bar{\mathrm{p}}$ annihilation on protons and different nuclear targets allows to deduce the J/ψ-nucleus dissociation cross section, a fundamental parameter to understand J/ψ suppression in relativistic heavy ion collisions interpreted as a signal for quark-gluon plasma formation.

- Open charm spectroscopy. The HESR running at full luminosity and at $\bar{\mathrm{p}}$ momenta larger than 6.4 GeV/c would produce a large number of D meson pairs. The high yield (e.g. 100 charm pairs per second around the $\psi(4040)$) and the well defined production kinematics of D meson pairs would allow to carry out a significant charmed meson spectroscopy program which would include, for example, the rich D and D_s meson spectra.

- Hypernuclear physics. Hypernuclei are systems in which up or down quarks are replaced by strange quarks. In this way a new quantum number, strangeness, is introduced into the nucleus. Although single and double Λ-hypernuclei were discovered many decades ago, only 6 double Λ-hypernuclei are presently known. The availability of $\bar{\mathrm{p}}$ beams at FAIR will allow efficient production of hypernuclei with more than one strange hadron, making $\overline{\mathsf{P}}$ANDA competitive with planned dedicated facilities. This will open new perspectives for nuclear structure spectroscopy and for studying the forces between hyperons and nucleons.

- Electromagnetic Processes. In addition to the spectroscopic studies described above $\overline{\mathsf{P}}$ANDA will be able to investigate the structure of the nucleon using electromagnetic processes, such as Deeply Virtual Compton Scattering (DCVS) and the process $\bar{\mathrm{p}}\mathrm{p} \rightarrow e^{+}e^{-}$, which will allow the determination of the electromagnetic form factors of the proton in the timelike region over an extended q^2 region.

1.3 High Energy Storage Ring – HESR

The HESR is dedicated to supply $\overline{\mathsf{P}}$ANDA with high-quality anti-proton beams over a broad momentum range from 1.5 to 15 GeV/c. In storage rings the complex interplay of many processes like beam-target interaction and intra-beam scattering determines the final equilibrium distribution of the

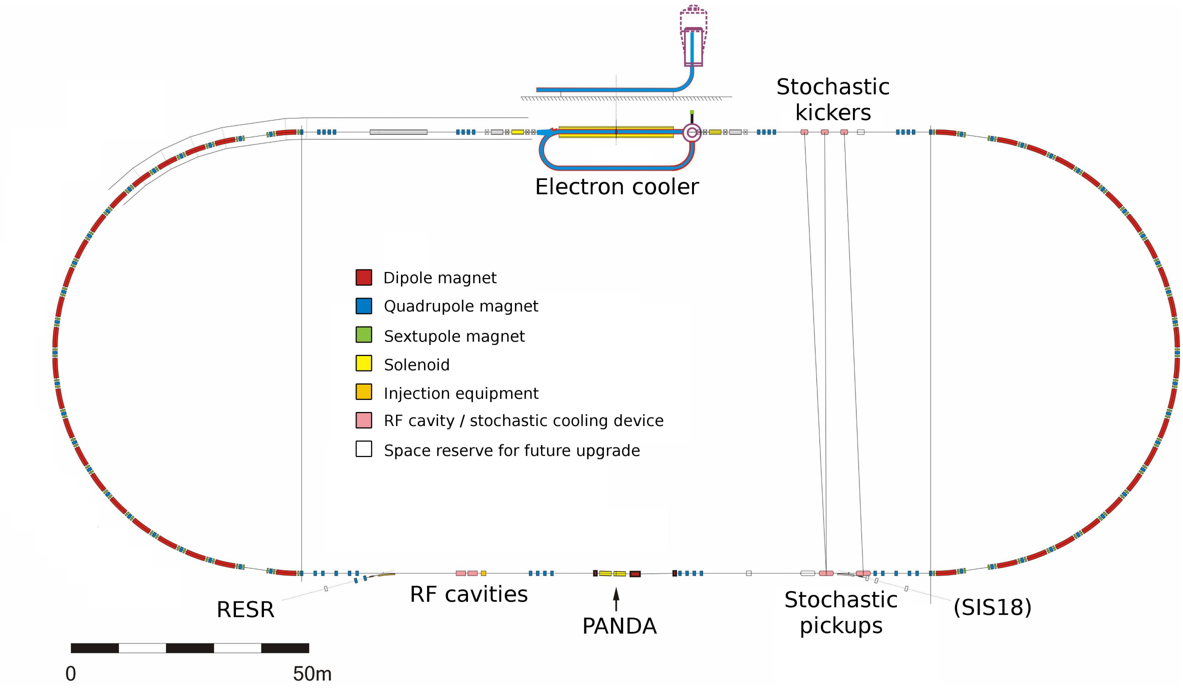

Figure 1.2: Layout of the High Energy Storage Ring HESR. The beam is injected into the lower straight section. Stochastic cooling and electron cooling is foreseen. The location of the $\overline{\text{P}}$ANDA target is indicated with an arrow at the bottom of the figure.

beam particles. Electron and stochastic cooling systems are required to ensure that the specified beam quality and luminosity for experiments at HESR [1, 2, 3, 4, 5, 6] is achieved. Two different operation modes have been worked out to fulfill these experimental requirements: High Luminosity (HL) and High Resolution (HR), respectively (Please also refer to [7] and references therein.)

1.3.1 Lattice Design and Experimental Requirements

The HESR lattice is designed as a racetrack shaped ring with a maximum beam rigidity of 50 Tm (see Fig. 1.2). The basic design consists of FODO cell structures in the arcs. The arc quadrupole magnets will be grouped into four families, to allow a flexible adjustment of transition energy, horizontal and vertical betatron tune, and horizontal dispersion.

A new 2 MV electron cooler is built in close collaboration with the Budker Institute for Nuclear Physics and will be installed at COSY in 2011 []. Technical developments for this electron cooler are important steps towards the 4.5 MV electron cooler. The HESR electron cooler layout will strongly benefit from the experience of the electron cooler operation at COSY. The measurement of beam cooling forces and other features of magnetized electron cooling at high energies are essential for the planned HESR electron cooler. For the start-up phase of the HESR this 2 MV electron cooler is also well suited for beam cooling and accumulation at injection energy.

Due to the modularized construction concept of FAIR, the planned 4.5 MV electron cooling system is postponed to a later stage [8].

Special requirements for the lattice are low dispersion in straight sections and small betatron amplitudes in the range between 1 and 15 m at the internal interaction point (IP) of the $\overline{\text{P}}$ANDA detector. In addition, the betatron amplitude at the electron cooler must be adjustable within a large range between 25 and 200 m. There are by now four defined optical settings: Injection, $\gamma_{tr} = 6.2$, $\gamma_{tr} = 13.4$, $\gamma_{tr} = 33.2$. Both betatron tunes will roughly be 7.62 for different optical settings and natural chromaticities will be ranging in X from -12 to -17 and in Y from -10 to -13. Examples of the optical functions of the $\gamma_{tr} = 6.2$ lattice are shown in Fig. 1.3.

The large aperture spectrometer dipole magnet also deflects the antiproton beam. To compensate for this two further dipole magnets surrounding the setup of the $\overline{\text{P}}$ANDA experiment will be used to cre-

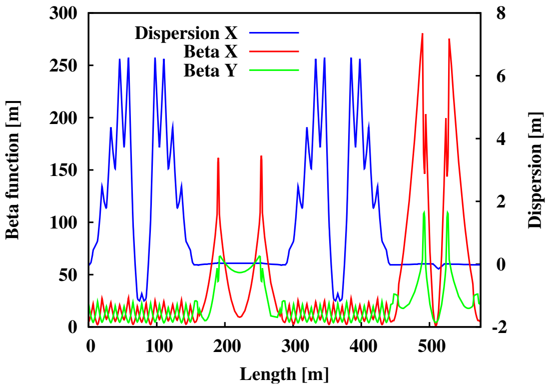

Figure 1.3: Optical functions of HESR lattice for $\gamma_{tr} = 6.2$ optical setting. Plotted are the horizontal dispersion, horizontal and vertical betatron functions. The electron cooler is located at a length of $s=$ 222 m, and the target at s=509 m, where a kink in the horizontal dispersion is generated by the $\overline{\mathsf{P}}$ANDA dipole chicane.

ate a beam chicane. To provide space for $\overline{\mathsf{P}}$ANDA, the two chicane dipoles will be placed 4.6 m upstream and 13 m downstream the $\overline{\mathsf{P}}$ANDA IP. This gives a boundary condition for the placement of the quadrupole elements closest to the experiment. For symmetry reasons, they have to be placed at ±14 m with respect to the IP. The asymmetric placement of the chicane dipoles will result in the experiment axis occurring at a small angle with respect to the axis of the straight section.

Special equipment like multi-harmonic RF cavities, electron and stochastic cooler will enable a high performance of this antiproton storage ring to be achieved, and therefore make high precision experiments feasible. Key tasks for the HESR design work to fulfill these requirements are:

- Design and testing of multi-harmonic RF cavities. Two identical cavities will be installed in the HESR. Both cavities will not only be used to accelerate/decelerate antiprotons in the HESR but also to build a barrier bucket during the experiment, and a moving barrier bucket during the accumulation;

- Development and testing of high-sensitivity stochastic cooling pickups for the frequency range 2 – 4 GHz. The main stochastic cooling parameters have been determined for a cooling system utilising pickups and kickers with a band-width of 2 – 4 GHz and the option for an extension to 4 – 6 GHz. Since stochastic filter-cooling is specified above and stochastic time-of-flight cooling below 3.8 GeV/c, the whole HESR momentum range can be covered by the stochastic cooling system;

- Technical design study and prototyping of critical elements for high-voltage electron cooling system. An electron beam with up to 1 A current, accelerated in special accelerator columns to energies in the range of 0.4 to 4.5 MeV is planned for the HESR. The 24 m long solenoidal field in the cooler section has a longitudinal field strength of 0.2 T with a magnetic field straightness in the order of 10^{-5}. This arrangement allows beam cooling between 1.5 GeV/c and 8.9 GeV/c. Since its design is modular, a future increase of high-voltage to 8 MV is possible, which would make electron cooling feasible in the whole HESR momenta range.

New high-sensitivity pickups for stochastic beam cooling have been designed and build for the HESR. They have been successfully tested with COSY beam and have proven their predicted performance.

Table 1.1 summarises the experimental requirements and operation modes for the full FAIR version. Demanding requirements for high intensity and high quality beams are combined in two operation modes: high luminosity (HL) and high resolution (HR), respectively. The HR mode is defined in the momentum range from 1.5 to 9 GeV/c. To reach a relative momentum spread down to a few times 10^{-5}, only 10^{10} circulating particles in the ring are anticipated. The HL mode requires an order of magnitude higher beam intensity with reduced momentum resolution to reach a peak luminosity of $2\times10^{32}\text{cm}^{-2}\ \text{s}^{-1}$ in the full momentum range up to 15 GeV/c.

1.3.2 Closed orbit correction and Local Orbit Bumps

Closed orbit correction and local orbit bumps at dedicated locations at the accelerator ring are crucial to meet requirements for the beam-target interaction in terms of maximized ring acceptance and optimum beam-target overlap [9].

The most serious causes of closed orbit distortions are angular and spatial displacements of magnets. Alignment and measurement errors of beam position monitors also contribute to closed orbit distortions. Both types of errors have been included in the simulations.

The goal of the orbit correction scheme is to reduce maximum closed orbit deviations to below 5 mm while not exceeding 1 mrad of corrector strength.

Experimental Requirements	
Ion species	Antiprotons
$\bar{p}$ production rate	2×10^7/s (1.2×10^{10} per 10 min)
Momentum / Kinetic energy range	1.5 to 15 GeV/c / 0.83 to 14.1 GeV
Number of particles	10^{10} to 10^{11}
Betatron amplitude at IP	1 – 15 m
Betatron amplitude E-Cooler	25 – 200 m

Operation Modes	
High resolution (HR)	Peak Luminosity of $2{\times}10^{31}\mathrm{cm}^{-2}\ \mathrm{s}^{-1}$ for 10^{10} $\bar{p}$ assuming $\rho_{target} = 4 \cdot 10^{15}$ atoms/cm^2 RMS momentum spread $\sigma_p/p \leq 4 \times 10^{-5}$, 1.5 to 8.9 GeV/$c$
High luminosity (HL)	Peak Luminosity up to $2{\times}10^{32}\mathrm{cm}^{-2}\ \mathrm{s}^{-1}$ for 10^{11} $\bar{p}$ assuming $\rho_{target} = 4 \cdot 10^{15}$ atoms/cm^2 RMS momentum spread $\sigma_p/p \sim 10^{-4}$, 1.5 to 15 GeV/c,

Table 1.1: Experimental requirements and operation modes of HESR for the full FAIR version.

The inverted orbit response matrix method was utilised to obtain the necessary corrector strengths. In this simulation the correction scheme consists of 64 beam position monitors and 48 orbit correction dipoles. In order to verify the possibility to improve the closed orbit, Monte-Carlo methods have been used. More than 10000 different sets of displacement and measurement errors have been applied. For all defined optical settings the effectiveness of the developed closed orbit correction scheme could be demonstrated.

Additionally, the influence of the electron cooler toroids had to be investigated. Toroids are used in beam guiding systems of the electron cooler to overlap the electron beam with the antiproton beam. Since antiprotons are much heavier than electrons, the deflection of the antiprotons by toroids is much smaller. The deflection angles are different for the two transverse directions. To compensate this deflection four additional correction dipoles have to be included in the HESR lattice around the electron cooler. The inner ones need to be placed very close to the toroids to keep orbit deviations as small as possible.

There are a few positions in the straights of the HESR where orbit bumps will have to be used, e.g. at the target. Therefore, all closed orbit correction dipoles in the straights are designed to provide an additional deflection strength of 1 mrad. Investigations have shown that this is sufficient to set angle and position of the circulating beam in the desired ranges.

1.3.3 Luminosity Considerations for Different Hydrogen Targets

In this section beam parameters and luminosities are discussed for the full FAIR version. The FAIR start version will be modularized with a stepwise approach [8].

The maximum average luminosity depends on the antiproton production rate $dN_{\bar{p}}/dt = 2 \cdot 10^7/s$ and consumption rate

$$L_{\max} = \frac{dN_{\bar{p}}/dt}{\sigma_{\mathrm{tot}}} \qquad (1.1)$$

as given in Table 1.2 for different beam momenta.

Beam losses are the main restriction for high luminosities, since the antiproton production rate is limited. Three dominating contributions of beam-target interaction have been identified: Hadronic interaction, single Coulomb scattering and energy straggling of the circulating beam in the target. In addition, single intra-beam scattering due to the Touschek effect has also to be considered for beam lifetime estimates. Beam losses due to residual gas scattering can be neglected compared to beam-target interaction, if the vacuum is better than 10^{-9} mbar. A detailed analysis of all beam loss processes can be found in Ref. [3, 4].

The relative antiproton consumption rate for the total cross section $\sigma_{\mathrm{tot}}$is given by the expression

$$(\tau_{cons}^{-1}) = n_t \sigma_{\mathrm{tot}} f_0 \qquad (1.2)$$

where (τ_{cons}^{-1}) is the relative beam loss rate, n_t the target thickness and f_0 the revolution frequency. In

Table 1.2 the upper limit for beam consumption and corresponding lifetimes are listed for a transverse beam emittance of 1 mm · mrad, a longitudinal ring acceptance of $\Delta p/p = \pm 10^{-3}$ and 10^{11} circulating particles in the ring.

For beam-target interaction, the beam lifetime is independent of the beam intensity, whereas for the Touschek effect it depends on the beam equilibria and beam intensity. Beam lifetimes are ranging from 1540 s to 7100 s. Beam lifetimes at low momenta strongly depend on the beam cooling scenario and the ring acceptance.

The dependence of the cycle averaged luminosity on the cycle time is shown for different antiproton production rates in Fig. 1.4.

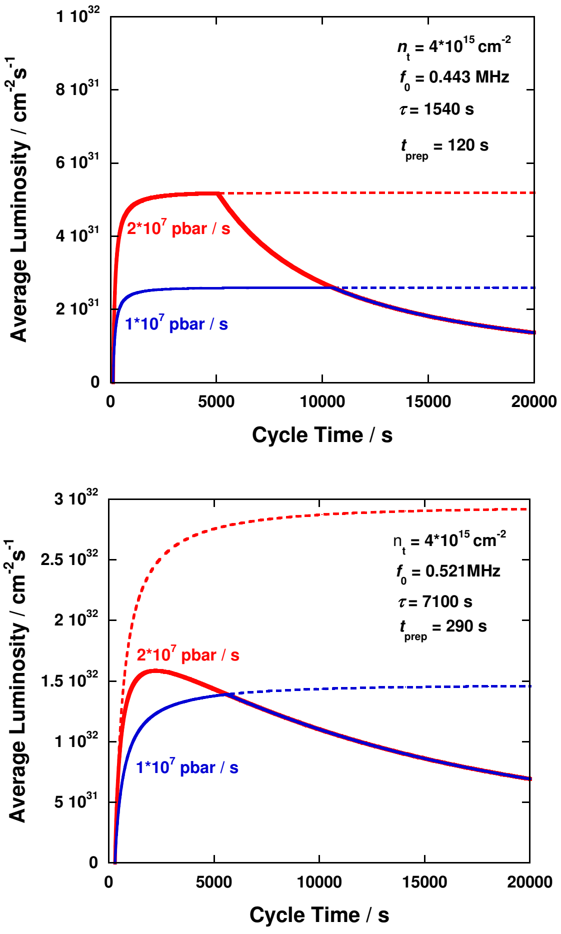

Figure 1.4: Cycle averaged luminosity vs. cycle time at 1.5 GeV/c (top) and 15 GeV/c (bottom). Assuming unlimited maximum number of particles inside the HESR ring one obtains the dashed lines with a production rate of 1 or $2\times10^7\bar{p}$/s (blue or red, respectively). In a more realistic scenario the number of particles which can be stored is limited to 10^{11} (solid lines).

With limited number of antiprotons of 10^{11}, as specified for the high-luminosity mode, cycle averaged luminosities of up to $1.6 \cdot 10^{32}$ cm^{-2}s^{-1} can be achieved at 15 GeV/c for cycle times of less than one beam lifetime. If one does not restrict the number of available particles, cycle times should be longer to reach maximum average luminosities close to $3{\cdot}10^{32}$ cm^{-2}s^{-1}. This is a theoretical upper limit, since the larger momentum spread of the injected beam would lead to higher beam losses during injection due to the limited longitudinal ring acceptance. For the lowest momentum, more than 10^{11} particles can not be provided in average, due to very short beam lifetimes. As expected, cycle average luminosities are below 10^{32} cm^{-2}s^{-1}.

To calculate the cycle average luminosity, machine cycles and beam preparation times have to be specified. After injection, the beam is pre-cooled to equilibrium (with target off) at 3.8 GeV/c. The beam is then ac-/decelerated to the desired beam momentum. A maximum ramp rate of 25 mT/s is specified. After reaching the final momentum beam steering and focusing in the target and beam cooler region takes place. Total beam preparation time t_{prep} ranges from 120 s for 1.5 GeV/c to 290 s for 15 GeV/c. A typical evolution of the luminosity during a cycle is plotted in Fig. 1.5 versus time in the cycle.

In the high-luminosity mode, particles should be re-used in the next cycle. Therefore the used beam is transferred back to the injection momentum and merged with the newly injected beam. A bucket scheme utilizing broad-band cavities is foreseen for beam injection and the refill procedure. During acceleration 1% and during deceleration 5% beam losses are assumed. The cycle average luminosity reads

$$\bar{L} = f_0 N_{i,0} n_t \frac{\tau \left[1 - e^{-t_{\text{exp}}/\tau}\right]}{t_{\text{exp}} + t_{\text{prep}}} \qquad (1.3)$$

where τ is the $1/e$ beam lifetime, t_{exp} the experimental time (beam on target time), and t_{cycle} the total time of the cycle, with $t_{\text{cycle}} = t_{\text{exp}} + t_{\text{prep}}$. $N_{i,0}$ is the number of available particles after the target is switched on. One elegant way to provide constant event rates is given by the possibility to compensate the antiproton consumption during an accelerator cycle by the increase of the cluster/pellet beam density. Alternatively, using a constant target beam density the beam-target overlap might be increased adequately to the beam consumption.

Table 1.2: Max. cycle averaged luminosity for a H_2 pellet target.

	1.5 GeV/c	9 GeV/c	15 GeV/c
Total hadronic cross section/ mbar	100	57	51
Target density: / cm^{-2}	$4 \cdot 10^{15}$	$4 \cdot 10^{15}$	$4 \cdot 10^{15}$
Antiproton production rate: $/s^{-1}$	$2 \cdot 10^{7}$	$2 \cdot 10^{7}$	$2 \cdot 10^{7}$
Beam preparation time: /s	120	140	290
Optimum cycle duration: /s	4820	1400	2230
1/e Beam lifetime: /s	~ 1540	~ 6000	~ 7100
Max Cycle Averaged Luminosity: $/cm^{-2}s^{-1}$	$0.53 \cdot 10^{32}$	$1.69 \cdot 10^{32}$	$1.59 \cdot 10^{32}$

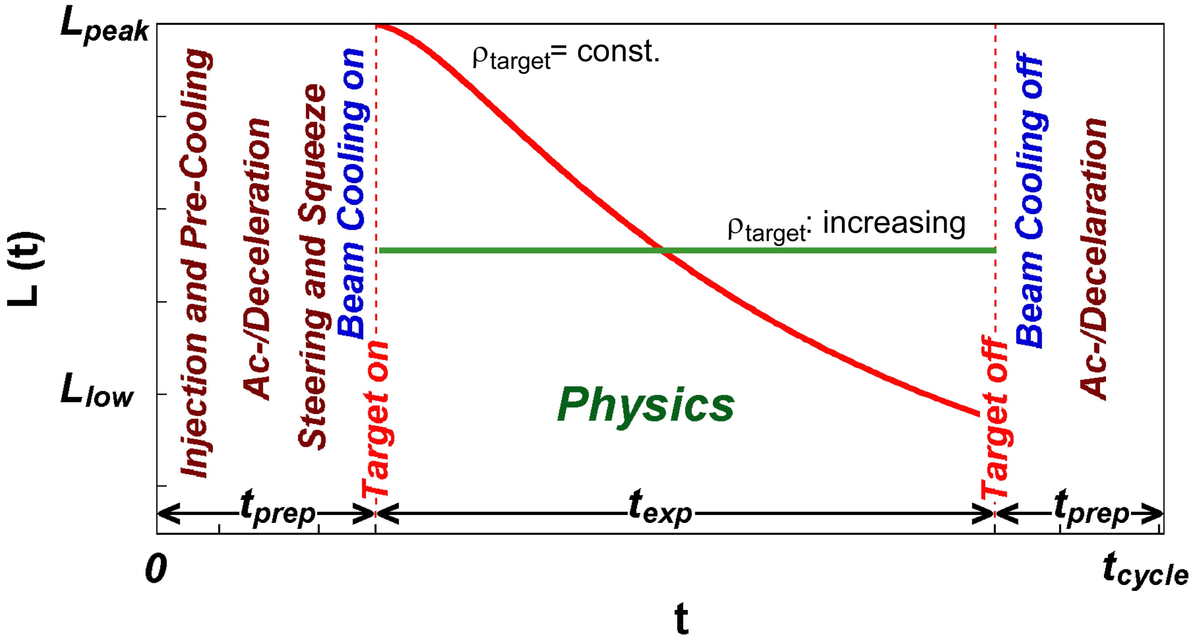

Figure 1.5: Time dependent macroscopic luminosity during the cycle $L(t)$ versus time in cycle. Different measures for beam preparation are indicated.

1.3.4 Hydrogen Pellet Target

1.3.4.1 Beam equilibria

Beam equilibria with electron cooling

The empirical magnetised cooling force formula by V.V. Parkhomchuk is generally used for electron cooling [10], and an analytical description for intra-beam scattering [11]. Beam heating by beam-target interaction is described by transverse and longitudinal emittance growth due to Coulomb scattering and energy straggling [12, 13]. Beam equilibria with electron cooled beams in the HESR have been investigated in detail [14]. In the HR mode RMS relative momentum spreads are ranging from 7.9×10^{-6} (1.5 GeV/c) to 2.7×10^{-5} (8.9 GeV/c), and 1.2×10^{-4} (15 GeV/c) [1].

Beam equilibria with stochastic cooling

Beam equilibria have been simulated based on a Fokker-Planck approach. Applying stochastic cooling with a band-width of 2 – 6 GHz one can achieve a RMS relative momentum spread of 5.1×10^{-5} (3.8 GeV/c), 5.4×10^{-5} (8.9 GeV/c) and 3.9×10^{-5} (15 GeV/c) for the HR mode [15]. In the HL mode RMS relative momentum spread of roughly 10^{-4} can be expected. Transverse stochastic cooling can be adjusted independently to ensure sufficient beam-target overlap.

The relative momentum spread can be further improved by combining electron- and stochastic cooling.

1.3.5 Hydrogen Cluster Target

Calculations have also been performed for a hydrogen cluster target with an effective target thickness of $8 \cdot 10^{14}$ atoms/cm^2. Beam loss and luminosity estimates for a cluster target are discussed in this paragraph. Beam equilibria are expected to be equal to the case of pellet targets since beam heating is dominated by intrabeam scattering for the considered phase space densities.

1.3.5.1 Beam losses and luminosity estimates

In Table 1.3 relative beam loss rates, beam lifetimes and the maximum average luminosities with cluster target are summarized for different beam momenta. These estimates are base on the same beam conditions and machine parameters as for pellet targets (see last paragraph).

With cluster targets beam lifetimes are roughly 2.5 to 5 times larger compared to pellet targets. The maximum achievable luminosity does not depend on the target thickness. Theoretically, maximum luminosities could be achieved with a much larger number of circulation antiprotons. The dependence of the cycle averaged luminosity on the cycle time is shown for different antiproton production rates in Fig. 1.6. The same beam preparation times have been applied for both target types.

As expected, cycle averaged luminosities are roughly a factor of two to five smaller for cluster targets compared to pellet targets if the maximum number of antiprotons in the HESR is limited to 10^{11}. Cycle averaged luminosities of $3.7 \cdot 10^{31}\mathrm{cm}^{-2}\mathrm{s}^{-1}$ can be achieved at 15 GeV/c and $2.9 \cdot 10^{31}\mathrm{cm}^{-2}\mathrm{s}^{-1}$ at 1.5 GeV/c for maximum antiproton production rate. By increasing the maximum number of antiprotons in the HESR the cycle averaged luminosity using a cluster target can be significantly enhanced up to the maximum possible value shown in Table 1.3. An increased number of antiprotons would result in higher intrabeam scattering rates and thus in larger beam equilibria. Also the injection and accumulation process would lead to larger beam losses during injection due to the limited longitudinal ring acceptance and cooling power.

Due to the lower target density by a factor of five the achievable luminosity will be smaller compared to the pellet operation. For the high luminosity mode the cycle averaged luminosity is only reduced by roughly a factor of one to four, depending on the beam momentum and antiproton production rate. The specified beam equilibria in the high-resolution mode can also be reached with approximately the same reduction of the cycle averaged luminosities.

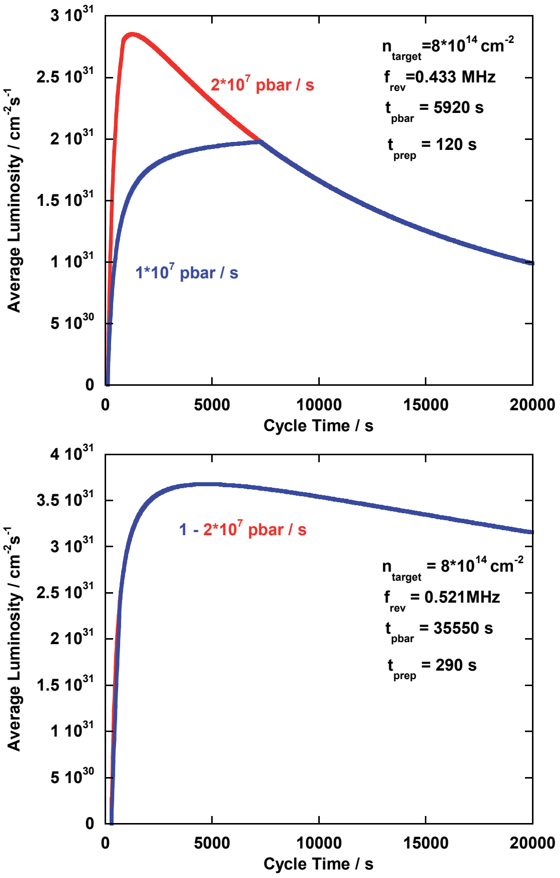

Figure 1.6: Cycle averaged luminosity vs. cycle time at 1.5 GeV/c (top) and 15 GeV/c (bottom). Assuming a limited maximum number of particles of $n = 10^{11}$ inside the HESR ring, one obtains two different luminosity estimates for a production rate of 1 or $2 \times 10^7 \bar{p}$/s (blue or red, respectively).

1.3.6 Time Structure of the Luminosity

Contrary to homogeneous cluster beams, a distinct time structure of the luminosity distribution is expected for the granular volume density distribution of a pellet beam. The time structure depends on the transverse and longitudinal overlap between single pellets and the circulating antiproton beam in the interaction region. Therefore, details of the pellet beam distribution have to be included in calculations of the time dependent luminosity distribution.

Two different time-scale processes have to be distinguished:

- Long-term processes are mainly depending on general antiproton and pellet beam parameters like particle number, transverse and longitudi-

Table 1.3: Max. cycle averaged luminosity for a H_2 cluster target.

	1.5 GeV/c	9 GeV/c	15 GeV/c
Target density: /cm^{-2}	$8 \cdot 10^{14}$	$8 \cdot 10^{14}$	$8 \cdot 10^{14}$
Antiproton production rate: /s^{-1}	$2 \cdot 10^{7}$	$2 \cdot 10^{7}$	$2 \cdot 10^{7}$
Beam preparation time: /s	120	140	290
Optimum cycle duration: /s	1280	2980	4750
1/e Beam lifetime: /s	~ 5920	~ 29560	~ 35550
Max Cycle Averaged Luminosity: /cm^{-2}s^{-1}	$0.29 \cdot 10^{32}$	$0.38 \cdot 10^{32}$	$0.37 \cdot 10^{32}$

nal profiles. Beam losses and beam equilibria caused by target heating, intrabeam scattering and beam cooling are sufficient to characterize the long-term luminosity performance. Characteristic time scales for those processes are in the order of few minutes up to hours and have been discussed in the previous chapter.

- Short-term processes are caused by luminosity variations while single pellets are crossing the antiproton beam and take place on a microsecond time scale. An algorithm was developed and implemented into the BETACOOL that calculates time-dependent luminosity distributions in the microsecond regime [16]. For benchmarking of the implemented algorithm, results of an experiment with the WASA pellet target at the COSY storage ring have been compared to simulation results. During the COSY run in mid 2008 time-dependent luminosity distributions have been recorded. The comparison of simulations with the recorded data showed a good agreement [17].

1.3.7 Effective Luminosities

Based on the new algorithm implemented in the BETACOOL code the effective luminosity on short-time scales have also been simulated for the PANDA experiment with pellet targets [16]. If the detector is overloaded its counting rate is no longer proportional to the provided luminosity, but depends on the capability of the readout and data acquisition system. In such a case the ratio of peak to mean luminosity can reach unacceptable large values. The short-time luminosity variation has been calculated with an integration step of a microsecond for two ultimate types of detector response. If the single detectors are overloaded, the count rate value is saturated and equal to the detector limit (”top-cut” model) or the detectors are completely closed and cannot accept any event anymore - the count rate is zero (“full-cut”). The response of real detectors will certainly be in between these two ultimate cases.

The numerical simulation of the effective luminosity was done for two operational regimes of the $\overline{\text{P}}$ANDA experiment: with high-luminosity (HL) and high resolution (HR) modes. The dependence of the effective luminosity on the pellet size for different detector limits was investigated in detail.

The simulation results show that the effective luminosity for the HR mode equals the mean luminosity if the pellet size is less than 20 μm and all single detectors of $\overline{\text{P}}$ANDA are designed for the maximum luminosity values of $2 \cdot 10^{32}$ cm^{-2}s^{-1}. In the case of the high luminosity mode the effective luminosity is rather different for ”top-cut” and ”full-cut” models. For the ”top-cut” model the maximum pellet size has to be less than 20 μm if the detector limits are below a mean luminosity of $2 \cdot 10^{33}$ cm^{-2}s^{-1}. For the ”full-cut” model the pellet size has to be less than 10 μm and detector limit is sufficiently higher than $2 \cdot 10^{33}$ cm^{-2}s^{-1}. Therefore, the pellet target operation for the high luminosity mode requires either a detector design close to ”top-cut” mode, more than 20 times higher detector limits compared to the mean luminosity or a pellet size of less than 10 μm.

Depending on the detector performance (maximum acceptable luminosity and dead-time characteristics) the difference of the event rate between cluster-jet and pellet target operation is expected to be even smaller than the one for cycle averaged luminosities.

1.4 The $\overline{\text{P}}$ANDA Detector

The main objectives of the design of the $\overline{\text{P}}$ANDA experiment are to achieve 4π acceptance, high resolution for tracking, particle identification and calorimetry, high rate capabilities and a versatile readout and event selection. To obtain a good momentum resolution the detector will be composed of two magnetic spectrometers: the *Target Spectrometer (TS)*, based on a superconducting solenoid magnet surrounding the interaction point, which will be used to measure at large angles and the *For-*

ward Spectrometer (FS), based on a dipole magnet, for small angle tracks. A silicon vertex detector will surround the interaction point. In both spectrometer parts, tracking, charged particle identification, electromagnetic calorimetry and muon identification will be available to allow to detect the complete spectrum of final states relevant for the $\overline{\text{P}}$ANDA physics objectives.

1.4.1 Target Spectrometer

The Target Spectrometer will surround the interaction point and measure charged tracks in a highly homogeneous (better than ±2%) solenoidal field of 2 T. In the manner of a collider detector it will contain detectors in an onion shell like configuration. Pipes for the injection of target material will have to cross the spectrometer perpendicular to the beam pipe.

The Target Spectrometer will be arranged in three parts: the barrel covering angles between 22° and 140°, the forward end cap extending the angles down to 5° and 10° in the vertical and horizontal planes, respectively, and the backward end cap covering the region between about 145° and 170°. Please refer to Fig. 1.7 for an overview.

1.4.1.1 Target

The compact design of the detector layers nested inside the solenoidal magnetic field, combined with the request of minimal distance from the interaction point to the vertex tracker, leaves only a very restricted space for the target installations. In order to reach the design luminosity of 2×10^{32} $\mathrm{s}^{-1}\mathrm{cm}^{-2}$ a target thickness of about 4×10^{15} hydrogen atoms per cm^2 is required assuming 10^{11} stored anti-protons in the HESR ring.

These conditions pose a real challenge for an internal target inside a storage ring. At present, two different, complementary techniques for the internal target are being developed further: the cluster-jet target and the pellet target. Both techniques are capable of providing sufficient densities for hydrogen at the interaction point, but exhibit different properties concerning their effect on the beam quality and the definition of the interaction point. In addition, internal targets also of heavier gases, deuterium, nitrogen or argon can be made available.

For non-gaseous nuclear targets the situation is different, in particular in the case of the planned hypernuclear experiment. In these studies, the whole upstream end cap and part of the inner detector geometry will be modified.

Cluster-Jet Target The expansion of pressurised cold hydrogen gas into vacuum through a Laval-type nozzle leads to a condensation of hydrogen molecules forming a narrow supersonic jet of hydrogen clusters. The cluster size varies from 10^3 to 10^6 hydrogen molecules tending to become larger at higher inlet pressure and lower nozzle temperatures. Such a cluster-jet with density of 10^{15} atoms/cm^2 acts as a very diluted target since it may be seen as a localised and homogeneous monolayer of hydrogen atoms being passed by the antiprotons once per revolution.

Fulfilling the luminosity demand for $\overline{\text{P}}$ANDA still requires a density increase compared to current applications. Additionally, due to detector constraints, the distance between the cluster-jet nozzle and the target will be larger than usual. The great advantage of cluster targets is the homogeneous density profile and the possibility to focus the antiproton beam at highest phase space density. Hence, the interaction point is defined transversely but has to be reconstructed longitudinally in beam direction. In addition the low β-function of the antiproton beam keeps the transverse beam target heating effects at the minimum. The possibility of adjusting the target density along with the gradual consumption of antiprotons for running at constant luminosity will be an important feature.

Pellet Target The pellet target features a stream of frozen hydrogen micro-spheres, called pellets, traversing the antiproton beam perpendicularly. Typical parameters for pellets at the interaction point are the rate of $15 - 150 \times 10^3\,\mathrm{s}^{-1}$, the pellet size of $10 - 30\,\mu$m, and the velocity of about 60 m/s. At the interaction point the pellet train has a lateral spread of $\approx$ 11.5 mm and an interspacing of pellets that varies between 0.5 to 4 mm. With proper adjustment of the β-function of the coasting antiproton beam at the target position, the design luminosity for $\overline{\text{P}}$ANDA can be reached in time average. The present R&D is concentrating on minimising the luminosity variations such that the instantaneous interaction rate does not exceed the rate capability of the detector systems. Due to the large number of interactions expected in every pellet, and thanks to the foreseen pellet tracking system, a resolution in the vertex position of $50\,\mu$m will be possible with this target.

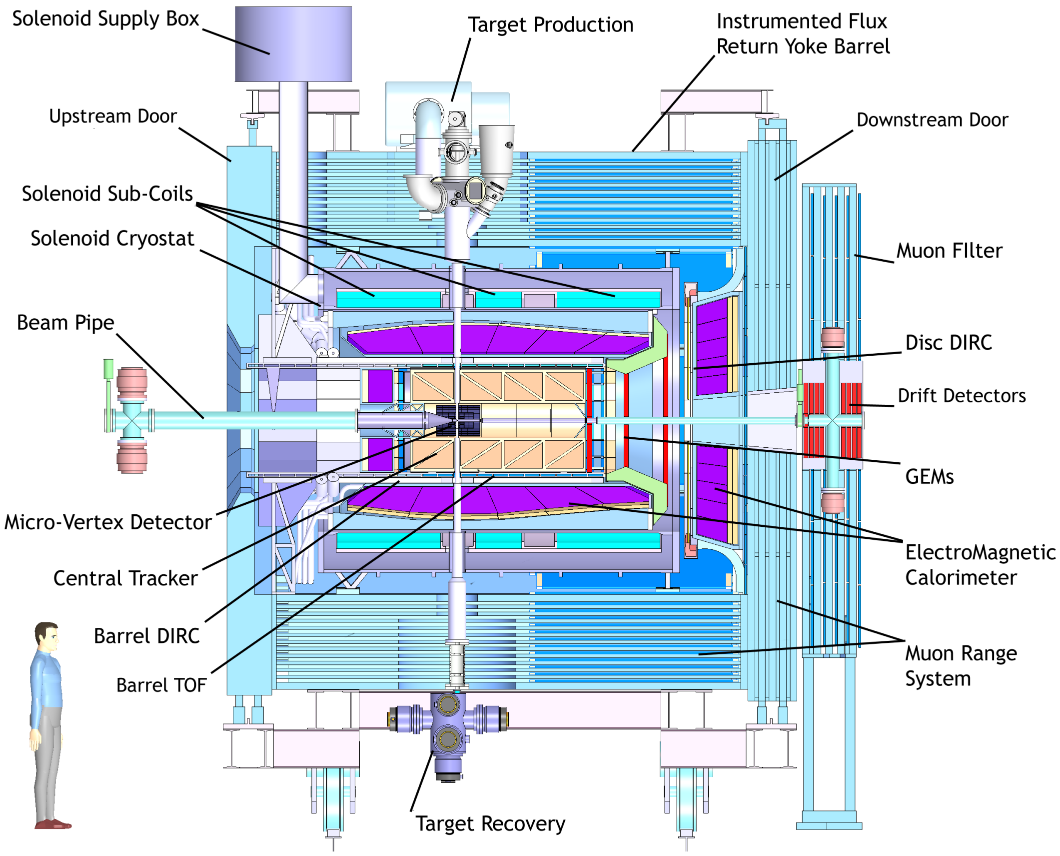

Figure 1.7: Artistic side view of the Target Spectrometer (TS) of $\overline{\mathrm{P}}$ANDA. To the right of this the Forward Spectrometer (FS) follows, which is illustrated in Fig. 1.12.

Other Targets are under consideration for the hypernuclear studies where a separate target station upstream will comprise primary and secondary target and detectors. Moreover, current R&D is being undertaken for the development of a liquid helium target. A wire target may be employed to study antiproton-nucleus interactions.

1.4.1.2 Solenoid Magnet

The magnetic field in the Target Spectrometer will be provided by a superconducting solenoid coil with an inner radius of 105 cm and a length of 2.8 m. The maximum magnetic field needs to be 2 T. The field homogeneity is foreseen to be better than 2% over the volume of the vertex detector and central tracker. In addition the transverse component of the solenoid field should be as small as possible, in order to allow a uniform drift of charges in the time projection chamber. This is expressed by a limit of $\int B_r/B_z dz < 2\,\mathrm{mm}$ for the normalised integral of the radial field component.

In order to minimise the amount of material in front of the electromagnetic calorimeter, the latter will be placed inside the magnetic coil. The tracking devices in the solenoid will cover angles down to 5°/10° where momentum resolution is still acceptable. The dipole magnet with a gap height of 1.4 m provides a continuation of the angular coverage to smaller polar angles.

The cryostat for the solenoid coils is required to have two warm bores of 100 mm diameter, one above and one below the target position, to allow for insertion of internal targets.

The proposed $\overline{\mathrm{P}}$ANDA Target Spectrometer solenoid is comparable by dimensions and field to the solenoid built in the late eighties for the ZEUS experiment at HERA, the proton electron collider of the DESY laboratory at Hamburg.

The winding construction proposed for the solenoid is based on the well proven technique used for the superconducting coils used since the beginning of the eighties in the High Energy Physics and nuclear physics experiments. We propose to use the same technology used for superconducting solenoids like CELLO and ZEUS (DESY), ALEPH, DELPHI, ATLAS, CMS (CERN), BABAR (SLAC), CDF (FERMILAB), BELLE (KEK), FINUDA, KLOE (LNF_INFN).

1.4.1.3 Micro-Vertex Detector

The design of the micro-vertex detector (MVD) for the Target Spectrometer is optimised for the detection of secondary vertices from D and hyperon decays and maximum acceptance close to the interaction point. It will also strongly improve the transverse momentum resolution. The setup is depicted in Fig. 1.8.

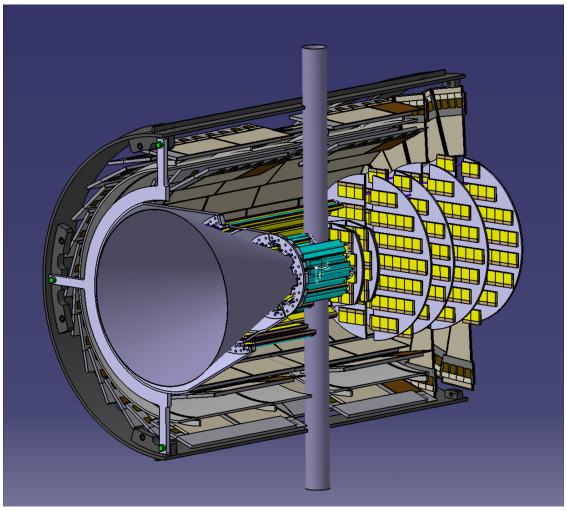

Figure 1.8: The Micro-Vertex Detector (MVD) of the Target Spectrometer surrounding the beam and target pipes seen from upstreams. The outer barrel layers are cut for visibility.

The concept of the MVD is based on radiation hard silicon pixel detectors with fast individual pixel readout circuits and silicon strip detectors. The layout foresees a four layer barrel detector with an inner radius of 2.5 cm and an outer radius of 13 cm. The two innermost layers will consist of pixel detectors and the outer two layers will consist of double sided silicon strip detectors.

Eight detector wheels arranged perpendicular to the beam will achieve the best acceptance for the forward part of the particle spectrum. Here again, the inner four layers will be made entirely of pixel detectors, the following two will be a combination of strip detectors on the outer radius and pixel detectors closer to the beam pipe. Finally the last two wheels, made entirely of silicon strip detectors, will be placed further downstream to achieve a better acceptance of hyperon cascades.

1.4.1.4 Central Tracker

The charged particle tracking devices must handle the high particle fluxes that are anticipated for a luminosity of up to several $10^{32}\,\mathrm{cm^{-2}s^{-1}}$. The momentum resolution $\delta p/p$ has to be on the percent level. The detectors should have good detection efficiency for secondary vertices which can occur outside the inner vertex detector (e.g. K^0_S, Λ, Ξ). This will be achieved by the combination of the silicon vertex detectors close to the interaction point (MVD) with two outer systems. One system will cover a large area and is designed as a barrel around the MVD. This will be either a stack of straw tubes (STT) or a time-projection chamber (TPC). The forward angles will be covered using three sets of GEM trackers similar to those developed for the COMPASS experiment at CERN. The two options for the central tracker are explained briefly in the following.

Straw Tube Tracker (STT) This detector will consist of aluminised Mylar tubes called *straws*, which will be self supporting by the operation at 1 bar overpressure. The straws are to be arranged in planar layers which are mounted in a hexagonal shape around the MVD as shown in Fig. 1.9. In total there are 27 layers of which the 8 central ones are tilted to achieve an acceptable resolution of 3 mm also in z (parallel to the beam). The gap to the surrounding detectors will be filled with further individual straws. In total there will be 4636 straws around the beam pipe at radial distances between 15 cm and 41.8 cm with an overall length of 150 cm. All straws have a diameter of 10 mm. A thin and light space frame will hold the straws in place, the force of the wire however is kept solely by the straw itself. The Mylar foil is 27 μm thick, the wire is made of 20 μm thick gold plated tungsten. This design results in a material budget of 1.2 % of a radiation length.

The gas mixture used will be Argon based with CO_2 as quencher. It is foreseen to have a gas gain no greater than 10^5 in order to warrant long term operation. With these parameters, a resolution in x and y coordinates of less than 150 μm is expected.

Time Projection Chamber (TPC) A challenging alternative to the STT is a TPC, which would combine superior track resolution with a low material

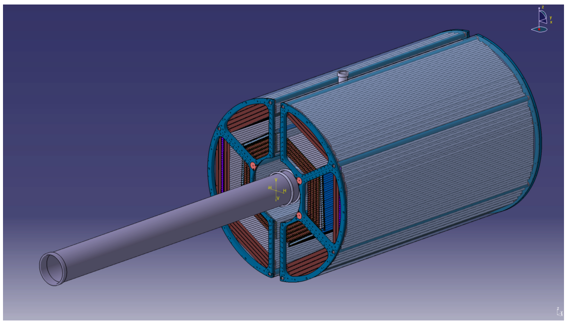

Figure 1.9: Straw Tube Tracker (STT) of the Target Spectrometer with beam and target pipes seen from upstreams.

budget and additional particle identification capabilities through energy loss measurements.

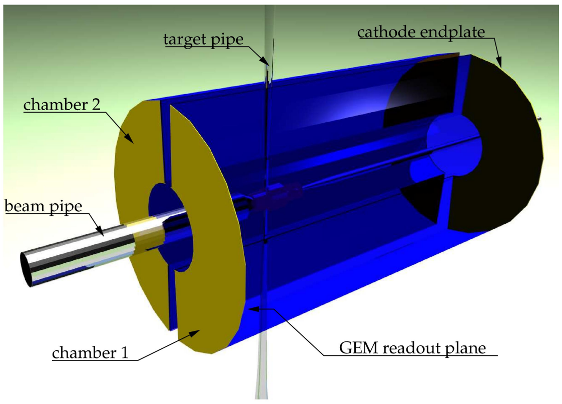

Figure 1.10: GEM Time Projection Chamber (TPC) of the Target Spectrometer with beam and target pipes seen from upstreams.

The planned TPC depicted in a schematic view in Fig. 1.10 will consist of two large gas-filled half-cylinders enclosing the target and beam pipe and surrounding the MVD. An electric field along the cylinder axis separates positive gas ions from electrons created by ionising particles traversing the gas volume. The electrons drift with constant velocity towards the anode at the upstream end face and create an avalanche detected by a pad readout plane yielding information on two coordinates. The third coordinate of the track comes from the measurement of the drift time of each primary electron cluster. In common TPCs the amplification stage typically occurs as in multi-wire proportional chambers. These are gated by an external trigger to avoid a continuous back flow of ions in the drift volume which would distort the electric drift field and jeopardise the principle of operation. In $\overline{\mathrm{P}}$ANDA the interaction rate will be too high and there is no fast external trigger to allow such an operation. Therefore a novel readout scheme will be employed which is based on Gas Electron Multiplier (GEM) foils as amplification stage.

From the viewpoint of the $\overline{\mathrm{P}}$ANDA solenoid magnet, the compatibility with the TPC requires a very good homogeneity of the solenoid field with a low radial component. The solenoid magnet was designed, anyhow, to comply with the most stringent requirements coming from both solutions.

Forward GEM Detectors Particles emitted at angles below 22° which are not covered fully by the Straw Tube Tracker or TPC will be tracked by three stations of Gas Electron Multiplier (GEM) detectors placed 1.1 m, 1.4 m and 1.9 m downstream of the target. The chambers have to sustain a high counting rate of particles peaked at the most forward angles due to the relativistic boost of the reaction products as well as due to the small angle $\bar{p}p$ elastic scattering. With the envisaged luminosity, the expected particle flux in the first chamber in the vicinity of the 5 cm diameter beam pipe will be about $3 \times 10^4\,\mathrm{cm}^{-2}\mathrm{s}^{-1}$. Gaseous micro-pattern detectors based on GEM foils as amplification stages are chosen. These detectors have rate capabilities three orders of magnitude higher than drift chambers. In the current layout there will be three double planes with two projections per plane.

1.4.1.5 Cherenkov Detectors and Time-of-Flight

Charged particle identification of hadrons and leptons over a large range of angles and momenta is an essential requirement for meeting the physics objectives of $\overline{\mathrm{P}}$ANDA. There will be several dedicated systems which, complementary to the other detectors, will provide means to identify particles. The main part of the momentum spectrum above 1 GeV/c will be covered by Cherenkov detectors. Below the Cherenkov threshold of kaons several other processes have to be employed for particle identification. In addition a time-of-flight barrel will identify slow particles.

Scintillator Tile Barrel Time-of-Flight For slow particles at large polar angles particle identification will be provided by a time-of-flight detector. This detector also provides precision timing of tracks for event building and fast software triggers.

The detector is based on scintillator tiles of 28.5×28.5 mm^2 size read out individually by two Silicon Photomultipliers per tile and it should achieve a time resolution of 100 ps. The detector is positioned just outside the fused silica radiator of the Barrel DIRC described in the next paragraph. It can also detect photon conversions in the DIRC radiator. The full system consists of 5760 tiles in the barrel and can be augmented also by approx 1000 tiles in forward direction just in front of the endcap disc DIRC.

This concept takes the optimization of material and thickness to the extreme implementing a timing detector with less than 2% of a radiation length and less than 2 cm radial thickness including readout and mechanics. It can also be used as well timed input with a good spatial granularity for online pattern recognition.

Barrel DIRC At polar angles between 22° and 140°, particle identification will be performed by the detection of internally reflected Cherenkov (DIRC) light as realised in the BaBar detector [18]. It will consist of 1.7 cm thick fused silica (artificial quartz) slabs surrounding the beam line at a radial distance of 45 - 54 cm. At BaBar the light was imaged across a large stand-off volume filled with water onto 11 000 photomultiplier tubes. At $\overline{\text{P}}$ANDA, it is intended to focus the images by lenses onto micro-channel plate photomultiplier tubes (MCP PMTs) which are insensitive to magnet fields. This fast light detector type allows a more compact design and the readout of two spatial coordinates.

The DIRC design with its compact radiator mounted close to the EMC will minimise the conversions. Part of these conversions will be recovered with information from the DIRC detector, as was shown by BaBar [19].

Forward End-Cap DIRC A similar concept can be employed in the forward direction for particles between 5° and 22°. The same radiator, fused silica, is to be employed however in shape of a disk. The radiator disk will be 2 cm thick and will have a radius of 110 cm. It will be placed directly upstream of the forward end cap calorimeter. At the rim around the disk the Cherenkov light will be measured by focusing elements. In addition measuring the time of propagation the expected light pattern can be distinguished in a 3-dimensional parameter space. Dispersion correction is achieved by the use of alternating dichroic mirrors transmitting and reflecting different parts of the light spectrum. As photon detectors either silicon photomultipliers or microchannel plate PMTs are considered.

1.4.1.6 Electromagnetic Calorimeters

Expected high count rates and a geometrically compact design of the Target Spectrometer require a fast scintillator material with a short radiation length and Molière radius for the construction of the electromagnetic calorimeter (EMC). Lead tungsten ($PbWO_4$) is a high density inorganic scintillator with sufficient energy and time resolution for photon, electron, and hadron detection even at intermediate energies [20, 21, 22].

The crystals will be 20 cm long, i.e. approximately $22\,X_0$, in order to achieve an energy resolution below 2 % at 1 GeV [20, 21, 22] at a tolerable energy loss due to longitudinal leakage of the shower. Tapered crystals with a front size of $2.1\times 2.1\,\text{cm}^2$ will be mounted in the barrel EMC with an inner radius of 57 cm. This implies 11360 crystals for the barrel part of the calorimeter. The forward end cap EMC will be a planar arrangement of 3600 tapered crystals with roughly the same dimensions as in the barrel part, and the backward end cap EMC comprises of 592 crystals. The readout of the crystals will be accomplished by large area avalanche photo diodes in the barrel and in the backward end cap, vacuum photo-triodes will be used in the forward end cap. The light yield can be increased by a factor of about 4 compared to room temperature by cooling the crystals down to -25°C. The arrangement of the barrel and forward end cap calorimeters is shown in Fig. 1.11.

The EMC will allow to achieve an e/π ratio of 10^3 for momenta above 0.5 GeV/c. Therefore, e-π-separation will not require an additional gas Cherenkov detector in favour of a very compact geometry of the EMC. For further details please refer to Ref. [23].

1.4.1.7 Muon Detectors

In the barrel region the yoke is segmented and will consist of 13 layers in total: the innermost layer will have a thickness of 6 cm equal to the outermost one, in between 11 layers of 3 cm thickness will be located. The gaps for the detectors will be 3 cm wide. This is enough material for the absorption of pions in the momentum range in $\overline{\text{P}}$ANDA at these angles. In the forward end cap more material is needed. Since the downstream door of the return yoke has to fulfil constraints for space and accessibility, the muon system will split in several layers.

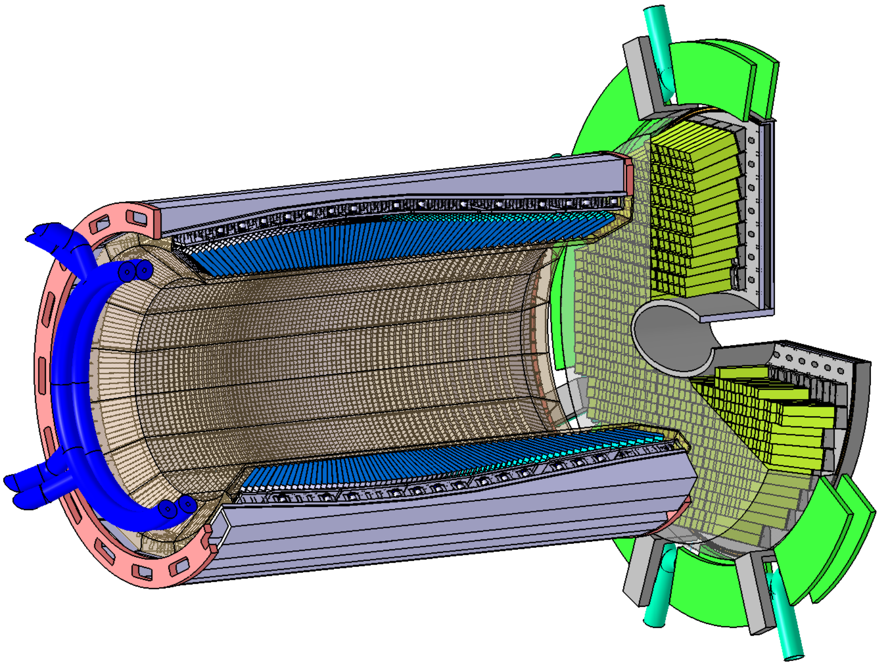

Figure 1.11: Barrel and forward end cap of the Electro-Magnetic Calorimeter (EMC) with its mounting structures and cooling pipes. These structures will be mounted directly inside the cryostat and forward end of the flux return yoke.

Six detection layers will be placed around five iron layers of 6 cm each within the door, and a removable muon filter with additional five layers of 6 cm iron is located in the space between the solenoid and the dipole. This filter has to provide cut-outs for forward detectors and pump lines and has to be built in a way that it can be removed with few crane operations to allow easy access to these parts. The integration with the muon system was the most challenging requirement for the instrumented flux return yoke design.

As detector within the absorber layers rectangular aluminum drift tubes will be used as they were constructed for the COMPASS muon detection system. They are essentially drift tubes with additional capacitive coupled strips read out on both ends to obtain the longitudinal coordinate.

1.4.1.8 Hypernuclear Detector

The hypernuclei study will make use of the modular structure of $\overline{\text{P}}$ANDA. Removing the backward end cap calorimeter will allow to add a dedicated nuclear target station and the required additional detectors for γ spectroscopy close to the entrance of $\overline{\text{P}}$ANDA. While the detection of anti-hyperons and low momentum K^+ can be ensured by the universal detector and its PID system, a specific target system and a γ-detector are additional components required for the hypernuclear studies.

Active Secondary Target The production of hypernuclei proceeds as a two-stage process. First hyperons, in particular $\Xi\bar{\Xi}$, are produced on a nuclear target. In some cases the Ξ will be slow enough to be captured in a secondary target, where it reacts in a nucleus to form a double hypernucleus.

The geometry of this secondary target is determined by the short mean life of the Ξ^- of only 0.164 ns. This limits the required thickness of the active secondary target to about 25–30 mm. It will consist of a compact sandwich structure of silicon micro strip detectors and absorbing material. In this way the weak decay cascade of the hypernucleus can be detected in the sandwich structure.

Germanium Array An existing germanium-array with refurbished readout will be used for the γ-spectroscopy of the nuclear decay cascades of hypernuclei. The main limitation will be the load due to neutral or charged particles traversing the germanium detectors. Therefore, readout schemes and tracking algorithms are presently being developed

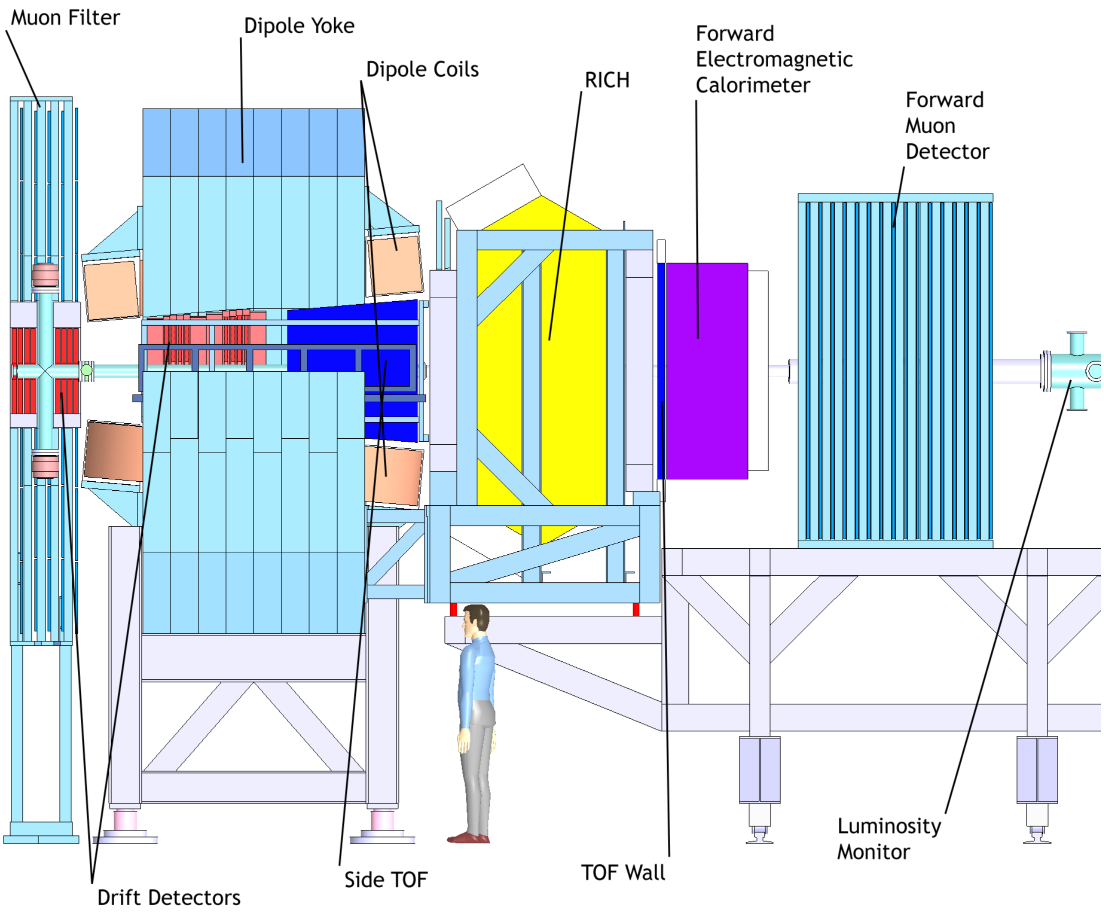

Figure 1.12: Artistic side view of the Forward Spectrometer (FS) of $\overline{\mathrm{P}}$ANDA. It is preceded on the left by the Target Spectrometer (TS), which is illustrated in Fig. 1.7.

which will enable high resolution γ-spectroscopy in an environment of high particle flux.

1.4.2 Forward Spectrometer

The Forward Spectrometer (FS) will cover all particles emitted in vertical and horizontal angles below ±5° and ±10°, respectively. Charged particles will be deflected by an integral dipole field of 2 Tm. Cherenkov detectors, calorimeters and muon counters ensure the detection of all particle types. Please refer to Fig. 1.12 for an overview.

1.4.2.1 Dipole Magnet

A 2 Tm dipole magnet with a window frame, a 1 m gap, and more than 2 m aperture will be used for the momentum analysis of charged particles in the Forward Spectrometer. In the current planning, the magnet yoke will occupy about 1.6 m in beam direction starting from 3.9 m downstream of the target. Thus, it covers the entire angular acceptance of the Target Spectrometer of ±10° and ±5° in the horizontal and in the vertical direction, respectively. The bending power of the dipole on the beam line causes a deflection of the antiproton beam at the maximum momentum of 15 GeV/c of 2.2°. The designed acceptance for charged particles covers a dynamic range of a factor 15 with the detectors downstream of the magnet. For particles with lower momenta, detectors will be placed inside the yoke opening. The beam deflection will be compensated by two correcting dipole magnets, placed around the $\overline{\mathrm{P}}$ANDA detection system.

1.4.2.2 Forward Trackers

The deflection of particle trajectories in the field of the dipole magnet will be measured with three pairs of tracking drift detectors. The first pair will be placed in front, the second within and the third behind the dipole magnet. Each pair will contain two autonomous detectors as described below. Thus, in total, 6 independent detectors will be mounted. Each tracking detector will consist of four double-layers of straw tubes (see Fig. 1.13), two with vertical wires and two with wires inclined by a few degrees. The optimal angle of inclination with respect to vertical direction will be chosen on the basis of ongoing simulations. The planned configuration of double-layers of straws will allow to reconstruct tracks in each pair of tracking detectors separately, also in case of multi-track events.

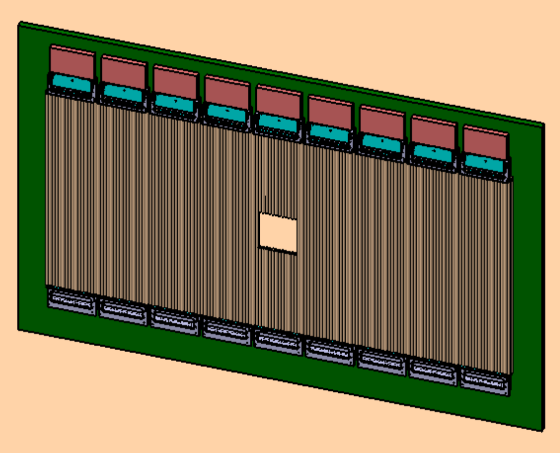

Figure 1.13: Double layer of straw tubes with preamplifier cards and gas manifolds mounted on rectangular support frame. The opening in the middle of the detector is foreseen for the beam pipe.

1.4.2.3 Forward Particle Identification

RICH Detector To enable the π/K and K/p separation also at the highest momenta a RICH detector is proposed. The favoured design is a dual radiator RICH detector similar to the one used at HERMES [24]. Using two radiators, silica aerogel and C_4F_{10} gas, provides π/K/p separation in a broad momentum range from 2 to 15 GeV/c. The two different indices of refraction are 1.0304 and 1.00137, respectively. The total thickness of the detector is reduced to the freon gas radiator (5% X_0), the aerogel radiator (2.8% X_0), and the aluminum window (3% X_0) by using a lightweight mirror focusing the Cherenkov light on an array of photo-tubes placed outside the active volume.

Time-of-Flight Wall A wall of slabs made of plastic scintillator and read out on both ends by fast photo-tubes will serve as time-of-flight stop counter placed at about 7 m from the target. In addition, similar detectors will be placed inside the dipole magnet opening, to detect low momentum particles which do not exit the dipole magnet. With the expected time resolution of $\sigma = 50\,\text{ps}$ π/K and K/p separation on a $3\,\sigma$ level will be possible up to momenta of 2.8 GeV/c and 4.7 GeV/c, respectively.

1.4.2.4 Forward Electromagnetic Calorimeter

For the detection of photons and electrons a Shashlyk-type calorimeter with high resolution and efficiency will be employed. The detection is based on lead-scintillator sandwiches read out with wavelength shifting fibres passing through the block and coupled to photo-multipliers. The technique has already been successfully used in the E865 experiment [25] and it has been adopted for various other experiments like PHENIX and LHCb. An energy resolution of $4\%/\sqrt{E}$ [26] has been achieved. A view of a 3x3 matrix of Shashlyk modules with lateral size of 110 mm x 110 mm and a length of 680 mm ($= 20X_0$) is shown in Fig. 1.14. To cover the forward acceptance, 351 such modules arranged in 13 rows and 27 columns at a distance of 7.5 m from the target are required.

Figure 1.14: 3×3 matrix of prototype Shashlyk modules as they should be employed for the $\overline{\text{P}}$ANDA Forward Electromagnetic Calorimeter.

1.4.2.5 Forward Muon Detectors

For the very forward part of the muon spectrum, a further range tracking system consisting of interleaved absorber layers and rectangular aluminium drift-tubes is being designed, similar to the muon system of the Target Spectrometer, but laid out for higher momenta. The system allows discrimination of pions from muons, detection of pion decays and, with moderate resolution, also the energy determination of neutrons and anti-neutrons. The forward muon system will be placed at about 9 m from the target.

1.4.3 Luminosity monitor

In order to determine the cross section for physical processes, it is essential to determine the time integrated luminosity L for reactions at the $\overline{\mathsf{P}}\mathsf{ANDA}$ interaction point that was available while collecting a given data sample. In the following we concentrate on elastic antiproton-proton scattering as the reference channel. For most other hadronic processes that will be measured concurrently in $\overline{\mathsf{P}}\mathsf{ANDA}$ the precision is rather poor with which the cross sections are known.

The basic concept of the luminosity monitor is to reconstruct the angle of the scattered antiprotons in the polar angle range of 3-8 mrad with respect to the beam axis. Due to the large transverse dimensions of the interaction region when using the pellet target, there is only a weak correlation of the position of the antiproton at e.g. $z = +10.0\,\mathrm{m}$ to the recoil angle. Therefore, it is necessary to reconstruct the angle of the antiproton at the luminosity monitor. As a result the luminosity monitor will consist of a sequence of four planes of double-sided silicon strip detectors located as far downstream and as close to the beam axis as possible. The planes are separated by 20 cm along the beam direction. Each plane consists of 4 wafers (e.g. $2\,\mathrm{cm}\times 5\,\mathrm{cm}\times 200\,\mu\mathrm{m}$, with $50\,\mu\mathrm{m}$ pitch) arranged radially to the beam axis. Four planes are required for sufficient redundancy and background suppression. The use of 4 wafers (up, down, right, left) in each plane allows systematic errors to be strongly suppressed.

The silicon wafers will be located inside a vacuum chamber to minimize scattering of the antiprotons before traversing the 4 tracking planes. The luminosity monitor can be located in the space between the downstream side of the forward muon system and the HESR dipole needed to redirect the antiproton beam out of the $\overline{\mathsf{P}}\mathsf{ANDA}$ chicane back into the direction of the HESR straight stretch (i.e. between $z = +11\,\mathrm{m}$ and $z = +13\,\mathrm{m}$ downstream of the target).

As pilot simulations show, at a beam momentum of $6.2\,\mathrm{GeV}/c$ the proposed detector measures antiprotons elastically scattered in the range $0.0006(\mathrm{GeV})^2 < -t < 0.0035\ (\mathrm{GeV})^2$, which spans the Coulomb-nuclear interference region. Based upon the granularity of the readout the resolution of t could reach $\sigma_t \approx 0.0001\ (\mathrm{GeV})^2$. In reality this value is expected to degrade to $\sigma_t \approx 0.0005\ (\mathrm{GeV})^2$ when taking small-angle scattering into account. At the nominal $\overline{\mathsf{P}}\mathsf{ANDA}$ interaction rate of $2\times 10^7/\mathrm{s}$ there will be an average of $10\,\mathrm{kHz/cm}^2$ in the sensors. In comparison with other experiments an absolute precision of about 3% is considered feasible for this detector concept at $\overline{\mathsf{P}}\mathsf{ANDA}$, which will be verified by more detailed simulations.

1.4.4 Data Acquisition

In $\overline{\mathsf{P}}\mathsf{ANDA}$, a data acquisition concept is being developed to be as much as possible matched to the high data rates, to the complexity of the experiment and the diversity of physics objectives and the rate capability of at least 2×10^7 events/s.

In our approach, every sub-detector system is a self-triggering entity. Signals are detected autonomously by the sub-systems and are preprocessed. Only the physically relevant information is extracted and transmitted. This requires hit-detection, noise-suppression and clusterisation at the readout level. The data related to a particle hit, with a substantially reduced rate in the preprocessing step, is marked by a precise time stamp and buffered for further processing. The trigger selection finally occurs in computing nodes which access the buffers via a high-bandwidth network fabric. The new concept provides a high degree of flexibility in the choice of trigger algorithms. It makes trigger conditions available which are outside the capabilities of the standard approach.

1.4.5 Infrastructure

The target for antiproton physics will be located in the straight section at the east side of the HESR. At this location an experimental hall with $43\,\mathrm{m}\times 29\,\mathrm{m}$ floor space is planned. To allow for access during HESR operation the beam line is shielded by a concrete radiation shield of 2 m thickness on both sides and is covered on top by concrete bars of 1 m thickness. Within the elongated concrete cave the $\overline{\mathsf{P}}\mathsf{ANDA}$ detector together with auxiliary equipment, beam steering, and focusing elements will be housed. It is planned that it will be possible to open the roof of the cave as well as its wall, so that heavy components can be hoisted in by crane.

The shielded beam line area for the $\overline{\mathrm{P}}$ANDA experiment including dipoles and focusing elements is foreseen to have 37 m × 9.4 m floor space and a height of 8.5 m with the beam line at a height of 3.5 m. The general floor level of the HESR is planned to be 2 m higher. This level will be kept for a length of 4 m in the north as well as the south of the hall (right part in Fig. **??**), to facilitate transport of heavy equipment into the HESR tunnel.

The Target Spectrometer with electronics and supplies will be mounted on rails which makes it retractable to parking positions outside of the HESR beam line area (i.e. into the eastern part of the hall in Fig. **??**). The experimental hall will provide additional space for delivery of components and assembly of the detector parts. With the concrete blocks in place, this area will be sufficiently shielded from radiation to allow access during commissioning and running of HESR. In the south corner of the hall, a counting house complex with five floors is foreseen. The lowest floor will contain various supplies for power, high voltage, cooling water, gases etc. The next higher level is planned for readout electronics and data processing. The third level will house the online computing farm. The fourth floor will be at level with the surrounding ground and will house the control room, a meeting room and social rooms for the shift crew. Above this floor, hall electricity supplies and ventilation is placed. A crane spans the whole area with a hook at a height of about 10 m. Sufficient (300 kW) electric power will be available.

Liquid helium coolant may come from the main cryogenic liquefier for the SIS rings. Alternatively, a separate small liquefier (50 W cooling power at 4 K) would be installed. The supply point will be at the north-east area of the building. All other cabling, which will be routed starting at the counting house, will join these supply lines at the end of the rails system of the Target Spectrometer at the eastern wall. The temperature of the building will be moderately controlled. More stringent requirements with respect to temperature and humidity for the detectors have to be maintained locally. To facilitate cooling and avoid condensation, the Target Spectrometer will be kept in a tent with dry air at a controlled temperature.

References

[1] D. Reistad et al., Calculations on High-Energy Electron Cooling in the HESR, in *Proceedings of the Workshop on Beam Cooling and Related Topics COOL2007, Bad Kreuznach, MOA2C05, p. 44*, 2007.

[2] H. Stockhorst et al., Stochastic Cooling Developments for the HESR at FAIR, in *Proceedings of EPAC08, Genoa, Italy THPP055, p. 3491*, 2008.

[3] A. Lehrach, O. Boine-Frankenheim, F. Hinterberger, R. Maier, and D. Prasuhn, Nucl. Instrum. Meth. **A561**, 289 (2006).

[4] F. Hinterberger, in *Beam-Target Interaction and Intra-beam Scattering in the HESR Ring*, Report of the Forschungszentrum Jülich, 2006, Jül-4206, ISSN 0944-2952.

[5] FAIR Technical Design Report, HESR, Technical report, Gesellschaft für Schwerionenforschung (GSI), Darmstadt, 2008, `http://www-win.gsi.de/FAIR-EOI/PDF/TDR_PDF/TDR_HESR-TRV3.1.2.pdf`.

[6] A. Lehrach et al., Int. J. Mod. Phys. **E18**, 420 (2009).

[7] A. Lehrach et al., Beam dynamics of the High-Energy Storage Ring (HESR) for FAIR, in *Conference Proceedings*, STORI08, Journal of Modern Physics E.

[8] FAIR - Facility for Antiproton and Ion Research, Green Paper - The Modularized Start Version, Technical report, 2009.

[9] D. Welsch et al., Closed Orbit Correction and Sextupole Compensation Schemes for Normal-Conducting HESR, in *the European Accelerator Conference EPAC2008, Genoa, THPC076, p. 3161*, 2008.

[10] V. Parkhomchuk, Nucl. Instrum. Meth. **A441**, 9 (2000).

[11] A. Sørensen, in *CERN 87-10, 135*, 1987.

[12] F. Hinterberger, T. Mayer-Kuckuk, and D. Prasuhn, Nucl. Instrum. Meth. **A275**, 239 (1989).

[13] F. Hinterberger and D. Prasuhn, Nucl. Instrum. Meth. **A279**, 413 (1989).

[14] O. Boine-Frankenheim, R. Hasse, F. Hinterberger, A. Lehrach, and P. Zenkevich, Nucl. Instrum. Meth. **A560**, 245 (2006).

[15] H. Stockhorst et al., Calculations on High-Energy Electron Cooling in the HESR, in *Proceedings of the Workshop on Beam Cooling and Related Topics COOL2007, Bad Kreuznach, MOA2C05, p. 30*, 2007.

[16] A. Smirnov et al., Effective luminosity simulation for PANDA experiment at FAIR, in *Proceedings of COOL2009, Lanzhou, China, THPMCP002*, 2009.

[17] A. Smirnov et al., Simulation of pellet target experiments with Betacool Code, in *Proceedings of RuPAC 2008, Zvenigorod, Russia, `http://cern.ch/AccelConf/r08/papers/MOAPH04.pdf`*, 2008.

[18] H. Staengle et al., Nucl. Instrum. Meth. **A397**, 261 (1997).

[19] A. Adametz, "Preshower Measurement with the Cherenkov Detector of the BABAR Experiment Aleksandra Adametz", Diploma thesis, Master's thesis, University Heidelberg, 2005.

[20] K. Mengel et al., IEEE Trans. Nucl. Sci. **45**, 681 (1998).

[21] R. Novotny et al., IEEE Trans. Nucl. Sci. **47**, 1499 (2000).

[22] M. Hoek et al., Nucl. Instrum. Meth. **A486**, 136 (2002).

[23] $\overline{\mathsf{P}}$ANDA collaboration, EMC Technical Design Report, Technical report, Darmstadt, 2008, arXiv:0810.1216v1.

[24] N. Akopov et al., Nucl. Instrum. Meth. **A479**, 511 (2002).

[25] G. S. Atoyan et al., Nucl. Instrum. Meth. **A320**, 144 (1992).

[26] I.-H. Chiang et al., (1999), KOPIO Proposal.

2 Overview of the project and the requirements

2.1 The charged particle tracking system

2.1.1 General requirements

The PANDA experiment has a wide range physics program [1] which is summarized in section Sec. 1.2. In order to fulfill the scientific goals of this program, the PANDA detector has to be capable to identify final states with both charged and neutral particles with the best possible phase space coverage. With the range of incident antiproton momenta from 1.5 GeV/c to 15 GeV/c the momenta of the produced particles may range from the order of 100 MeV/c up to 10 GeV/c or more, corresponding to polar angles ranging from the backward hemisphere to very small forward angles. Many of the interesting physics channels, such as e.g. those with charmed hadrons in the final state, have small or very small cross sections, and thus have to be identified at the presence of a huge background.

The different physics issues, each of which is scientifically well justified, will impose specific optimization criteria and requirements to design and performance of the detection system, which in general deviate from those given by the other topics of the program. This is also the case for the requirements to the tracking detector system which is the essential detector component for the reconstruction of the momentum vectors of the charged particles produced in the reaction. The optimum tracking detector design thus depends on the relative weight which is given to the different physics topics. Obviously, there is no unique solution to this optimization problem. We are convinced that the design of the detector components described in this report is based on a reasonable synthesis of the different physics requirements. Thus the chosen detector design allows to pursue the full PANDA physics program in all its aspects. In addition, an important consequence of the general purpose concept is the large degree of flexibility to address new key questions which may arise during the lifetime of the experiment.

2.1.1.1 Acceptance

PANDA is a fixed-target experiment with incident antiproton momenta of $1.5 - 15\,\mathrm{GeV}/c$. For a proton target (and equivalently a nucleon at rest in a nuclear target) this implies a Lorentz boost γ_{CM} of the center of mass ranging from 1.20 to 2.92. This large dynamic range in the Lorentz boost corresponds to a large difference in the typical event topologies at low and at high antiproton momenta. Particularly at higher antiproton beam momenta the vast majority of the produced particles in the final state will be emitted into the forward hemisphere. Heavy unstable particles produced in $\bar{p}p$ annihilation or other inelastic reactions comparatively close to the respective energy threshold will even be confined to a narrow forward cone. Heavier stable hadrons at the end of the subsequent decay chains like e.g. (anti-)nucleons are still likely to be emitted at small forward angles. In contrast, light particles like $e^{\pm}$, $\mu^{\pm}$ or $\pi^{\pm}$ may well be emitted into the backward hemisphere also at the highest incident antiproton momenta.

The critical value of the center of mass momentum of a particle x that can result in backward emission in the laboratory frame is given by $p_{\mathrm{crit}} = \beta_{CM} \cdot \gamma_{CM} \cdot m_x = (p_{\bar{p}}/\sqrt{s}) \cdot m_x$. As an example, in case of pions backward emission is possible for $p_{cm} > 93$ MeV/c at $p_{\bar{p}} = 1.5$ GeV/c, and for $p_{cm} > 380$ MeV/c at $p_{\bar{p}} = 15$ GeV/c. Since muon-pion separation requires passage through a large amount of material and thus high momenta to efficiently suppress the much more abundant pions, muon detection at backward angles doesn't seem to be feasible. However, in the tracking of electrons and pions coverage of a significant fraction of the backward hemisphere is required.

An example for the need of backward charged particle tracking is the measurement of the time-like proton form factor in the reaction $\bar{p}p \rightarrow e^{+}e^{-}$ for which the full angular distribution has to be measured in order to determine the electric and magnetic parts independently. At $q^2 = 14\,\mathrm{GeV}/c^2$, that is at $p_{\bar{p}} = 6.45\,\mathrm{GeV}/c$, $\theta_{CM} = 160^o$ corresponds to electrons with a momentum of 0.70 GeV/c at $\theta_{lab} = 113^o$. Detection of pions in the backward hemisphere is also important in studies of strange, multi-strange and charmed baryon resonances in

$\bar{p}p \rightarrow Y^{\star}\bar{Y}'$ (+c.c.) reactions where the excited hyperon $Y^{\star}$ decays by single or double pion emission. Also higher charmonium states may emit pions with decay energies above the critical value for backward emission in the laboratory. The PANDA tracking detectors therefore have to cover the full range of polar angles between 0^o (for particles with p/q different from that of the antiproton beam) and about 150^o.

Full 2π azimuthal coverage is mandatory in order to allow identification of multi-particle final states and studies of correlations within the produced particles. In particular, the spectroscopy program of charmed and strange hadrons requires the measurement of Dalitz plot distributions of three-body final states, which requires a smooth acceptance function across the full phase space. Particular care has to be taken to avoid gaps in the acceptance function and to minimize the effect of discontinuities induced by the transition between adjacent sub-detector components, by detector frames or by mechanical support structure.

Besides the solid angle of the detector also the acceptance in momentum space has to be considered. The magnetic solenoid field in the target spectrometer results in a circular transverse motion of charged particles with non-zero transverse momentum. Often the final state contains charged particles with very large and with very small transverse momentum components which need to be reconstructed at the same time. Given the strength of the solenoid field of 2 T (at $p_{\bar{p}} \geq 3.8\,\mathrm{GeV}/c$) required to determine the momentum vector of the high transverse momentum particle, the radius of the transverse motion of the low transverse momentum particle may be small. Sufficient tracking capability already at small distance from the beam axis is therefore mandatory. As an example one may consider the reaction $\bar{p}p \rightarrow D^{*+}D^{*-}$ close to threshold with $D^{*+} \rightarrow D^0\pi^+$ (& c.c.) and 39 MeV/c momentum of the decay particles in the $D^{*\pm}$ rest frame. The $D^0 \rightarrow K^-\pi^+$ (& c.c.) decay particles have 861 MeV/c momentum in the $D^0/\bar{D}^0$ rest frame. Thus in the solenoid field the transverse motion of the charged pion of the $D^{*\pm}$ decay reaches almost a distance of 7 cm from the beam axis, whereas the charged pions and kaons from the $D^0/\bar{D}^0$ decay may have helix diameters up to almost 1.5 m. Charged pions from the decay of $D^{*\pm}$ produced close to threshold therefore do not reach the Central Tracker having an inner radius of 15 cm and need to be reconstructed based on the track information from the MVD only.

2.1.1.2 Delayed Decay Vertex Detection

An important part of the PANDA physics program involves final states consisting of hadrons with open charm or strangeness which decay by weak interaction and thus have macroscopic decay lengths. The decay length of charmed hadrons is of the order of $100\,\mu$m ($\sim 310\,\mu$m for $D^{\pm}$, $\sim 150\,\mu$m for $D_s^{\pm}$, $\sim 120\,\mu$m for D^0, $\sim 130\,\mu$m for Ξ_c^+, $\sim 60\,\mu$m for Λ_c^+, and $\sim 30\,\mu$m for Ξ_c^0). The PANDA detector is designed according to the goal to detect decay vertices of particles with decay lengths above about $100\,\mu$m. In order to achieve sufficient separation of the reconstructed decay vertex, the inner part of the tracking system has to be located very close to the interaction point, both in longitudinal and in radial direction. This requirement is fulfilled in the design of the MVD.

The identification of hyperons and K_S mesons requires the reconstruction of delayed decay vertices at much larger distances. Λ and Ξ hyperons have comparatively large decay lengths of about 8 cm and 5 cm, respectively. Due to the Lorentz boost this may result in vertices which are displaced by tens of cm from the interaction point mostly in the downstream direction. The considerations in the previous section concerning the required acceptance thus apply with respect to the shifted emission points of charged particles. The PANDA tracking system, in particular the Micro-Vertex-Detector (MVD) as the inner part, therefore needs sufficient extension to the downstream direction in order to also deliver sufficient track information for charged particle tracks originating from these displaced vertices.

2.1.1.3 Momentum and Spatial Resolution

The spatial resolution of the tracking detectors is important in two aspects. In the vicinity of the interaction point it directly determines the precision to which primary and displaced decay vertices can be reconstructed. Further on, based on the deflection of charged particles in both solenoid and dipole magnetic fields, it is an essential contribution to the momentum resolution of charged particles in all three coordinates.

The detection of displaced vertices of charmed hadrons imposes particular requirements to the spatial resolution in close vicinity of the interaction point. With a typical Lorentz boost $\beta\gamma \simeq 2$, D meson decay vertices have a displacement of the order of a few $100\,\mu$m from the primary production point. To distinguish charged daughter particles of

D mesons from prompt particles a vertex resolution of $50\,\mu$m or better is required. Clearly, the position resolution is less demanding for the reconstruction of strange hadrons having decay lengths on the scale of centimeters. In this case a vertex resolution of a few mm is sufficient. However, since the decay particles of hyperons in general due to the significant longitudinal Lorentz boost and the small decay energy have small opening angles, a required value of the resolution in longitudinal direction corresponds to a much better resolution in the transverse direction.

The resolution in the determination of the momentum vectors of the final state particles directly determines the invariant or missing mass resolution of the particles that are to be reconstructed. Typically, the width of hadrons unstable with respect to strong interaction (except for certain narrow states like e.g. charmonium below the $D\bar{D}$ threshold) is of the order of 10 to 100 MeV. As an instrumental mass resolution much below the natural width is without effect, a value of a few 10 MeV seems to be acceptable for the identification of known states or for the mass measurement of new states. With a typical scale of GeV for the particle momenta this translates to a relative momentum resolution σ_p/p of the order of 1% as the target figure for the design of the PANDA tracking detectors.

The achievable momentum resolution is a complex function of the spatial resolution of the tracking sub-detectors, the number of track-points, the material budget of active and passive components resulting in multiple scattering, the strength and homogeneity of the magnetic field, and of the particle species, its momentum and its emission angle. Due to the respective momentum dependence, it is generally expected that multiple scattering limits the momentum resolution of low energy particles, whereas for high energy particles the smaller curvature of the tracks is the dominant contribution to the resolution. Simulation results presented in this report demonstrate that with the chosen design of the tracking detectors the achieved mass and momentum resolution fulfills the requirements given above.

2.1.1.4 Count rate capability

The average hadronic reaction rate in PANDA is limited by the maximum antiproton production rate of 2×10^7 /s. In the ideal case, that is losses through single Coulomb scattering and residual gas interaction can be neglected, antiproton consumption is entirely due to hadronic interactions with the target material. For a hydrogen gas jet or pellet target the condition that the hadronic interaction rate is larger than the loss rate due to single Coulomb scattering is well fulfilled.

Using targets with an inhomogeneous density distribution within the beam profile such as a pellet or a wire target the maximum instantaneous reaction rate will be higher than the average rate. Clearly, the ratio of maximum instantaneous and maximum average rate, which is determined by the target and beam parameters, should be kept as close to unity as possible. With appropriate choice of target and HESR operation parameters, a ratio of 2-3 and thus a maximum instantaneous reaction rate of $\sim 5 \times 10^7$ /s seems to be achievable.

Typically only a few charged particles are produced in $\bar{p}p$ annihilation. Even if secondary particles are taken into account, the number of charged particles per event will not be much larger than 10 in most cases. Thus the detector must able to cope with a rate of 5×10^8 particles/s within the full solid angle. While the total rate is of importance for DAQ design and online event filtering, the relevant quantity for detector design and performance is the rate per channel, which is a function of the granularity per detector layer and of the angular distribution of the emitted particles. The latter depends on the final state considered and on the $\bar{p}$ momentum in a complex way which cannot be discussed in this general section.

Particular attention has to be paid to elastic $\bar{p}p$ scattering since this process contributes significantly to the particle load in two regions of the detector: scattering of antiprotons at small forward angles and the corresponding emission of recoil protons at large angles close to 90^o. This affects primarily the inner region of the MVD disc layers and the forward tracking detector as well as the MVD barrel part and the central tracker. This issue will be addressed in detail in the respective sections in this report.

In contrast to the intuitive expectation, the use of nuclear targets will not create higher particle rates than obtained with a hydrogen or deuterium target. This is due to single Coulomb scattering which dramatically increases with the nuclear charge ($\propto Z^4$) and results in $\bar{p}$ losses with no related signals in the detector. With given $\bar{p}$ consumption rate, the hadronic interaction rate thus correspondingly decreases with the nuclear charge of the target material. In the extreme case of a gold target, the achievable luminosity is reduced by a factor $\sim$ 1000 at 1.5 GeV/c and by a factor $\sim$ 100 at 15 GeV/c as compared to $\bar{p}p$ collisions. At least for direct annihilation products like pions the particle multiplicity is roughly independent of the target mass number [?, ?]. In additions a number of low energy nucleons, dominantly neutrons, are evaporated from the nuclear residue with a nearly isotropic angular distribution. While the neutrons in most cases are not seen in the tracking detectors, a few evaporation protons per $\bar{p}A$ collision will be visible in the inner MVD layers. Heavier nuclear fragments will all be stopped in the beam pipe.

In contrast to $\bar{p}p$ collisions in $\bar{p}A$ collisions no high rate of recoil particles close to 90^o is expected. The emission angles of recoil protons from quasi-free $\bar{p}p$ scattering are smeared by Fermi momentum and rescattering, while recoil nuclei, if they at all survive the momentum transfer, are too low energetic to pass through the beam pipe.

2.1.1.5 Particle Identification

Charged particle identification over a wide range of momentum and emission angle is an essential prerequisite for the capability of PANDA to accomplish the envisaged physics program. Charged particles with higher momenta will be identified via Cerenkov radiation by the DIRC detector in the Target Spectrometer and by the forward RICH detector in the Forward Spectrometer. While almost all particles emitted within the acceptance of the Forward Spectrometer are above the Cerenkov threshold due to the forward Lorentz boost, a number of interesting reaction channels have final states with heavier charged particles ($K^{\pm}, p, \bar{p}$ at larger angles with momenta below the DIRC threshold. For positive charged kaon-pion separation in the DIRC about 800 MeV/c momentum is required. In order to separate these low energy kaons from the much more abundant pions, particle identification capability based on energy loss information has to be supplied by the central tracking detector. The required separation power and thus quality of the dE/dx measurement in the central tracker depends on whether or not a TOF barrel, delivering independent information on the particle velocity, will be included in the Target Spectrometer.

2.1.1.6 Material Budget

Any active or passive material inside the detector volume contributes to multiple scattering of charged particles, electron bremsstrahlung and photon conversion, and thus reduces the momentum resolution for charged particles in the tracking detectors, and detection efficiency and energy resolution for photons in the EMC. Therefore the material budget has to be kept as low as possible. Following the more demanding requirements to meet the performance criteria of the EMC, a total material budget of MVD and Central Tracker below 10% is still considered to be acceptable [2].

References

[1] PANDA Collaboration, Physics Performance Report, Mar.2009, arXiv:0903.3905v1.

[2] PANDA Collaboration, Technical Design Report for $\overline{\mathsf{P}}$ANDA Electromagnetic Calorimeter, Oct.2008, arXiv:0810.1216v1.

3 The Straw Tube Tracker

3.1 General overview

This volume illustrates the technical layout and the expected performance of the Straw Tube Tracker (STT) of the $\overline{\text{P}}$ANDA experiment. The STT is one of the possible options for tracking the charged particles inside the target spectrometer. The proposed layout fulfill all the requirements of the $\overline{\text{P}}$ANDA scientific program, and the illustrated performance is based on prototype tests and MonteCarlo simulation studies. The goal of this document is to demonstrate that a central tracker based on straw tubes is feasible and ready to be constructed.

3.2 Straw tube description

Straws are gas-filled cylindrical tubes with a conductive inner layer as cathode and an anode wire stretched along the cylinder axis. A high electric field between the wire and the outer conductor separates electrons and positive ions produced by a charged particle along its trajectory through the gas volume. Usually, the wire is on positive voltage of a few kV and collects the electrons while the ions drift to the cathode. By choosing thin wires, with a diameter of few tens of μm, the electric field strength near the wire is high enough to start further gas ionizations by electron collisions. Depending on the high voltage set and the gas characteristics an amplification of about $10^4 - 10^5$ of the primary charge signal is possible, which is then high enough to read out the signal.

By measuring the drift time of the earliest arriving electrons one gets the information about the minimum particle track distance from the wire. The isochrone contains all space points belonging to the same electron drift time and describes a cylinder around the wire axis. The characteristic relation between drift time and isochrone is given by the electron drift velocity, depending on specific gas parameters, electric and magnetic field. Therefore, this fundamental relation has to be calibrated using reference tracks with known space and drift time information. The particle track is reconstructed by a best fit to the isochrones measured in a series of several straw tubes with the same orientation. Additional skewed straw layers provide a full stereo view of the particle trajectory.

The specific energy loss of a charged particle in the straw gas volume can be used to identify the particle species and can be derived from the number of ionization electrons which generated the straw signal. Since the specific ionization in gas with about 100 ion pairs per cm for minimum ionizing particles is quite low and shows in addition a strong fluctuation described by an asymmetric Landau distribution, a higher number of measurements is needed to get a sufficient precision for the particles energy loss. The truncated mean method, which reject from many samples those with the largest energy losses due to the fluctuations, can help to improve the resolution.

Straw detectors exhibit the most simple geometry of highly symmetric, cylindrical tubes and have several advantages which are summarized in the following:

- robust electrostatic configuration. The shielding tube around each high voltage wire suppresses signal cross-talk and protects neighbor straws in case of a broken wire;
- robust mechanical stability if the straws are arranged in close-packed multilayers;
- high tracking efficiency due to minimal dead zones (~1 %) at tube ends and between neighbor straws if close-packed;
- high spatial resolution, $\sigma_{r\varphi}$ <150 μm depending on tube diameter and gas characteristics. Simple calibration of space-drift time relation due to the cylindrical isochrone shape;
- small radiation length, X/X_0 ~0.05 % per tube, if straws with thinnest (~30 μm) film tubes are used;
- high rate capability can be improved by reducing the occupancy using smaller tube diameter and/or choosing a fast drift gas.

3.2.1 Straw materials

The $\overline{\text{P}}$ANDA straw tubes have a length of 1500 mm, 10 mm inner diameter, and a total wall thickness of 27 μm. They are made of two layers of 12 μm thin aluminized mylar [1] films by wrapping two long film strips around a rotating mandrel and gluing the two half-overlapping strips together. Then the cylindrical film tube is stripped off. The aluminization at the inner tube wall is used as the cathode

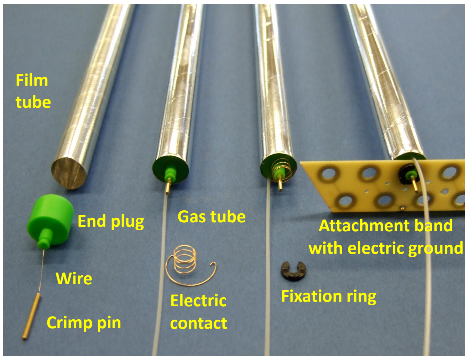

Figure 3.1: A straw consists of a mylar film tube which is closed by two end plugs, each containing a crimp pin to fix the anode wire in the center and a gas tube to provide a gas flow through the tube. The contact springs inserted in the small film overlap at both tube ends provide the electric cathode contact. The straw ends are fixed by a plastic ring to an attachment band which contains on the inner side the electric ground.

whereas the aluminization of the second, outer strip layer is used to prevent light incidence.

A gold-plated tungsten-rhenium wire with 20 μm diameter is used as anode. Cylindrical precision end plugs made from ABS [2] with a wall thickness of 0.5 mm close the tube at both ends (Fig. 3.1). They are glued to the mylar film leaving a small 1.5 mm film overlap on both ends. There, a gold-plated copper-beryllium spring wire is inserted to provide the electric cathode contacting. The springs allow 2 mm tube elongation with a typical spring force equivalent to 10 g. The end plugs have a central hole with a 3 mm thick cylindrical nose to insert and glue a crimp pin for the wire. A micro PVC (medical quality grade) tube is fed through another hole and glued in the end plugs to provide a gas flow through the tube. The total weight of a fully assembled straw is 2.5 g. The anode wire is stretched by a weight of 50 g and crimped in the copper pins at a gas overpressure in the straw tube of 1 bar.

Table 3.1 lists the different straw components and their thickness in radiation lengths. The chosen film tubes are the thinnest used for straw detectors, but still show sufficient mechanical stability for the assembly to self-supporting double-layers. For the proposed $\overline{\text{P}}$ANDA straw tracker the total radiation length of the straw volume is 1.2 % with a maximum number of 27 hit straw layers for a traversing particle track in radial direction.

3.2.2 Pressurized straws

Both, efficiency and resolution of a straw are best for a perfect cylindrical shape of the film tube and the wire being highly concentrically in the cylinder axis. With a wire tension[1] of about 50 g inside a 1.5 m long, horizontal straw tube the maximum sag due to gravitation in the tube center is less than 35 μm. For the 4636 straws of the $\overline{\text{P}}$ANDA central tracker this adds up to a wire tension equivalent to about 230 kg which must be maintained. Usually, this is done by fixing the straw tubes inside a strong and massive, surrounding frame or by adding reinforcement structures like CF-strips along the tubes to keep them straight. All methods inevitably increase the detector thickness given in radiation length by this additional materials.

Therefore a new technique based on self-supporting straw layers with intrinsic wire tension developed for the COSY-TOF straw tracker [3] has been adopted for the $\overline{\text{P}}$ANDA central tracker. The straw tubes are assembled and the wire is stretched by 50 g at an overpressure of about 1 bar. Then the tubes are close-packed and glued together to planar double-layers on a reference table which defines a precise tube to tube distance of 10.1 mm. At the gas overpressure of 1 bar the double-layer maintains the nominal wire tension of 50 g for each tube, i.e. becomes self-supporting.

The precision of the tube and wire stretching method by the gas overpressure for the used thin film tubes was studied in more detail for the COSY-TOF straw tubes. Fig. 3.2 shows the measured tension with decreasing gas overpressure. A well-defined tension is seen, even down to vanishing overpressure where only the stiffness of the mylar film tube maintains a wire tension of 28 g. The nominal tension for the COSY-TOF 1 m long straws was 40 g at 1.2 bar overpressure. For the $\overline{\text{P}}$ANDA 1.5 m long straws the nominal tension is 50 g at 1.0 bar overpressure.

3.2.3 Gas mixture

The need of high spatial resolution in the STT requires high amplitude anode signals even for the single electron clusters, thus requiring high gas gain. On the other side, a high gas gain significantly reduces the chamber lifetime. For the optimum gas amplification choice both these factors should be taken into account properly. Table 3.2 shows the main parameters of some of the most used gas and

---

[1] Usually given as the mass weight used to stretch the wire.

Table 3.1: Mean thickness in radiation lengths of the different straw tube components. The number for the gas mixture is evaluated at 20° and 2 atm.

Element	Material	X[mm]	X_0 [cm]	X/X_0
Film Tube	Mylar, 27 μm	0.085	28.7	3.0×10^{-4}
Coating	Al, $2\times0.03\,\mu$m	2×10^{-4}	8.9	2.2×10^{-6}
Gas	Ar/CO_2(10 %)	7.85	6131	1.3×10^{-4}
Wire	W/Re, 20 μm	3×10^{-5}	0.35	8.6×10^{-6}
			$\sum_{straw}$	4.4×10^{-4}

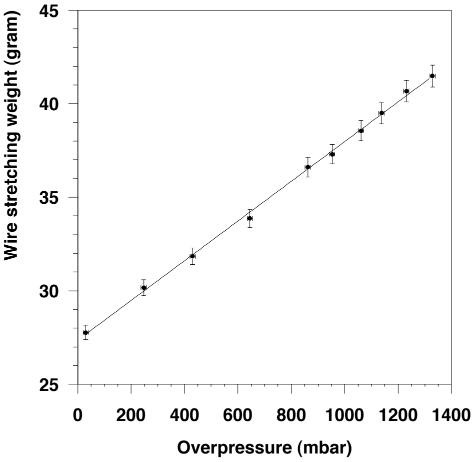

Figure 3.2: Measured wire tension (weight equivalent) at different gas overpressure inside a straw. The nominal tension is 40 g at 1.2 bar overpressure for the COSY-STT straws.

gas mixtures. In order to select the most suited gas mixture for the STT detector, it is useful to consider two essentially different situations. Some gas mixtures, if a low electric field is set up, can effectively quench the electron kinetic energy, preventing them to gain enough energy between collisions. In this case, electrons are in thermal equilibrium with the surrounding medium and the drift velocity is proportional to the electric field tension. Such gases are usually called “cold” for that given electric field strength.

On the contrary, if the electron average kinetic energy differs from the thermal energy, the drift velocity behavior becomes more complicated. In many gas mixtures the drift velocity becomes saturated and does not depend on the electric field strength. That makes the reconstruction of the track coordinates easier. However, to get high spatial resolution in this “hot” gas mixtures become difficult, in principle, due to the large diffusion. The standard choice of many experiments is to have a “hot” or “warm” gas mixture, that has a weak dependence of the drift velocity on the applied electric field. In this case, the electric field inhomogeneities do not play a significant role, which makes the calibration simpler. An overpressure can be used in these cases to reduce the diffusion.

The main requirements, that should be taken into account for the choice of the most suited gas mixture, are:

- good spatial resolution;
- rate capability;
- radiation hardness;
- radiation length;
- chemical inactivity;
- working voltage;
- working pressure;
- accessibility on the market and price.

For the $\overline{\text{P}}$ANDA CT the spatial resolution, the rate capability and the radiation hardness are the points of highest importance. Initially a “cold” gas mixture of He + 10%i C_4H_{10} was proposed for the Conceptual Design Report [4]. Although this gas mixture has one undoubted advantage, the long radiation length X_0, it has a long drift time, which is a disadvantage more or less peculiar for all “cold” gases. As a result, a gas mixture based on Ar + 10%CO_2 has been suggested.

In Fig. 3.3 and Fig. 3.4 are shown the results of the simulation for the spatial resolutions achievable for the Ar + 10%CO_2 and He + 10%iC_4H_{10} for 1

Table 3.2: Properties of different gases and gas mixtures. Z and A are charge and atomic weight, for molecules the total number have to be taken, N_p and N_t are the number of primary and total electrons per cm, respectively, E_x and E_i are the excitation and ionization energy, respectively, W_i is the average energy required to produce one electron-ion pair in the gas, $(dE/dx)_{mip}$ is the most probable energy loss by a minimum ionizing particle and X_0 is an radiation length. For gas mixtures, weighted average value have to be taken.

Gas or gas mixture	Z	A	E_x [eV]	E_i [eV]	W_i [eV]	dE /dx [keV/cm]	N_p [cm^{-1}]	N_t [cm^{-1}]	X_0 [m]
He	2	4	19.8	24.5	41	0.32	4.2	8	5299
Ar	18	40	11.6	15.7	26	2.44	23	94	110
CO_2	22	44	5.2	13.7	33	3.01	35.5	91	183
iC_4H_{10}	34	58	6.5	10.6	23	5.93	84	195	169
Ar+10%CO_2	-	-	-	-	26.7	2.5	24.6	93	117
He+10%iC_4H_{10}	-	-	-	-	39.2	0.88	12.7	26.7	1313
He+20%iC_4H_{10}	-	-	-	-	37.4	1.44	20.6	45.4	749

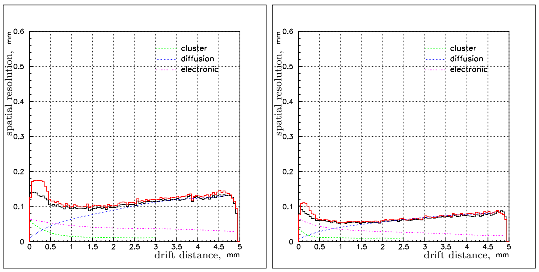

a) b)

Figure 3.3: The spatial resolution for the Ar+10%CO_2 gas mixture for 1 a) and 2 atm b) pressures. The red line corresponds to an ideal r(t) relation, the black one to the measured. The main contributions to the resolution are also shown in different colors

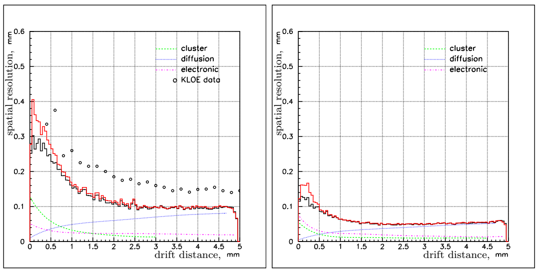

a) b)

Figure 3.4: Space resolution in He+10% i-C_4H_{10} with 1 a) and 2 atm b). The red line corresponds to an ideal r(t) relation, the black one to the measured. The main contributions to the resolution are also shown in different colors. The experimental spatial resolution of the KLOE drift chamber, denoted by the open circles, is given for comparison [6]

and 2 atm gas pressure. The simulations have been performed using the GARFIELD program and the build-in MAGBOLTZ package [5]. The good agreement of these simulation data with the experimental results obtained by the KLOE drift chamber prototype [6], as shown in Fig. 3.4, can be interpreted as a proof of the validity of the simulations of the straw tube parameters.

The spatial resolution of the Ar + 10%CO_2 mixture is satisfactory even at 1 atm pressure, while the spatial resolution in the He + 10%iC_4H_{10} is worse than the required 150 μm, and only an increase of the pressure could improve this situation. The total drift time is also an important parameter. The Ar+10%CO_2 mixture has a drift time of 80 ns for a 4 mm drift path. The He+10%iC_4H_{10} has double the drift time. Since the average time between two events in PANDA will be ∼ 100 ns, when using the He+10%iC_4H_{10} gas mixture, the information from two consecutive events could be contained in the STT at any time. This event mixing in the tracker will result in a significant complication of the trigger logic and of the pattern recognition algorithm. By increasing the pressure two times, the drift time for the He+10%iC_4H_{10} grows by 50 ns, while for the Ar + 10%CO_2 only by 10 ns. That makes the situation with the event mixing even more difficult.

The effect of the electronics threshold on the spatial resolution has also been studied. The average gas gain have been reduced by a factor two using the same electronic threshold. Fig. 3.5 shows only a small deterioration of the Ar+10%CO_2 resolution and a strong worsening in the case of the He+10%iC_4H_{10} gas mixture. This is one more argument in favor of the Ar + 10%CO2 usage.

All these considerations shows strong advantages for the Ar + 10%CO_2 gas mixture for the $\overline{\text{P}}$ANDA STT compared with He + 10%iC_4H_{10} gas compos-

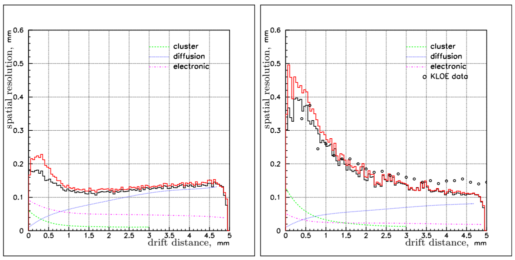

a) b)

Figure 3.5: The spatial resolution for the Ar+10%CO_2 a) and the He+10%iC_4H_{10} b) gas mixtures at 1 atm pressures. The gas gain has been reduced by a factor two compared with Fig. 3.3 and Fig. 3.4. The red lines correspond an "ideal" r(t) relation, while the black one corresponds to the measured one. Contributions from the main limiting process are shown by dashed lines. The spatial resolution of the KLOE drift chamber, denoted by the open circles, is given for comparison [6].

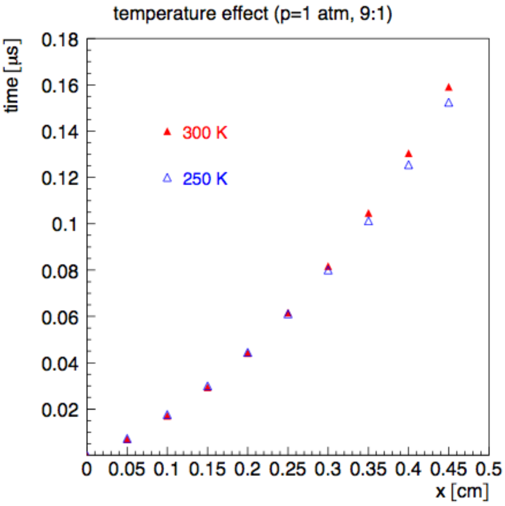

Figure 3.6: Space time relation for the Ar+10%CO_2 mixture at 1 atm for two different temperatures.

ite. Parameters of the Ar + CO_2 gas mixture can be modified in the future, by changing pressure, CO_2 percentage or admixture of other gases, in order to sligthly tune STT performance.

The variations of the gas mixture performance due to changes of the absolut temperature have been studied. The space time relation for the Ar+10%CO_2 mixture at 1 atm for two different temperatures, 250 and 300 K, is shown in Fig. 3.6. No significant differences are present between the two curves. Therefore, it will not be necessary to keep under control the temperature variation.

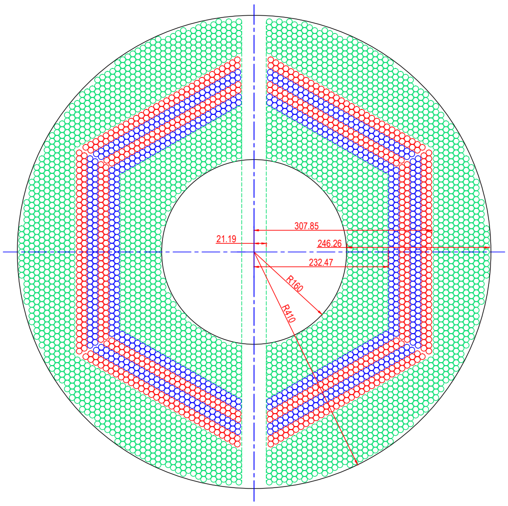

Figure 3.7: General layout of the Straw Tube Tracker. The straws marked in green are parallel to the beam axis. The blue and red marked straw layers are skewed relative to the axial straws by +2.89° and −2.89°, respectively.

3.3 The layout of the whole detector

$\overline{\text{P}}$ANDA STT will occupy a cylindrical volume with an internal diameter of 150 mm and an external one of 418 mm. Due to the presence of the target pipe, in the x,y plane this volume will be divided in two halves, with a gap of 42 mm in between. Along z, the allowed space is 1500 mm, plus 150 mm in the upstream region for electronics, gas supplies, and other services.

3.3.1 Detector geometry

To fill up this volume, it has been decided to use planar double-layers using the same technique developed for the COSY-TOF modules. The $\overline{\text{P}}$ANDA STT will consist of planar straw double-layers arranged in a hexagonal layout to an almost cylindrical shape. A straw double-layer consists of 2 close-packed, staggered layers; the position of the straws in the second layer has an offset of 1/2 straw diameter (5.05 mm) compared to the lower one. Each layer consists of close-packed straws glued together on a reference plate with precise positioning (50 μm). The straw to straw distance is 10.1 mm. Dots of glue fix each straw tube to the neighbouring along its length, leaving sufficient space for tolerances of the outer film tube diameter, and increased diameter at overpressure. To reduce the weight of the support structures of the tubes to a minimum, the straw double-layers are highly self-supporting. This is realized by using the technology of intrinsic wire tension and tube stretching by the applied gas overpressure described in the previous section. More details on the assembly procedure of the double-layers can be found in Sec. 3.4.2.

The proposed arrangement will have 4 double-layers parallel to the detector axis, 4 skewed double-layers, with an angle, with respect to the beam axis, of about ±3^o, and further 2 straight double-layers. Finally, to approach the cylindrical shape, 7 layers with a decrasing number of straws layers will be placed in the outer region.

Moving from the inner to the outer of the detector, the number of straws changes from layer to layer. The general arrangement of the STT double-layers is shown in Fig. 3.7. The total number of straw tubes is 4636.

3.4 Mechanics and detector installation

In order to support the straw tubes and to precisely position them in space, dedicated mechanical structures are necessary. These mechanical supports have, moreover, the task to move the entire detector along the beam axis for installation and maintenance purposes.

These structures have to be rigid enough to support the weight of the straws themselves and of all the service elements of the detector, *i.e* the electronics, the cables, the gas manifolds and pipes, and also some neighboring components: the vertex detector and the beam and target croos-pipe that are enclosed by the central tracker.

3.4.1 The straw tubes support structure

In order to obtain a structure with high mechanical accuracy but being extremely light, we have conceived a solution simple and of easy realization using aluminum or carbon fiber. Following the experience gained in previous experiments [7, 8], it has been designed the solution that is shown in Fig. 3.8.

This structure consists of two equal flanges, shaped and drilled individually, connected with screws to six precise tubular spacers. The two internal ones, are necessary only during the mounting phase and could be removed after the installation of the straw tubes.

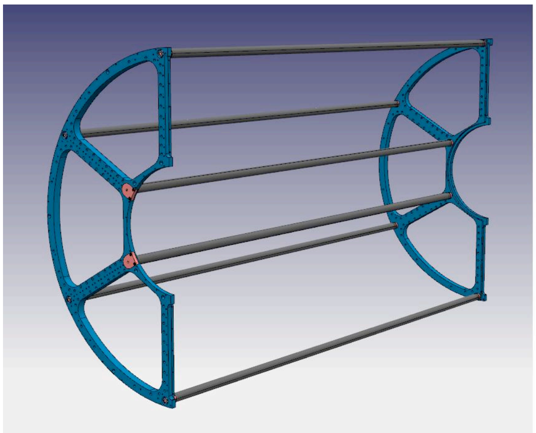

Figure 3.8: Pictorial drawing of the straw tubes support structure.

2 End-plates	60 N
6 Connecting bars	30 N
2100 Straw Tubes	80 N
Electronics, gas, services	110 N
Total weight	**280 N**
Density	2.7 g/cm^3
Youngs modulus	70 GPa
Radiation length (X_0)	9 cm
Thermal expansion	24 ppm/^{o}C

Table 3.3: Data used for the FEA (Finite Elements Analysis) of the support structure.

The flanges have semi-circular shape and leave along the vertical axial plane enough space for the installation of the target pipes.

On the spokes of the flanges high precision holes are realized (± 0.05 mm). These allow to mount the straw tubes layers with the accuracy requied.

In order to check this solution, it has been performed a thorough finite elements analysis (FEA) on the whole structure whom results confirmed the validity of the adopted choices, either from the functional and the structural point of view. The input parameters of this analysis are listed in Table 3.3 in the case of Aluminum. The Fig. 3.9 shows graphically the stress on the structure. The maximum value of the deflection expected on the frame is 0.03 mm. The biggest stress is suffered by the backward flange (Fig. 3.9 central panel) since this is supporting the load of the electronics and of the

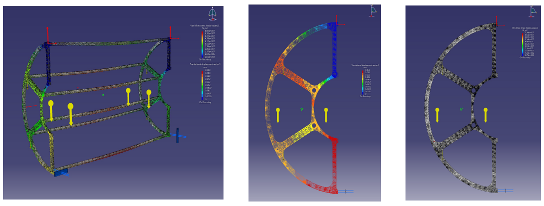

Figure 3.9: Results of the FEA of the STT support structure; the maximum deflection of the frame is 0.03 mm.

services of the detector. The two internal rods (see Fig. 3.8) are needed only during the straw layers mounting phase and then could be removed reducing furtherly the material budget.

3.4.2 Double-layers assembly procedure

The straw tube assembling procedure for the P̄ANDA STT consists of subsequent steps. First of all, single tubes are constructed and tested, then they are assembled in multi-layer modules and finally they are mounted in the mechanical frame. In the following, the main steps of such a procedure are described.

- Mylar straws are cutted to the nominal length and gas pipes are glued to the end-plugs. The glue used for this operation is a plastic glue (Pattex plastik [9]).
- The anode wire is feed through the crimp pins, end-plugs, and mylar film tube. Crimp pins are then glued in the end-plugs, and sub-sequently the end-plugs are glued inside the straw tube. This glueing has to leave ~ 1.5 mm film overlap at both ends to performe, later, the spring insertion that allow electric groundig and elastic elongation compensation of the straw. The glue used here is a 2-component epoxy adhesive (UHU endfest 300 [10]) with 2 h working time, and 12 h setting time.
- After glue hardening, the straws are placed in a groove v-shaped. The wire is then crimped in one of the two end-plugs and stretched by a weight of 50 g. The straws are now connected to a gas system and the pressure inside is raised smoothly to the nominal overpressure value. Then, the wire is crimped in the second end-plug.

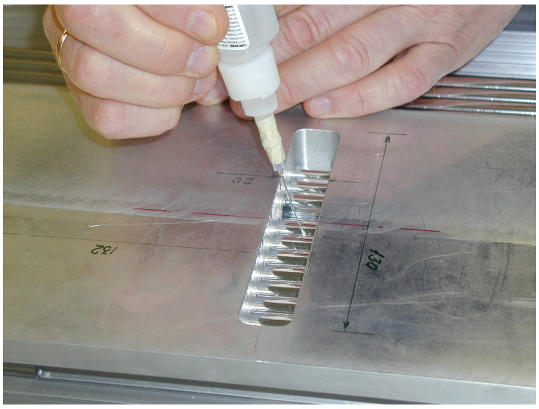

Figure 3.10: The glueing operation of straw tubes in multi-layers.

- Assembled straws are then tested for gas leakage and for broken wires. The wire tension is measured by placing the pressurized tube in a strong magnetic field, an AC-current is applyed to the wire and the first harmonic of the oscillating wire is measured. Tubes showing a strong deviations from the nominal 50 g wire tension are rejected.
- Straws are then placed as a mono-layer onto a reference groove plate (Fig. 3.11), connected to gas and pressurized to the nominal pressure. They are aligned with high precision by puting reference plates on top of them and glued to the neighbouring at several defined points along their length. The glue used here is an instant cyanoacrylate adhesive (Loctite 408 [11]). After that, the second layer of straws is precisely positioned on top to the first one, pressurized to the nominal pressure and the single tubes are then glued to neighbouring and lower straws with glue dots.
- Springs at both straw ends are inserted and finally side-bands are fixed to both ends of the straw double-layer by means of elastic rings places on each end-plug (see Fig. 3.12 and Fig. 3.1).

Fig. 3.10 shows a picture taken during the glueing of the straws.

3.4.3 Installation of the straw tubes layers on the support structure

After the construction, the straw tube layers will be mounted inside the support structure starting with

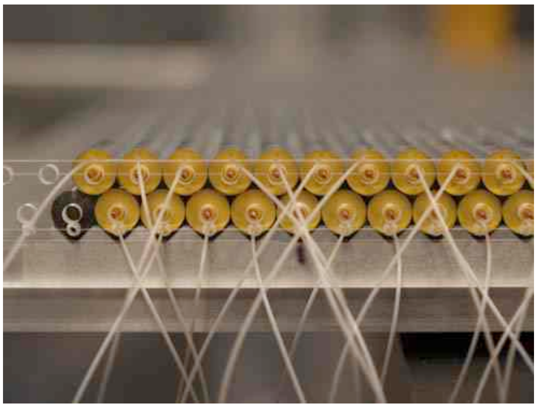

Figure 3.11: Straw tube double-layers during the assembly procedure on the reference plate.

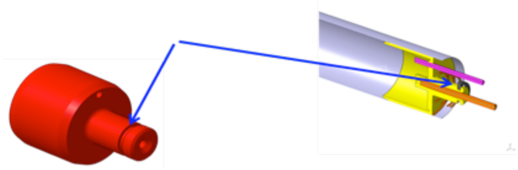

Figure 3.12: Straw tube end-plug. A groove (indicated by the arrows) is present to fix it, with an elastic ring, to the side-band.

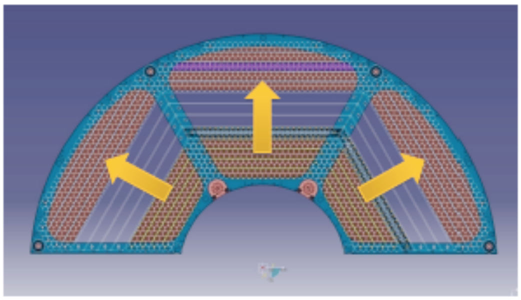

Figure 3.13: Mounting scheme of straw tube layers inside the support structure. The free space in the middle will be filled up with double-layers with skew tubes.

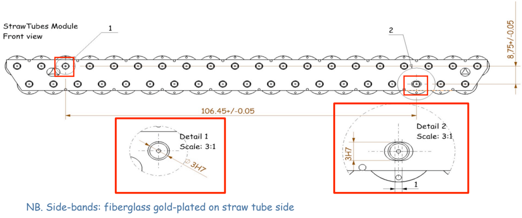

Figure 3.14: Side-bands to fix straw tube double-layers to the mechanical structure. The insets show in detail the more precise holes needed to give mechanical precision to the module.

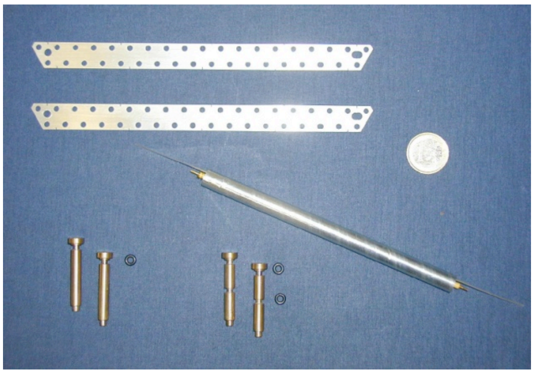

Figure 3.15: Prototypes of the side bands used to fix straw tube double-layers to the mechanical structure

the inner axial ones. Fig. 3.13 shows the details of the mounting scheme.

Each straw tube double-layer will be equipped with two side-bands having a multiple function. These will be light fiberglass strips, 0.7 mm thick, gold-plated on the straw tubes side to allow the electrical grounding, with a circular hole for each straw tube. The tubes are fixed to the side-bands with elastic rings placed on the end-plug (see Fig. 3.12). All the circular holes on the side bands have a diameter of 3.2 mm except one that has a diameter of 3.0 mm (H6) and the last one, that actually has a button-hole shape (height 3 mm(H6)). These two more precise holes are needed to give mechanical precision to the double-layer. The side bands are also used to fix the straw double-layers to the mechanical support frame. This is done by means of two extra holes through which fixing pins are inserted. Fig. 3.14 shows a picture of the side band prototypes made of Aluminum.

3.4.4 Mechanical tests

To check the previously described solution, a prototype of the flanges of the STT support structure have been realized at LNF and mounted on dummy supports. Some straw tube double-layers have been realized in Jülich and shipped to Frascati for the mounting tests. Those modules have been built using end-plugs that are not the final ones. Therefore the side-bands have been fixed to the modules with

Figure 3.16: A full size prototype of the mechanical frame that has to support one half of the STT.

4 Kevlar strings. The side bands used for this mechanical test were made of Aluminum. The test has proved that the solution is feseable, even if, to have a better fixation, it has been decided to thread the dowel pins and to block them with a nut. A full scale prototype of the mechanical frame has been then realized in Aluminum (see Fig. 3.16).

3.5 The central frame

The tracking system is strictly connected to other neighboring detectors and equipments of the $\overline{\mathrm{P}}$ANDA apparatus. Therefore, to support and install it a general Central Frame (CF), able to serve all the central region, has been designed.

The task of the CF is to support many devices: the beam-target cross-pipe, the Micro Vertex Detector (MVD), the central tracker, and all their services *i.e.* the gas pipes, the electronics and all the cables. All these equipments will be mounted on the central frame that then will be inserted inside the target spectrometer. To do maintenance operation it would be necessary to do the same operations in reverse order. To allow this, three skates on top, and two others on bottom will be fixed on it. The skates will move along rails placed on two beam parallel to the spectrometer axis.

Figure 3.17: Prototype of the central frame.

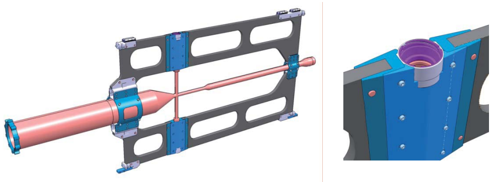

Figure 3.18: The central frame carrying the beam-target cross-pipe (left), detail of the target pipe junctions (right).

The central frame has a total thickness of 20 mm and consist of a sandwich made with a central soul of honeycomb covered on both sides with pasted skins of carbon fiber. The proposed solution (see Fig. 3.17) is very thin and light. The most massive parts of the structure are those necessary to fix the beam-target cross-pipe. In fact, on top and bottom, the fixing pads must be able to support the torque of 100 Ncm that will be applied when the target beam pipes will be connected. Moreover, the backward support of the beam pipe must allow the passage of some of the cables of the MVD. Therefore, it has two rectangular housing, located top and bottom. The last attaching point of the beam pipe in the forward region is the less critical. Fig. 3.18 shows the CF after the mounting of the beam-target cross-pipe and a detail of the top/bottom target pipe junctions.

Table 3.4 reports the data used for the mechanical calculation of the CF. The FEA performed on the structure (see Fig. 3.19) gave the following results: maximum equivalent stress: 25 MPa (the limit is 95 MPa); maximum sag: 0.5 mm.

In order to test the adopted solution and the mounting sequence, a prototype of the CF has been realized by the INFN Torino mechanical workshop.

Straw tubes tracker	700.0 N
Beam pipes	45.0 N
Micro vertex	300.0 N
Gas pipes, electronics, cables, others	100.0 N
Safety load	250.0 N
Total Load	**1395.0 N**

Table 3.4: Data used for the mechanical FEA calculations of the central frame.

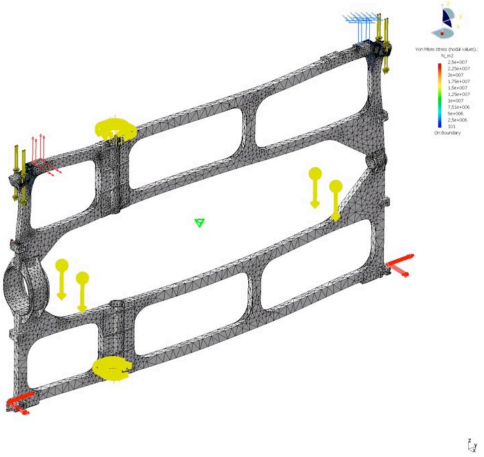

Figure 3.19: Results of the FEA analysis of the central frame.

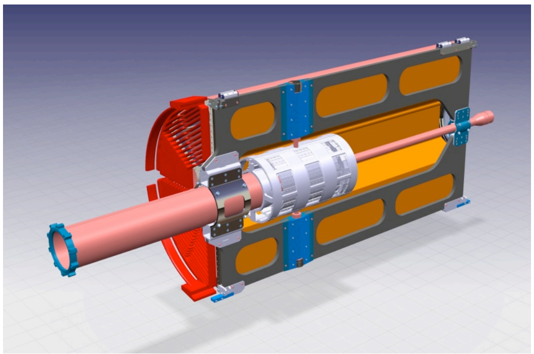

Figure 3.20: The central frame with the target-beam cross-pipe, the micro vertex detector and half of the central tracker already mounted.

Fig. 3.20 shows the CF with the target-beam cross-pipe, the micro vertex detector and half of the central tracker already mounted.

3.6 The gas system

The preferred gas mixture for the $\overline{\text{P}}$ANDA-STT is Argon with an admixture of about 10–20 % CO_2 as the quenching component because of its capability to tolerate highest irradiation levels (see Sec. 3.10.3). For this gas mixture no deposits on the straw tube electrodes from polymeric reactions occur, supposed there is a clean gas environment including all materials and parts of the detector and gas supply system in contact with the gas. For both gas components a high purity grade is required (Argon with grade 5.0, CO_2 with 4.8). The supply lines consist of polished stainless steel pipes and thermoplast (PA) tubings where a higher flexibility is needed. Since Argon and CO_2 are non-flammable, not expensive, and components of the atmosphere, no recirculation and containment of the gas mixture is needed, and the gas supply of the detector is done in flushing mode. The STT will be operated at a gas pressure of about 2 bar (absolute) and preferably at room temperature. The total STT gas volume of about 1040 l (520 l × 2 bar) is exchanged typically every six hours with a flow rate of about 3 l per minute to refresh the gas mixture and to prevent an accumulation of contaminants in the detector and gas system.

The gas system of the STT consists of high pressure, supply gas bottles for each mixture component, cleaning filters in the gas lines, a mixing section with ratio-based mass flow controllers, regulated by a pressure transducer inserted in the STT volume to set a constant absolute pressure of about 2 bar in the detector, the supply lines in and out of the detector and outlet valves to a dedicated exhaust line at the $\overline{\text{P}}$ANDA experimental area. The scheme of the gas distribution system is shown in Fig. 3.21. The mass flow controller and meter devices [12] are based on digital electronics. In these devices the analog sensor signal is sent directly to a micro processor. By doing so, optimum signal stability and accuracy is achieved. An integral alarm function continuously checks the difference between the set point and the measured value. If the supply pressure drops the instrument gives a warning. In addition the instrument runs a self diagnostics routine, and controller settings can be remotely adjusted with a hand terminal or a computer using an RS-485 busline. For the Ar/CO_2 gas mixture the required accuracies of the settings and control have to be better than 0.3 % (absolute) for the mixture ratio, about 1-2 mbar for the pressure, and 1 K for the temperature.

The $\overline{\text{P}}$ANDA straw tubes are arranged in six sectors

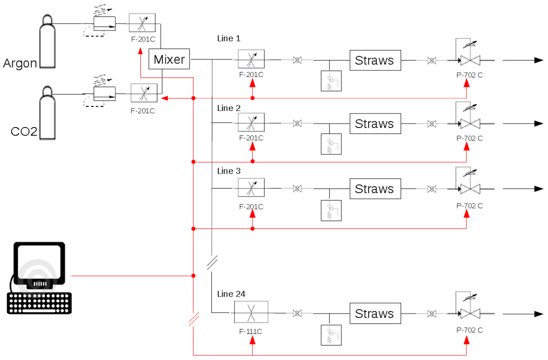

Figure 3.21: Scheme of the gas system.

forming an hexagon around the interaction point. Each sector can be further sub-divided in three regions: the internal and the most external ones, that are equipped with axial straws, and the middle section which houses stereo straw tubes, see Fig. 3.7 (more details of this arrangement can be found in Sec. 3.3). To flux the straws with the required, pressurized, two components gas mixture, the following guidelines have been followed:

- reducing the redundancy of the system to lower the costs and the complexity of the system;
- keeping the space needed for the system within reasonable boundaries (∼ few cm);
- assure a minimal redundancy to guaranty, in case of faults, the operation of at least parts of any sector;
- automatization and remote control of the flux parameters, with the possibility to switch to manual/local operation for:
  - proportion the two-components of the gas mixture;
  - quantify the fluxed mixture;
  - setting mixture overpressure;
  - controlling the temperature.

Following these guidelines we decided to have 24 independent lines, so organized:

- a line for each axial straw regions: $6 \times 2 = 12$;
- two lines for each of the stereo straw groups: $6 \times 2 = 12$.

With this selection of multiplicity and topology, in case of fault of one line, it is assured that at least one half of any sector remains operative. This is particularly important for the stereo tubes that allow to determine the z-coordinate of particle trajectories. These gas lines are then connected to gas distributors that finally bring the gas to each straw. Fig. 3.22 shows a first prototype of these distributors. It consist of a stainless steel pipe having a wall thickness of 0.1 mm and a diameter of 3 or 4 mm. On it, small capillaries (diam. 0.55 mm) are welded and will be connected to the individual straws. By connecting 2 straws in series it is possible to arrange the in- and outlet gas manifolds at the same end of the detector, preferable at the backward end.

Capacitance	8.9 pF/m
Sense wire resistance	258 Ω/m
Inductance	1.24 μH/m
Impedance	373 Ω
Analog cross talk	< 1 %

Table 3.5: Straw electrical properties.

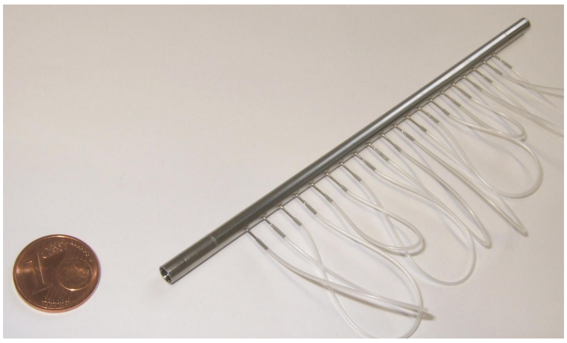

Figure 3.22: Prototype of a gas distributor consisting of a stainless steel pipe (4 mm diameter, 0.1 mm wall thickness) with small capillaries (0.55 mm diameter) for connecting the individual straws.

3.7 The readout electronics

3.7.1 Requirements

The input characteristics of the front end electronics should match the electrical properties of the straw tubes. These are listed in Table 3.5.

From the point of view of the pulse propagation, the straw tube acts as a coaxial lossy transmission

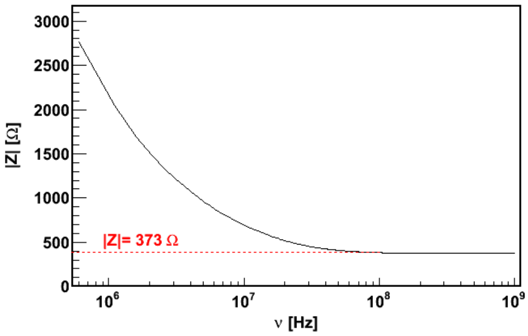

Figure 3.23: Straw tube impedance as a function of frequency $\nu = \omega/2\pi$ (solid black line). The high frequency limit is indicated with the red dashed line.

Peaking time	10 ns
Double pulse resolution	$\sim$ 150 ns
Intrinsic electronic noise	<1 fC
Discrimination threshold	≈5 fC
Max. drift time	150 ns
Max. occupancy	< 10%
TDC resolution	< 1 ns
Neutron exposure (10 years)	??? 1/cm^2
Radiation dose (10 years)	??? krad

Table 3.6: Front end electronics requirements.

line with an impedance given by the formula:

$$Z = \sqrt{\frac{R + i\omega L}{i\omega C}}, \tag{3.1}$$

where R is the electrical resistance, L is the inductance, C is the capacitance and ω is the angular frequency. For high frequencies ($> 100\,\text{MHz}$), the impedance of the straw tubes tends to the limit $Z \to \sqrt{\frac{L}{C}} = 373\,\Omega$ (see Fig. 3.23).

The basic requirements for the straw tube front-end electronics are listed in Table 3.6.

3.7.2 General concept

The CT consists of about 4640 tubes arranged into concentric layers (see sec. 3.3). The maximum counting rate of 800 kHz is expected for the innermost straws for the $\bar{p}p$ annihilations at the highest energy, and a frequency $2 * 10^7$ interactions/s. The maximum drift time is 150 ns for the selected cell geometry which results in an average double hit probability less than 10% for the innermost layers. The requested electronic time resolution should be below 1 ns, and the intrinsic noise level below 1 fC. The maximum anolog pulse duration should be comparable to the maximum drift time of 150 ns. To fullfill all these requirements, the proposed straw tube read-out organisation comprises 3 stages:

1. Front End Electronics (FEE) cards hosting 32 channels, each composed of: preamplifier, amplifier with analogue signal shaping and discriminator unit with differential output;
2. Digital Board (DB) with Time to Digit Converters (TDC), local FPGA for noise suppression, fast hit detection and slow control, memory buffer, and serial Gbit optical links for the data transmission;
3. Detector Concentrator Board (DCB) receiving and merging inputs from several DB in local memory buffer controlled by FPGAs. The board will provide derandomization and data buffering.

Data from the DCBs will be transferred via fast optical links to Compute Nodes for event building and subsequently for event selection. It will be possible to perform some local correlations on data to suppress noise and reduce amount of data sent from the board.

The $\overline{\text{P}}$ANDA data acquisition and filtering systems will implement a trigger-less architecture. Instead of a hardware trigger signal indicating the occurrence of a valid event, each DB will receive a precise clock signal distributed centrally from a single source: the Clock and Timing Distribution System (CTDS). The DB boards will continuously monitor the detector channels, and will generate data packets whenever the number of input signals exceed programmed thresholds. These data will be tagged with timestamps obtained from the CTDS. The data acquisition system will profit from the structured running mode of the HESR operation. Periods of 2μs with antiproton's interactions will be interleaved with periods of 400 ns of idle time. The information on the accelerator activity will be distributed to DCBs via the Clock and Timing Distribution System. The data recorded during the interaction intervals will be grouped together in DCB to form a burst which will be then uniquely tagged. Grouping of many bursts into predefined epogues (e.g. 500μs) is also considered in order to reduce network trafic. Data from all $\overline{\text{P}}$ANDA detectors tagged with the same burst identification number will be grouped together and will be made accessible to filtering algorithms implemented in the Compute Nodes (CN). Decisions produced by these al-

Table 3.7: Main parameters of new straw tube front-end chip (see text for more details)

Technology	0.35 μm CMOS
Number of channels	16
Input Resistance	∼120 Ω
Default gain	∼10 mV/fC
Peaking time (for delta)	10-15 ns
Timing resolution	1-2 ns
Equivalent (delta) input range	0-200 fC
Noise ENC	$< 0.4 fC$
Output standard	LVDS and analog
Power consumption	∼20 mW

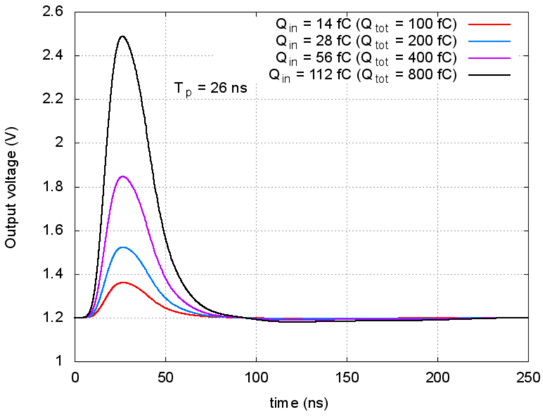

Figure 3.24: Examples of analog responses for various input charges.

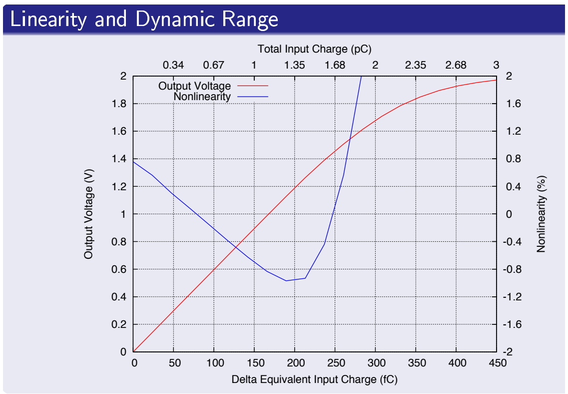

Figure 3.25: Simulated gain and linearity

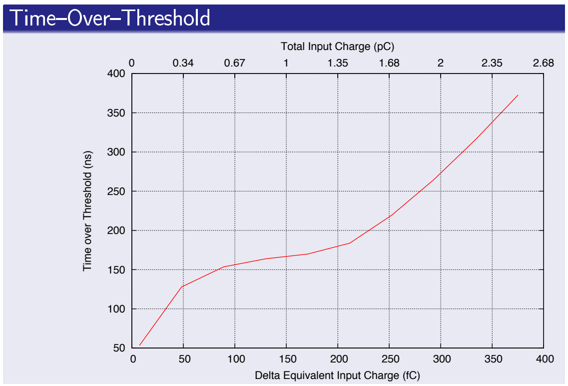

Figure 3.26: Simulated response of TOT vs charge

gorithms will thus be based on complete detector data with full granularity.

3.7.3 Front end board

An Application Specific Integrated Circuit (ASIC) is being developed in order to read the straw tube pulses. The main specification for this design is summarized in Table 3.7.

The ASIC's channel comprises charge preamplifier stage, pole-zero cancellation network (PZC), shaper stage, tail cancellation network, discriminator circuit, baseline holder (BLH), fast differential LVDS output and analog output. A typical simulated analog response of the amplifier for straw tube pulses has been generated with GARFIELD for different charge depositions and it is shown in Fig. 3.24. The charge depositions are expressed both as equivalent charges of delta like pulses and as integrated charge carried by pulses. The tail cancellation network assures that the pulse length is smaller than 100 ns. The simulated gain and linearity of the ASIC for the expected input charge range together with equivalent delta-like pulse are shown in Fig. 3.25. Estimated relation of the time over threshold to the input charge is shown in Fig. 3.26.

The discriminator circuit uses a simple leading edge configuration. The design of the described ASIC has been completed and submitted for manufacturing. The first prototypes are expected in mid 2011. The first prototype will contain 4 channels per chip. The final ASIC will have 16 channels.

A multilayer printed circuit board (PCB) will be designed to connect the signals from the straw anodes to the ASIC inputs. The PCB paths will connect dispersed anode connection points of straws to a front end connector. One unified 32-channel front end board (FEB) with two ASICs on it will be designed for the CT. The PCB will also deliver supply and threshold voltages to the FEBs. The FEB will have a separate output connector to send signals via flat twisted pair cable to the DB. The power and the slow control connectors will be placed on the PCB together with a number of Digital to Analog Converters (DAC) for the threshold setting. One, out of 6, CT sector composed of 768 straws will be read by 24, 32-channel FEBs. Thus, in total 6×24 twisted-pair flat cables will be needed to read the whole CT.

The solution for the new front-end should provide both the timing and the amplitude information. Since it is still under study whether the Time Over Threshold (TOT) technique or the true analog amplitude measurement will be used for the particle identification, the first ASIC prototype provides both the amplitude and TOT information. The block diagram of the designed prototype ASIC is shown in Fig. 3.27.

During the design phase of ASIC also several FEE prototypes, based on CARIOCA chips, have been tested with prototype chambers and showed satisfactory performance (see section ?).

The CARIOCA is 8 channel radiation hard ASIC (up to 20 Mrad dose) featuring preamplifier, shaper, base line restorer and discriminator. One single FEE board consists of four CARIOCA chips and allows for 32 channels read-out. FEE provides LVDS differential output which is connected by flat cable to the DB. The threshold for the CARIOCA's leading edge discriminators is set by the on-board DAC controled by the dedicated lines in the cable connection to the DB. The total power consumption per channel for CARIOCA amounts to 25 mW.

The most recent - second version - of the preamplifier/discriminator board is shown in Fig. 3.28. Its basic parameters are given in Table 3.9. The amplifier sensitivity curve is shown in Fig. 3.29).

The only limitation of the CARIOCA chip is the lack of signal amplitude information which is crucial for the CT in order to perform dE/dx measurements. However, it is still considered as a back-up solution for the Forward Tracker where dE/dx measurement is not required.

3.7.4 Time-to-digit converters

The DB will be located 5-6 meters outside chambers and will contain multi-hit TDC measuring the signal arrival time with respect to the external clock provided to the DB by the $\overline{\mathrm{P}}$ANDA CTDS as well as the length of the pulse.

A time measurement system based on the FPGA is foreseen for the CT. Recently, a time measurement board (TRBv3) based on Lattice ECP3 family, has been developed at GSI and Jagiellonian University. Implementation of TDC into FPGA allows for large flexibility in selection of main measurement parameteres like time range, binning etc., and makes this approach very attractive for broad range of aplications.Time measurements done at GSI demonstrate a $< 15\,ps$ resolution. For the CT detector TDC binning of 0.5 ns will be sufficient.

The block diagram of the TRBv3 is shown in Fig. 3.30. Four out of five FPGAs on the TRBv3 are located along the edges of the board. Each of them has a 208-pin input/output connector assigned. The fifth FPGA is located in the center of the board and coordinates the work of the edge FPGAs as well as communicates with the data acquisition system. The TRBv3 board may be equipped with four to eight optical SFP connectors. The maximum transmission speed of each optical connector is 3.2 Gbit/s. The input/output connectors are used to plug mezzanine cards in. The connector contains 188 general purpose lines and 6 high speed serial connections between edge FPGA and a mezzanine board. Eight lines are connected to the central FPGA from each connector. The design of the mezzanine card is left for future TRBv3 users. It may differ from a simple flat cable adapter to a sophisticated board (e.g multichannel ADC). A set of two connectors is placed on the bottom side of the TRBv3 allowing for yet another mezzanine card connection. All 160 general purpose lines from the bottom connectors are controlled by the central FPGA. Both top and bottom connectors provide a power and ground for mezzanine cards.

The edge FPGA may contain up to 50 time measurement channels. The DB TRBv3 for CT will have 48 TDC channels in FPGA giving the total number of 192 channels per board. Thus, four TRBv3 boards will collect data from one CT sector.

Former version, TRBv2, containing four HPTDC chips was used for the recent straw tube detector tests. It has been built in synergy with the HADES experiment at GSI [13] (schematics and photograph of TRBv2 are shown in Fig. 3.31 and Fig. 3.32, respectively). The HPTDC chip (32 channels) has been developed at CERN for LHC experiments. HPTDC can operate with a maximum trigger rate of 1 MHz and a maximum of 2 MHz hit rate per channel. 4 TDC binning widths (25, 100, 195 or 785 ps) can be selected by software during the chip initialization. For the straw tubes, binning of 785 ps has been selected. The measured hit times together with the trigger time stamp are stored in the local TDC memory (up to 256 hits/shared by 8 channels can be stored) and read-out from the TDC Read-

General parameters	Number of channels	8
	Radiation resistance	20 Mrad
	Technology	IBM CMOS 0.25 μm
Input parameters	Input impedance	45 Ω
	Range of input charge	2.5 ÷ 300 fC
	Peaking time	14 ns
	Sensitivity with detector capacitance 220 pF for	
	positive input	8.21 mV/fC
	negative input	7.7 mV/fC
	Width of output pulse for charge < 300 fC at	
	positive input	55 ns
	negative input	65 ns
	Minimum charge	
	positive input	2.4 fC (rms 0.37 fC)
	negative input	2.4 fC (rms 0.24 fC)
Output parameters	Standard of pulses	LVDS

Table 3.8: Basic technical parameters of the CARIOCA-10 chip.

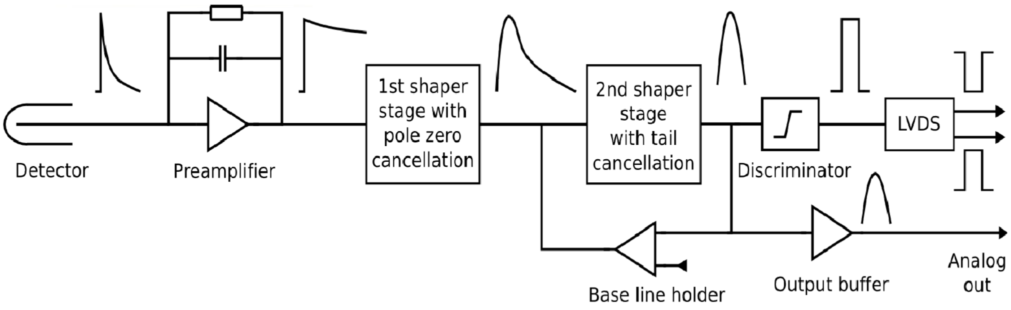

Figure 3.27: Block diagram of straw tube front-end.

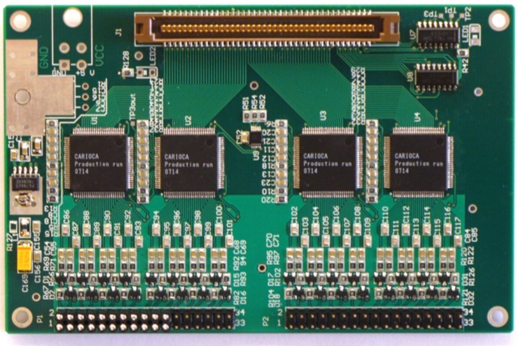

Figure 3.28: Prototype board of 32-channel preamplifier/discriminator based on CARIOCA-10 chips.

Supply voltage	+4.5 ÷ +12 V DC
Supply current	560 mA
Power consumption	3.3 W
Number of channels	32
Dimensions of board	124 mm x 80 mm x 16 mm

Table 3.9: Technical characteristics of the prototype preamplifier/discriminator board - version-2.

out FIFO (also 256 hits deep) with 40 MHz clock (8 bit parallel bus) to the DB local memory. Noise suppression and fast hit detection on single wires is performed in FPGA located on the board. HPTDC allows also to measure time over the threshold which is used for noise suppression. The FPGA controls also the data flow. The data are transmitted from the DB via 8b/10 serial 2.5 Gbit optical link driven by TLK2501 transceiver from Texas Instruments.

For tests an external trigger (clock) was connected to the TRBv2 by a dedicated line, not shown in

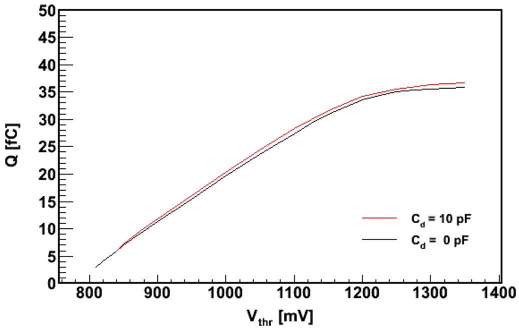

Figure 3.29: Discrimination threshold as a function of the control voltage measured for detector capacitance of 0 pF (black curve) and 10 pF (red curve).

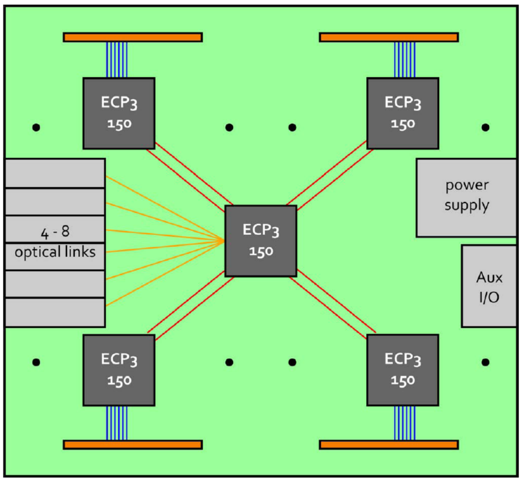

Figure 3.30: Block diagarm of TRBv3.

the schematics. Slow control, setting of the CARIOCA thresholds, is provided by the Etrax FS CPU running LINUX OS and EPICS client.

3.7.5 Data rate

An average maximum hit rate of 800 kHz per channel is expected for most inner starws at 2×10^7 proton-antyproton annihilations. One DB, with 196 channels, will provide in average 156.8 Mhits/s. TDC when measuring 1 us time range with 0.5 ns resolution will deliver 11-bit result. Time over threshold in range of 200 ns will deliver 8-bit result. 6 bits are necessary to code channel number (1-48) and 9 bits to code time stamp (1 - 500).The latter assumes that epoques of 500μs are stored in the DB buffer. Such memory (400 kB will be enough for one epoque can be easily implemented in the FPGA.

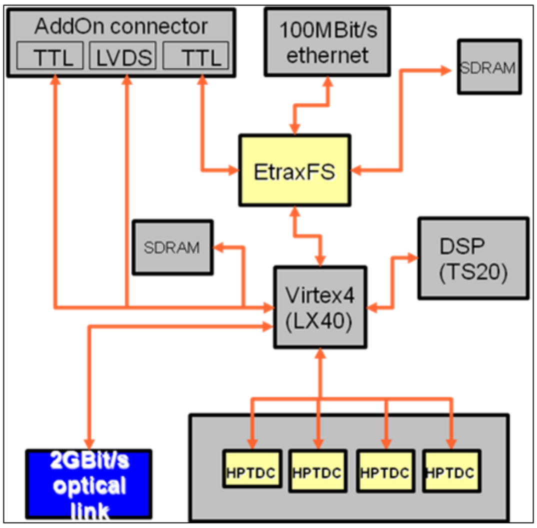

Figure 3.31: Schematics of the TRBv2 HADES board used for the time-of-flight measurements.

Altogether 34 bits represent one TDC channel result in a given TDC on the DB. Two more bits are necessary to distinguish the FPGA. Thus 5 bytes word is generated for each hit on the DB. Assuming 800 khits per second 4 MB/s is generated in each TDC channel. This results in 784 MB/s data rate from one DB. This data ratio can be handled by four 3.2 GBit/s optical serial links. Twenty four 196-channel DBs will be necessary for the full CT read-out.

Therefore, it seems to be reasonable to merge data from straw tube layers belonging to one sector and sent them to common DCB. Merged data could be then send to the CN by one fast optical link. Such layout can be more optimal for cluster search but is not mandatory since DB have also features of Detector concentrator (grouping of bursts in epoques).

A board which could be considered as a prototype of the $\overline{\text{P}}$ANDA DCB has been developed by HADES DAQ group (so called the optical hub module) and is currently installed in the Krakow straw tube test set-up. The prototype is equipped with several Small Form-factor Pluggable Transceivers (SFTP) serving as optical connectors and FPGAs controlling data transfer. An attractive feature of this unit is the possibility to create groups of links (4 in the present prototype) into one protocol standard. This is provided by FPGA controlling data flow (*i.e.* Lattice SCM 50 chip) which currently supports 8b/10b and GBitEthernet format. Optical links used on this prototype can send data with maximal speed of 3.8 Gbit/s.

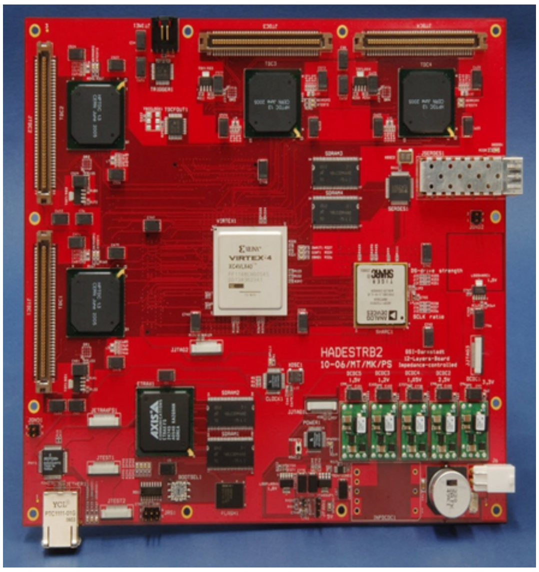

Figure 3.32: HADES TRBv2 board.

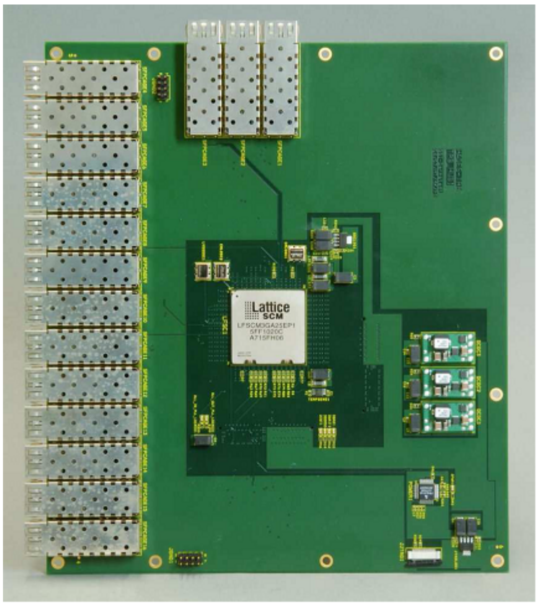

Figure 3.33: Optical HUB board from the HADES experiment.

3.8 The single straw tube simulation

3.8.1 The charge released into the tube

We have performed a detailed simulation of the charge generation and collection in a single straw tube.

In correspondence of an incident charged particle, we sample from the exponential distribution the point where an electron cluster is generated and from the proper distribution (see below) the number of electrons in the cluster. By stopping when the particle leaves the tube, we have the number of free electrons generated from a poissonian number of clusters. The mean number of clusters/cm is taken from ref. [14] (25 for Ar and 35.5 for CO_2). For the reliability of the simulation, it is crucial to know the cluster size distribution, that is the number of electrons per cluster. We use the theoretical calculations of [15] for Ar and the experimental data on Ar and CO_2 from [16]. The comparison with some available results in gas has shown that this choice is in reasonable agreement with data (see Fig. 3.34). By knowing the mean value of the energy spent per free electron (i. e. to create a ion pair), the overall energy loss of the projectile on the whole path can be calculated. The assumed values are $27\,eV$ for Ar and $33.5\,eV$ for CO_2 [14].

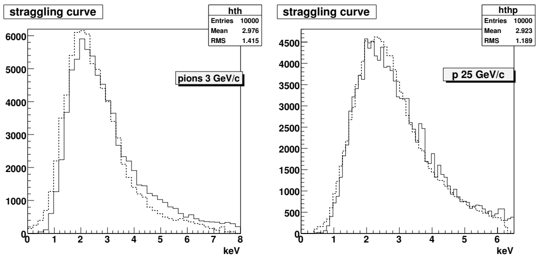

Figure 3.34: Comparison between the simulation of the energy lost in a 1.5 cm Ar/CO_2 layer (line) and the experimental values of Allison et al. [17] (dotted line).

As a further check, we compared the energy lost in the tube, for a variety of projectiles and energies, with the Urban model [18], which is used in GEANT3 and GEANT4 in the case of gaseous thin absorbers [19, 20]. The results, reported in Fig. 3.36, show good agreement with our simulation.

3.8.2 The drift process from GARFIELD

The tube response has been studied in detail giving as input to the GARFIELD code the tube dimensions, wire radii, high-voltage, gas mixture and magnetic field.

The mixture and the high voltage determine the kind of behaviour of a gas. In the weak electric field or in a mixture with high quenching the electrons are in thermal equilibrium with the surrounding medium and the drift velocity is proportional to

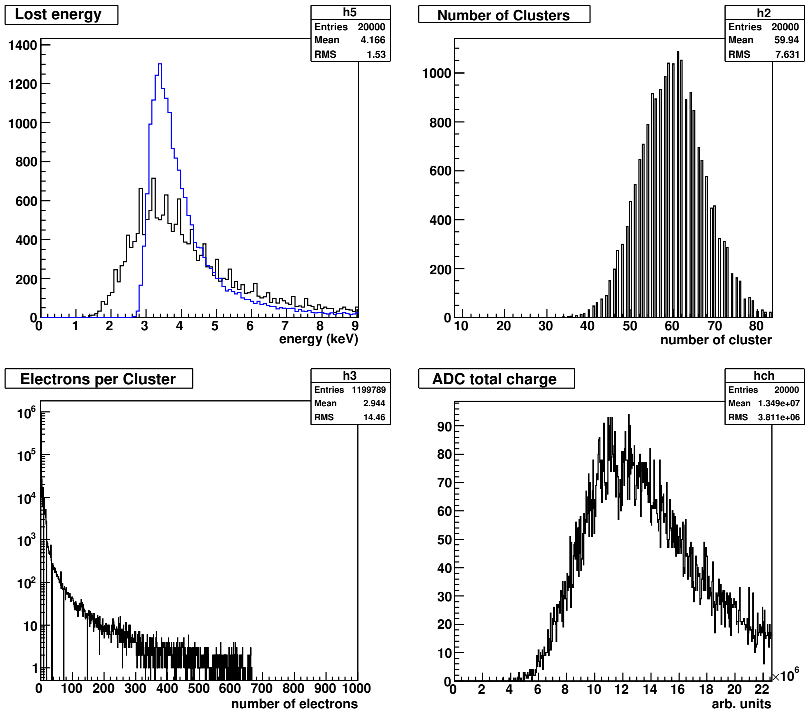

Figure 3.35: Results of the single tube simulation for a 1 GeV pion in a 2 atm pressure straw tube with a 90/10 Ar/CO_2 gas mixture. Upper left: energy lost in a tube compared with the sharper Landau distribution; upper right: poissonian distribution of the number of clusters; bottom left: cluster size distribution calculated as discussed in the text; bottom right: charge collected on the wire assuming a multiplication mechanism from the Polya distribution. By multiplying the number of clusters with the mean number of electrons per cluster, a mean number of primary electrons of about 200 is obtained.

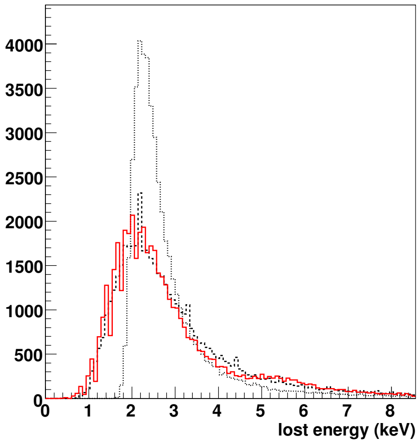

Figure 3.36: Energy loss of 1 GeV pion traversing a 1 cm of 90 % Ar 10 % CO_2 gas mixutre at NTP. Solid line: Urban distribution; dashed line: specific simulation model; dotted line: Landau distribution.

the electric field intensity. Such gases are usually called "cold".

On the contrary, if the electron average kinetic energy differs from the thermal energy, the drift velocity behaviour becomes saturated and tends to be constant and independent of the electric field strength, that is of the distance from the wire anode. In this way the main sources of systematic errors are removed and the track reconstruction is easier. Such gases are called "hot". However, the high spatial resolution in the hot gas mixtures is limited by the large diffusion, and can't be better than 50 μm.

The drift velocity as a function of the wire distance is reported in Fig. 3.37 showing that the increase of the CO_2 percentage tends to cool the gas, with a corresponding stronger dependence of the velocity from the wire distance. This effect could be recovered by an accurate self-calibration (see below), but makes the tube stability more critical, requiring a precision control of temperature and pressure.

The effect of the magnetic field transforms the small segment motion between two collisions of a moving charge into circular trajectories. With obvious notation, the electron Lorentz angle is [21]:

$$\tan\alpha = \tan\omega\tau = \frac{eB}{m_e}\tau$$

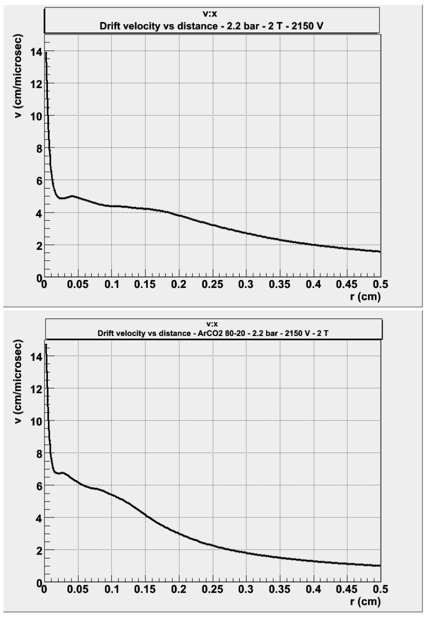

Figure 3.37: Drift velocity vs. wire distance in a straw tube of 0.5 cm radius, 1850 V voltage, 2.2 bar pressure and 2 T magnetic field for different gas mixtures: left, $90-10\,\%$ $Ar-CO_2$, right, $80-20\,\%$ $Ar-CO_2$.

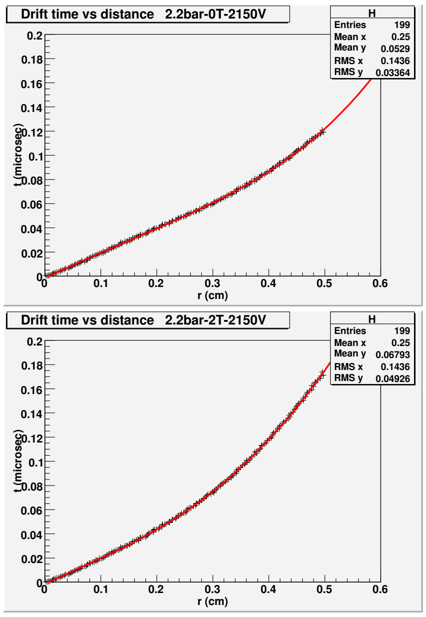

Figure 3.38: Drift time vs. wire distance in a $90-10\,\%$ $Ar-CO_2$ straw tube of 0.5 cm radius and 2.2 bar pressure: up, without magnetic field; down, with magnetic field of 2 T (from GARFIELD).

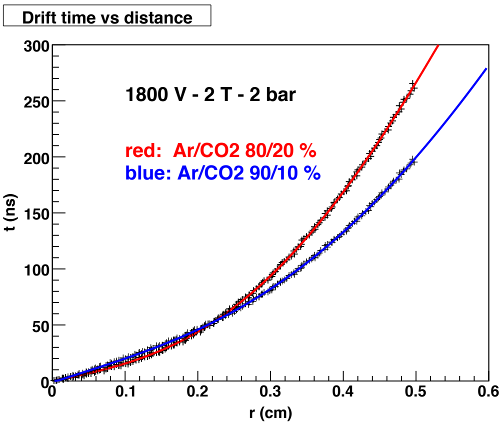

Figure 3.39: Time vs. wire distance for two different Ar/CO_2 mixtures in the presence of magnetic field (from GARFIELD).

where τ is the average time between collisions and ω is the Larmor frequency of the electron. In cold gases the drift velocity tends to be linear with the electric field E and τ is almost constant, whereas in hot gases, where the drift velocity is more constant, τ is inversely proportional to E. Due to the much lower elastic cross section, τ in hot gases is about one order of magnitude higher. Estimation from experimental data show that, for a 2T magnetic field and a 5 mm drift distance, the drift time for a CO_2/C_4H_{10} 90/10 mixture increase of 15 % in a magnetic field, that for a Ar/CO_2 90/10 mixture increases up to 50 % [22].

All these effects are reproduced in the GARFIELD results.

Typical time vs. distance curves for a hot like Ar/CO_2 90/10 mixture, with and without magnetic field, are reported in Fig. 3.38, where the increase of the drift time due to the field is clearly visible.

The increase in the drift time while increasing the CO_2 percentage is also clearly shown in Fig. 3.39.

Another important input to the simulation are the transverse and longitudinal diffusion curves, due to the thermal spreading of the electron clouds during the drift. The GARFIELD results show that the high diffusion values of the hot gas ($Ar/CO_2 = 90/10$) are partially compensated by increasing the pressure. At 2 atm pressure the longitudinal and transverse diffusion coefficients, at 5 mm distance from the wire, are 100 and 140 μm, whereas at 1 atm pressure the same coefficients are 120 and 220 μm, respectively.

Finally, the necessary input to the simulation is the gas amplification, that is the multiplication factor of the avalanche which is formed in the last tenth of microns of the primary electron path in its drift to the anode wire. This multiplication factor is given by [21]:

$$G = \exp\left(\int_a^x \alpha(x)\mathrm{d}x\right) ,$$

where $\alpha(x)$ is the Towsend coefficient (inverse of the mean free path for ionization), a is the anode wire radius and the integral is taken along the whole drift path. A typical behaviour of the gas gain, measured for our mixtures of interest is shown in Fig. 3.40, where one sees that in our case the tube remains in the region of direct proportionality.

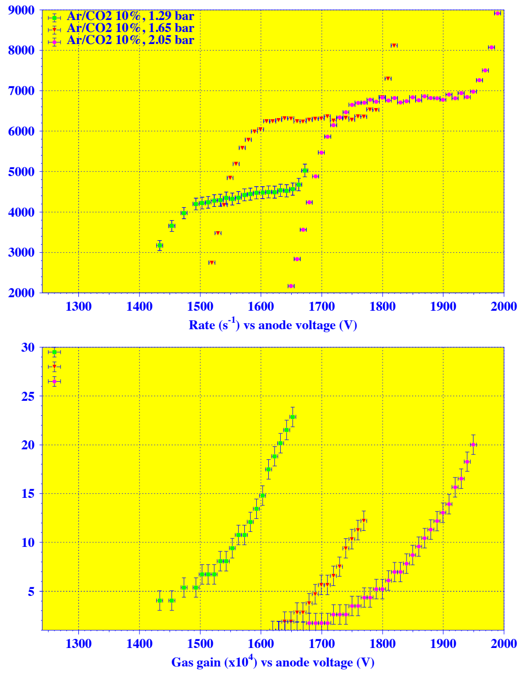

Figure 3.40: Experimental plots of the tube rate and gas gain relative to a $90 - 10\,\%$ $Ar - CO_2$ mixture.

3.8.3 Simulation of the drift process

Once the free electrons have been created in some points of the tube, their position is dispersed both longitudinally and transversally according to the GARFIELD diffusion curves and the time of arrival on the wire is calculated from the GARFIELD distance-time curves.

The arrival of each electron gives rise to a charge, which is obtained by sampling from a Polya distribution [21] having as a mean value the gain or multiplication factor (around $5 \cdot 10^4$). Then, by summing this signal over the number of electrons we obtain the total charge, as shown in Fig. 3.35.

3.8.4 The electrical signal

By taking into account the arrival time of each electron and assigning a Gaussian-shaped electrical response to each charge multiplication, we can reproduce also the shape of the electrical signal. We added also a white noise component equal to the 3 % of the primary signal peak value.

Some examples are shown in Fig. 3.41, where two typical signals are shown: the first one is generated from a track 1 mm near to the wire, the second one from a track 4 mm far from the wire. In the first case the clusters arrive dispersed in time, giving rise to an irregular structure of the signal. In this case the discrimination technique is crucial for a good time resolution. In the second case the cluster arrival is more concentrated and the signal structure appears more regular. These example show the importance of the electronic treatment of the signal and of the discrimination technique to be used for obtaining the drift time.

We consider two discrimination techniques: fixed (F) and constant fraction (CF) thresholds. The F thresold is set to about 5 % of the mean primary electron value, that is to 10 primary electrons in the 2 atm case (see Fig. 3.35). This is compatible with previous studies [23, 24]. The CF threshold is set to 5 % of the peak value of the current signal.

In the following, when no explicitly specified, the displayed results are obtained with the standard F threshold.

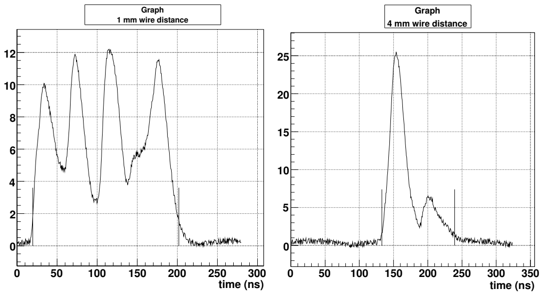

Figure 3.41: Straw tube signal simulated from a track near to (left) and far from (right) the wire.

3.8.5 Simulation of the self-calibration procedure

The primary information from the tube is the drift time distribution of the arriving signals, that is the number of tracks dN within the time interval dt. A typical distribution of this quantity, in the case of a parallel and uniform illumination of the tube is shown in Fig. 3.42 and in Fig. 3.43 (left) in the case of the absence and the presence of the magnetic field, respectively.

The self-calibration method exploits the properties of this distribution. Since the track density is constant over the tube diameter, one can write

$$\frac{\mathrm{d}N}{\mathrm{d}r} = \frac{N_{\mathrm{tot}}}{R} \ , \tag{3.2}$$

where N is the number of tracks, r is the wire distance, N_{tot} is the total number of tracks and R the tube radius. The number of tracks in a time interval can be otained directly from the above relation:

$$\frac{\mathrm{d}N}{\mathrm{d}t} = \frac{\mathrm{d}N}{\mathrm{d}r}\frac{\mathrm{d}r}{\mathrm{d}t} = \frac{\mathrm{d}r}{\mathrm{d}t}\frac{N_{\mathrm{tot}}}{R} \ . \tag{3.3}$$

After integration, one obtains the desired space-time relation $r(t)$ by integration of the time spectrum up to t:

$$r(t) = \frac{R}{N_{\mathrm{tot}}} \int_0^t \frac{\mathrm{d}N}{\mathrm{d}t}\,\mathrm{d}t \ . \tag{3.4}$$

The time spectrum and the space time relation $r(t)$ are shown in Fig. 3.42 (without magnetic field) and in Fig. 3.43 (with magnetic field). The result of this method of calibration is shown in Fig. 3.44.

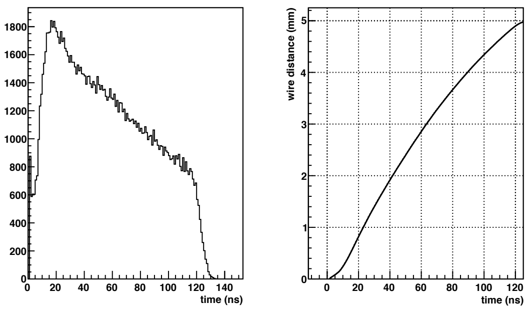

Figure 3.42: Simulated TDC spectrum without magnetic field of a single tube uniformly illuminated (left) and space-time relation obtained with the self-calibration method of Eq. 3.4.

This simulated procedure corresponds, during the real calibration, to have an accurate knowledge of the relationship between the measured drift time and the minimum approach distance of the particle trajectory to the wire. The mean value of the residuals of tracks is then used to correct the measured drift times until the residual distribution is symmetric about zero.

To explore the effect of the electronic threshold, we simulates also the resolution obtained by applying to the signal a constant fraction discrimination technique, simulated as a fixed pecentage (5 %) of the peak of the current signal.

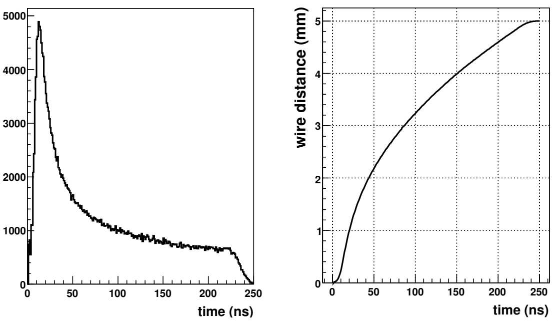

Figure 3.43: Simulated TDC spectrum for a 2T magnetic field of a single tube uniformly illuminated (left) and space-time relation obtained with the self-calibration method of Eq. 3.4.

The improvement in the resolution, showed in Fig. 3.45, demonstrates the importance of the discrimination of the tube signals.

3.8.6 Full and fast simulation

The full simulation reproduces the time output from the drift tube and the ADC response on the charge collected starting from the primary cluster formation as discussed in the sections above. Since the time required for each event is long, we also implemented into the simulation software a fast simulation option.

The spatial resolution is simply obtained through the MC truth for the true wire distance, which is used as the abscissa in Fig. 3.46 to extract the σ for the Gaussain smearing to obtain a realistic position determination of the tube.

The second important quantity, the charge collected on the wire, is simulated in a fast manner by sampling the energy lost from the Urban distribution as in Fig. 3.36, avoiding in this case the charged cluster generation.

In this way the time spent in the tube response simulation result to be negligible when compared with the other part of the software.

3.9 Calibration and Monitoring

In order to develop calibration techniques for the $\overline{\mathrm{P}}$ANDA Straw Tube Tracker, to understand signal formation and to optimise the matching of the straws with the electronics, a calibration procedure has been implemented and tested with the

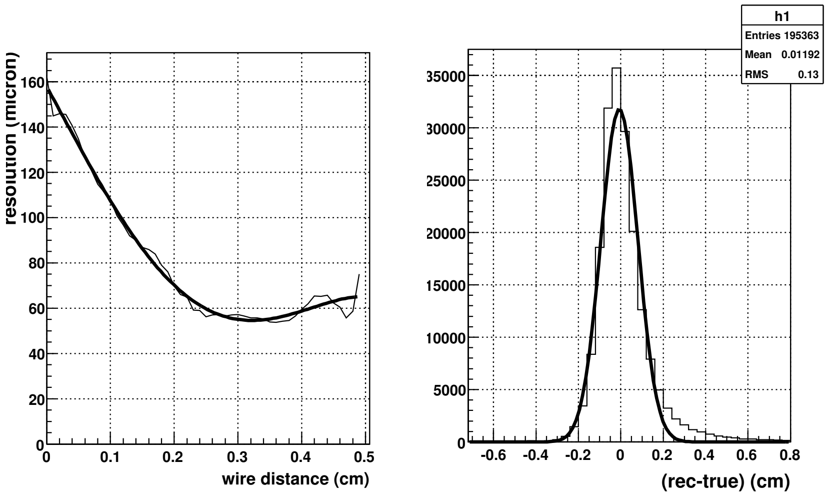

Figure 3.44: Simulated average residual width as a function of the track distance from the wire (left) and residual distribution of (reconstructed-true) wire distance. The bold line is the smoothing polynomial.

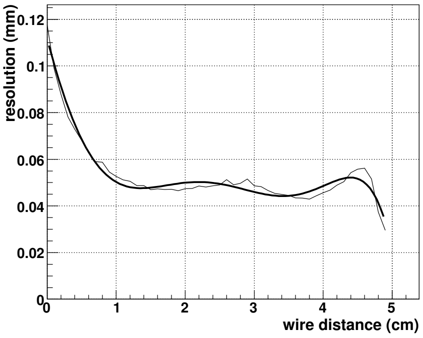

Figure 3.45: As in Fig. 3.44 with a constant fraction electronic discrimination.

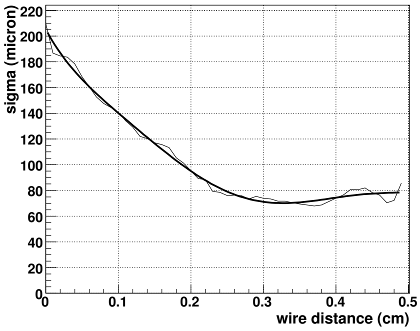

Figure 3.46: Standard deviation corresponding to the residual width resolution of Fig. 3.44 (left).

experimental data collected with two test systems (Sec. 3.10).

The algorithms, described in detail in the following, can be easily adapted for the $\overline{P}$ANDA–STT, since the calibration method will be very similar.

3.9.1 Straw tube calibration

3.9.1.1 Fit of TDC spectra

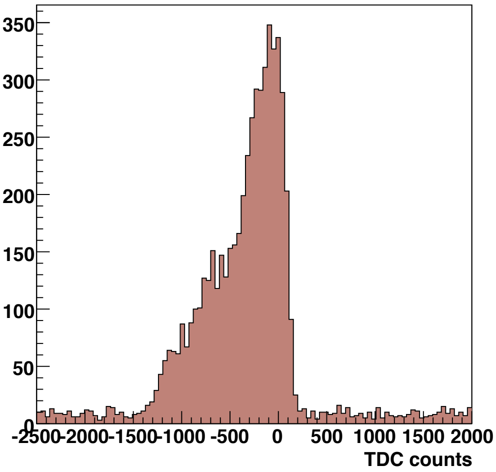

Figure 3.47: Example of a raw TDC spectrum. On the x axis, the time is expressed in TDC counts (in this case, one TDC channel corresponds to 130 ps) and runs from right to left.

Fig. 3.47 shows an example of the time spectrum for a uniformly illuminated tube. In this figure, time is expressed in TDC counts and runs from right to left. In order to get the time spectrum, TDC counts are converted into seconds and time is reversed; finally, the spectrum shown in Fig. 3.48 is obtained. The analysis of the individual tube time distributions allows the monitoring of the data quality: the minimum and the maximum drift times, t_0 and t_{max}, correspond to a track traversing the tube close to the wire and to the cathode wall, respectively. The value of t_0 depends on delays of the signal cables and front–end electronics as well as on discriminator threshold and HV setting. Nearby tubes sharing the same front–end electronics are expected to have very similar values of t_0; on the contrary, the drift time $\Delta t = t_{max} - t_0$ depends only on the drift properties of the tubes. The number of events outside the drift time window gives an estimate of the random, constant noise level over time range (Fig. 3.47) [25].

For each tube, the parameters of the drift time distribution are derived from a fit performed with the following empirical function [25, 26, 27]:

$$\frac{\mathrm{d}n}{\mathrm{d}t} = P_1 + \frac{P_2\,[1 + P_3\exp((P_5 - t)/P_4)]}{[1 + \exp((P_5 - t)/P_7)]\,[1 + \exp((t - P_6)/P_8)]}, \tag{3.5}$$

where P_1 is the noise level, P_2 is a normalisation factor, P_3 and P_4 are related to the shape of the distribution, P_5 and P_6 are the values of t_0 and t_{max}. P_7 and P_8 describe the slope of the leading and trailing edge of the distribution, so they are indicators of the drift tube resolution close to the wire and to the tube wall, respectively. In Fig. 3.48 the fit function is also shown (green line).

In order to do a unique calibration for all the tubes, their time spectra must have approximately the same shape and the same drift time Δt. A quality check on the uniformity of the tubes, as well as on the quality of the fit, can be done by looking at the distributions of the fit parameters.

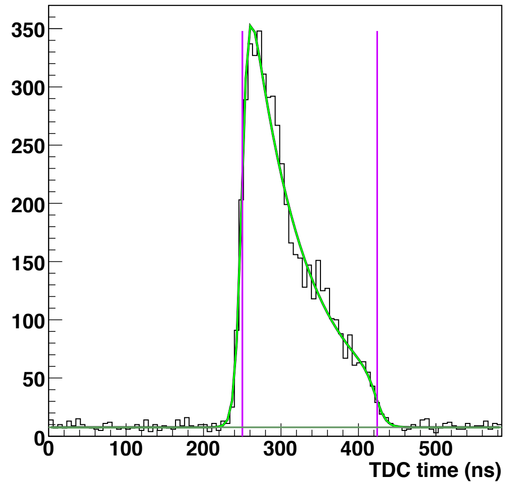

Figure 3.48: Example of a fitted TDC spectrum. The light green line is the fit of the distribution; the violet vertical lines correspond to the t_0 and t_{max} values determined by the fit. The dark green horizontal line indicates the noise level.

3.9.1.2 $r(t)$ calibration curve

After the selection of the similar spectra, their specific time offset t_0 is corrected and their noise level is subtracted; then, they are added into a sum spectrum, each in its Δt range.

Under the hypothesis of a uniform illumination of the tube and a constant efficiency over the tube volume, the isochrone radius – drift time relation ($r(t)$ relation in the following) can be obtained by the following integration:

$$r(t) = \frac{R_{\mathrm{tube}}}{N_{\mathrm{tot}}} \int_0^t \frac{\mathrm{d}n}{\mathrm{d}t'}\mathrm{d}t', \tag{3.6}$$

where n is the number of tracks, N_{tot} is the total number of tracks and R_{tube} the tube radius.

Taking into account the finite TDC resolution (bin size) and the wire radius R_{wire}, Eq. 3.6 becomes:

$$r(t_i) = \frac{\sum_{i=1}^{i_t} N_i}{N_{tot}} \cdot (R_{tube} - R_{wire}) + R_{wire}. \tag{3.7}$$

R_{wire} is the wire radius and N_{tot} is the sum of all bin entries N_i.

The obtained space–time relation is then parametrised as a polynomial function.

An example of the $r(t)$ curve is shown in Fig. 3.49; in this case, the space–time relation has been parametrised with a combination of Chebyshev polynomials of the first kind up to the fifth order:[2]

$$\begin{aligned} r(t) &= p_0 + p_1 t + p_2(2t^2 - 1) + p_3(4t^3 - 3t) \\ &+ p_4(8t^4 - 8t^2 + 1) + p_5(16t^5 - 20t^3 + 5t). \end{aligned} \tag{3.9}$$

Once the space–time relation is known, the isochrone radius of a certain tube is computed by substituting in Eq. 3.9 the measured drift time. This is calculated by subtracting from the measured drift “raw” time the time offset t_0 of that tube, obtained from the fit of Eq. 3.5.

---

[2] The Chebyshev polynomials of the first kind are defined by the recurrence relation:

$$\begin{aligned} T_0(x) &= 1, \\ T_1(x) &= x, \\ T_{n+1}(x) &= 2xT_n(x) - T_{n-1}(x). \end{aligned} \tag{3.8}$$

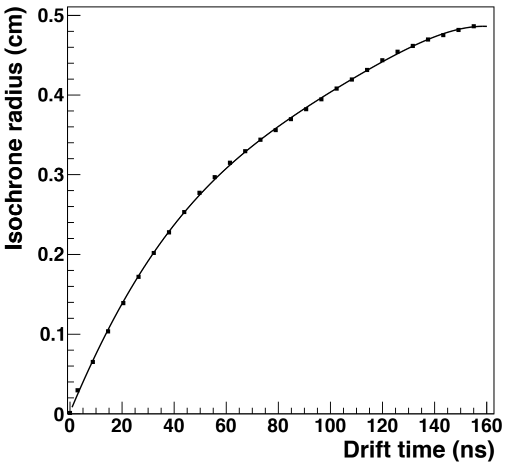

Figure 3.49: Isochrones radius – drift time relation ($r(t)$), parametrised using a combination of Chebyshev polynomials of the first kind, up to the fifth order.

3.9.2 Autocalibration

Once the calibration curve has been derived, it is possible to proceed with the track reconstruction.

In order to perform a good track fitting, it is necessary to know with high precision the relation between the measured drift time and the distance of closest approach of the particle trajectory to the wire. This implies an accurate knowledge of the $r(t)$ relation, that can be achieved with an iterative procedure called **autocalibration**, since it makes use just of the information from the tubes under investigation.

The autocalibration works as follows: at each step of the procedure, the $r(t)$ relation derived in the previous iteration is used to convert the measured drift times into drift radii, that will be used in the track fitting. At the first step, the $r(t)$ relation obtained directly from the integration of the drift time spectra (Sec. 3.9.1.2) is used.

Once a track candidate is been identified through dedicated pattern recognition algorithms, the track is reconstructed by using a track fitting algorithm. It allows to extract the (x, y) hit coordinates from the drift times and the (x, y) coordinates of the firing wires, which are the observables measured by the straw tubes.

The fitting algorithms implemented for the $\overline{\mathrm{P}}$ANDA–STT will be described in detail in Sec. 3.11; the tracking procedure used for the test systems will be briefly presented in Sec. 3.10.

In this last case, in general tracks are reconstructed as straight lines $y = a + bx$, where the parameters a and b are obtained by a least squares fit (χ^2) that minimizes the track residuals, i.e. the difference of the distances of closest approach of the best fit lines to the centers of the firing tubes and the corresponding isochrones calculated from the measured drift times using the $r(t)$ relation.

For each tube of the pattern associated with a track, the residuals are then computed and represented as a function of the N bins the drift time interval is divided into.

If the $r(t)$ relation was exact, the average residuals would be zero at all radii. An example of residual distribution is shown in Fig. 3.50: at this step, the mean value of the residuals varies from a minimum of $\sim$ -160 μm to a maximum of $\sim$ 320 μm for small radii.

These deviations from zero mean miscalibrations in the $r(t)$ relation, which is then directly corrected by using the average deviations themselves.

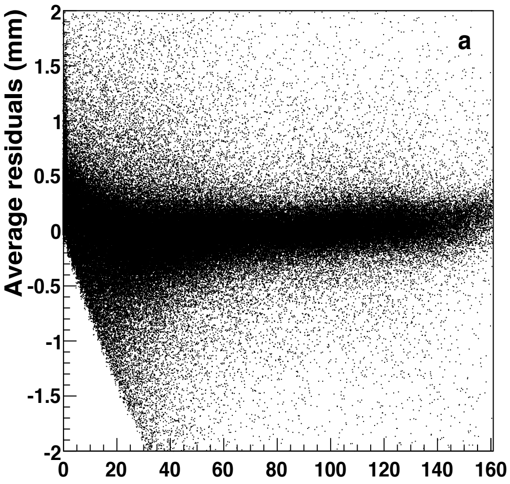

Figure 3.50: Distribution of the average residuals as a function of the drift time at the first iteration.

The track reconstruction and the $r(t)$ calibration by means of the residuals are then repeated until the corrections become less and less relevant, that is when the mean value of the residuals becomes closer to 0, as shown in Fig. 3.51.

To study the speed and stability of the convergence of the method, the following quantity (mean square correction):

$$\Delta_k^2 = \frac{\sum_{i=0}^{N} \delta_{ik}^2}{N}, \tag{3.10}$$

where δ_{ik} is the mean value of the residuals in the i^{th} time bin and N is the total number of bins, can be used as figure of merit (Fig. 3.52).

The recalibration procedure is iterated until the mean square correction has converged to a stable solution [28].

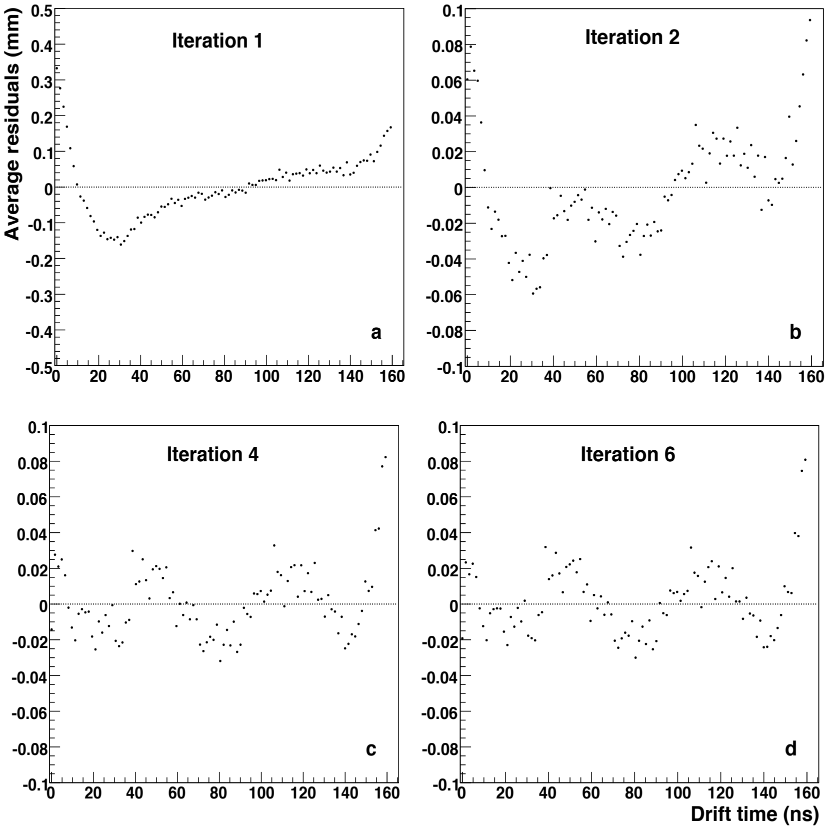

Figure 3.51: Distribution of the average residuals as a function of the drift time after one (a), two (b), four (c) and six (d) iterations of the autocalibration procedure.

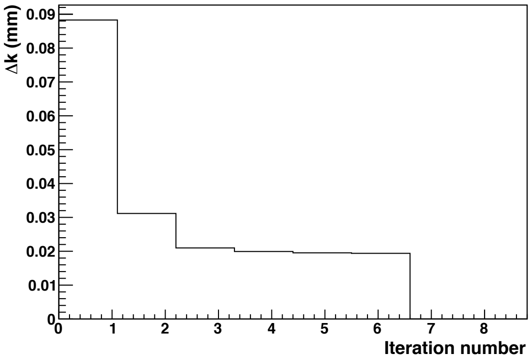

Figure 3.52: Root mean square correction from the autocalibration procedure.

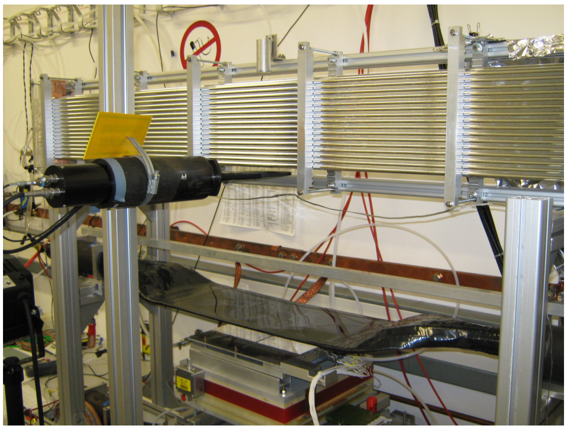

Figure 3.53: Straw tube prototype used at the Institut für Kernphysik at Forschungszentrum-Jülich. Design and construction by IKP-Jülich.

3.10 Prototype tests

3.10.1 Small–scale setup

3.10.1.1 Experimental setup

The setup is shown in Fig. 3.53: it consists of a dense array of 128 $\overline{\text{P}}$ANDA–type straw tubes, arranged in four double–layers of 32 straws each. The tubes, with an aluminised mylar wall 30 μm thick, are 150 cm long and have a diameter of 10 mm; in the centre of the tubes, a 20 μm anode wire is stretched. The tubes can be filled with different gas mixtures, like $ArCO_2$ or ArC_2H_6 (see the detail of the gas manifolds in Fig. 3.54), and can be operated at different conditions of high voltage and pressure. In addition, a drift chamber with two–dimensional readout for particle tracking, a hybrid drift chamber with a GEM amplification stage for clustering investigations and a small straw tube detector (24 cm long, 4 mm diameter) are included [29]. Finally, two scintillators are placed below the double–layers and used for triggering time to select the signal events when a coincidence occurs.

Half of the channels are equipped with the amplifier–discriminator chip CMP16[3], connected with the 64 channels time–to–digital converter based on the F1 TDC chip of the type used at WASA-at-COSY [30].

The anode signals of the other 64 channels are processed by modular fast current amplifiers with 8 ns rise time; thus, individual cluster or groups of few overlapping clusters created along the ionised track became visible in the signal structure.

The flash charge–to–digital converters FQDC analyse signals in terms of charge and pulse–height and disentangle signals into components originating from ionised clusters or groups of clusters in gaseous detectors.

The FPGA[4] controlling the readout of the QDC module are programmed for high flexibility to permit also total readout in the “oscilloscope mode” and to record single spectra in a self triggering mode for calibration measurements with Fe-55 β^+ sources. In view of the limited number of oscilloscope channels several amplifiers were fed via analog OR into the oscilloscope and then the data were transferred to a computer.

The actual number of firing straws in each event can be deduced from a multiplicity signal delivered by the 8-channel discriminator [31].

3.10.1.2 Spatial resolution

By analyzing the experimental data sets collected with the straw tube prototype described above, it has been possible to derive the spatial resolution σ for single straw tubes shown in Fig. 3.55 as a function of the drift distance [28].

It has been obtained in the following way: after the last iteration of the autocalibration procedure (Sec. 3.9.2), the tracking has been performed and a track hypothesis has been found, event by event.

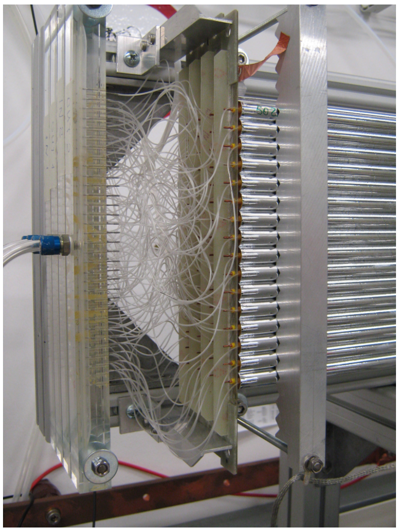

Figure 3.54: Detail of the prototype shown in Fig. 3.53.

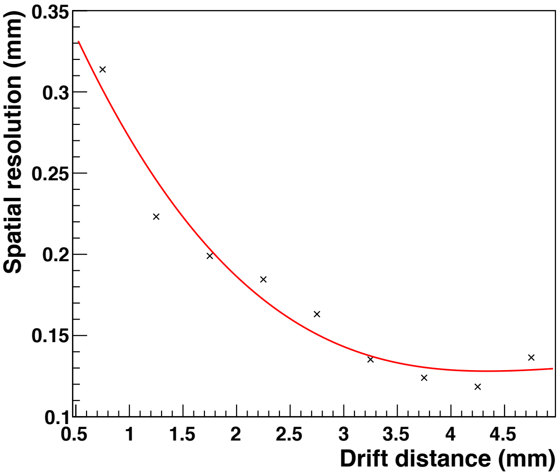

Figure 3.55: Mean spatial resolution σ for single tubes, obtained as explained in the text. The red line is the fit with a third order polynomial.

Depending on the track to wire distance, the corresponding distribution of the residuals has been filled.

For each interval, the obtained residual distribution has been fitted with two functions (two Gaussian or one Gauss function and a third order polynomial)

---

[3] The CMP16 board is based on an analog–to–digital converter chip with 16 channels which transforms analog signals to LVDS (Low–voltage Differential Signaling) standard. It can run at very high speed at reduced electromagnetic noise. The transfer characteristics of the amplification and discrimination are presented in [?].

[4] Field Programmable Gate Array.

in order to better describe both the peak and the tails of the distribution. An example of residual distribution for one interval is shown in Fig. 3.56.

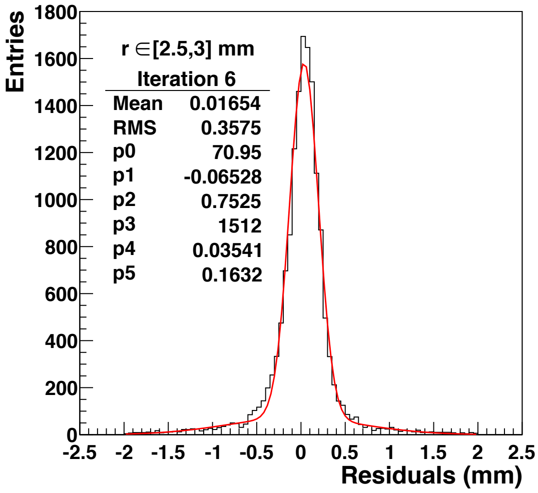

Figure 3.56: Distribution of the residuals for r in the range [2.5, 3] mm at the last step of the autocalibration. The distribution has been fitted with two Gauss functions; the parameters of the fit are in the box (p_3, p_4 and p_5 are the ones of the Gauss function that fits the peak).

The values of σ of each Gauss function that fits the peaks of the residual distributions has been then used to derive the single tube resolution shown in Fig. 3.55.

The mean value of the spatial resolution curve is in agreement with the deviation σ of about 177 μm (parameter p_5 of the fit) of Fig. 3.57. It shows the distribution of the mean residuals of 162385 straw hits after the sixth iteration of the autocalibration procedure, whatever the value of the corresponding track to wire distance was.

The distribution has been fitted with two Gauss functions, whose parameters are reported in the statistics box in figure: the first three refer to the Gauss function that fits the tails of the distribution, the other three refer to the one that fits the peak.

The distribution of the residuals is highly symmetric around a mean of about 14 μm (parameter p_4 of the fit), indicating no systematic errors. The deviation σ of about 177 μm (parameter p_5 of the fit) is a measure of the mean spatial resolution of a single straw and is compatible with the mean of the resolution curve in Fig. 3.55.

The obtained spatial resolution is strongly affected by the time resolution of the electronics the prototype was equipped with. Therefore, by using a dedicated electronics a better single tube resolution will be achieved.

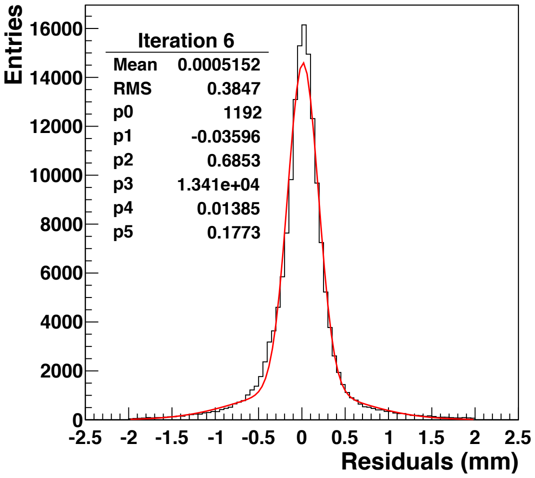

Figure 3.57: Distribution of the mean residuals after the sixth iteration of the autocalibration procedure. The parameters of the fit (red curve) are in the box: p_0, p_1 and p_2 are referred to the fit of the distribution tails; p_3, p_4 and p_5 are the parameters of the Gauss function that fits the peak.

3.10.1.3 Single tube resolution

The single tube resolution as a function of the drift distance obtained in the way previously described is "biased", since the tube whose resolution we are studying has not been excluded from the tracking. In addition, the errors on the parameters of the best fit line have not been subtracted.

In order to calculate the "unbiased" spatial resolution σ of a single tube, another method has been implemented and used. First off, tracks with $N \geq 16$ hits have been selected and fitted using $N-1$ space points. Then, the distribution of the residuals for the tube excluded from the fit has been computed as a function of the drift distance (see Fig. 3.58).

This distribution is the convolution of the resolution of the tube and the track extrapolation errors, due to the fit. In fact, both the intercept a and the slope b of the best fit line are affected by an error σ_a and σ_b, respectively, given by the covariance matrix of the Minuit fit in the refit step. Their correlation is expressed by the term $\rho \doteq \sigma^2_{ab}$. So the error on the distance of each point (x, y) to the best fit line can be computed as:

$$\sigma_d^2 = \left(\frac{\partial d}{\partial a}\right)^2 \sigma_a^2 + \left(\frac{\partial d}{\partial b}\right)^2 \sigma_b^2 + 2\rho \frac{\partial d}{\partial a}\frac{\partial d}{\partial b} \quad (3.11)$$

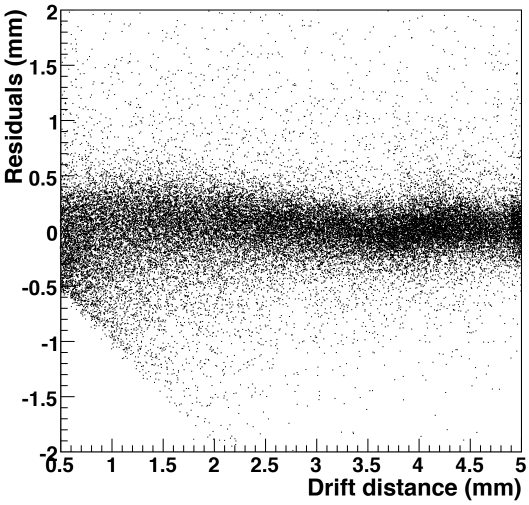

Figure 3.58: Residuals vs. drift distance.

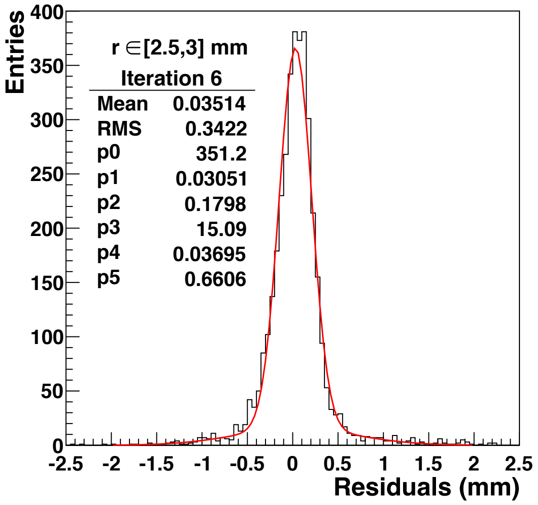

Figure 3.59: Distribution of the residuals for r in the range [2.5, 3] mm after the sixth iteration of the autocalibration, in case the hit tube is taken out from the track reconstruction (it is the analogous of Fig. 3.56). The distribution has been fitted with two Gaussian; the parameters of the fit are in the box (p_0, p_1 and p_2 are the ones of the Gaussian that fits the peak).

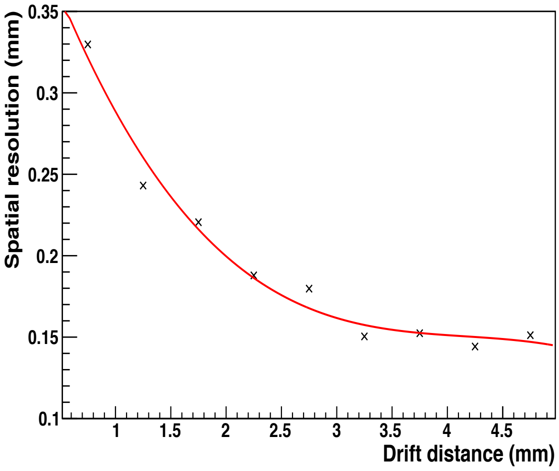

Figure 3.60: Single tube spatial resolution σ as a function of the drift distance.

where

$$\frac{\partial d}{\partial a} = -\frac{1}{\sqrt{1+b^2}}, \tag{3.12}$$

$$\frac{\partial d}{\partial b} = -\frac{x+by-ab}{(1+b^2)^{3/2}}. \tag{3.13}$$

In order to disentangle the intrinsic resolution of the tube from the other contribution, we have proceeded in the following way.

First off, the distribution of Fig. 3.58 has been sliced; for each interval, the residual distributions have been fitted with two Gauss functions, as in Fig. 3.59, and the mean value of σ_d has been calculated with Eq. 3.11, using all the space points belonging to that interval. Then, interval by interval, the obtained mean value of the error on the distance σ_d has been quadratically subtracted to the σ of the Gauss functions that fit the residual distribution of that interval.

The obtained values of σ are the ones used for the single tube spatial resolution, shown in Fig. 3.60.

3.10.1.4 Contribution of tubes mispositioning to spatial resolution

The resolution shown in the previous paragraph is the sum of two contributions:

$$\sigma^2_{overall} = \sigma^2_{cal} + \sigma^2_{pos}, \tag{3.14}$$

where σ_{cal} contains the contribution of the calibration but also of the electronic time measurements, primary ionization cluster effect and gas diffusion effect and σ_{pos} is due to the wire mispositioning ($\simeq$ 50 μm). In the following, it is explained how the last contribution has been estimated.

For each track, all the tubes have been taken out from the track reconstruction one by one and the distribution of the residuals of the single tubes has been computed. Fig. 3.61 shows two examples of residual distributions for two tubes: (a) tube 3 in layer 0 and (b) tube 7 in layer 2. The mean value of each histogram is a measure of the mispositioning of the single straws: if the wire positions were correct, the distributions should be centered around 0. As it is clear from Fig. 3.61.a, it does not always happen: in particular, in this case, the mispositioning ranges from few micrometers to more than 150 μm. The displacements from 0 are taken into account with their sign, meaning that the wires are shifted to the right and to the left with respect to their nominal positions.

To have an idea of the mean position error, the distributions of the residuals for each tube have been fitted with two Gauss functions and the mean values of the one that fits the peak have been reported in Fig. 3.62.a: the mean wire deviation is about 14 μm, which is negligible. This is in agreement with the mean value of the residuals shown in Fig. 3.57 (13.85 μm). These deviations are within 50 μm, as indicated by the RMS of the figure; this value is comparable with the mean of Fig. 3.62.b, where the absolute values of the wire deviations are reported. With $\sigma_{pos} \sim 50$ μm and $\sigma_{overall} \sim 177$ μm (see σ of the distribution in Fig. 3.57), it results:

$$\sigma_{cal} = \sqrt{\sigma^2_{overall} - \sigma^2_{pos}} \simeq 170 \ \mu\text{m}. \qquad (3.15)$$

So the main contribution to the overall resolution comes from the calibration and the position error has a very small influence on the global one. Hence, it is not necessary to iteratively correct the wire position of the individual straws.

3.10.2 Energy loss measurements

The central tracker has to help in the charged particles discrimination in the kinematical range below the momentum threshold of the DIRC, ~ 1 GeV/c. Thus, different experimental tests have been undertaken on the $\overline{\text{P}}$ANDA–STT to measure the specific energy loss of the particles.

Charged particle identification, based on energy loss measurements in drift chambers of comparable thicknesses and channel numbers of the $\overline{\text{P}}$ANDA–STT, performed by experiments like BABAR [32], BESIII [33] and especially HADES [34], are very encouraging.

Realistic simulations, performed within the framework of `PandaRoot` (Sec. 3.11), have defined the needed energy resolution for the $\overline{\text{P}}$ANDA–STT in order to resolve e, π, K and p in the low momentum range.

In all the gaseous detectors, with segmented readout, there are factors which limit the precision of the energy loss measurements for charged particles with energy around and below the minimum ionizing value. These are:

- the statistical nature of the ionization process that results in an extended and asymmetric energy loss distribution (Landau-curve shape);
- the limited numbers of sampling points used for the energy loss estimation;
- the long range of the drift time;
- the compromises necessary on the readout electronics, which should provide, at the same time, a "fast" time-information for an efficient tracking, and which have to integrate for a sufficiently "extended" time interval the charge necessary for energy loss measurements.

Experimental studies undertaken in order to evaluate the achievable energy resolution of $\overline{\text{P}}$ANDA–STT aimed at:

- fixing of the requirements for the readout electronics;
- selecting and optimizing the method of signal processing and data treatment;
- optimizing the detector performance, the electronics coupling and the noise suppression.

3.10.2.1 Tests

For the tests of the energy resolution of the STT, the prototype already described in Sec. 3.10.1 was used.

In order to test various techniques of signal analysis, the analog outputs, derived from the straw tubes, were recorded as a sampled waveform for further offline analysis.

The front-end transresistance amplifier of 8 ns rise-time and gain factor of 10 has been followed by a booster amplifier (gain factor 2) translating the differential outputs of transresistance amplifier into single-ended (LEMO) signals. The total integrating time-constant of both amplifiers was about 7 ns. An example of the straw tube signal induced by ^{90}Y/^{90}Sr β-particle processed by the transresistance and booster amplifiers is shown in Fig. 3.63. A structure, to some extent reflecting the cluster composition of the primary ionization, is still visible. These signals have been fed into a 16-ch 240 MHz flashADC. The sampling time of the flashADC was equal to 4.17 ns. An example of the recorded straw-signals is shown in Fig. 3.64. The limited precision of the sampling and the additional integration deteriorates further the shape of the initial signals. Nevertheless, the envelopes of the groups of

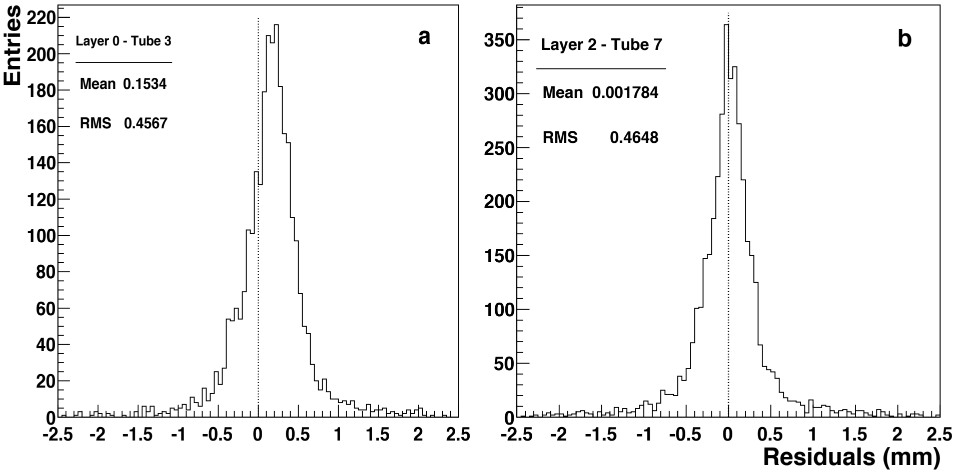

Figure 3.61: Examples of residual distributions for single tubes, which have been taken out from track reconstruction: (a) tube 3 in layer 0 and (b) tube 7 in layer 2. The distributions should be centered around 0 (dotted line).

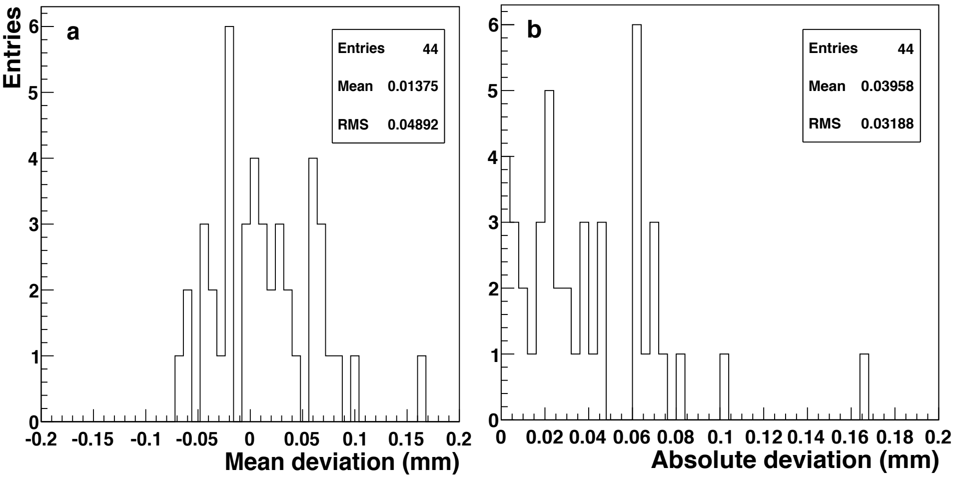

Figure 3.62: (a) Distribution of the mean deviations (with sign) of the wire positions from their nominal ones: this is a measure of the systematic shift of the wires. (b) Distribution of the absolute values of the deviations plotted in (a).

clusters are still visible. Since the detector works in proportional mode and the response of the electronics is almost linear, the area of the signal is directly proportional to the primary ionization in the straw tube, i.e. to the energy loss by the crossing particle. Initial checks of the detector response were performed by using β-particles from a ^{90}Y/^{90}Sr source. The geometry and the trigger conditions were optimized in order to select only the highest energy fraction of the β-decay spectrum containing minimum ionizing electrons. Fig. 3.65 shows the dependence of the energy loss of the β-particles on the number of traversed straws. The relation between the energy resolution and the number of traversed straws has also been tested and the result is presented in Fig. 3.66. In this case the energy loss spectra have been built integrating the area of the recorded signals. No further cuts were applied. The resolution is calculated as the ratio between the width and the mean value derived from the fit with a Landau curve. As expected, the energy dependence is perfectly linear and the resolution follows an inverse square-root relation to the number of fired straws.

Further tests were performed using monoenergetic proton beams extracted from the COSY synctrotron of the Jülich Research Center. The extracted beams were guided to the external exper-

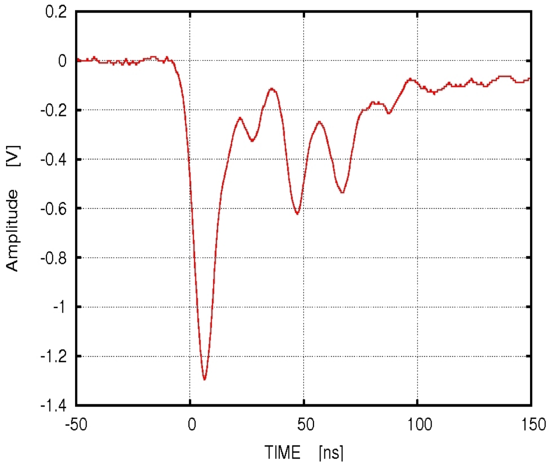

Figure 3.63: Example of an analog signal derived from the straw tubes by means of transresistance and buster amplifiers.

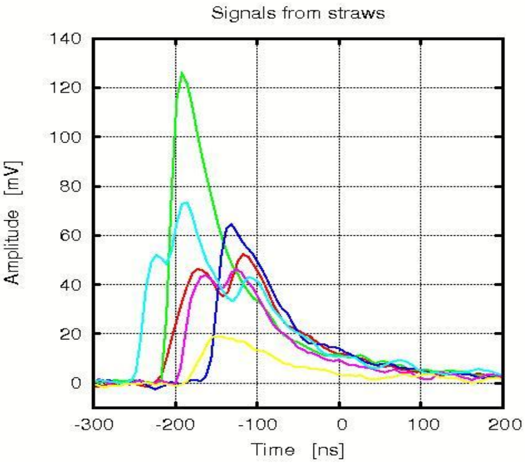

Figure 3.64: Analog signals from the straw tubes as recorded by a 240 MHz flashADC.

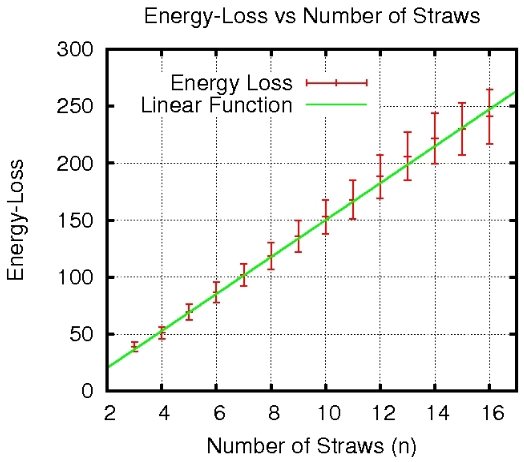

Figure 3.65: Dependence of energy loss for minimum ionizing β-particles on the number of traversed straws. Energy loss is given in arbitrary units.

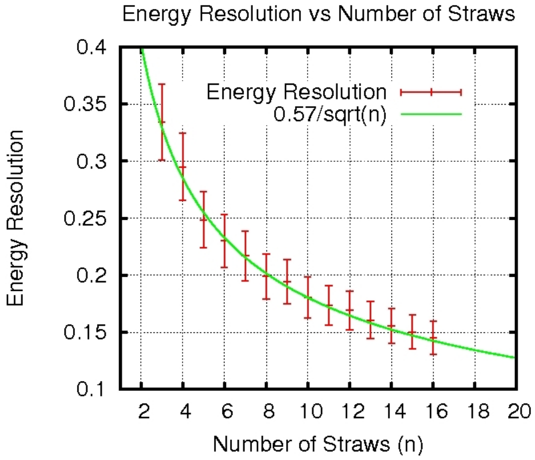

Figure 3.66: Dependence of the energy resolution for minimum ionizing β-particles on the number of traversed straws.

imental station where the STT-prototype was installed together with the auxiliary equipment. A low intensity beam (up to $1 \cdot 10^4$ protons/s) after passing a thin (150 μm) stainless-steel window was impinging directly onto the STT-prototype.

During the measurements the detector was first oriented perpendicular to the beam axis (c.f. Fig. 3.67 a) to have the protons impinging at 90° with respect to the straw axis. Then, it was turned by 45° as it is shown in Fig. 3.67 b. In vertical direction the straw tracker was positioned allowing the beam to pass parallel to the layer structure or with an angle of 5° in order to increase the number of crossed straw tubes and to enhance the merit of the isochrone calibration method: Fig. 3.67 c and Fig. 3.67 d, respectively. All these measurements were done with the beam hitting the straw in the middle. In order to test possible amplitude differencies along the straw length, the prototype was finally displaced by 32 cm. In this case, the beam entered the detector closer to the straw end equipped with the readout electronics (Fig. 3.67 e).

The trigger signal was generated by the coincidence of the signals of two small ($\sim$ 10 $\times$ 10 cm) and thin (5-10 mm) scintillation detectors situated upstream and downstream the STT-prototype. The beam was defocused in the vertical direction in or-

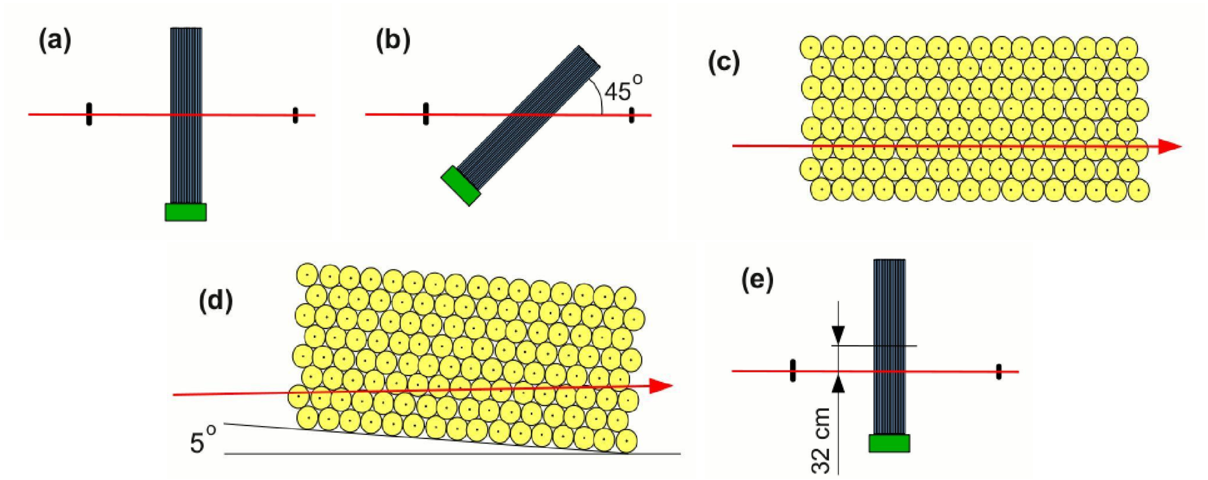

Figure 3.67: Configurations of the $\overline{\text{P}}$ANDA–STT prototype during the tests with the proton beam: (a) protons hit the straw tubes perpendicularly; (b) protons hit at 45° with respect to the straw axis; (c) the beam direction is parallel to the layers of straw tubes; (d) the prototype is rotated by 5°; (e) the prototype is displaced horizontally by 32 cm. The red lines indicate the beam.

der to cover a broad range of straws. The small sizes of the triggering scintillators assured a negligible horizontal angular spread of the beam.

The detector was filled with the Ar/CO2 (9/1) mixture at 1 bar overpressure. The HV was set to keep the gas gain factor at a moderate level of about $5 \cdot 10^4$.

3.10.2.2 Analysis

The shapes of the recorded signals (c.f Fig. 3.63 and Fig. 3.64) do not allow to estimate the particle energy losses from the numbers and the distributions of the initial ionization clusters. The energy losses can be deduced only from the integrated charge of the output signal, or from any other parameter which is linear or related through an other known function to the collected charge. Two different methods have been tested: the so called $Truncated\ Mean$ and the $Time\ over\ Threshold$. The methods and their results are described in the following.

Selection of events

The sampling frequency of the used flashADC allows for the drift time estimation with a precision of 4.17 ns. Under this limitation the drift time spectra were built (Fig. 3.68), and the isochrone calibration was performed as it is described in Sec. 3.9.1. The tracking procedure allowed the selection of the fired straws belonging to an event and the calculation of the particle path length (Fig. 3.69). The signals from the fired straws were then used to build the energy loss distribution. The energy loss distribution for 2.95 GeV/c momentum protons is shown in Fig. 3.70. As expected, it shows a Landau distribution shape. The tail of the distribution extends to higher energies deteriorating the separation between the neightbouring ionization curves. In order to avoid the tail of the energy distribution a conversion of the Landau function into a symmetric Gaussian-like function by means of the so called "$Truncated\ Mean$" is performed.

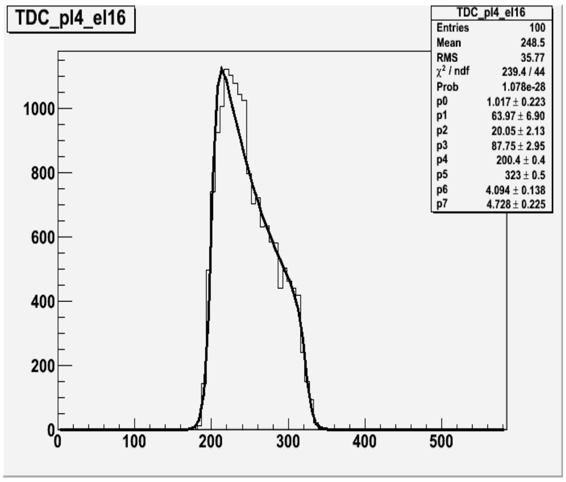

Figure 3.68: Drift time distribution for a straw irradiated with the 2.95 GeV/c proton beam. The used gas mixture is Ar/CO2 (9/1). The fit is perfromed with the procedure described in Sec. 3.9.1.

Truncated Mean

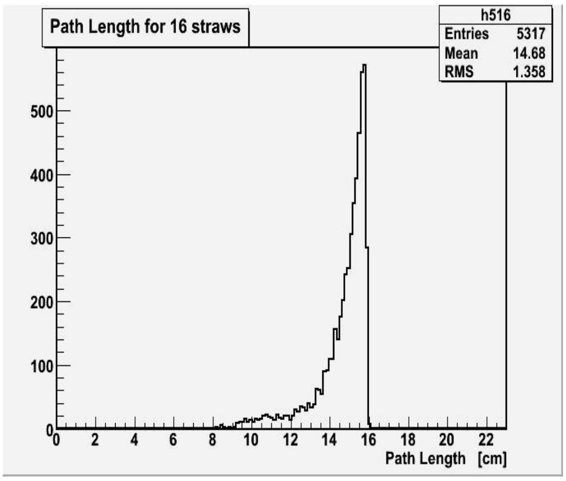

Figure 3.69: Path length distribution for reconstructed tracks where 16 straw tubes were hit.

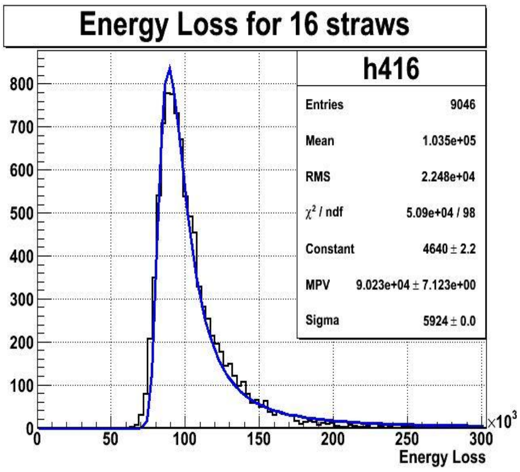

Figure 3.70: Energy loss distribution for 2.95 GeV/c protons for reconstructed tracks hitting 16 straw tubes. Energy is in arbitrary units. The histogram is fitted with a Landau function.

The *Truncated Mean* is a commonly used procedure allowing to transform an initial tailed distribution into a symmetric one resembling a normal-Gaussian function. By removing from the initial distribution a fixed fraction of the highest energy components of each event (i.e. straws signals belonging to the reconstructed track) a more and more symmetric and compact shape can be obtained (c.f. Fig. 3.71). For the analyzed data it has been determined that the most suitable truncation fraction is 30 %. An example is given in Fig. 3.80.

The energies of the truncated distributions have then to be divided by the appropriate reconstructed path lengths. The energy loss distribution 30 % truncated, corrected for the path length for protons of 2.95 GeV/c momentum, is shown in Fig. 3.72. The distribution has a shape well resembling the normal distribution and the fit with a Gaussian curve permits to derive the parameters of the distribution biased only by minimal uncertainties.

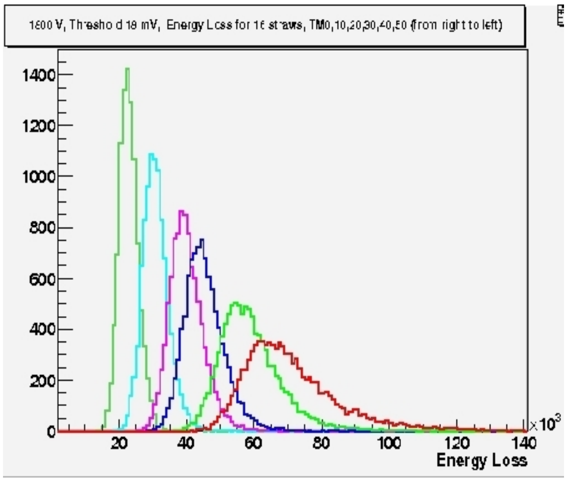

Figure 3.71: Modification of the experimental Landau distribution by the so called *Truncated Mean* method. From right to left: original distribution, truncated by 10 %, 20 %, 30 %, 40 % and 50 %. Energy loss is in arbitrary units.

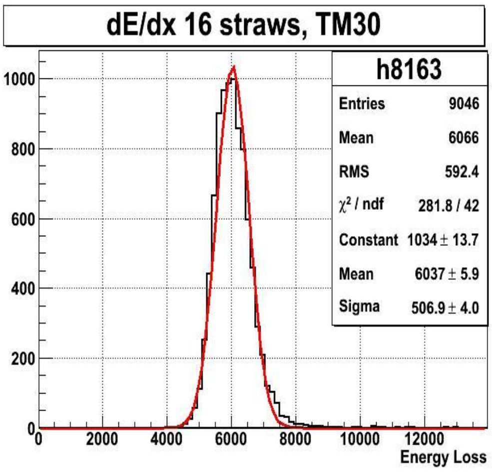

Figure 3.72: dE/dx distribution for monoenergetic protons of 2.95 GeV/c fitted with a Gaussian curve. Only events hitting 16 straw tubes are included. 30 % *Truncated Mean* is applied.

Time over Threshold

An other technique that can be used to determine particle energy loss, avoiding two electronic-readout branches (time and amplitude), is the so called

Time over Threshold (*ToT*). This method postulates that the energy deposit inside the drift cell could be realted to the time duration of the output signal and has been exploited by the ATLAS experiment [35, 36, 37].

Utilizing the recorded signal shapes from the $\overline{\text{P}}$ANDA–STT prototype, it was checked that the direct measurement of the signals duration does not give a satisfactory relation with the specific energy loss for any reasonable threshold value. Only a coarse relation between the time width and the deposited charge is observed. Moreover, for high counting rates it is not affordable to follow the output signal over the whole drift time.

A most successful compromise solution, utilizing only a sensible fraction of the output signals, has been worked out and applied in the HADES experiment [34]. Unfortunately, due to the lack of a proper readout electronics, this method could not be checked in the tests we performed. However, since the characteristics of the signals of the HADES drift chambers are similar to those of the $\overline{\text{P}}$ANDA–STT, the method and theresults obtained by the HADES collaboration are recalled here as an example of what could be achieved with the use of timing electronics only.

In HADES the *ToT* was used for particle discrimination by means of dE/dx measurements in Mini-Drift Chambers (MDC), a four sections gaseous tracker. Each section of the detector consists of 6 separate drift chambers forming in total a 24 layer structure. Hence, particles traversing the tracking system may induce up to 24 individual output signals per track. The drift cells of each section have different dimensions and alternates from 5 × 5 mm for the first section, up to 14 × 10 mm for the chambers in section IV. The chamber windows are made of 12 μm aluminized mylar foils. Aluminum, tungsten, bare and gold-plated wires are used for anodes, cathodes and field-shaping. Diameters of the wires vary from 20 to 100 μm. The detector is filled with an Helium/Isobutane gax mixture (6/4) at atmospheric pressure.

The outputs of the sense wires are connected to analog boards [38] allowing for differential amplification, shaping and discrimination. The signals are digitized by means of an ASD8-B chip [39], which deliver a logical (LVDS) signal whose width is proportional to the time that the shaped signal remain above a fixed threshold value. Logical signals are then fed to multi-hit TDCs allowing both the time stamping with a 0.5 ns precision (from the leading edge of the signal), as well as the *ToT* evaluation (from the signal width). The method is illustrated in Fig. 3.73. In order to extract the energy loss from the measured *ToT* a careful calibration has been performed. For each particle species the non-linear correlation function has been determined by means of a fitting procedure taking into account various incident angles and drift distances (in bins of 5° and 100 μm, respectively). Finally, the *Truncated Mean* method, similar to that already described, has been applied.

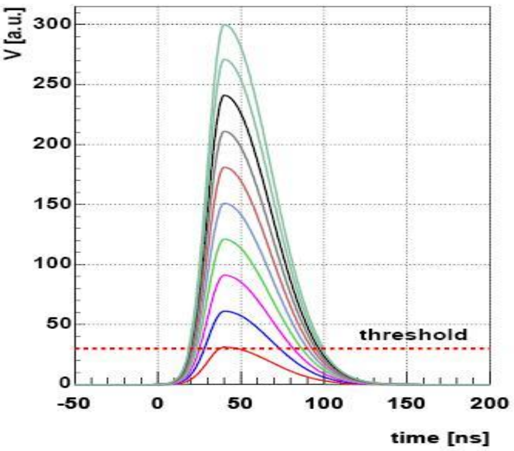

Figure 3.73: Illustration of the *Time over Threshold* dependence on a preshaped fraction of the initial signals from the MDC-drift cells of the HADES experiment[34].

Eventually, an energy resolution of the order of 7 % has been obtained for minimum ionizing particles, whereas for higher ionizing particles the achieved resolution was about 4 % [34].

3.10.2.3 Results

In this subsection the results obtained with the use of the *Truncated Mean* method are reported.

Truncated energy loss distributions for different proton beam momenta and for selected tracks of high statistics are shown in Fig. 3.74, for 2.95 and 1.0 GeV/c and in Fig. 3.75 for 0.64 GeV/c. Gaussian fits are superimposed and the fit parameters are given. The results for the 0.64 GeV/c protons cannot be presented on the same energy scale of the results of 1.0 and 2.95 GeV/c due to the lower number of hit straws (16 instead of 18), and because a higher threshold was used during the analysis of this data set. This was necessary since a higher pick-up noise was observed during this measurement created by an insufficient shielding of the scintillator bases. The selected threshold was two time higher than that set for the other tests. In all cases the applied HV was the same: 1800 V (gas gain of about $5 \cdot 10^4$).

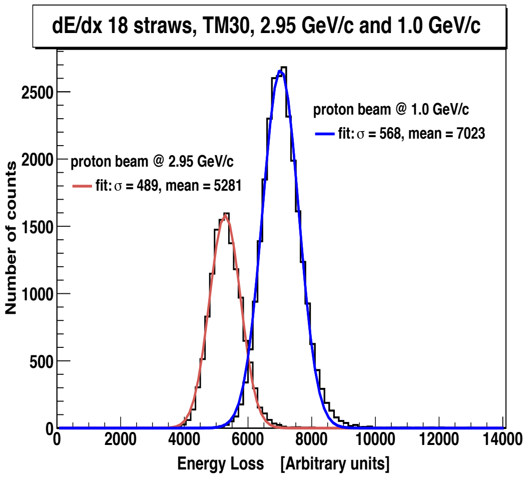

Figure 3.74: dE/dx distributions for monoenergetic protons of 2.95 GeV/c (left one) and 1.0 GeV/c (right one) with Gaussian fits. Only events with reconstructed tracks of 18 straw tubes are included. *Truncated Mean* of 30 % is applied.

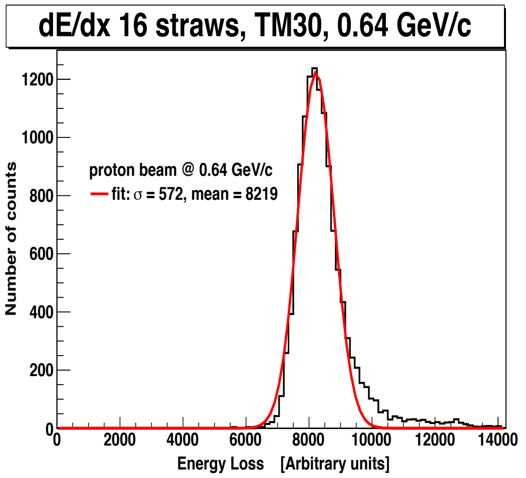

Figure 3.75: dE/dx distribution for monoenergetic protons of 0.64 GeV/c with Gaussian fit. Only events with reconstructed tracks of 16 straw tubes are included. *Truncated Mean* of 30 % is applied. Due to a higher offline threshold used during the analysis, and to the lower number of straw tubes fired, this distribution can not be placed on the same energy scale of the distributions presented in Fig. 3.74.

Fig. 3.76 and Fig. 3.77 present the energy resolution dependence on the number of straws used to reconstruct the track for various geometrical configuration of the detector for 2.95 and 1.0 GeV/c proton momentum, respectively. The dependence of the dE/dx on the number of straws in the track for protons at 0.64 GeV/c momentum is shown in Fig. 3.78. Due to technical problems, for this beam momentum the inclined tracks could not be registered. In this case the beam passed parallel to the detector layers and the highest statistics was obtained for reconstructed tracks with only 16 hits. Results for two different values of HV: normal one (1800 V) and decreased by 50 V (1750 V), are given. No significant difference in resolution for the lower voltage is observed. The presented results show that within the geometrical constrains of the laboratory test and in the kinematical momentum range of interest, the achievable energy resolution is equal to 8 % for 1.0 GeV/c proton momentum and improves at lower momenta with the increase of the particle energy deposit. At 0.64 GeV/c, with only 16 straws in the track, the resolution is equal to 7 %. For tracks inclined by 45° a systematical deterioration of the resolution of 1 % is observed. For minimum

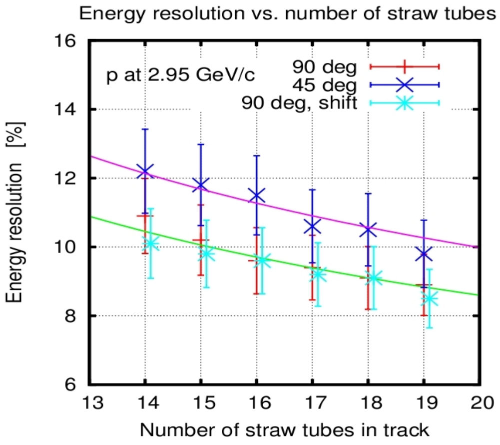

Figure 3.76: Dependence of the energy resolution on the number of straws in the reconstructed track obtained for 2.95 GeV/c protons. Red symbols show the results for protons crossing the detector perpendicularly to the straw axes (as it is presented in Fig. 3.67 a). Results of tracks tilted by 45° (c.f. Fig. 3.67 b) are given in deep blue. A systematic deterioration of the resolution of about 1.5 % is observed for this case. Light blue symbols represents data collected when detector was displaced by 32 cm (Fig. 3.67 e), a slight improvement of the resolutions of about 0.2 % is obtained. Error bars of 10 % of the given values are introduced in order to reflect the systematic uncertainties caused by limited precision of the tracking. The superimposed curves, introduced for guiding the eyes, are functions $Const \cdot (n)^{-1/2}$, where n is the number of straws used to reconstruct the track diminished by the truncation factor.

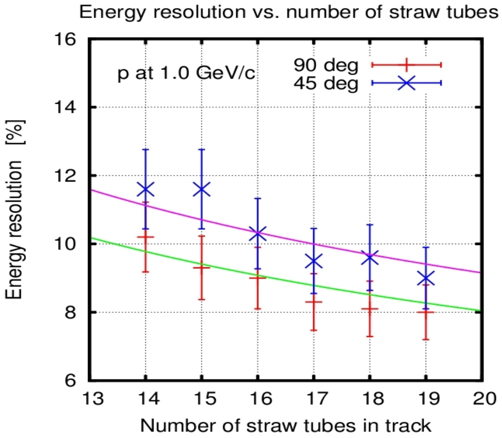

Figure 3.77: The same as in Fig. 3.76 but here for protons at 1.0 GeV/c. No result for longitudinal displacement of the detector is available. Tracks inclined by 45° spoil the resolution by about 1 %.

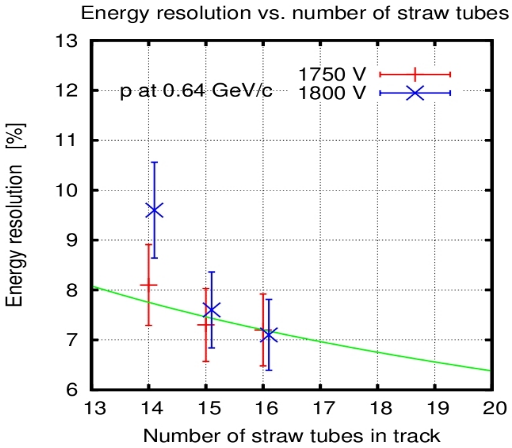

Figure 3.78: The dependence of the dE/dx on the number of straws in the track for protons at 0.64 GeV/c momentum is presented for two different HV supplied to the sense wires of the straws. For this beam momentum the detector was not tilted vertically, thus the best statistics was obtained for the tracks containing up to 16 straws.

ionizing protons of 2.95 GeV/c, which are however beyond the momentum range where the $\overline{\mathsf{P}}$ANDA–STT has to performe PID, the energy resolution is about 9 %, and for tracks at 45° it is worse of 1.5 %. No significant effect on the energy resolution is observed for tracks hiting the straws at different longitudinal positions.

In order to check the possibility to perform dE/dx measureents also for high particle rates, that are expected in the innermost layers of $\overline{\mathsf{P}}$ANDA–STT, and the possibility to use the ToT method for the energy loss determination, we explored the possibility of shortening the signal integration time.

By using the recorded analog signals of protons of 1.0 GeV/c momentum, an analysis changing the fractions of the integrated signals has been performed. The concept of this analysis is shown in Fig. 3.79. The signals have been integrated over 4, 8, 16, 30, 60 and 100 flashADC samples (sample width is equal to 4.17 ns). The resulting energy loss distributions have been truncated and a Gaussian fit has been performed. The results for events with 18 straws per track are shown in Fig. 3.80. For this analysis, the path length correction has been applied before making the tail truncation (this was not done for the results shown above). A small deterioration of the resolutions is obtained in comparison with that presented in Fig. 3.77.

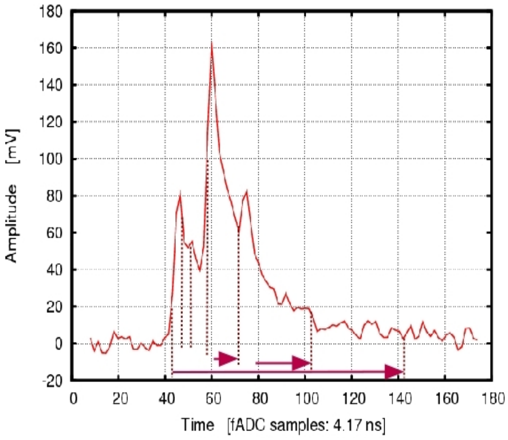

Figure 3.79: Straw tube signal recorded by the 240 MHz flashADC. Integration ranges are indicated. Signals were integrated over 4, 8, 16, 30, 60 and 100 samples (sample width 4.17 ns).

Since almost the whole charge of the signals is contained within the first 40 - 60 samples, there is not a significant decreasing of the energy resolution measured, when the integration range extends beyond 30 samples. On the other hand, the 16 sample resolution is worse by 1 % with respect to that obtained with the whole integration, and any further reduction of the integration range causes big worsening of the resolution. For the shortest integration time, only 4 samples, the energy resolution increases by an additional 3 - 4 %. This result is shown in Fig. 3.81. Here the energy resolution and its dependence on the number of hit straws is pre-

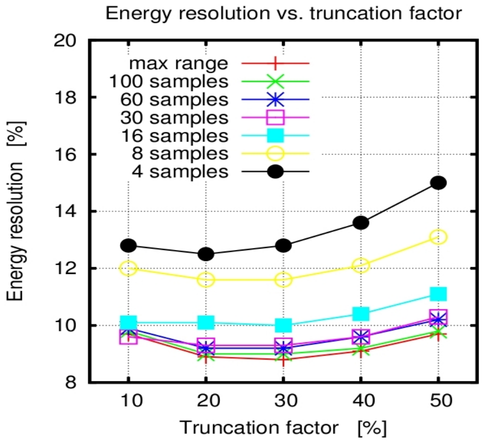

Figure 3.80: Energy resolution as a function of the truncation factor for various fractions of the deposited charge for tracks with 18 straws. A significant deterioration of the energy resolution is observed when the integration range is reduced to less then 16 samples. "max range" means that the integration is done over the whole time window of the flashADC.

sented. The energy resolution is evaluated with a truncation factor of 30 % only, which gives the best results.

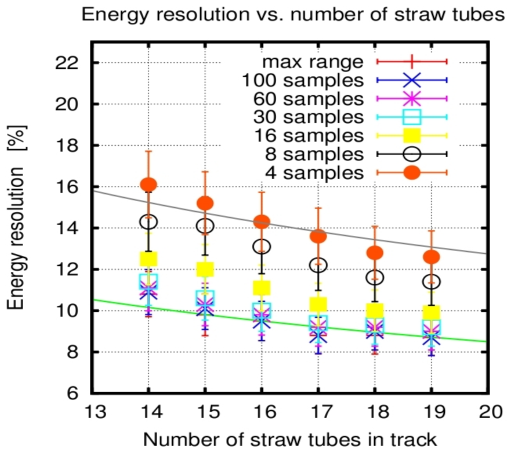

Figure 3.81: Deterioration of the energy resolution by decreasing the fraction of the integrated charge. On the horizontal axis the number of hit straws per track is given. The energy resolution is calculated by applying a trunction of 30 %. "max range" means that the integration is over the whole time window of the flashADC. For superimposed curves refer to Fig. 3.76.

The presented analysis, indicates that in order to obtain a satisfactory energy resolution with the $\overline{\text{P}}$ANDA–STT, there is no need to integrate the signal charges over the whole drift time. A preshaping over 65 ns would be sufficient in order to keep the energy resolution below 10 %, if the amplitude is used to measure the energy loss. On the other hand, if *ToT* is used, in the version developed in the HADES experiment, the integration time could be even shorter. In HADES the charge is integrated over few tens of ns. Further test exploring the possibility of using this technique will be done.

3.10.3 Aging tests

A degradation of the straw tube properties like a specific gas gain reduction or high voltage instabilities during operation caused by irradiation is expressed as aging. In general, aging is induced by the plasma-chemical processes during the gas amplification processes with a high density of ions, electrons, excitation photons, free radicals and possible molecular dissociations and polymerizations. A complete overview and description of the aging phenomenons in gaseous detectors can be found in [40] which is a summary of a dedicated workshop with about 100 detector experts, held at DESY (Hamburg, Germany) in 2001. In the following the main aspects relevant for the $\overline{\text{P}}$ANDA-STT are discussed.

Two main sources of aging have been identified in wire chambers. A growth of polymeric deposits on the electrodes which can change the electric field, create sparking, produce dark- or even self-sustaining (Malter) currents. At high irradiation densities and high gas gains already trace contaminations on the sub-ppm level in the gas can lead to such deposits. Another aging source is a possible oxidation of the sense wire. Usually the wire is protected by an outer gold-plating layer which makes the wire highly inert to chemical reactions. If oxygen produced in the amplification avalanche penetrates through the gold-layer to the inner wire by permeation or at imperfection spots (holes) it can oxidize the wire with a swelling of the inner wire diameter and a cracking of the gold-plating layer [41]. The increased wire diameter reduces the gas gain at a given voltage by the lower electric field strength on the wire surface. A quantitative description of the aging process is difficult due to the high complexity with an influence for instance of the gas mixture and purity, trace contaminations, construction materials, gas flow, irradiation area and intensity, ionization density, high voltage setting, particle type and energy.

The proposed Ar/CO_2 gas mixture is known as being one of the best gas mixtures for high-rate hadronic environments due to the absence of polymeric reactions of the components. Contaminations of the gas or detector materials with silicone, e.g. from lubricants must be avoided, since they produce a strong growth of non-volatile SiO_2 crystals on the wire. An admixture of CF_4 to the gas can remove such SiO_2 deposits, but due to its high additional wire etching capability special care is needed. Hydrocarbons are better quenching agents compared to CO_2, but not considered for the $\overline{\mathsf{P}}$ANDA–STT because of their high polymerisation rate, which can lead to deposits on the electrodes. In particular deposits on the cathode can produce self-sustaining currents with a possible high voltage breakdown (Malter-effect) [40]. In general a moderate gas gain of about 5×10^4 is recommended which reduces the occurrence of limited streamer mode pulses with an increased avalanche size and possible accelerated aging [42].

The behaviour of the straw tubes under very high irradiation was studied at COSY with a proton beam. The goal was to check the influence of the beam exposure and charge deposition on the straw gas gain, high voltage operation stability and to verify that all assembled materials including the gas system do not create harmful pollution, e.g. by out-gassing. Within the short time of about 10 days beam irradiation it was possible to collect a charge deposition in single tubes up to about 1.2 C/cm comparable to several years of operation of the $\overline{\mathsf{P}}$ANDA detector at full luminosity.

The straw setup consisted of a planar double-layer of 32 close-packed tubes installed behind the COSY-TOF apparatus and exposed to the residual proton beam with a momentum of about 3 GeV/c. The straw design and all materials were the same as used for the COSY-TOF straw tracker assembly, i.e. 30 μm thick mylar film tubes with 10 mm diameter and a length of 105 cm. For the $\overline{\mathsf{P}}$ANDA detector the same straw tube design is proposed, but with a length of 150 cm. Due to the horizontal placement of the double-layer and a beam spot of about $2\times2\,\mathrm{cm}^2$ the particle rate through all tubes was almost the same. The surrounding alignment frame consisted of sandwich bars with a Rohacell core reinforced by Carbon fiber skins [3]. Therefore, interaction of the beam with this low-density foam material (ρ=0.05 g/cm^3) was negligible.

The gas supply was divided into four parallel gas lines, each serving eight straws. Thus, it was possible to test at the same time straws filled with four different gas mixtures and gas gains with the same particle rates. The chosen gas mixtures were argon based, with different fractions of CO_2 (10 % and 30 %) and one mixture with 10 % ethane. The gas pressure for all mixtures was 1650 mbar. The typical gas flow was one volume exchange per hour. In total, 16 high voltage supply channels (one channel per two straws) allowed to operate the straws at different voltage levels and gas gains. The current of every voltage channel was monitored with a resolution of 2 nA. All straws were equipped with preamplifiers and 30 m long signal cables ending in the counting room. Therefore, it was possible to check analog signal shapes and signal rates during beam irradiation for every straw. Table 3.10 lists the straw settings during the beam test.

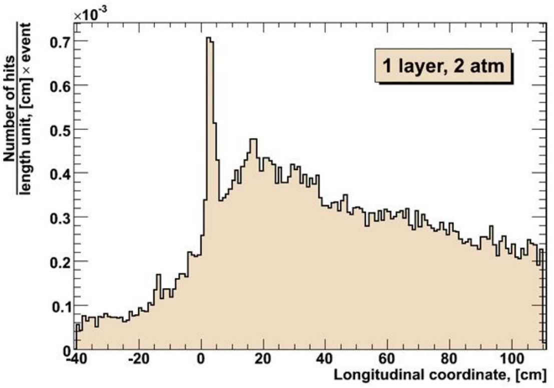

Figure 3.82: Simulation of $\bar{p}p$ reactions and number of hits per event and per cm along the tubes in the innermost layer of the $\overline{\mathsf{P}}$ANDA straw tube tracker. The target position is at z=0 cm.

The expected particle rates for the individual tubes in the $\overline{\mathsf{P}}$ANDA central tracker volume were derived from a simulation of $\bar{p}p$ interactions and assuming an event rate of $2\times10^7\ \mathrm{s}^{-1}$ (see Fig. 3.82). The mean particle flux for straws in the innermost layer was $\simeq$800 kHz per 1500 mm long tube and about $\simeq$7 kHz/cm in the forward region (z>0 cm). The maximum flux of $\simeq$14 kHz/cm in the tube was concentrated within z=2±1 cm (target position at z=0 cm) coming from $\bar{p}p$ elastic interactions with a laboratory scattering angle $\theta \simeq 90^o$ and relatively low momentum. These particles crossing the tubes around z=2±1 cm were highly ionizing and produced a high charge load of $\simeq$1 C/cm, if one assumed a typical gas gain inside the tubes of 5×10^4. At all other positions, which represent 99.7 % of the STT volume, the mean charge load was about 0.2 C/cm. All quoted charge loads were equivalent to an expected typical beam time for $\overline{\mathsf{P}}$ANDA of one year with 50 % live-time.

The total live-time with beam on the straws was 199 hours after correcting the COSY spill time structure and beam breaks. All straws were exposed to the proton beam at the same longitudinal position, in the middle of each tube. The beam rate and cross section profile was measured by a scintillating fiber hodoscope placed behind the COSY-TOF apparatus and in front of the straw setup. The derived proton intensity per straw diameter during extraction was about $2.3\times10^6\,s^{-1}$. The slightly lower pulse rate of $\simeq2.0\times10^6\,s^{-1}$ measured for the single straws could be explained by losses of low amplitude signals due to the damping inside the 30 m long cables.

During the beam time no high voltage failures, dark currents or broken wires due to the high charge load were observed. A high maximum current of a single straw wire of up to 2.3 μA was measured.

A possible gas gain reduction due to the proton beam irradiation was checked after the beam time by exposing all straw tubes to a ^{55}Fe radioactive source with 5.9 keV γ-emission. In the argon-based gas mixtures the photo-absorption produces a localized ionization spot with a characteristic number of about 220 electrons. Therefore, the recorded signal amplitude height was a direct measure of the gas gain. The amplitude heights were checked for each straw at different longitudinal positions around the beam irradiation spot and normalized to the amplitude heights far from the irradiation spot (see Fig. 3.83). A lower amplitude height indicates a reduction of the gas gain ($\Delta A/A_0=\Delta G/G_0$). The estimated resolution error of the measurement was about 2 % of amplitude height.

It can be seen that for all straws filled with 30 % CO_2 or 10 % ethane in argon no gas gain reduction was measured, even for the highest charge loads up to 1.2 C/cm. Some but not all straws filled with 10 % CO_2 in argon showed a small gas gain loss of up to 7 % at the beam irradiation spot. A clean spatial correlation between the reduced gas gain and beam intensity distribution, measured by the scintillating fiber hodoscope in front of the straws, was observed. The results of the gas gain measurement together with the total charge loads for all 32 straws are summarized in Table 3.10.

The absence of any aging in the straws filled with ethane or the higher CO_2 percentage in argon indicated no general problem with the gas purity, and a pollution by the used straw materials or gas system could be excluded. The small gas gain reduction observed only for some of the straws operated with the lower 10 % CO_2 admixture might be explained by the known poor quenching capabilities of CO_2, together with the very high irradiation perpendicular to the wire and concentrated at a small spot of about 2 cm along the wire during the beam test. Due to the incomplete avalanche quenching the occurrence of limited streamer mode pulses, with the characteristic double-peak signal shape, was higher for that gas mixture. The high ionization density with a large number of produced oxygen ions and radicals increased the probability of oxygen permeation through the gold-layer to the inner wire. The oxidation of the inner tungsten-rhenium wire caused a swelling of the wire diameter, and as a result the electric field strength at the wire surface was reduced ($E\propto 1/r$) which lowered the gas gain at the same high voltage setting. Since the observed gas gain reduction was very small the occurring aging processes were rather weak. To clearly identify the sources of aging, dedicated investigations with a higher charge load over a much longer time period would be needed.

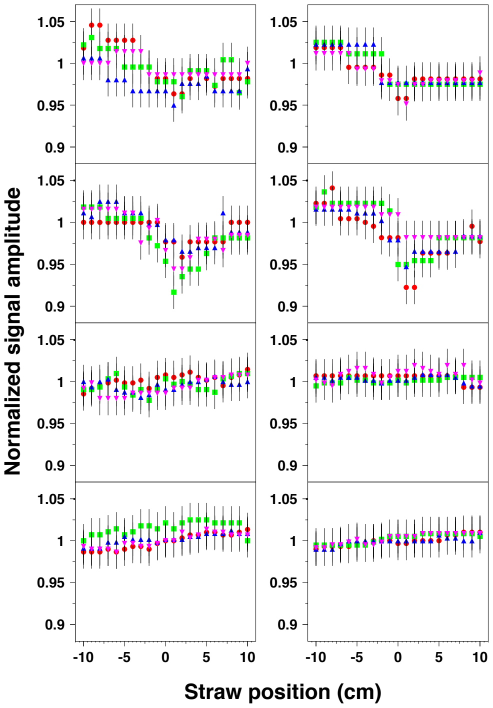

Figure 3.83: Measured normalized gas gain reduction ($\Delta G/G_0$) along the tube for all 32 straws, shown in groups of 4 straws. Straw no. 1–4 (upper left) to straw no 29–32 (lower right). The beam hit all tubes around 0 cm longitudinal position.

Ar/CO_2 is the preferred gas mixture for the $\overline{\text{P}}$ANDA–STT since it is highly tolerant to highest irradiation, not expensive, and non-flammable. The measurements confirm that the straw design and all used materials are suited and will not limit the life time of the detector. No aging in the straws is expected at moderate gas gains of about 5×10^4

Table 3.10: List of straw settings and charge load during the beam test. The last column shows the normalized gas gain reduction in the irradiated straw region with a measurement resolution of about 2 %. The aging intervals give the minimum and maximum gain reductions, e.g. 0–7 % means that at least one straw showed no gain reduction and one a maximum of 7 %.

Straw no.	Gas mixture	Voltage (V)	$\sum Q$ (C/cm)	Aging $\Delta G/G_0$
1–8	Ar/CO_2 (10 %)	1750	0.72	0–3 %
9–16	Ar/CO_2 (10 %)	1700	0.58	0–7 %
17–20	Ar/CO_2 (30 %)	2200	1.23	no
21–24	Ar/CO_2 (30 %)	2100	0.79	no
25–32	Ar/C_2H_6 (10 %)	1550	0.87	no

for 99.7 % of the STT volume during more than 5 years of $\overline{\mathsf{P}}$ANDA operation at full luminosity. A small aging on the low percent level may start first in the region at z=2±1 cm (= 0.3 % of STT volume) after about 2 years of operation, caused by low energy protons from elastic scattering. The modular mechanical design of the $\overline{\mathsf{P}}$ANDA–STT allows to replace even single straws showing aging or other failures inside the layer modules after some years of operation during the $\overline{\mathsf{P}}$ANDA maintenance time.

3.10.4 The COSY-TOF Straw Tube Tracker

The technique of pressurized, self-supporting straw tube layers was first developed for the Straw Tube Tracker of the COSY-TOF experiment (COSY-STT) at the COSY-accelerator (Juelich, Germany). The used straw tube materials and dimensions, and the geometry of planar, close-packed multi-layers are the same or quite similar as for the $\overline{\mathsf{P}}$ANDA–STT. Although the COSY-STT is a non-magnetic spectrometer, the calibration methods for the straw tube positions and isochrone radius - drift time relation are similar for both detectors. The operation of the COSY-STT with about 275 l gas volume in surrounding vacuum is an outstanding technical challenge. The required minimal leakage of the detector in vacuum is a strong and sensitive proof of all straw materials, glueing and assembly techniques, which are also crucial for the $\overline{\mathsf{P}}$ANDA–STT. The COSY-STT is considered to be a global test system for the $\overline{\mathsf{P}}$ANDA–STT and its properties and performance results are summarized in the following.

The COSY-STT was installed in 2009 as an upgrade of the COSY-TOF spectrometer, which consists of a large 25 m^3 vacuum barrel with a liquid hydrogen target cell at the entrance, followed by a start detector, silicon-microstrip detector, the straw tube tracker (STT), and scintillator hodoscopes covering the barrel walls and end cap. The apparatus allows to measure kinematically complete the time-of-flight and space directions of the reaction particles of hyperon production in proton-proton and proton-deuteron collisions with polarized proton beam. The vacuum ensures lowest background produced by beam and reaction particles with up to 3.5 m track lengths. More details about the experimental program and the STT installation can be found in [43] and [44]. A first experiment beam time of hyperon production with polarized proton beam was carried out in 2010.

The COSY-STT consists of 2704 straw tubes, each with a length of 1050 mm, inner diameter of 10 mm, and 32 μm wall thickness of aluminized mylar film. The tubes are arranged as a vertical stack of 13 close-packed double-layers with three different orientations (ϕ=0°, 60°, 120°) for a 3-dimensional track reconstruction. A $15\times15\,mm^2$ beam hole in the center of every double-layer is realized by splitting the 4 central straws into 8 straws with about half length (see Fig. 3.84). The straws are filled with a gas mixture of Ar/CO_2 (80/20%) at a pressure of 1.25 bar. The typical operation voltage is 1840 V. The electronic readout consists of low-power transimpedance preamplifiers directly connected to each straw in vacuum and feeding the signals through 13 m coaxial signal cables to ASD8B-discriminators and TDCs, which are located outside the vacuum barrel.

The COSY-STT is now since two years in surrounding vacuum and no real leakage sources of the detector, caused by dissolving glue spots, brittle materials, or loose gas connections, have been observed. The gas leakage stays on the permeation level, which is caused by the flow of the gas

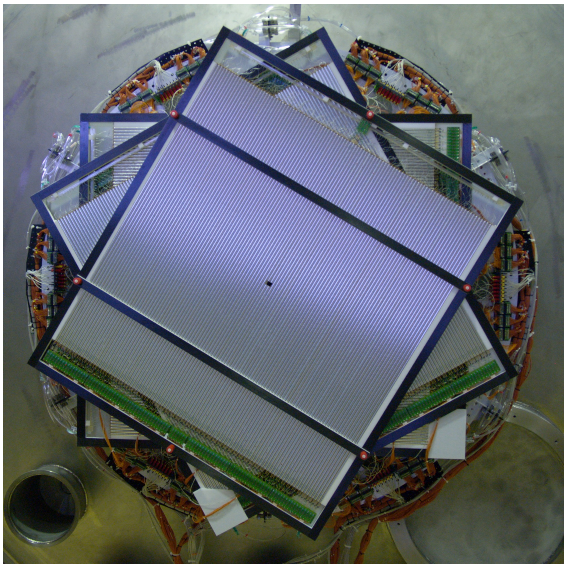

Figure 3.84: The COSY-STT mounted at the front cap of the COSY-TOF spectrometer. The detector consists of 2704 straw tubes of 1 m length and 10 mm diameter, arranged as a vertical stack of 13 close-packed double-layers at three different orientations.

molecules inside the straws through the thin mylar film wall to outside vacuum. Fig. 3.85 shows the gas loss by measuring the pressure drop inside the straws in surrounding vacuum if the STT is filled with pure argon and pure CO_2. The difference in the gas loss rate for argon and CO_2 of about a factor of 10 is characteristic for the different permeation of the specific gas molecules through the mylar film and in accordance with reference measurements by the manufacturer (DuPont Teijin Films, USA). For the used gas mixture of Ar/CO_2 (80/20 %) the total leakage is about 2 % of the STT volume per day. The typical gas flow during the high voltage operation is about four times the STT volume per day (=1000 l/day).

The calibration of the STT consists of the determination of the isochrone radius - drift time relation and the adjustment of the straw positions and is performed as an iterative procedure. At first, the isochrone - drift time relation ($r_{iso}(t)$ in the following) is parametrized as a polynomial function of 4th order and obtained by an integration of the time offset corrected drift time spectrum (see Sec. 3.9.1.2)

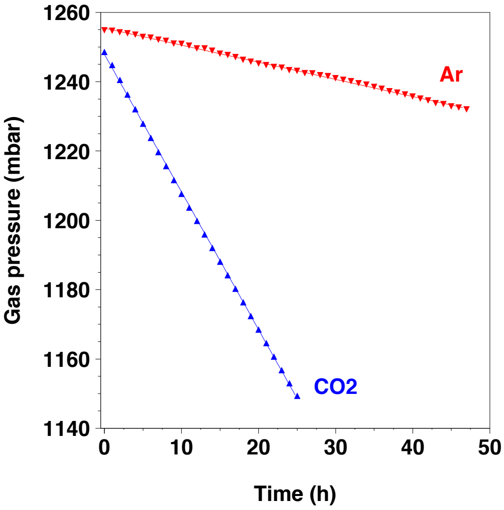

Figure 3.85: Gas leakage of the COSY-STT filled with pure argon (red) and pure CO_2 (blue), measured by the gas pressure drop of the straws in surrounding vacuum.

$$r_{iso}(t) = \sum_{i=0}^{4} P_i \times t^i. \tag{3.16}$$

Then, tracks are reconstructed as straight lines with a least squares fit (χ^2) to the isochrones calculated from the measured drift times using the defined $r_{iso}(t)$-relation. Fig. 3.86 shows for all reconstructed tracks the distances to the fired straw wires versus the measured drift times. A systematic deviation in the track distance for single straws or straw groups from the expected $r_{iso}(t)$-relation is corrected by adjusting the straw position accordingly. Here, the assembly technique of the STT simplifies the position calibration to a large extent. Individual deviations of single tubes in the close-packed double-layers are not possible and only the vertical position of the 13 double-layers have to be adjusted. The track reconstruction is repeated using the new straw layer positions, the distances are checked and the positions are corrected again untill the systematic deviations vanish. Finally, also the $r_{iso}(t)$-relation is verified by a new parameter fit of the reconstructed track to wire distances to the measured drift times.

The distribution of the finally obtained residuals of the reconstructed tracks to the isochrones is a measure of the spatial resolution of the STT and is shown in Fig. 3.87. Only a simple filter for single hits from delta-electrons with large distortions to the fitted track has been applied. No drift time correction due to the signal propagation time along the wire and the particle time-of-flight have been made. The estimated drift time error is about

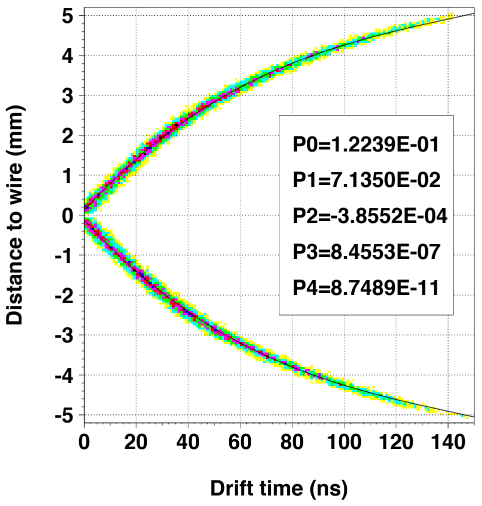

Figure 3.86: Track to wire distances and measured drift times for the reconstructed tracks. The r_{iso}(t)-relation (black line) is parametrized as a polynomial function of 4th order with the parameters P_0–P_4.

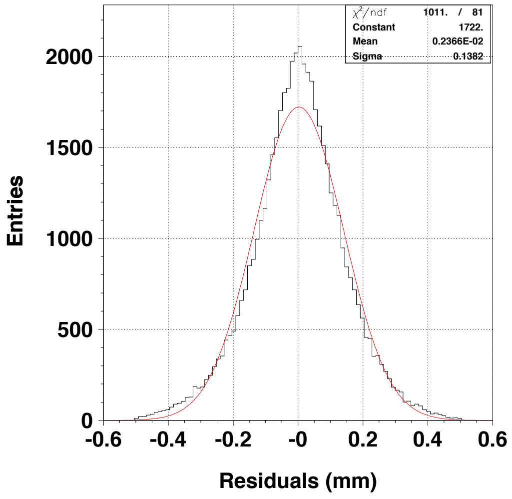

Figure 3.87: Distribution of the residuals of all reconstructed tracks as a measure of the COSY-STT spatial resolution. The width of 138 μm (σ) and mean of 2 μm are the results from the gaussian fit (red line).

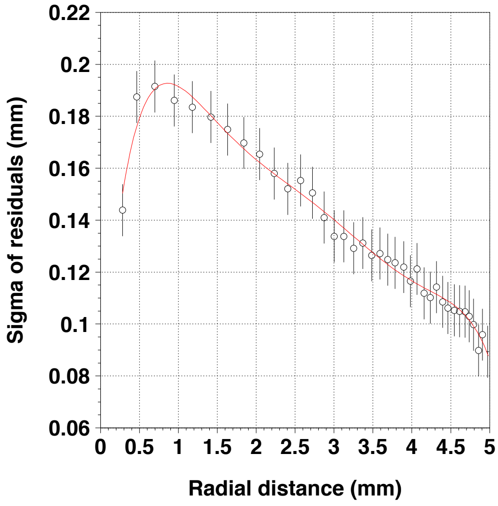

Figure 3.88: Width (sigma) of the residual distributions for different intervals of the radial distances to the wire.

Δt=2 ns. Also the reconstruction of a straight line track does not take into account multiple-scattering inside the STT which contributes to a maximum of about 100 μm for the first and last layers. The spatial resolution of the STT is given by the width of the residual distribution, which is 138 μm (σ) for the gas mixture of Ar/CO_2 (80/20%) at an absolute pressure of 1.25 bar. The shape of the distribution is nicely symmetric with a low mean of 2 μm, showing no distortion by additional systematic errors.

The variation of the spatial resolution depending on the radial distance to the wire is shown in Fig. 3.88. Close to the wire the resolution is about 190 μm, dominated by the primary ionization cluster spacing and time jitter together with higher drift velocities. Both effects are reduced more and more for larger distances to the wire and the resolution improves to about 100 μm close to the straw cathode, where the electron diffusion during their drift to the anode is the limiting factor.

The results obtained from the COSY-STT can be extrapolated to the $\overline{\text{P}}$ANDA-STT. Both detectors have a similar material budget and number of straw layers for the tracking. The main differences are the operation of the $\overline{\text{P}}$ANDA-STT inside a solenoid field and at a higher straw gas pressure of about 2 bar. The additional Lorentz force will change the radial drift path for the electrons inside a straw to a longer, spiral drift path and increased drift times. Still the isochrones have a cylindrical shape, only the r_{iso}(t)-relation will be different. The higher gas pressure will increase the maximum drift times and the ionization density which improves the spatial resolution. Therefore, assuming a comparable resolution of the drift time measurement of about Δt=2 ns the spatial resolution of the $\overline{\text{P}}$ANDA-STT is expected to be better than 140 μm.

3.11 Simulations

The simulation and reconstruction code for the STT is fully integrated in the $\overline{\text{P}}$ANDA code framework `PandaRoot`.

In this section, a quick overview of the software framework will be given, with particular attention to the STT related code. The software and the procedure used to perform the tests which will be reported in Sec. 3.12 will be addressed.

3.11.1 The `PandaRoot` framework

The `PandaRoot` code is based on the Virtual Monte Carlo (VMC) [45, 46] a tool developed at CERN by the ALICE collaboration, which allows the user to change the engine for the transport of particles in matter (`geant3`, `geant4`) at runtime without the need to change the input/output structure and to adapt the geometry description of the detector.
The VMC classes, in fact, decouple the user classes from the Monte Carlo ones, and act like an interface allowing the interchange of the Monte Carlo codes. The setup of a specific VMC requires the implementation of four base classes:

- `TVirtualMC`: it is the interface to the Monte Carlo code. It supplies methods for:
  - building/accessing geometry and materials;
  - setting up physics;
  - accessing particle properties during stepping;
  - run control.

  The implementation of this class for `geant3` is placed in the C++ class `TGeant3`, which holds the C++ functions to access the `Geant3` FORTRAN commons: it is contained in the `geant3` package, distributed by CERN, together with the original `geant321` FORTRAN code. The one for `geant4` is contained in the package `geant4_vmc`, distributed by CERN too.
- `TVirtualMCApplication`: it is the interface to the Monte Carlo application of the user and defines user actions at each stage of the run, such as:
  - geometry construction and initialization;
  - generation of primaries;
  - event starting and ending instructions;
  - stepping actions;
- `TVirtualMCStack`: it defines a user defined particle stack interface.
- `TVirtualMCDecayer` (optional): it defines a interface to an external decayer.

When setting up the VMC base classes, the user needs to implement his/her own `MCApplication` class (for example in the `PandaRoot` code this is done in `base/FairMCApplication`). The different routines, to be performed at event time, take the name of *tasks*.

3.11.2 The STT simulation and reconstruction

The STT specific classes are all contained in the `stt` directory of `PandaRoot`. A full simulation chain can be characterized by four main steps: simulation, digitization, reconstruction and analysis. In this section only the simulation and reconstruction code, that provide the tracks used for the analysis, will be addressed. The digitization has already been described in Sec. 3.8.

3.11.2.1 Simulation and Digitization

During this step, realistic data, resembling the ones that will be available from the operating system, are generated, ready for the reconstruction.
It can be divided in two parts, concerning, respectively, the tracker setup and its response to the passage of the particles.

The **detector description** is contained in the `PndStt` class, where the geometry is loaded and the sensitive material is set to collect signals from charged particle transversing it.
The straw tubes are built and positioned in an ascii geometry file; for each tube, the coating, the filling gas mixture and the wire materials are implemented. The passive elements of the tube such as the plugs have not been implemented yet. On the other side, the support passive elements, which surround the central tracker, are present. It is however forseen to insert all the information on passive elements in the future. Moreover, since the presence of many details will slow down the simulation, it is foreseen that the final geometry description will contain only *average* materials to take into account the correct material budget but be fast enough to grant good time performances.
At the simulation stage the geometrical parameters of the tube are saved in the parameter file in order to be retrievable at any stage of the recostruction.

After the collection of MC points from charged particles, the detector response of the STT is simulated as described in Sec. 3.8 during the

digitization step which provides the collection of realistic hits. These hits contain the information on the drift radius and the energy deposit.

3.11.2.2 Reconstruction

In a tracking detector, the aim of the reconstruction is to collect the hits, assign them to the different tracks and then fit the obtained track candidates to get the momentum of each particle.
The STT does not provide the x, y, z spatial coordinates of the point where the particle passed. When a tube is hit by a particle, the only available information for the track reconstruction is the measured drift radius, together with the position and orientation in space of the tube itself. A specific track finding (described in Sec. 3.11.3) and fitting (described in Sec. 3.11.4) procedure has been developed relying only on this information.
This procedure takes place through a chain of tasks, each one performing operations at event stage. Different packages devoted to the global tracking are available in `PandaRoot` [47, 48, 49]: only the procedure and the code used to obtain the results presented in Sec. 3.12 will be described in Sec. 3.11.3 and Sec. 3.11.4.

3.11.3 The pattern recognition

The track finder procedure for tracks crossing the STT detector is divided in several steps:

- STT local track finding
- MVD + STT track finding
- GEM extension

3.11.3.1 STT local track finding

3.11.3.2 MVD + STT track finding

3.11.3.3 The GEM extension

Once the MVD + STT track finder has been run and a track hypothesis is available, the GEM hit problem can be addressed. In the angular region where the tracks can cross both MVD/STT and the GEM detectors ($7^o < \theta < 21^o$), a simple extrapolation of the tracks using the track follower GEANE[5] [50] from the last point of the central tracker on each plane of the GEM detector is the starting point to add the GEM hits to the tracks. For each extrapolation the distance between the extrapolated point and the error associated to it are calculated. The hit is associated to the track if the distance is within $5\,\sigma$.
The GEM detector is composed of three stations, with two sensor each. Every sensor has two views. When more than one track hits the GEM stations, combinatorial background is present and has to be suppressed. A specific test has been written to take care of this: the two sensors on each section are overlapped and only when a hit has its counterpart on the other sensor, within 1 cm, is considered *true*, otherwise it is flagged as *fake*. Once that a true couple of hits has been found all the other hits on the same sensors coming from the same energy deposits are considered as combinatorial background. Only true hits are used for the assignement to the tracks. The tracks are eventually refined by requiring that each GEM hit is associated to at most one track and each track is associated to at most one hit on every measurement plane.
Once the hits have been attached to a track, the Kalman filter is applied on that track, using the GEM measured hits: this is necessary because the extrapolation with GEANE is always performed with the mass hypothesis of the muon and this could lead to an underestimation or overesimation of the energy loss between the GEM stations, causing the propagated point to be too far from the measured one. The application of the Kalman filter forces the track to stick to the measured hits and allows to retrieve some hits formerly missed due to the wrong mass hypothesis.
Concerning the helix parameters found in the previous step, they are not recalculated since the GEM planes lie in the region between the solenoidal an dipolar magnetic field, which is highly inhomogeneous.

3.11.4 The Kalman filter

The track fitting is finally performed through the Kalman filter procedure, using the hits coming from MVD, STT and GEM where available and, as starting position and momentum, the values inferred by the pattern recognition, nacktracked to the point of closest approach to the interaction point.
In this section a short summary of the Kalman fit procedure [51, 52] is reported. A more detailed description of this topic can be found in [53] and [54]

---

[5] GEANE is a track follower distributed within the `geant3` package. It is written in FORTRAN and a C++ interface has been developed in `fairroot` and is used also in the extrapolation step of the Kalman fit.

and references quoted therein. The package devoted to the Kalman fit procedure is `genfit` [55].

The Kalman fit is an iterative procedure which, unlike global methods such as the helix fit, takes into account the energy loss, the magnetic field inhomogeneities and the multiple scattering.
The aim of the Kalman filter is to find the best estimation of the true track point f_i at the i-th detector plane by minimizing the χ^2:

$$\begin{aligned}\chi^2(\boldsymbol{f}) &= \sum_i [(\boldsymbol{e}_i[\boldsymbol{f}_{i-1}] - \boldsymbol{f}_i)\boldsymbol{W}_{i-1}(\boldsymbol{e}_i[\boldsymbol{f}_{i-1}] - \boldsymbol{f}_i)] \\ &\quad +(\boldsymbol{x}_i - \boldsymbol{f}_i)\boldsymbol{V}_i(\boldsymbol{x}_i - \boldsymbol{f}_i) \qquad (3.17)\end{aligned}$$

where $\boldsymbol{e}$ are the extrapolated points (i.e. the predicted position of the track on the i-th detector plane starting from the $i-1$-th one) and $\boldsymbol{x}$ are the measured ones; $\boldsymbol{W}$ and $\boldsymbol{V}$ are the weight matrices containing respectively the tracking and the measurement errors.
The minimization of Eq. 3.17 gives:

$$\begin{aligned}\frac{\partial\chi^2}{\partial\boldsymbol{f}_i} &= \boldsymbol{W}_{i-1,i}(\boldsymbol{e}_i[\boldsymbol{f}_{i-1}] - \boldsymbol{f}_i) + \boldsymbol{V}(\boldsymbol{x}_i - \boldsymbol{f}_i) \qquad (3.18) \\ &\quad -\boldsymbol{T}(l_{i+1}, l_i)\,\boldsymbol{W}_{i,i+1}(\boldsymbol{e}_{i+1}[\boldsymbol{f}_i] - \boldsymbol{f}_{i+1}) = 0\ ,\end{aligned}$$

The Kalman filter is a method to solve Eq. 3.18. Usually this is done through three steps [56, 57]:

- the first step is the *extrapolation* of the previous Kalman value $\boldsymbol{k}_{i-1}$ to the i-th plane:

  $$\boldsymbol{e}_i \equiv \boldsymbol{e}_i(\boldsymbol{k}_{i-1}) = \boldsymbol{G}(\boldsymbol{k}_{i-1}) \qquad (3.19)$$

  $$\begin{aligned}\boldsymbol{\sigma}^2[\boldsymbol{e}_i] &= \boldsymbol{T}(l_i, l_{i-1})\,\boldsymbol{\sigma}^2[\boldsymbol{k}_{i-1}]\,\boldsymbol{T}^T(l_i, l_{i-1}) \\ &\quad +\boldsymbol{W}_{i-1,i}^{-1} \qquad (3.20)\end{aligned}$$

- the second step is the calculation of the *Kalman filter value* at the i-th detector plane. This is a preliminary evaluation of the track parameters $\boldsymbol{k}_i$, making a "weighted mean" between the measured value and the predicted value on plane i:

  $$\begin{aligned}\boldsymbol{k}_i &= \boldsymbol{\sigma}^2[\boldsymbol{k}_i](\boldsymbol{\sigma}^{-2}[\boldsymbol{e}_i]\,\boldsymbol{e}_i \qquad (3.21) \\ &\quad +\boldsymbol{V}_i\boldsymbol{x}_i)\end{aligned}$$

  $$\boldsymbol{\sigma}^{-2}[\boldsymbol{k}_i] = \boldsymbol{\sigma}^{-2}[\boldsymbol{e}_i] + \boldsymbol{V}_i \qquad (3.22)$$

  These equations are simply the weighted average in the 5-fold track space;

- the third step is the *backward smoothing* of the Kalman point solution of the second step to get the final estimate of the value $\boldsymbol{f}_i$

  $$\boldsymbol{f}_i = \boldsymbol{k}_i + \boldsymbol{A}_i\,(\boldsymbol{f}_{i+1} - \boldsymbol{e}_{i+1}) \qquad (3.23)$$

  $$\begin{aligned}\boldsymbol{\sigma}^2[\boldsymbol{f}_i] &= \boldsymbol{\sigma}^2[\boldsymbol{k}_i] + \qquad (3.24) \\ &\quad +\boldsymbol{A}_i\left(\boldsymbol{\sigma}^2[f_{i+1}] - \boldsymbol{\sigma}^2[\boldsymbol{e}_{i+1}]\right)\boldsymbol{A}_i^T\end{aligned}$$

  $$\boldsymbol{A}_i = \boldsymbol{\sigma}^2[\boldsymbol{k}_i]\,\boldsymbol{T}^T(l_{i+1}, l_i)\,\boldsymbol{\sigma}^{-2}[\boldsymbol{e}_{i+1}] \qquad (3.25)$$

  This last step is often substituted by an alternative option: to perform a so-called "backtracking", i.e. steps 1 and 2 while extrapolating in backward direction, from the last point of the track to the first one.

If the track follower and all the measured points are *not* expressed with the same set of track variables the so called *measurement matrix* $\mathbf{H}$ is used, to make the two representations comparable, setting:

$$\boldsymbol{x}_i = \boldsymbol{H}_i\boldsymbol{e}_i + \epsilon_i\ , \qquad (3.26)$$

where ϵ is the random part introduced by the measurement.

3.11.5 The dE/dx simulation

The STT can also contribute to the particle identification in the low energy region, by means of the specific energy loss measurements.
For gaseous detectors the particle identification is obtained from the simultaneous measurement of the dE/dx and the momentum. For a 1 GeV/c track, the STT detector allows about 25 energy loss measurements. Although this is usually considered as a too low number for a good particle identification, some capability exists in the low energy range. Fig. 3.89 shows the distribution of specific energy loss for different particles plotted versus the momentum.

The various regions have been identified as bands, with a mean value and an amplitude, as shown in Fig. 3.90, using a sample composed by all the five types of particles (electrons, muons, pions, kaons and protons). They have been simulated, digitized and fully reconstructed in a momentum range between 0.05 GeV/c and 0.8 GeV/c. In each tube, the deposited energy was reproduced with a fast simulation tuned on the real data results. The radial path has been reconstructed by the measured drift radius and by the dip angle resulting from the fit. The dE/dx has been calculated with the truncated

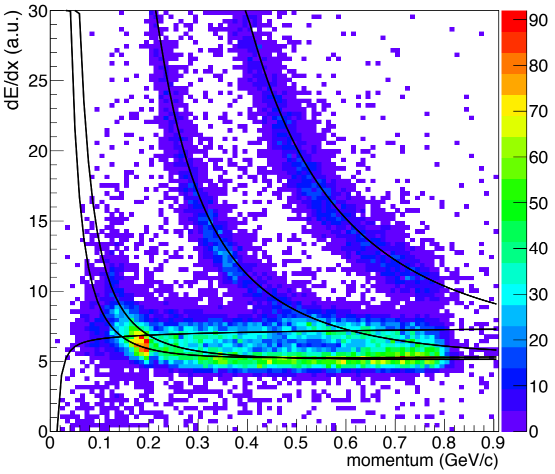

Figure 3.89: Distribution of dE/dx vs reconstructed momentum for electrons, muons, pions, kaons and protons. The superimposed lines are the mean value of the bands. The procedure to find them is described in the text.

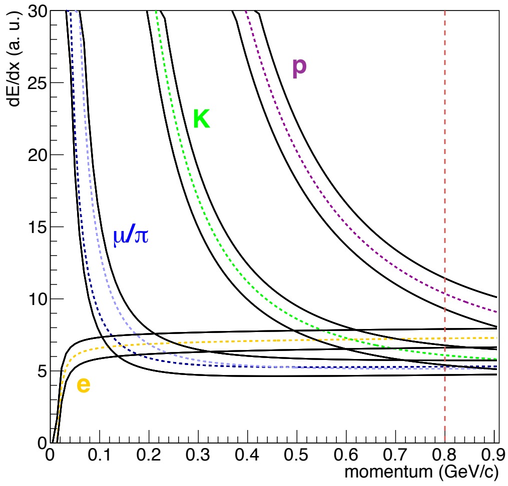

Figure 3.90: The bands identifying the regions of dE/dx vs. momentum found for the different particles with the procedure described in the text are drawn (the tracks have been Kalman fitted with the mass hypothesis of muon). The muon and pion bands are highly overlapped due to the similarity in their masses: it is not possible to distinguish between these two particles in a reliable way with this method. The vertical line shows the threshold value of 0.8 GeV/c: the particle identification with the STT is possible only for particles below this limit.

mean at 70 % in order to cut off the higher dE/dx tail. The momentum has been obtained fitting the hits from MVD, STT and GEM detectors, with the Kalman filter procedure.

Since at fixed momentum the dE/dx values distribute as a gaussian, the momentum range has been divided in many intervals $\sim$ 30 MeV/c large and for each interval the dE/dx distribution has been fitted (Fig. 3.91): the obtained mean and sigma values as a function of the momentum, whose graphs are shown in Fig. 3.92, have been fitted to obtain the bands.

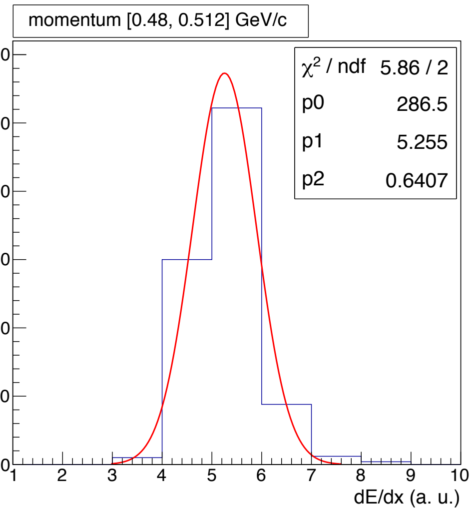

Figure 3.91: Example of dE/dx distribution for muon tracks with momentum in the range [0.48, 0.512]GeV/c: it has a gaussian shape as expected.

When a particle of unknown mass has to be identified with this method, the dE/dx and momentum are reconstructed and a point is identified in the plot of energy loss as a function of the momentum, where the bands are known. Then, for every particle hypothesis, the gaussian corresponding to the reconstructed momentum of the track is chosen and it is evaluated at the measured track dE/dx. The resulting value, which comes from a standard normalized gaussian, is the probability density function (p.d.f.) value for that hypothesis. Since the momentum is the outcome of the Kalman filter procedure, for which a mass hypothesis has been used, two strategies can be followed: either the Kalman fit is run on a track with all the mass hypothesis or the track is fitted with a unique mass hypothesis. In the first case, the particle identification from dE/dx is used just to give the probability that the Kalman mass hypothesis was

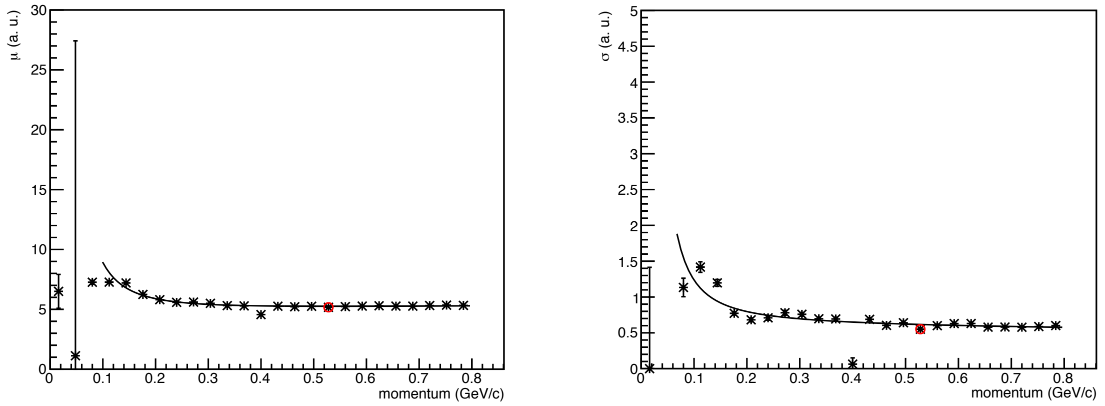

Figure 3.92: Plot of the mean and sigma values of the gaussians as a function of the momentum. The red circles correspond to the values for the momentum interval of figure Fig. 3.91. From the fitting of these graphs the bands of dE/dx vs momentum are obtained. The points at the left extremity are not used since the statistic there is too low to perform a reliable fit.

right: only the couples of reconstructed track and particle identification ouput with the same mass hypothesis are then taken into account (e.g., p.d.f. of the electron hypothesis for the momentum reconstructed with Kalman as an electron, p.d.f. of the muon hypothesis for the momentum reconstructed as a muon and so on as shown in Fig. 3.93). They are normalized to their sum and the highest value gives the conclusive hypothesis.

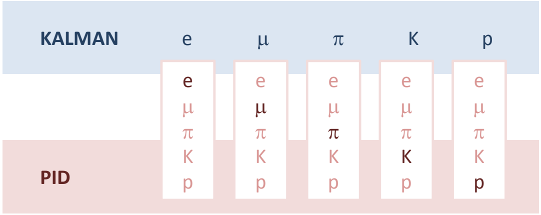

Figure 3.93: Sketch of the association between the p.d.f. value from the particle identification (PID) procedure and the Kalman fitted track.

In the second case the track has only one reconstructed momentum and the particle identification is used to determine the mass hypothesis. After this the track should be refitted with the correct mass.

Two different sets of bands have been identified.

To evaluate the performances of such a particle identification technique, a sample of particles of each kind, simulated with momentum between 0.05 GeV/c and 0.8 GeV/c has been used. In fact for higher momenta the p.d.f value is set equal to 1 for all the hypotheses, i.e. the procedure is not able to identify the particle mass.

		frequencies of p.i.d. (%)				
		e	μ	π	K	p
true part.	e	78.9	5.2	5.6	10.1	0.2
	π	9.0	47.2	40.7	2.9	0.2
	K	22.3	8.0	1.6	65.1	3.0
	p	0.1	[0.01]	0.1	1.0	98.8

Table 3.11: Results of the performance test of particle identification: for each row the frequency, in percentages, with which the simulated particle is recognized as electron, muon, pion, kaon and proton is written. Each row percentages sum up to 100 %. The correct association is the one on the diagonal. The muon and pion frequencies must be summed, since with this method muons and pions can be hardly distinguished.

Each track has been recostructed with the muon mass hypothesis (default in the code). For each reconstructed momentum, the p.d.f. values for the five particle hypotheses are extracted from the dE/dx vs. momentum. The one with the highest value determines the identified particle: the obtained results is shown in table 3.11.

The separation power $S = 2\,\Delta E$ between two particles is defined as the distance between the centres of the two bands $\langle E_1 \rangle$ and $\langle E_2 \rangle$, measured in terms of the standard deviations σ_1 and σ_2 [58]:

$$\Delta E = \frac{E - \langle E_1 \rangle}{\sigma_1} = \frac{\langle E_2 \rangle - E}{\sigma_2} \; . \qquad (3.27)$$

Eliminating E from the previous equation and recalculating S the following sparation power is obtained:

$$S = \frac{\langle E_2 \rangle - \langle E_1 \rangle}{\sigma_1/2 + \sigma_2/2} \; , \qquad (3.28)$$

when $\langle E_2 \rangle > \langle E_1 \rangle$ or

$$S = \frac{| \langle E_2 \rangle - \langle E_1 \rangle |}{\sigma_1/2 + \sigma_2/2} \; , \qquad (3.29)$$

in general, which is shown in Fig. 3.94. This plot demonstrates clearly the capability of the STT detector in the low energy PID.

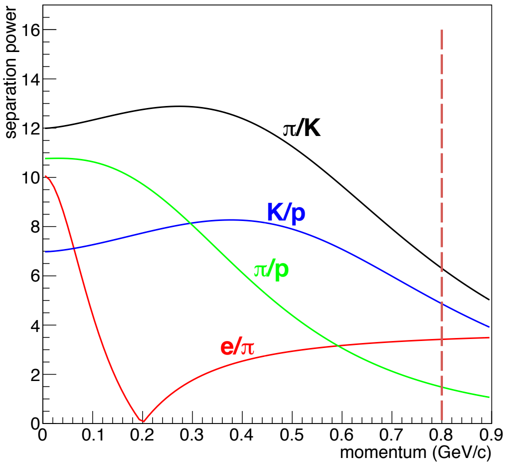

Figure 3.94: Separation power in the STT detector for the bands built with particles all tracked with the same muon mass hypothesis. The vertical line at 0.8 GeV/c is the chosen threshold for the momentum to perform the particle identification in the STT.

3.11.5.1 Effect of pressure and gas mixture

A simulation has been performed to investigate the relationship between gas pressure and dE/dx resolution, for two different gas mixtures. The test has been performed with a simple setup, with 22 samplings of 1GeV/c pions from a single straw tube and using the truncated mean at 70%.

Fig. 3.95 and Fig. 3.96 show the different dE/dx distributions with a gas mixture of Ar and CO_2 in different ratios and at different pressures. The change in CO_2 percentages does not produce observable effects, while the change in operating pressure improves of about 20% the specific energy resolution.

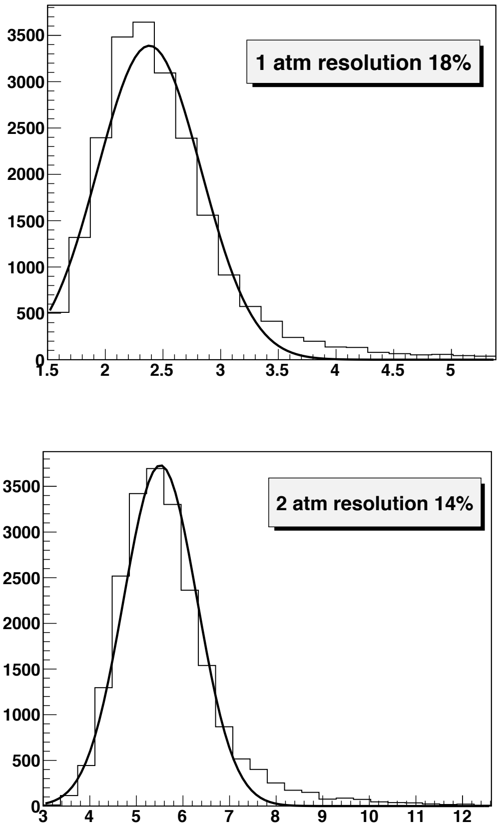

Figure 3.95: Upper figure shows the dE/dx resolution at 1atm absolute pressure, lower figure at 2atm: increasing the gas pressure a gain in resolution of about 20% is obtained. Both resolutions have been obtained with a gas mixture $Ar(90\%)/CO_2(10\%)$.

3.11.6 Simulation environment for the tests

A summary of the choices made to perform the tests is given here.

The target spectrometer was simulated to have a realistic material budget. Specifically, the list of the simulated subdetectors contains: Micro Vertex Detector (MVD), STT, Electromagnetic Calorimeter, TOF detector, Muon Chambers, the Cherenkov detectors and forward GEM stations. In addition also the passive elements have been positioned, to take into account the right material amount: the Solenoid Magnet, the Target and Beam Pipes.

The full magnetic field map has been used, to account for magnetic inhomogeneities.

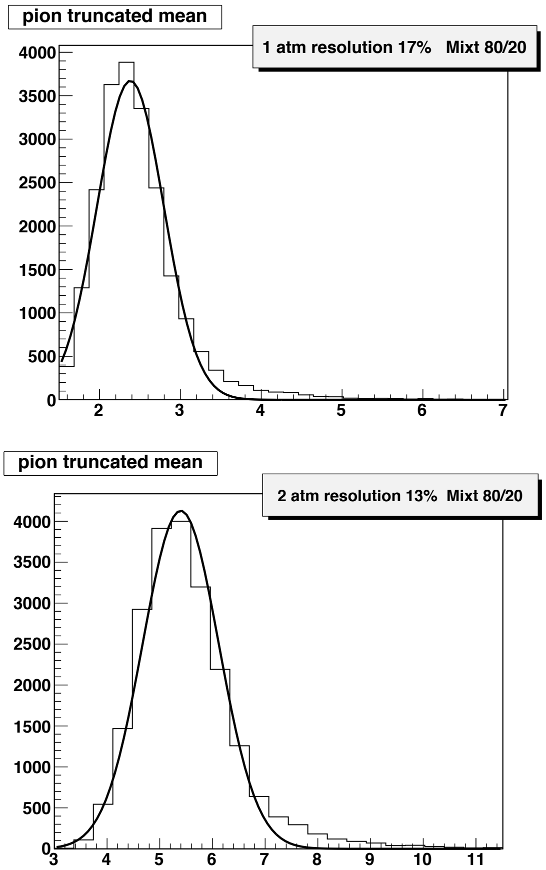

Figure 3.96: The same as Fig. 3.95, but with a gas mixture $Ar(80\%)/CO_2(20\%)$.

Each test required the generation of a different kind of sample, hence in every single case the most suitable event generator has been chosen among the particle generators available in `PandaRoot`. In particular, for the single track tests (Sec. 3.12.2) the `BoxGenerator` has been used (to select ranges of momentum, both magnitude and direction, in addition to particle type and multiplicity), for the generation of physical events `EvtGen` [59] has been used and for background events the `DpmGen` (Dual Parton Model) [60, ?] generator has been used.

For each tracker (MVD, STT and GEM), the digitization was performed in a realistic way, to get a reliable detector response and hits on which be able to perform the reconstruction.

The pattern recognition procedure is summarized here:

1) MVD local track finder: MVD alone.
2) STT local track finder: STT alone.
3) MVD + STT track finder: performs pattern recognition starting from the tracks found at points 1 and 2.
4) MVD + STT + GEM track finder: extends the tracks found in point 3 to the GEM stations, in the overlap region of the three detectors, i.e. for $7° \leq \theta \leq 21°$.

After the track finding, the Kalman filter was applied to the tracks, using the package `genfit` [55] (see Sec. 3.11.4) The starting point for the Kalman procedure was chosen by extrapolating the helix fitted tracks to the point of closest approach to the interaction point. The xy plane was chosen as starting plane and only one iteration was performed in the fit procedure; this means that the filter step is performed on the plane corresponding to each measurement, both in the forward and in the backward direction.

3.12 Performances

In order to study the performances of the designed $\overline{\text{P}}$ANDA Straw Tube Tracker in terms of geometrical acceptance of the layout, momentum resolution and reconstruction efficiency, systematic studies have been performed with single track events.
The complete simulation – digitization – reconstruction chain has been run with the simulation environment described before. The digitization step has been performed only for MVD, STT and GEM in order to save computation time, since the studies would have been dedicated only to the Central Tracker. We recall that the pattern recognitions are all real, with no information taken from the Monte Carlo truth.

3.12.1 Studies on the number of hits per track

In order to check the geometrical acceptance of the layout, the distributions of the number of hits coming from axial, skewed and short straws have been studied for particles generated at fixed values of the polar angle θ and as function of the azimuthal ϕ angle.
10^4 μ^+ and 10^4 μ^- single track events at 1

GeV/c, random ϕ ($\phi \in [-90°, +90°]$) and $\theta = 20°,\ 90°,\ 140°\ (\pm 5°)$ have been simulated.
Fig. 3.97 shows the distributions of the number of hits vs. ϕ for $\theta = 90° \pm 5°$.

The plots show that the minimum number of hit straws is $12 - 13$ for the axial straws and $7 - 8$ for the skewed ones. These numbers correspond to the minimum number of layers (axial and skewed, respectively) that a particle flying at $\phi = \pm 30°$ can traverse. For ϕ values corresponding to regions of the detector where there are additional single–layers parallel to the beam axis, the number of axial hit straws increases up to $18 - 20$.
The low number of hit straws at $\phi = \pm 90°$ is due to the gap for the target pipe. Concerning $\phi = \pm 30°$, the losses are caused by the fact that in the corners of the hexagonal STT layout there are short tubes, which do not fill completely the volume, leaving empty spaces. As shown in Fig. 3.98.b, these losses are negligible: only $\sim 4.4\%$ of the total number of events hits less than 5 skewed straws. Nevertheless, there is a gain in efficiency when including in the z reconstruction also the hits from the MVD.
So this study demonstrates that the minimum number of hit straws obtained with such a layout is enough to perform a robust track reconstruction.

3.12.2 Studies on momentum resolution and reconstruction efficiency

3.12.2.1 Studies with uniform $\cos\theta$

10^4 μ^- single track events have been generated in the interaction point I.P. ($x = y = z = 0$), with uniform azimuthal angle $\phi \in [0°, 360°]$ and uniform $\cos\theta$ ($\theta \in [7.8°, 159.5°]$) at fixed values of total momentum (0.3, 1, 5 GeV/c).
The reconstructed momentum distributions are shown in Fig. 3.99 for particles at (a) 0.3, (b) 1 and (c) 5 GeV/c. The red dashed histograms show the prefit results (the outcome of the pattern recognition, Sec. 3.11.3), while the blue histograms reproduce the Kalman fit result.
Each histogram has been fitted with a Gauss function in the range $[\mu - 3\sigma, \mu + 3\sigma]$, where μ is the mean value of the momentum distribution and σ has been calculated by dividing the FWHM of the histogram by 2.35.
Table 3.12 summarises the obtained values of momentum resolution and efficiency. The resolution is calculated as σ/μ, using the μ and σ values from the gaussian fit; it is then reported in percentage. The efficiency is defined by the integral below the histogram fitted region, divided by the number of generated tracks. In addition, the efficiency "in peak" is reported: it is the number of tracks in the fitted range ($\mu \pm 3\sigma$) with respect to the total number of tracks.
In all cases the Kalman fit results are better than the prefit ones (as expected), both in terms of mean value and sigma of the distributions. In fact the Kalman fit improves the helix fit results both reducing the width of the distribution (i.e. improving the resolution) and shifting the distribution mean value towards a more correct value. On the other hand, the helix fit introduces a systematic offset in the momentum determination giving an underestimated value.

3.12.2.2 Studies at fixed θ values

A systematic scan of the momentum resolutions and efficiencies has been performed with fixed angle generated particles.
10^4 μ^- single track events have been generated at the interaction point with fixed total momentum (0.3, 1, 2 and 5 GeV/c) and random ϕ ($\phi \in [0°, 360°]$). The θ angular range has been scanned as follows:

i. $\theta = 10°,\ 12°,\ \ldots,\ 24°$ in steps of $2°$ $(\pm 1°)$;

ii. $\theta = 30°,\ 40°,\ \ldots,\ 90°$ in steps of $10°$ $(\pm\ 5°)$;

iii. $\theta = 112.5° \pm 17.5°$ and $145° \pm 15°$.

Finally, the events have been reconstructed and the Kalman fit has been performed.
The values of momentum resolution and efficiency in peak (see previous paragraph for the meaning) are summarised in Tables 3.13 – 3.16. The momentum resolution and efficiency plots as function of the θ angle are shown in Figs. 3.100–3.107.

Apart from the 0.3 GeV/c set of simulated events, for which a dedicated comment is needed, common conclusions can be drawn for the other event sets generated at 1, 2 and 5 GeV/c.
Concerning the momentum resolution, a common behaviour can be identified by looking at Figs. 3.102–3.104–3.106: the resolution improves for θ values up to $\sim 21°$, then starts to worsen again. This is due to geometrical reasons: concerning the straw trackers, tracks travelling with $\theta < 11.6°$ hit just few straw layers, in particular the axial ones, preventing the reconstruction of the z coordinate of the straw tube hits (Sec. 3.11.3); this turns out in a low spatial (and hence momentum)

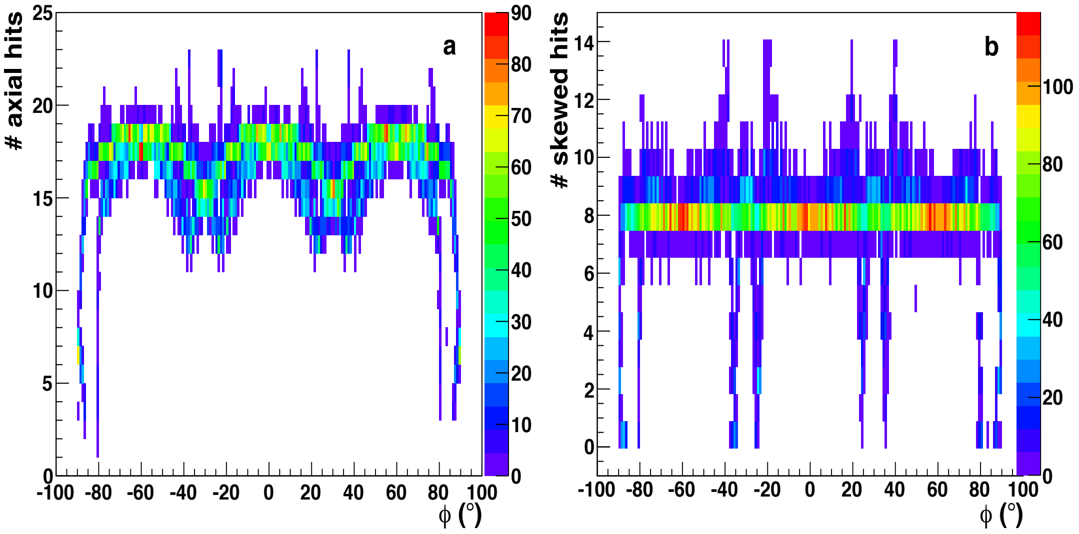

Figure 3.97: Distribution of the number of axial (a) and skewed (b) hit straws as a function of the ϕ angle for 20000 μ generated with a momentum of 1 GeV/c at $\theta = 90° \pm 5°$.

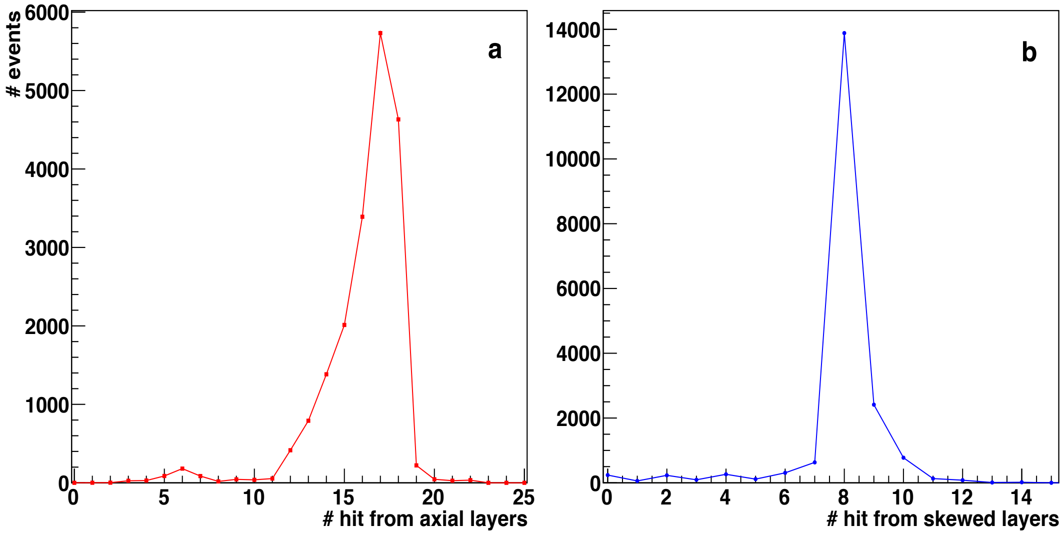

Figure 3.98: Distribution of the mean number of axial (a) and skewed (b) hit straws per event.

Table 3.12: Momentum resolution and reconstruction efficiency for 10^4 μ^- (Fig. 3.99).

Momentum	Resolution (%)		Efficiency (%)		Eff. in peak (%)	
(GeV/c)	Prefit	Kalman	Prefit	Kalman	Prefit	Kalman
0.3	3.63 ± 0.04	1.32 ± 0.02	90.14 ± 0.29	80.28 ± 0.39	86.53 ± 0.34	63.89 ± 0.48
1.0	3.42 ± 0.14	1.79 ± 0.01	93.47 ± 0.14	93.11 ± 0.15	90.34 ± 0.17	90.96 ± 0.17
5.0	4.41 ± 0.04	3.61 ± 0.03	91.48 ± 0.28	91.36 ± 0.28	88.60 ± 0.32	87.95 ± 0.32

resolution of the STT hits. On the other hand, the tracking in this forward angular region is performed mainly with the hits produced in the MVD and in the GEM chambers, which are very precise detectors.

As the θ value increases, tracks hit more and more

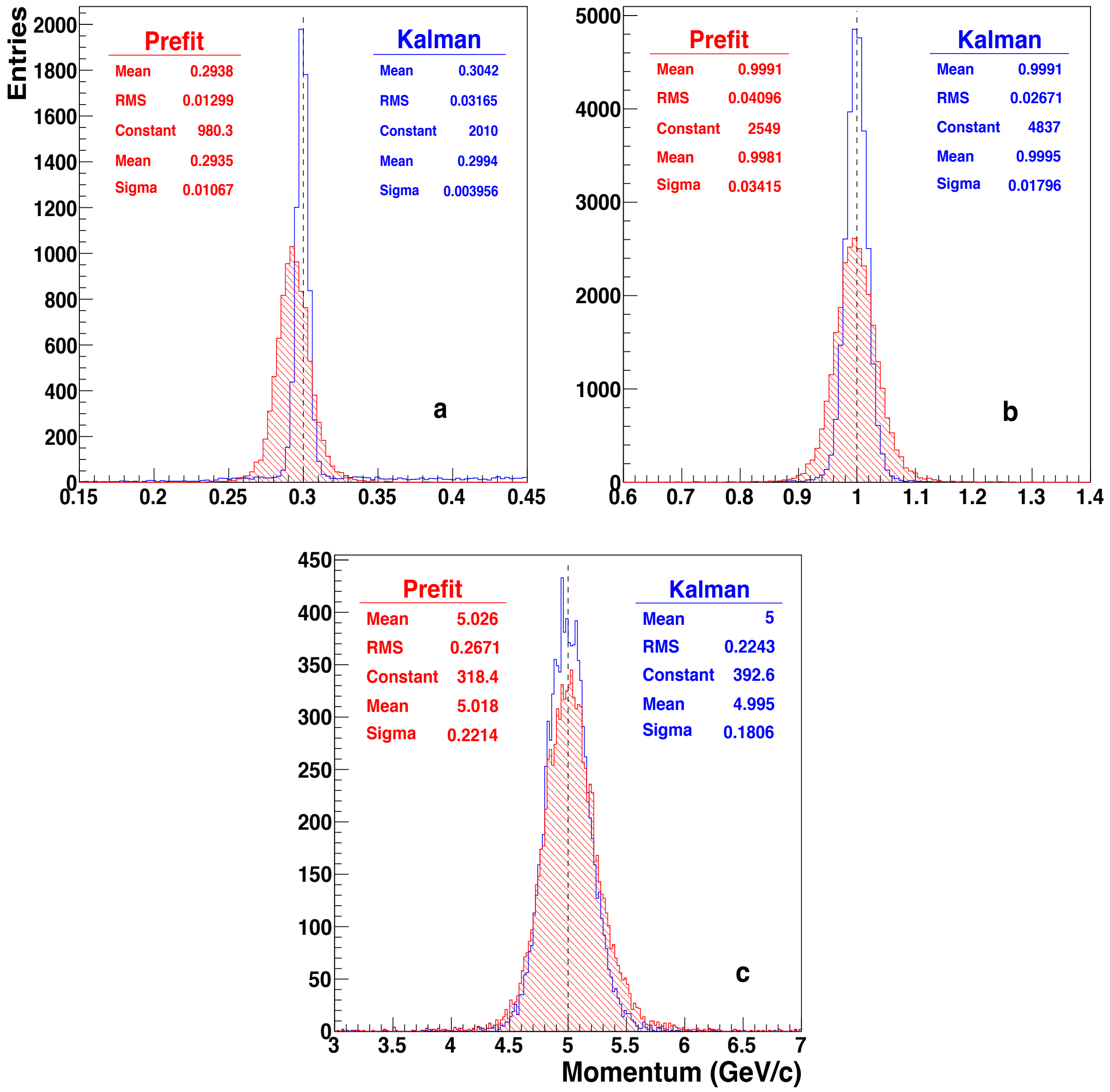

Figure 3.99: Momentum distributions for (a) 0.3, (b) 1 and (c) 5 GeV/c μ^-, reconstructed with helix (red dashed) and Kalman (blue) fits. The statistic boxes report the mean values and RMS of the non fitted histograms, as well as mean and sigma values of the gaussian fits, before and after the Kalman fit.

straw layers, allowing a better track reconstruction in the tracker. This, combined with the good resolution of the MVD and GEM hits, results in a better global momentum resolution.
Then, for $21° < \theta < 133°$, tracks traverse the MVD and all the straw layers; so the resolution obtained by the STT alone is improved, with respect to that at lower θ values, but it suffers from the fact that there are no more hits in the GEM chambers. So the resolution is globally a bit worse.
Finally, for $\theta > 133°$ tracks are going in the backward direction and traverse a lower number of straw layers as the angle increases: consequently, since the decreased number of hits is not compensated by any other outer tracking detector (like the GEMs in the forward direction), the resolution becomes worse.

Concerning the reconstruction efficiency, shown in Figs. 3.103–3.105–3.107, it is quite low around $\theta = 10°$, because the tracking procedure fails when the number of reconstructed hits is too low, as here; then, it increases up to more than 90% in the central angular region. The efficiency presents a dip around $\theta = 90°$, due to the tracks that are lost because they go into the target pipe. Finally, for tracks travelling in the backward direction, the efficiency starts to decrease because of the reduced number of hits per track, that may cause problems in the reconstruction.

Table 3.13: Momentum resolution and reconstruction efficiency for 10^4 μ^- single track events generated at 0.3 GeV/c and fixed θ angle.

θ (°)	Resolution (%)	Efficiency (%)	Efficiency in peak (%)
10	4.78 ± 0.06	1.90 ± 0.14	1.35 ± 0.12
12	2.84 ± 0.08	24.81 ± 0.43	17.80 ± 0.38
14	2.59 ± 0.06	52.10 ± 0.49	35.84 ± 0.48
16	2.67 ± 0.07	53.92 ± 0.49	34.95 ± 0.48
18	2.50 ± 0.06	53.35 ± 0.49	32.55 ± 0.47
20	1.89 ± 0.05	49.28 ± 0.49	26.74 ± 0.44
22	1.41 ± 0.06	45.13 ± 0.49	21.90 ± 0.41
24	1.50 ± 0.06	39.56 ± 0.49	17.21 ± 0.38
30	1.57 ± 0.04	54.40 ± 0.49	28.84 ± 0.45
40	1.63 ± 0.02	80.50 ± 0.39	65.24 ± 0.48
50	1.38 ± 0.02	88.24 ± 0.32	78.20 ± 0.41
60	1.32 ± 0.01	90.18 ± 0.29	82.32 ± 0.38
70	1.25 ± 0.01	91.21 ± 0.28	82.75 ± 0.38
80	1.22 ± 0.01	82.90 ± 0.38	75.38 ± 0.43
90	1.26 ± 0.01	81.33 ± 0.39	73.37 ± 0.44
112.5	1.28 ± 0.01	74.31 ± 0.44	62.51 ± 0.48
145	2.04 ± 0.05	38.78 ± 0.49	23.44 ± 0.42

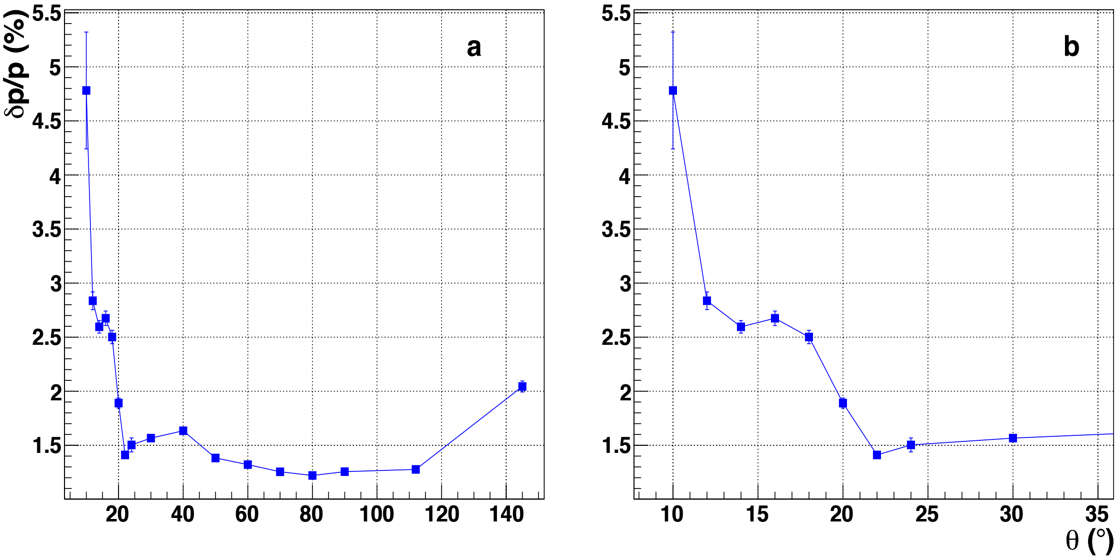

Figure 3.100: Momentum resolution vs. θ starting angle for 0.3 GeV/c μ^- single track events, in the full angular range $\theta \in [9°, 160°]$ (a) and in the forward region $\theta \in [9°, 35°]$ (b) (see Table 3.13).

Concerning the events at 0.3 GeV/c, the results are not so reliable as at the others described above, in particular for small values of θ. The reason is that the Kalman fit produces long tails in the momentum distributions (see Fig. 3.99.a), even if the outcome of the prefit does not present these tails.

This Kalman behaviour affects both the momentum resolution and the reconstruction efficiency, shown in Figs. 3.100–3.101; it is probably due to a code bug, which has still to be deeply investigated and corrected.

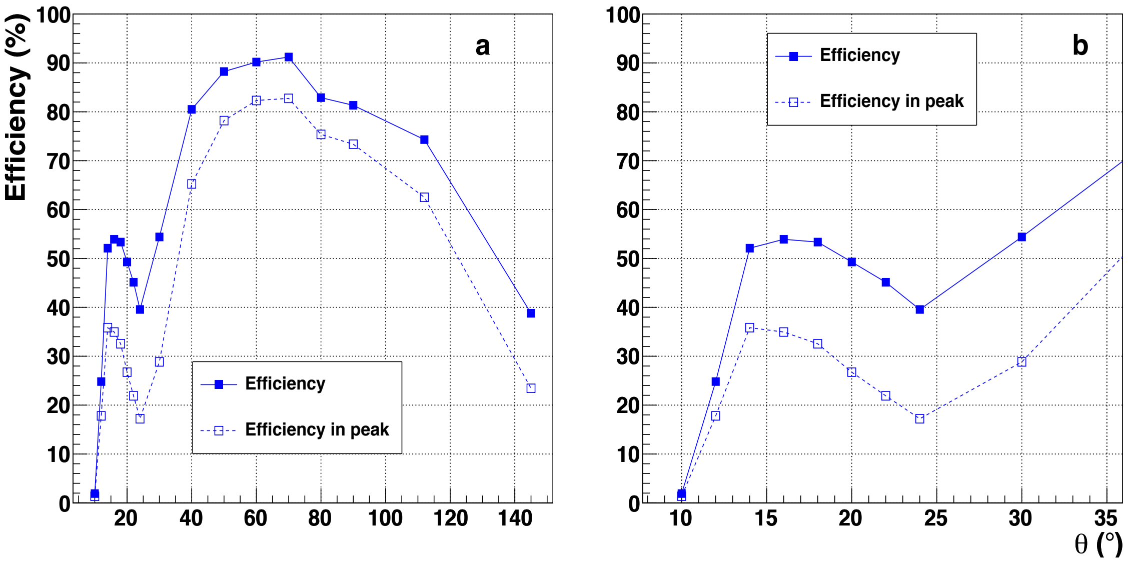

Figure 3.101: Track reconstruction efficiency vs. θ starting angle for 0.3 GeV/c μ^- single track events, in the full range $\theta \in [9°, 160°]$ (a) and in the forward region $\theta \in [9°, 35°]$ (b) (see Table 3.13).

Table 3.14: Momentum resolution and reconstruction efficiency for 10^4 μ^- single track events generated at 1 GeV/c and fixed θ angle.

θ (°)	Resolution (%)	Efficiency (%)	Efficiency in peak (%)
10	2.47 ± 0.06	20.66 ± 0.40	18.63 ± 0.39
12	2.24 ± 0.03	88.42 ± 0.32	80.80 ± 0.39
14	1.87 ± 0.02	93.66 ± 0.24	87.86 ± 0.33
16	1.60 ± 0.02	93.94 ± 0.24	90.76 ± 0.29
18	1.37 ± 0.02	94.45 ± 0.23	88.28 ± 0.32
20	1.24 ± 0.01	98.15 ± 0.13	92.85 ± 0.26
22	1.68 ± 0.02	98.71 ± 0.11	86.53 ± 0.34
24	1.79 ± 0.02	98.65 ± 0.12	94.70 ± 0.22
30	1.78 ± 0.02	97.71 ± 0.15	94.06 ± 0.24
40	1.79 ± 0.02	95.91 ± 0.19	92.57 ± 0.26
50	1.74 ± 0.02	95.18 ± 0.21	92.13 ± 0.27
60	1.79 ± 0.02	95.28 ± 0.21	92.96 ± 0.26
70	1.81 ± 0.02	94.44 ± 0.23	92.84 ± 0.26
80	1.75 ± 0.02	86.86 ± 0.34	84.23 ± 0.36
90	1.83 ± 0.02	85.69 ± 0.35	84.54 ± 0.36
112.5	1.72 ± 0.02	92.74 ± 0.26	82.08 ± 0.38
145	2.63 ± 0.04	57.42 ± 0.49	49.10 ± 0.49

3.12.2.3 Studies at fixed transverse momentum

The performances of the Straw Tube Tracker in terms of momentum resolution and reconstruction efficiency have been studied also through simulations of 10^4 μ^- single track events generated at the interaction point I. P., with $\phi \in [0°, 360°]$ and $\theta \in [7°, 160°]$.
The tracks have been generated at the following values of fixed p_T: 0.2, 0.4, 0.6, 0.8, 1.0, 1.5, 2.0 and 2.5 GeV/c.
The momentum resolution and efficiency plots as function of the p_t values are shown in Figs. 3.108–3.109; the obtained values are reported in Table 3.17.
As shown by the plots, the momentum resolution is almost linear with p_T, as expected.

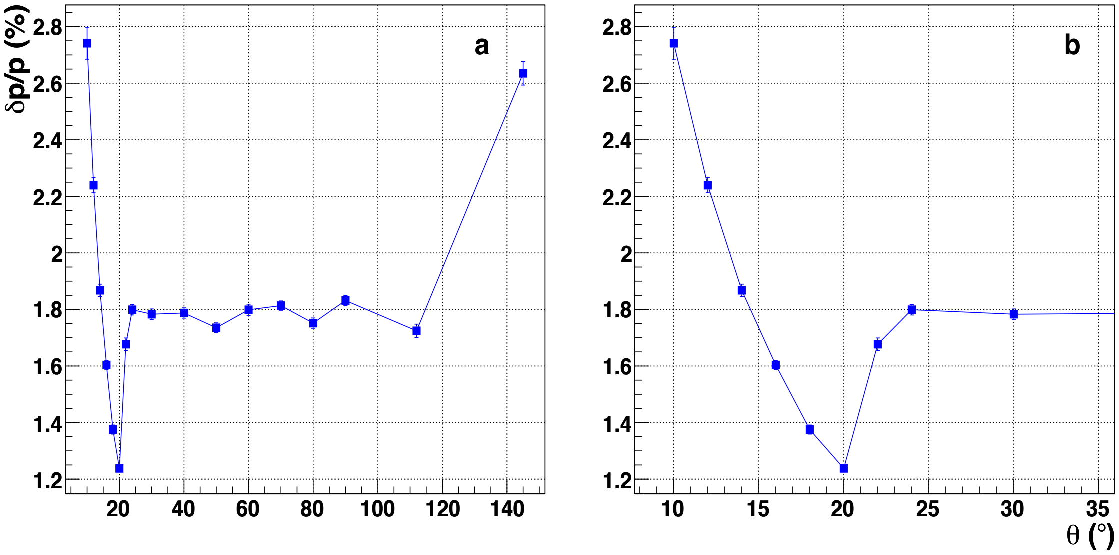

Figure 3.102: Momentum resolution vs. θ starting angle for 1 GeV/c μ^- single track events, in the full angular range $\theta \in [9°, 160°]$ (a) and in the forward region $\theta \in [9°, 35°]$ (b) (see Table 3.14).

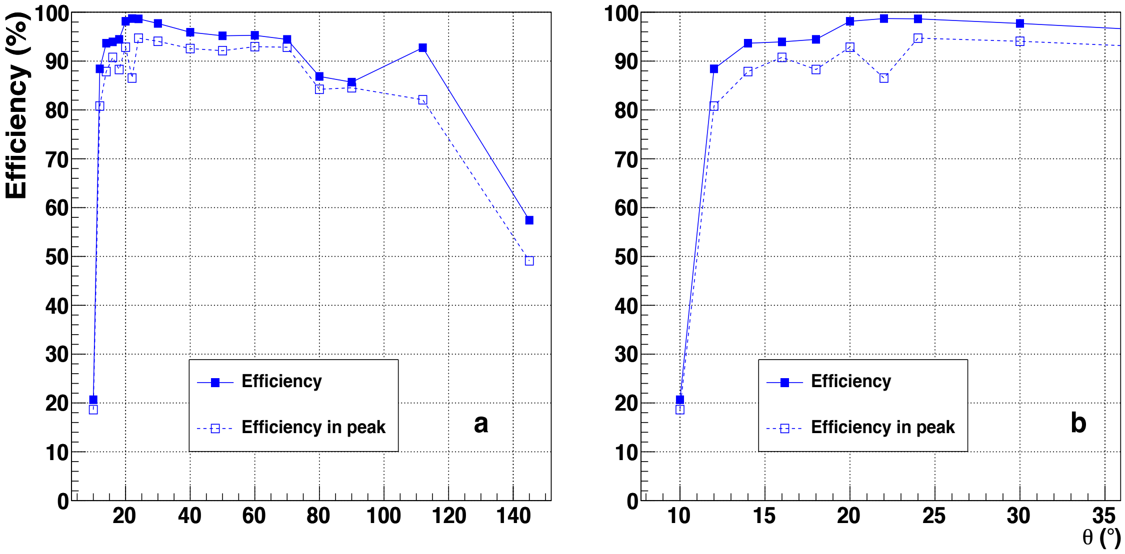

Figure 3.103: Track reconstruction efficiency vs. θ starting angle for 1 GeV/c μ^- single track events, in the full range $\theta \in [9°, 160°]$ (a) and in the forward region $\theta \in [9°, 35°]$ (b) (see Table 3.14).

3.12.2.4 Summary of the results

The performances of the Central Tracker have been investigated through the simulation of different sets of single track (muon) events, generated at the interaction point at different momentum values, polar angle θ and uniform azimuthal angle ϕ.
The tracks have been fitted by applying the procedure summarised in Sec. 3.11. The attention has then been focused on the momentum resolution of the generated particles and on the tracking efficiency.

In all the sets of simulations, the improvements due to the Kalman filter is evident, in particular in terms of momentum resolution: the mean values of the momentum distributions after the Kalman fit are more centered around the correct value than the ones obtained after the global helix fit. In addition, the Kalman distributions are narrower than the helix ones, resulting in better resolution values.

Tests with tracks generated with random θ and ϕ show that the momentum resolution ranges

Table 3.15: Momentum resolution and reconstruction efficiency for 10^4 μ^- single track events generated at 2 GeV/c and fixed θ angle.

θ (°)	Resolution (%)	Efficiency (%)	Efficiency in peak (%)
10	3.13 ± 0.08	23.03 ± 0.42	16.76 ± 0.37
12	2.56 ± 0.03	89.81 ± 0.30	84.48 ± 0.36
14	2.02 ± 0.02	92.49 ± 0.26	88.04 ± 0.32
16	1.66 ± 0.02	93.54 ± 0.25	88.48 ± 0.32
18	1.42 ± 0.02	93.29 ± 0.25	88.09 ± 0.32
20	1.31 ± 0.01	95.64 ± 0.20	90.53 ± 0.29
22	2.19 ± 0.02	95.25 ± 0.21	91.53 ± 0.27
24	2.23 ± 0.02	95.39 ± 0.21	92.33 ± 0.27
30	2.28 ± 0.02	94.07 ± 0.24	91.76 ± 0.27
40	2.32 ± 0.02	94.03 ± 0.24	90.61 ± 0.29
50	2.35 ± 0.02	94.73 ± 0.22	92.01 ± 0.27
60	2.49 ± 0.02	95.16 ± 0.21	93.49 ± 0.25
70	2.46 ± 0.02	93.31 ± 0.25	90.24 ± 0.29
80	2.51 ± 0.02	86.60 ± 0.34	84.06 ± 0.37
90	2.49 ± 0.03	85.74 ± 0.35	84.74 ± 0.38
112.5	2.42 ± 0.02	92.10 ± 0.26	90.10 ± 0.29
145	3.42 ± 0.05	58.28 ± 0.49	50.35 ± 0.49

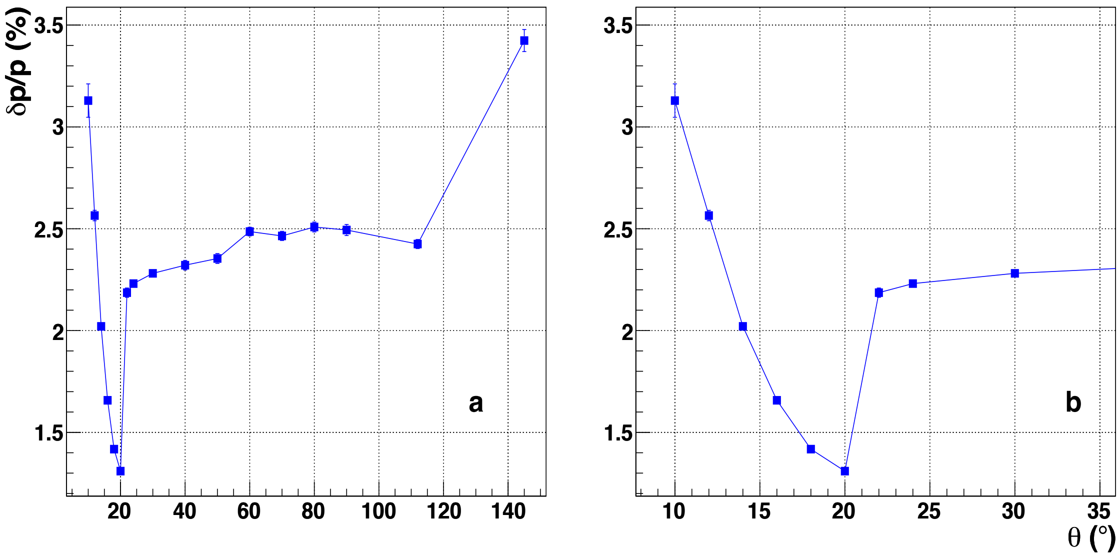

Figure 3.104: Momentum resolution vs. θ starting angle for 2 GeV/c μ^- single track events, in the full angular range $\theta \in [9°, 160°]$ (a) and in the forward region $\theta \in [9°, 35°]$ (b) (see Table 3.15).

from $\sim$ 1.32% in case of 0.3 GeV/c tracks, to $\sim$ 3.61% for 5 GeV/c tracks (Fig. 3.99, Table 3.12).

A more detailed investigation has been performed through the simulation of tracks scanning the whole CT angular region in fine steps. The results are shown in Figs. 3.100–3.107 and reported in detail in Tables 3.13–3.16.
The resolution improves up to $\sim$ 21°, thanks to the increasing number of straw layers traversed by the tracks and to the high precision of the MVD and GEM hits.
In the central angular region, the resolution is almost constant, ranging from 1.3% at 0.3 GeV/c, to 1.8% at 1 GeV/c, 2.3% at 2 GeV/c and 3.6% at 5 GeV/c.

In addition, a set of simulations at fixed values of

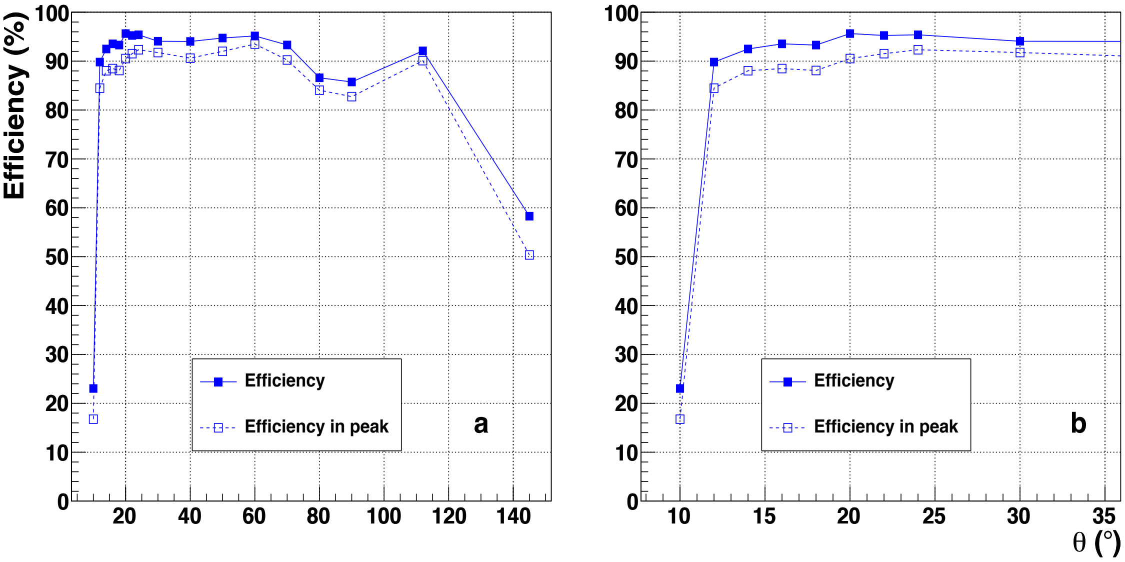

Figure 3.105: Track reconstruction efficiency vs. θ starting angle for 2 GeV/c μ^- single track events, in the full range $\theta \in [9°, 160°]$ (a) and in the forward region $\theta \in [9°, 35°]$ (b) (see Table 3.15).

Table 3.16: Momentum resolution and reconstruction efficiency for 10^4 μ^- single track events generated at 5 GeV/c and fixed θ angle.

θ (°)	Resolution (%)	Efficiency (%)	Efficiency in peak (%)
10	4.68 ± 0.09	22.26 ± 0.41	19.21 ± 0.39
12	3.61 ± 0.03	88.54 ± 0.32	85.21 ± 0.35
14	2.64 ± 0.02	92.53 ± 0.26	89.34 ± 0.31
16	2.05 ± 0.02	92.95 ± 0.25	89.93 ± 0.30
18	1.65 ± 0.02	92.80 ± 0.26	89.54 ± 0.31
20	1.54 ± 0.02	94.18 ± 0.23	89.48 ± 0.31
22	2.93 ± 0.03	93.65 ± 0.24	90.34 ± 0.29
24	3.07 ± 0.03	93.86 ± 0.24	90.56 ± 0.29
30	3.22 ± 0.03	94.06 ± 0.24	91.31 ± 0.28
40	3.49 ± 0.03	94.26 ± 0.23	91.96 ± 0.27
50	3.55 ± 0.03	94.66 ± 0.22	90.81 ± 0.29
60	3.84 ± 0.03	94.72 ± 0.22	92.90 ± 0.26
70	3.91 ± 0.04	92.49 ± 0.26	90.09 ± 0.29
80	3.73 ± 0.04	86.34 ± 0.34	84.32 ± 0.36
90	3.68 ± 0.03	84.99 ± 0.36	82.89 ± 0.38
112.5	3.74 ± 0.03	91.82 ± 0.27	89.84 ± 0.30
145	5.21 ± 0.07	58.36 ± 0.49	52.25 ± 0.49

transverse momentum have been performed. The obtained resolution is reported in Table 3.17 and in Figs. 3.108–3.109. As shown in the plots, the resolution presents an almost linear behaviour as a function of the p_T values, as expected.

3.13 Organization

3.13.1 Organization

3.13.1.1 Production Logistics

The $\overline{\mathrm{P}}$ANDA-STT is a modular detector. It consists of a set of indipendet objects that can be produced and tested indipendently before the final installa-

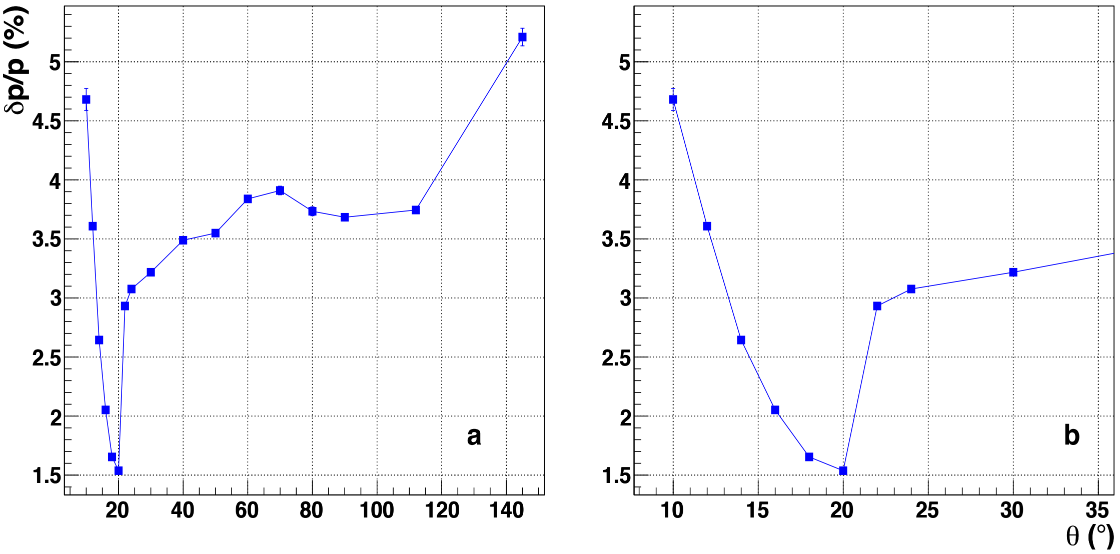

Figure 3.106: Momentum resolution vs. θ starting angle for 5 GeV/c μ^- single track events, in the full angular range $\theta \in [9°, 160°]$ (a) and in the forward region $\theta \in [9°, 35°]$ (b) (see Table 3.16).

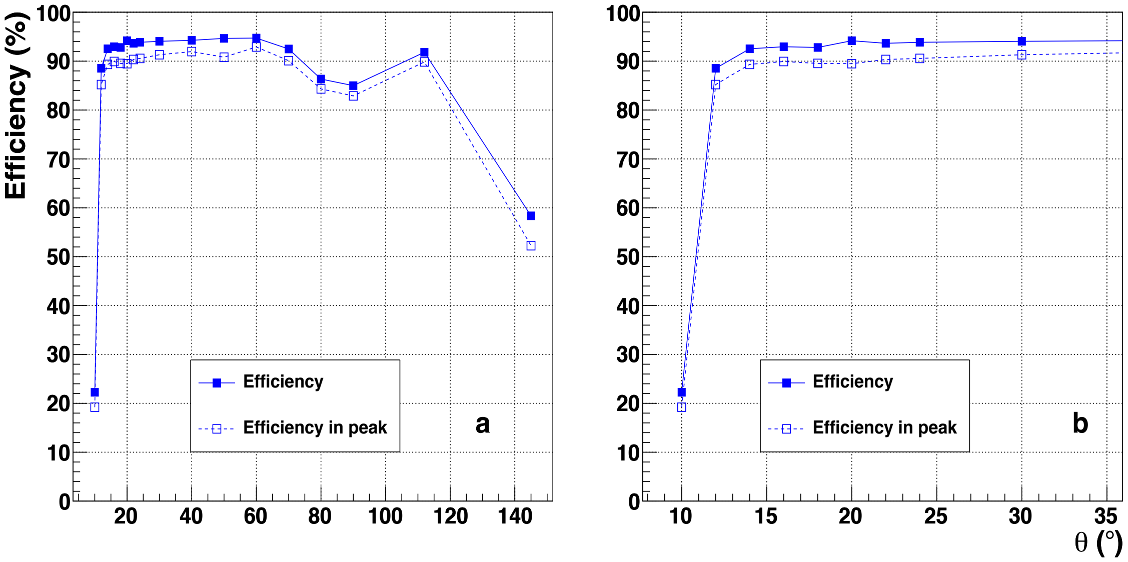

Figure 3.107: Track reconstruction efficiency vs. θ starting angle for 5 GeV/c μ^- single track events, in the full range $\theta \in [9°, 160°]$ (a) and in the forward region $\theta \in [9°, 35°]$ (b) (see Table 3.16).

tion.

The construction procedure (see Sec. 3.4.2) is such that the realization of the whole detector could be easily split on different sites. First of all, single tubes are assembled and tested individually; then multi-layer modules are realized; finally, the modules are mounted in the mechanical support. This will be extremely usefull to reduce the time needed for the detector construction.

Even if the straw tubes are operated with an overpressure of about 1 bar of the gas mixture, they have enough strength to keep the 50 g wire tension even if no gas is inside. Therefore, single tubes can be constructed and stored in proper places to be ready for the multi-layer assembling later on.

At present, either the Forschungszentrum Jülich and the LNF laboratories are equipped with the necessary tools to start the production of straw tubes and modules. They both have a clean room (10000 class), a v-shaped reference plane (Fig. 3.110) and the same expertise for starting a mass production. The need of a clean room, it is

Table 3.17: Momentum resolution and reconstruction efficiency for 10^4 μ^- single track events generated at fixed transverse momentum.

p_t (GeV/c)	Resolution (%)	Efficiency (%)	Efficiency in peak (%)
0.2	1.21 ± 0.01	71.66 ± 0.45	64.00 ± 0.48
0.4	1.26 ± 0.01	82.76 ± 0.38	79.57 ± 0.40
0.6	1.43 ± 0.01	86.37 ± 0.34	83.16 ± 0.37
0.8	1.59 ± 0.01	85.47 ± 0.35	83.08 ± 0.37
1.0	1.79 ± 0.02	86.35 ± 0.34	81.51 ± 0.39
1.5	2.24 ± 0.02	85.37 ± 0.35	83.76 ± 0.37
2.0	2.49 ± 0.02	85.43 ± 0.35	84.37 ± 0.36
2.5	2.79 ± 0.02	85.34 ± 0.35	84.43 ± 0.36

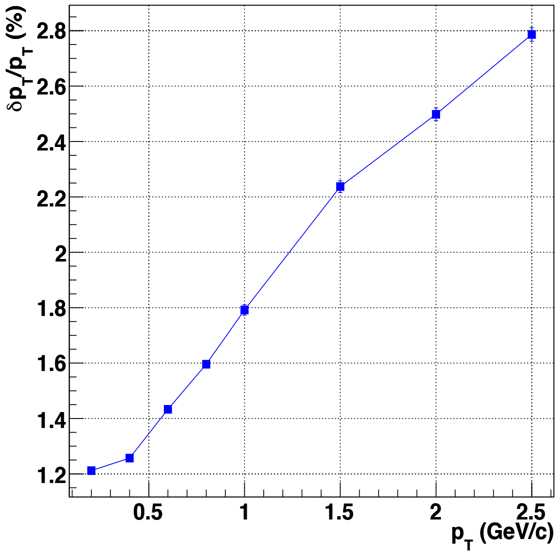

Figure 3.108: Momentum resolution vs. p_T for μ^- single track events, in the angular ranges $\phi \in [0°, 360°$ and $\theta \in [7°, 160°]$ (see Table 3.17).

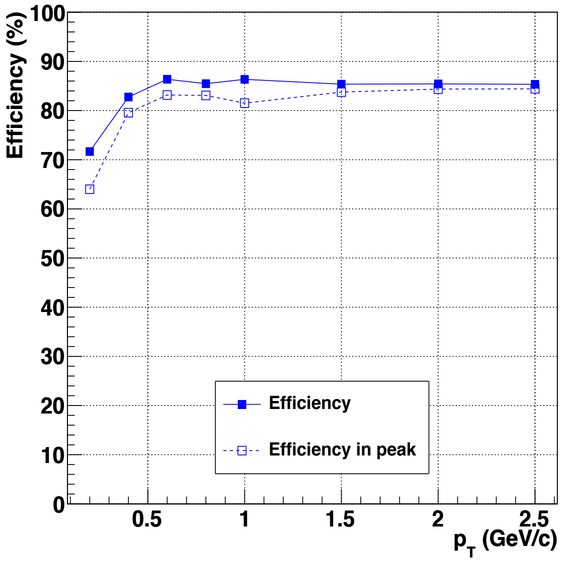

Figure 3.109: Reconstruction efficiency vs. p_T for μ^- single track events, in the angular ranges $\phi \in [0°, 360°$ and $\theta \in [7°, 160°]$ (see Table 3.17).

actually not absolutely necessary. Straw tube components: cathodes, pins, end-plugs, etc., have to be cleaned before starting the assembling procedure. Thus, if this work is realized in an environment where the dust concentration is under control, this could be done once at all before starting the single tubes production. If a clean room is not available, greater care has to be placed in this cleaning phase, that has to precede immediatly the straw tube assembly. The only needful tool to produce straw tube modules is the v-shaped reference plane. This object is a precisely manufactured mechanical plate that guarantees that the spacing of the straw wires within a multi-layer is the needed one (± 50 μm).

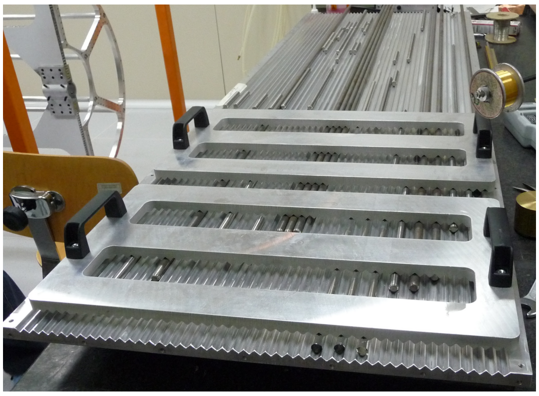

Figure 3.110: v-shaped reference plate for multi-layer assembly.

3.13.1.2 Safety

The design details and construction of the STT including the infrastructure for operation will be done according to the safety requirements of FAIR and the European and German safety regulations. All electrical equipment and gas systems will comply with the legally required safety code and concur to standards for large scientific installations to ensure the protection of all personnel working at or close to the components of the PANDA experimental facility. Hazardous voltage supplies and lines will be marked visibly and protected from damage by any equipment which may cause forces to act on them. All supplies will be protected against overcurrent and overvoltage and have appropriate safety circuits and fuses. All cabling and connections will use non-flammable halogen-free materials according to up-to-date standards and will be dimensioned with proper safety margins to prevent overheating. A safe ground scheme will be employed throughout all electrical installations of the experiment. Smoke detectors will be mounted in all appropriate locations. The gas system is based upon non-flammable gasses and thus do not pose a fire hazard. The maximum pressure of the gas will be regulated, and the system is designed such that a sudden failure of one tube (operating at maximally 2 Bar) can not damage the adjacent tubes (that have equal or higher pressure than the escaping gas), and thus a chain reaction is ruled out. Appropriate measures will be taken during installation and maintenance to avoid damage to or by the STT. The outer foil will protect the device against potential condensation risks from other components of PANDA. More specific safety considerations are discussed in the respective sections throughout this document.

3.13.1.3 Timeline

The projected timeline of the STT construction is based on the experience gained during the R&D and prototyping phase of the STT project and similar, former detector projects of the different group institutions. In particular the construction experience from the Straw Tube Tracker at COSY, consisting of about 3200 straws in total and similar assembly techniques, is a major input for the definition of the construction packages and time scales for the P̄ANDA-STT realization.

The timeline of the STT construction consists of four main periods: the workout of the final design; the main construction phase; the final assurance test of the assembled STT with cosmics; and the pre-assembly of the STT in the PANDA central spectrometer. The detailed timeline shown in Fig. 3.111 lists the different construction items and their projected time slots. After the decision of the central tracker option is made the funding applications will start and workshop time slots for the project will be booked.

The first phase of the STT construction with the definition of the complete final design has already started and will be finished by the middle of next year, 2012. Here, all designs, the mechanical parts with straws and frame structure as well as the electronic readout parts, cables, and systems, have to be workout in detail. The integration of the detector in the P̄ANDA central spectrometer will be made and the main dimensions, environment conditions, and requirements will be defined and assigned. Few aspects are still under discussion concerning the final mechanical layout, including cable and services routing, and the final electronic readout design. The latter decision between the two current electronic readout options will be based on further test measurements with existing prototype setups, consisting of up to 400 straws. Within the next 12 months this decision will be made, latest by the middle of next year, 2012.

At the end of the design phase all technical specifications are fixed and technical drawings are prepared to start the tendering and order processes at the external production companies. Since most of the involved production companies have been already contacted during the R&D phase of the project or during former similar projects, we estimate not more than about 18 months for sending out tenders, placing orders, and delivery times for the external components.

The main construction phase of the STT assembly will take about 30 months for the mass production of 6000 straw tubes (about 30 % spare), gluing of the straw layers, construction of the mechanical frame, and insertion of the straw layers in the frame structure. The assembly will be split between the two main involved laboratories, Forschungszentrum Jülich and INFN Frascati. At both sites clean rooms (class 5) are available for the construction works. The straw mass production already includes assurance tests of gas leakage and wire tension measurements of every assembled straw. Individual straws showing a gas leakage, deviation from the nominal wire tension, or a broken wire are rejected. For the previous prototype constructions with about 1000 straws, the fraction of straws showing such failures was on the low percent level.

The straws are glued to the axial and stereo layer modules with integrated gas manifolds and elec-

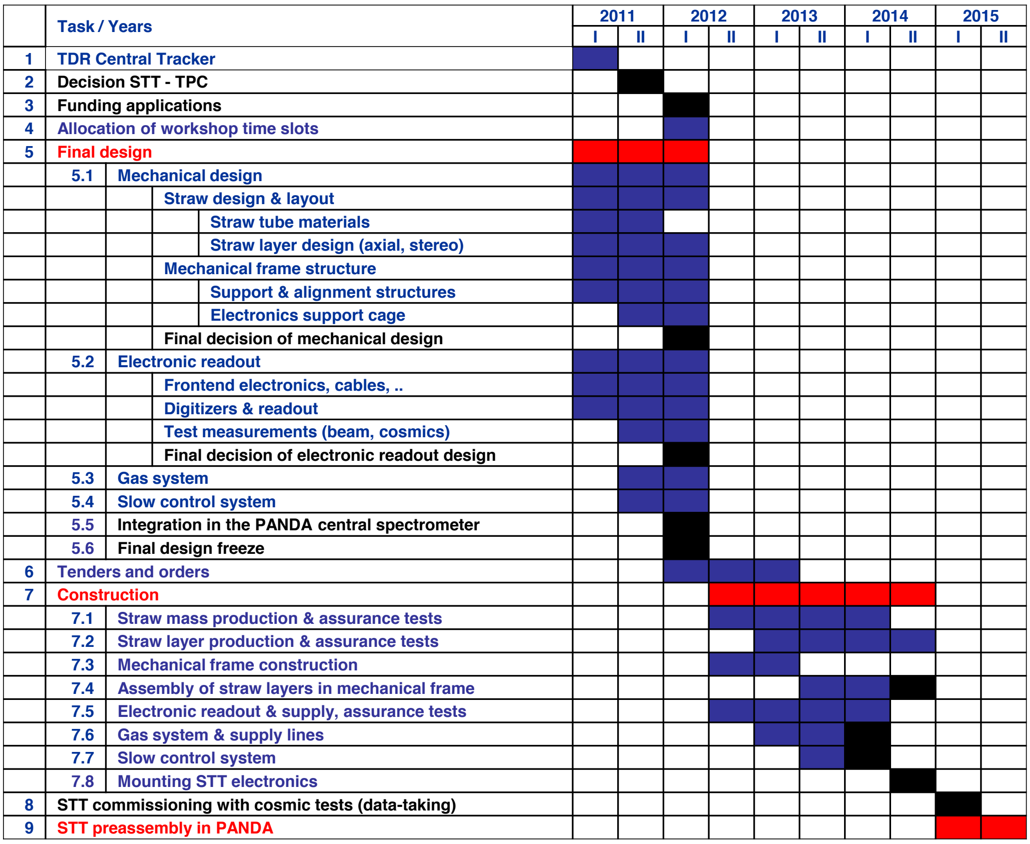

	Task / Years	2011		2012		2013		2014		2015	
		I	II	I	II	I	II	I	II	I	II
1	TDR Central Tracker	🟦									
2	Decision STT - TPC		⬛								
3	Funding applications			⬛							
4	Allocation of workshop time slots			🟦							
5	Final design	🟥	🟥	🟥							
5.1	Mechanical design	🟦	🟦	🟦							
	Straw design & layout	🟦	🟦	🟦							
	Straw tube materials	🟦	🟦								
	Straw layer design (axial, stereo)	🟦	🟦	🟦							
	Mechanical frame structure	🟦	🟦	🟦							
	Support & alignment structures	🟦	🟦	🟦							
	Electronics support cage		🟦	🟦							
	Final decision of mechanical design			⬛							
5.2	Electronic readout	🟦	🟦	🟦							
	Frontend electronics, cables, ..	🟦	🟦	🟦							
	Digitizers & readout	🟦	🟦	🟦							
	Test measurements (beam, cosmics)		🟦	🟦							
	Final decision of electronic readout design			⬛							
5.3	Gas system		🟦	🟦							
5.4	Slow control system		🟦	🟦							
5.5	Integration in the PANDA central spectrometer			⬛							
5.6	Final design freeze			⬛							
6	Tenders and orders			🟦	🟦	🟦					
7	Construction				🟥	🟥	🟥	🟥	🟥		
7.1	Straw mass production & assurance tests				🟦	🟦	🟦	🟦			
7.2	Straw layer production & assurance tests					🟦	🟦	🟦	🟦		
7.3	Mechanical frame construction				🟦	🟦					
7.4	Assembly of straw layers in mechanical frame						🟦	🟦	⬛		
7.5	Electronic readout & supply, assurance tests				🟦	🟦	🟦	🟦			
7.6	Gas system & supply lines					🟦	🟦	⬛			
7.7	Slow control system						🟦	⬛			
7.8	Mounting STT electronics								⬛		
8	STT commissioning with cosmic tests (data-taking)									⬛	
9	STT preassembly in PANDA									🟥	🟥

Figure 3.111: Timeline for the STT realization. Milestones are marked in black.

tronic coupling boards. For the final assurance test of all straws in a layer module, the module is flushed with an Ar/CO$_2$ gas mixture, straws are set on high voltage, a test board containing a preamplifier circuit is connected to the coupling boards and the signals from cosmic tracks are checked to identify dead or improper straws. Bad identified straws are removed from a layer module and replaced by single new straws. The modular layout of the STT allows to carry out the most time consuming construction steps of the straw mass production and layer module assembly highly in parallel. As soon as the first hundreds straws are produced and tested, we can start with the construction of the first layer modules. After the completion of the mechanical frame structure the layer modules are inserted and fixed to the frame.

In parallel to the mechanical STT assembly the electronic parts, cables, and readout boards will be produced and the complete readout system will be set up. After a test of all electronic channels with test pulses, the readout will be mounted in the STT mechanical frame structure and connected to the straws. By the end of 2014 the construction phase will be finished including the setup of the gas system and slow control system.

By the beginning of 2015 the final commissioning of the full STT detector will be done with datatakings of cosmic ray tracks to set up the whole electronic readout and to calibrate the STT geometry with reconstructed tracks. After finishing these tests the detector will be ready for installation and pre-assembly in the PANDA central spectrometer.

3.13.1.4 Work packages and Contributing Institutes

The design, construction and installation of the STT will be performed by a number of institutions which have gained specific expertise in past and ongoing large scale experiments at several accelerator facilities. The responsibilities for the various work packages are listed in Table 3.18, in which the coordinating group of the task is denoted by boldface. A short summary of the participating groups, their principal investigators and available facilities

Table 3.18: work package list with involved institutions

work package	involved institutes
Straw tube materials	**FZ-J** LNF
Mechanical frame	**LNF** FZ-J
Front End Electronics, DAQ, Low and High voltages	**FZ-J** AGH **JU** IF-J
Crates, cables	LNF FZ-J IFIN-HH
Slow control	**IFIN-HH**
Gas system	**LNF**
Monitoring calibration	**PV** Fe

is given below:

- IFIN-HH Bucharest, Romania (D. Pantea, M. Bragadireanu) (**IFIN-HH**);
- IFJ PAN, Cracow, Poland (P. Kulessa, K. Pysz) (**IFJ**);
- Jagiellonian University of Cracow, Poland (J. Smyrzki, P. Salabura, M. Kajetanowicz) (**JU**);
- AGH Cracow, Poland (M. Idzik), (**AGH**);
- INFN Frascati, Italy (**LNF**) (B. Dulach, P. Gianotti, V. Lucherini, E. Pace);
- FZ Jülich, Germany (H. Kleines, G. Kemmerling, J. Ritman, P. Wintz) (**FZ-J**);
- INFN and Univ. of Pavia, Italy (**PV**) (A. Rotondi, P. Montagna);
- INFN and Univ. of Ferrara, Italy (**Fe**) (D. Bettoni, M. Savriè).

References

[1] Mylar, polyester film, registered trademark of DuPont, `www.dupont.com`.

[2] Thermo-plastic, Acrylonitrile-Butadiene-Styrene.

[3] P. Wintz, in *AIP Conf. Proc, Alushta, Ukraine*, volume 698, pages 789–792, 2004.

[4] L. Aysto et al., (2001), Conceptual Design Report, GSI, Darmstadt.

[5] R. Veenhof, *GARFIELD, Simulation of gaseous detectors*, version 7.04 edition, CERN Program library write-up W 5050.

[6] C. Avanzini et al., Nucl. Instrum. Meth. **A449**, 237 (2000).

[7] L. Benussi et al., Nucl. Instrum. Meth. **A419**, 648 (1998).

[8] E. Basile et al., IEEE Trans. Nucl. Sci. **53**, 1375 (2006).

[9] Pattex plastik is an Henkel product, `www.pattex.de/Pattex_Plastic.1514.0.html`.

[10] UHU endfest 300, UHU GmbH & Co. KG - P.O. Box 1552, D-77813 Bühl, `www.uhu.de`.

[11] Loctite 408.

[12] Bronkhorst High-Tech,Nijverheidsstraat 1A, NL-7261 AK Ruurlo (NL). http://www.bronkhorst.com.

[13] C. Ugur, GSI annual report 2010.

[14] F. Sauli, *Principles of operation of multiwire proportional and drift chambers*, Technical report, CERN 77-09, Geneva, 1977.

[15] F. Lapique and F. Piuz, Nucl. Instrum. Meth. **175**, 297 (1980).

[16] J. Fischle, H. Heintze and B. Schmidt, Nucl Instrum. Meth. **A301**, 202 (1991).

[17] J. Allison et al., Nucl. Instrum. Meth. **133**, 325 (1976).

[18] K. Lassilla-Perini and L. Urban, Nucl. Instr. Meth **A362**, 416 (1995).

[19] Geant3 manual, Technical report, 1993, CERN program library W5013.

[20] *GEANT4: An object oriented toolkit for simulation in HEP*, Technical report, Geneva, 1998, `http://geant4.cern.ch`.

[21] W. Blum and R. Rolandi, *Particle detection with drift chambers*, Springer Verlag, Berlin, 1994.

[22] S. Biagi, Nucl. Instrum. Meth. **A421**, 234 (1999).

[23] P. Branchini et al., IEEE Trans. on Nuclear Sc. **53**, 317 (2006).

[24] W. Riegler et al., Nucl. Instrum. Meth **A443**, 156 (2000).

[25] G. Avolio et al., Nucl. Instrum. Meth. **A523**, 309 (2004).

[26] A. Biscossa et al., Nucl. Instrum. Meth. **A419**, 331 (1998).

[27] M. Bellomo et al., Nucl. Instrum. Meth. **A573**, 340 (2007).

[28] S. Costanza, *Design of the Central Tracker of the $\overline{\mathsf{P}}$ANDA experiment*, PhD thesis, Università degli Studi di Pavia, 2010.

[29] K. Pysz, *Report on activities performed in the frame of external Research and development Program (FFE) of the Forschungszentrum Jülich*, 2007, Jülich.

[30] K. Pysz, V. Serdyuk, P. Kulessa, H. Ohm, and P. Wintz, *First measurements of energy-loss using $\overline{\mathsf{P}}$ANDA–type straw tubes*, Technical report, Forschungszentrum Jülich, 2010, IKP Annual Report 2009.

[31] V. Serdyuk et al., *A new setup for measuring the energy loss of particles in the $\overline{\mathsf{P}}$ANDA STT*, Technical report, Forschungszentrum Jülich, 2010, IKP Annual Report 2009.

[32] B. Aubert et al., Nucl. Instr. and Meth. **A479**, 1 (2002).

[33] M. Ablikim et al., Nucl. Instr. and Meth. **A614**, 345 (2010).

[34] G. Agakishiev et al., Eur. Phys. J. **A41**, 243 (2009).

[35] B. Dolgoshein, Nucl. Instr. and Meth. **A433**, 533 (1999).

[36] V. Bashkirov et al., Nucl. Instr. and Meth. **A433**, 560 (1999).

[37] T. Akesson et al., Nucl. Instr. and Meth. **A474**, 172 (2001).

[38] E. Badura et al., Particles and Nuclei, Letters **1**, 73 (2000).

[39] M. Newcomer, IEEE Trans. Nucl. Sci. **40**, 630 (1993).

[40] M. Hohlmann, C. Padilla, N. Tesch, and M. Titov, Nucl.Instrum.Meth. **A494**, 179 (2002).

[41] T. Ferguson et al., Nucl.Instrum.Meth. **A478**, 254 (2002).

[42] M. Titov, arXiv:physics/0403055v2 (2004).

[43] A. e. "Gillitzer, *Strangeness Physics at COSY-TOF*, Technical report, Forschungszentrum Jülich, 2007, COSY Proposal no. 178.

[44] P. "Wintz, *Commissioning of the COSY-TOF Straw Tube Tracker and the silicon-microstrip Quirl*, Technical report, Forschungszentrum Jülich, 2007, COSY Proposal no. 179.

[45] `http://root.cern.ch/drupal/content/vmc`.

[46] I. Hřivnàčovà et al., (2003).

[47] $\overline{\mathsf{P}}$ANDA Computing Group, *A data analysis and simulation framework for the $\overline{\mathsf{P}}$ANDA collaboration*, Technical report, 2006, Scientific Report GSI.

[48] $\overline{\mathsf{P}}$ANDA Computing Group, *Status of the pandaroot simulation and analysis framework*, Technical report, 2007, Scientific Report GSI.

[49] A. Wronska, Simulation of the $\overline{\mathsf{P}}$ANDA experiment with pandaROOT, in *Proceedings of MENU2007*, page 307, eConf C070910, 2007.

[50] V. Innocente et al., CERN Program Library **W5013-E** (1991).

[51] R. E. Kalman, J. Basic Eng. **82**, 34 (1961).

[52] R. Fruhwirth et al., Nucl. Instr. and Meth. **A262**, 444 (1987).

[53] A. Fontana, P. Genova, L. Lavezzi, and A. Rotondi, *Track following in dense media and inhomogeneous magnetic fields*, Technical report, 2007.

[54] L. Lavezzi, *The fit of nuclear tracks in high precision spectroscopy experiments*, PhD thesis, Università degli Studi di Pavia, 2007.

[55] C. Höppner et al., Nucl. Instrum. Meth. **A620**, 518 (2010).

[56] R. Fruhwirth et al., *Data Analysis Techniques For High Energy Physics*, Cambridge University Press, 1990.

[57] V. Innocente and E. Nagy, Nucl. Instrum. Meth. **A324**, 297 (1993).

[58] G. Schepers et al., *Particle Identification at $\overline{P}$ANDA*, Technical report, 2009, Report of the PID TAG.

[59] `http://www.slac.stanford.edu/~lange/EvtGen`.

[60] A. Galoyan and V. V. Uzhinsky, AIP Conf.Proc. **796**, 79 (2005).

4 The Time Projection Chamber

4.1 Introduction

A Time Projection Chamber (TPC) [1] with its low material budget constitutes an ideal device for tracking charged particles in 3-dimensional space, fulfilling all the requirements on $\overline{\mathsf{P}}$ANDA tracking. TPCs have been and currently are successfully employed in many experiments such as PEP-4 [2], ALEPH [3], DELPHI [4], NA49 [5, 6], STAR [7, 8], ALICE [9]. In its standard form, a TPC consists of a large gas-filled cylindrical volume inside a solenoid magnetic field, surrounding the interaction point, and covering the full 4π solid angle [10]. Fig. 4.1 shows a schematic view of a TPC.

An electric field along the cylinder axis separates positive gas ions from electrons created by ionizing particles traversing the gas volume. The primary electrons then drift towards the readout anode located at end cap of the cylinder, the transverse diffusion being reduced by the strong magnetic field parallel to the drift direction. At the end cap avalanche amplification occurs typically in Multiwire Proportional Chambers (MWPCs), the induced signals being detected by an arrangement of pad electrodes measuring the projection of the track onto the end plane. The third coordinate of the track comes from a measurement of the drift time of each primary electron cluster, requiring a precise knowledge of the electric drift field in the chamber. Distortions of the electric field in the drift volume due to the accumulation of space charge from primary ions or avalanche ions drifting back into the drift volume deteriorate the resolution and have to be kept at a minimum. To this end all TPCs up to now have been operated in a pulsed mode, where an electrostatic gate to the readout region is opened only when an interaction in the target has occurred, and is closed immediately thereafter, preventing avalanche ions from penetrating the drift volume.

Owing to the beam properties at the High Energy Storage Ring (HESR) of FAIR, with its high luminosity of $2 \cdot 10^{32}\,\mathrm{cm}^{-2}\,\mathrm{s}^{-1}$ corresponding to $2 \cdot 10^{7}$ $\bar{\mathrm{p}}$ annihilations per second, the TPC in $\overline{\mathsf{P}}$ANDA has to operate continuously, i. e. the technique of gating cannot be applied. Ions created in the multiplication region have to be prevented from drifting back into the drift volume by other means.

This will be achieved by using Gas Electron Multiplier (GEM) [11] foils as charge amplifier instead of conventional MWPCs. The GEM consists of a $50\,\mu$m thin insulating Polyimide foil with Cu-coated surfaces, typically $2-5\,\mu$m thick. The foil is perforated by photo-lithographic processing, forming a dense, regular pattern of (double-conical) holes. Usually the holes have an inner diameter of $\sim 50\,\mu$m. Figure 4.2 shows an electron microscope photograph of a GEM foil, also indicating the typical dimensions.

The small dimensions of the amplification structures lead to very large field strengths $\mathcal{O}(50\,\mathrm{kV/cm})$ inside the holes of the GEM foil when a moderate voltage difference of typically $300-400\,\mathrm{V}$ is applied between the metal layers, sufficient for avalanche creation inside the GEM holes. The avalanche electrons are extracted from the bottom side of the foil, and can be collected or transferred to the next amplification stage. Typically three GEM foils are

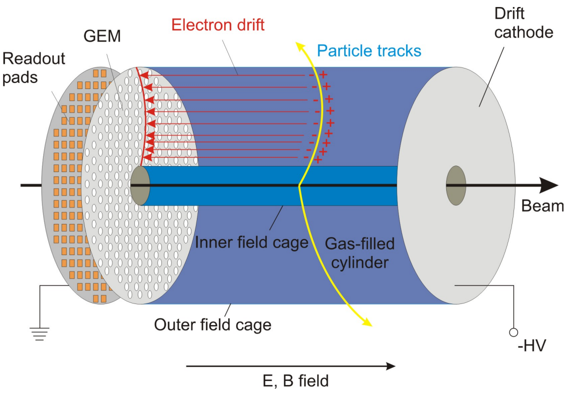

Figure 4.1: Schematic view of a GEM-based TPC.

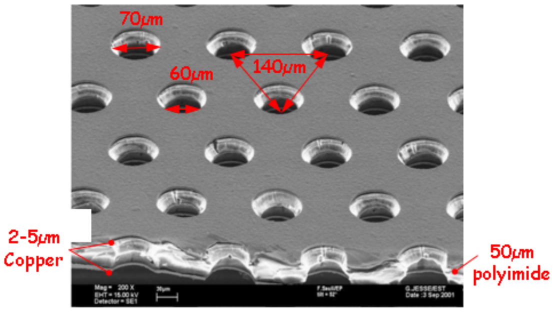

Figure 4.2: Electron microscope photograph of a GEM foil with typical dimensions.

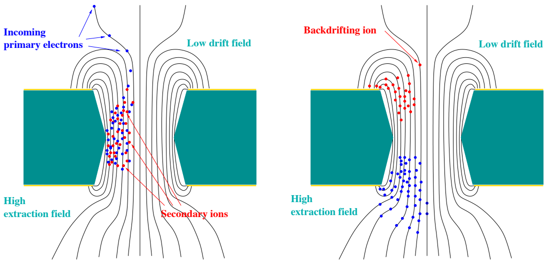

Figure 4.3: Working principle of a GEM: (a) electrons are guided into the holes by the low drift field, where avalanches of electron-ion pairs are generated. (b) The asymmetric field configuration of low drift field and higher extraction field together with the small ion mobility lead to efficient back flow suppression.

combined in a stack, leading to effective gains (see Eq. 4.10) of $\sim 10^4$ and at the same time guaranteeing a stable operation without the occurrence of discharges [12].

The back flow of ions from the amplification region is suppressed in a configuration with asymmetric electric fields above and below the GEM foil, as shown in Fig. 4.3. Electrons are guided into the GEM holes by the drift field, where they produce an avalanche. The ions created in the avalanche are mainly collected on the top side of the GEM foil, if the extraction field is much higher than the drift field.

Detectors based on GEM amplification have been pioneered by the COMPASS experiment at CERN [13, 14, 15, 16], and are now routinely used in several particle physics experiments like LHCb [17], PHENIX [18], and TOTEM [19]. New applications include the use of GEM-based detectors in KLOE-2 [20] and CMS [21]. Its main features, rendering possible a continuously operating TPC, are:

- suppression of ion back flow in an asymmetric field configuration,
- high granularity,
- high rate capability,
- no preferred direction (as for wires), therefore isotropic $\boldsymbol{E} \times \boldsymbol{B}$ effects.

The GEM readout scheme is also envisaged for the TPC of the International linear Collider ILC [22], and combined efforts are currently concentrating on further developing this technique. The increased granularity of such a detector necessarily leads to larger event sizes and requires substantial data reduction already at the level of front-end electronics.

The ungated, continuous operation mode of the TPC at the envisaged event rates at $\overline{\mathsf{P}}$ANDA gives rise to about 3000 tracks which are superimposed in the drift volume at any given time. The association of these tracks to distinct physics events ("event deconvolution") requires fast online tracking capabilities of the data acquisition system.

In conclusion, a TPC read out by the Gas Electron Multiplier (GEM) will fulfill all the requirements to the Central Tracker of the $\overline{\mathsf{P}}$ANDA experiment. Its stand-alone momentum resolution is sufficiently high such that also the momenta of tracks not traversing the MVD, like from Λ decays, can be determined with the required precision. Its low material budget will minimize multiple scattering of charged particles and photon conversion, thus optimizing the resolution of the spectrometer both for charged and neutral particles. The large number of 3-D space points ($\sim 50 - 100$) measured for each track greatly simplifies pattern recognition in a complex and dense environment. This is especially important for low-momentum particles which do not leave the Central Tracker, but spiral with a small radius of the order of a few cm along the z direction, and for the detection of neutral particle decays or kinks. Monte-Carlo simulations have shown that about 40% of charmonium decays have tracks going in forward direction, i.e. passing the Central Tracker through its forward end cap. In this region of phase space, the bending power of the solenoid magnet is small and the number of points measured on a given track is small. Therefore it is vital that the Central Tracker is able to contribute with a substantial number of hits, also providing z information for these hits. Finally, the TPC will contribute to the identification of charged particles by measuring the specific energy loss, $\mathrm{d}E/\mathrm{d}x$ of each particle track, especially at momenta below $1\,\mathrm{GeV}/c$, which is essential for background suppression.

4.2 General Detector Layout

4.2.1 Design rules

Throughout the layout the following goals where formulated and respective general design rules were deduced from them.

Minimization of risks and failures will be done by maximizing the modularity of functional units and keeping diversity in the design wherever it is possible and feasible. We try to minimize any bias on physical quantities by reducing the material budget of all structural elements maximizing at the same

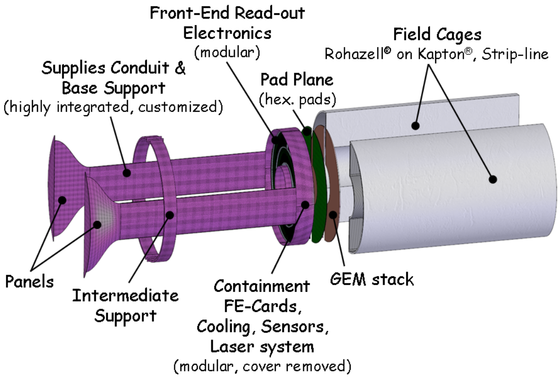

Figure 4.4: Conceptual Design of the $\overline{\text{P}}$ANDA GEM-TPC; only the basic modules of the detector are shown.

time the geometrical yield, acceptance and active volume. In all phases of the life cycle of the detector system such as: design, part production, mounting, adjustment, calibration, operation and maintenance we try to minimize the required effort, work load and costs. This immediately calls for flexibility in the overall design and a maximum compactness of all modules. We try to take advantage of symmetries especially with respect to the required support structures, and make use of pre-fabrication and premounting as much as reasonably possible.

4.2.2 Detector structure

The envisaged sections of the $\overline{\text{P}}$ANDA GEM-based TPC are visualized schematically in Fig. 4.4. They are composed of:

- A detection volume where traversing particles ionize the gaseous detection medium producing positive and negative charge carriers in an electrical drift field. This field, which is oriented parallel to the beam-axis, is spawned between a cathode end cap downstream of the target position and the anode layer upstream of it. A field-defining system, the so called 'field cage', is required to keep the gradient of the field constant throughout the active volume. All electrode structures, made by metallic material patterned on a carrier material, are optimized in terms of achievable field homogeneity and material budget (see Sec. 4.3).

- An amplification stage that serves to multiply the ionization electrons after they have traversed the drift volume. In case of a GEM-TPC this is done by a GEM stack which is composed of a plane-parallel set of GEM foils oriented perpendicular to the beam axis (see Sec. 4.4 for details).

- A patterned electrode structure on the anode layer, the so called pad plane (see Sec. 4.4.4), where the signals corresponding to the collected charges are detected.

- The electronic readout system (see Sec. 4.8).

- The support and alignment structures and its fixation points.

- The supplies like gaseous and fluid media lines, low and high voltage and the respective cables, pipes and terminals (panels).

- A system of various detector-near sensors monitoring all relevant operation parameters like temperature, pressure and flow of gas and cooling media, high and low voltages (see Sec. 4.7).

4.2.3 Overall configuration

The configuration of the $\overline{\text{P}}$ANDA GEM-TPC is shown in Fig. 4.4 and Fig. 4.5. The whole structure will be self-supporting; the overall center of gravity of the set up will be close to the backward end-cap. As a consequence, the external support structures may be minimized, mainly requiring only a few fixation points: one carrying the main load of approximately 150 kg (field cage: 2 × 22 kg, rest: 106 kg) including cabling and terminals, one on the intermediate support structure giving the orientation, and one installed in the vicinity of the cathode end-cap. The fixation points are represented by the red circles in Fig. 4.5.

Due to the target tube traversing the TPC vertically, the cylindrical field cage of the GEM-TPC is split into two identical and independent volumes of half-circular cross-section. They are both flanged to a common support structure as shown in Fig. 4.5. The whole apparatus therefore falls into three mechanically separable parts:

- Two half cylinder-like individual vessels containing the detection gas, with an inner bore of 300 mm diameter, an outer diameter of 833 mm, and a length of 1554 mm. With a structural thickness of the barrel walls of 11 mm, and of the end-cap of 15 mm, the active gas volume extends from an inner diameter of 322 mm to an outer diameter of 811 mm, with a length of 1539 mm. A volume-to-surface ratio of the active drift volume of less than 0.1 m is obtained on the base of the geometry and the

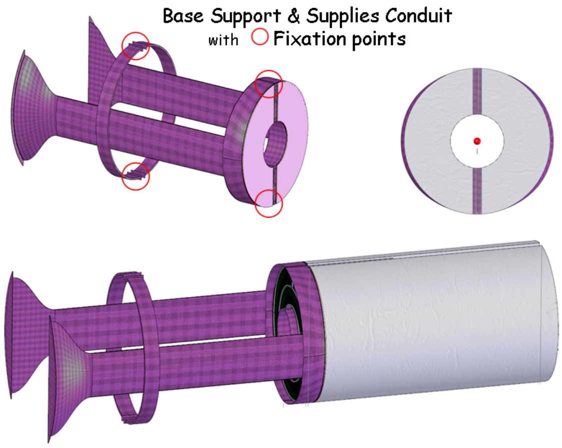

Figure 4.5: Conceptual Design of the $\overline{\mathrm{P}}$ANDA GEM-TPC. The supplies-conduit and base support is made from one piece of carbon reinforced plastics (CRP) to assure stability and proper adjustment. The upper right part shows the front view visualizing the shape of the two independent drift volumes mounted on the same support. The lower part of the figure shows the overall assembly of the TPC.

thicknesses of the walls of the detection volume (see Sec. 4.3.1).

- The base support comprising the structural elements like e.g. support, supplies, readout, and amplification stage; it has an overall length of about 1.9 m in beam direction including the readout electronics as well as the supplies and patch panels.

The overall length of the TPC will be 1704 mm without the support and conduit structures and 3454 mm including them.

We have foreseen a security shell of additional 4 mm free space enclosing all the elements shown in Fig. 4.5 which is not shown there. Furthermore, we are aiming for dimensional accuracies of about 0.1 mm in all parts to be manufactured.

Fig. 4.6 and Fig. 4.7 show a schematic side and top view of the active volume of the $\overline{\mathrm{P}}$ANDA GEM-TPC.The angular acceptance of the detector with respect to the nominal position of the target point will range from 8 ° to 158 ° in polar angle, and from 5 ° to 175 ° and from 185 ° to 355 ° in azimuthal angle with a cone-shaped cut-out in the forward and backward direction of 1.8 ° and 5.3 °, respectively. These numbers are also compiled in Tab. 4.1.

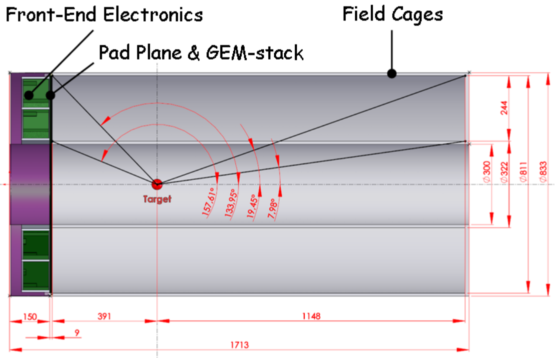

Figure 4.6: Schematic side view of the $\overline{\mathrm{P}}$ANDA GEM-TPC describing the positioning inside the Target Spectrometer and the resulting acceptance in the (y,z)-plane.

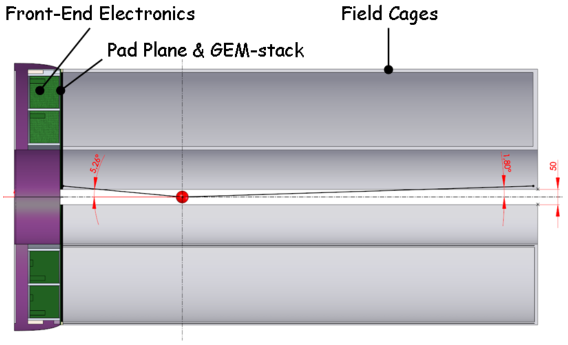

Figure 4.7: Schematic top view of the $\overline{\mathrm{P}}$ANDA GEM-TPC describing the positioning inside the Target Spectrometer and the resulting acceptance in the (x,z)-plane.

Table 4.1: Compilation of basic figures of the $\overline{\mathrm{P}}$ANDA GEM-TPC. The numbers in brackets give effective values taking into account structural and functional thicknesses, e.g. of walls.

Feature	Value (mm, kg, °)
Inner diameter	300 (322)
Outer diameter	833 (811)
Length of drift	1554 (1539)
Length (z) of readout electronics	150
Length (z) of detector	1704
Length (z) overall	3454
Angular acceptance θ (y, z)	8 - 158
Angular acceptance ϕ (x, y)	5 - 175
Weight	150

The rear view of the GEM-TPC in beam direction is shown in Fig. 4.8. The readout structure will be built out of one piece. This way, the routing necessary for the number of channels envisaged is best accommodated (see Sec. 4.4.4); the cooling structures and the overall mounting and adjustment can be simplified saving valuable space and material inside the magnetic field. The stiff containment will be made from carbon reinforced plastics (CRP) with a shape conformal to the volume available for the

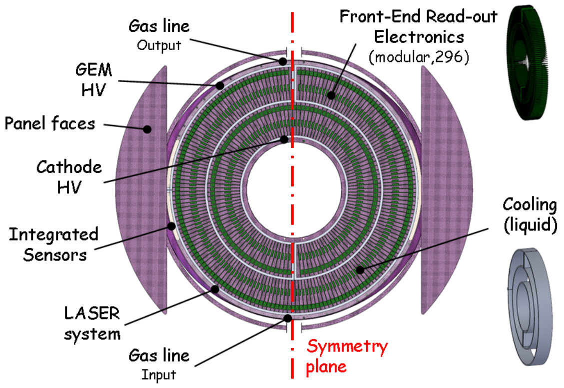

Figure 4.8: Conceptual design of the $\overline{\text{P}}$ANDA GEM-TPC. The cross section at the longitudinal position of the read-out electronics is shown in the left part of the picture. The upper right part shows some details of the radial circular arrangement of the front-end electronic cards (FEC). The lower right part of the figure shows a sketch of the cooling surfaces and guidance structures for the FECs.

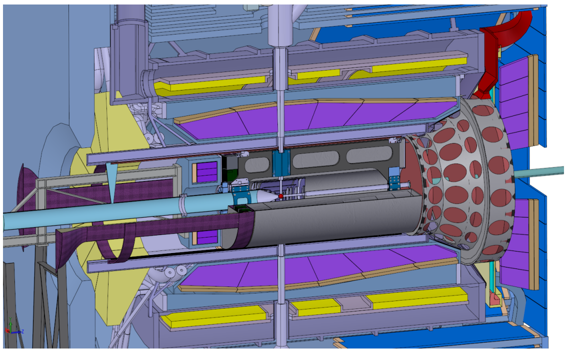

Figure 4.9: $\overline{\text{P}}$ANDA GEM-TPC mounted inside the Target Spectrometer. The upper-right part of the TPC detector has been cut away to allow view to the support and holding structure of the central tracker, the target-pipe crossing, the beam line tubes as well as the Micro Vertex Detector (MVD).

detector system, taking into account the space requirements of e.g. the backward EMC.

Fig. 4.9 shows the $\overline{\text{P}}$ANDA GEM-TPC mounted inside the Target Spectrometer. The base support already comprises all the supply lines condensed into the stiff supplies conduit which ends in two identical terminals outside the magnet structures. This facilitates mounting and saves space inside the magnetic volume.

4.3 Field Cage

The field cage (FC) is one of the main components of the TPC and combines multiple functionality. Its main purpose is to define a homogeneous electrostatic field in the contained gas volume in order to ensure constant transport properties of the generated charges. The material composition and layers sequences are optimized with respect to the radiation length requirements. Great care has been taken in the choice of the insulator with respect to the surface resistivity to avoid charge build-up and breakdowns. The walls are gas tight and mechanically stable against changes in gas pressure and temperature. Several supply lines are incorporated in this structure, like the high voltage trace to the cathode end-cap, a gas distribution system and light guides for the laser infrastructure. These lines have been placed preferably at the edges of the vessels and are evenly distributed inside the inner sandwich layer. Since they are glued to the surrounding matrix, they also serve as mechanical stiffeners. The tunnels for the gas distribution system coincide with the SMD resistors soldered to the outer surface of the FC foils, providing a homogeneous gas distribution and cooling of the resistors at the same time. The vessel is fully electrically insulated from the high-voltage lines. It is shielded by an aluminum coating on its outside surface which is connected to detector-ground potential and which forms a Faraday cage to shield the detector from external electromagnetic signals.

4.3.1 Mechanical Structure

The layer stacking envisaged for the walls of the field cage is shown in Fig. 4.10. This baseline version may still be subject to further optimization. In order to minimize the losses of active volume, a part of the infrastructure has to be incorporated into the walls, such as e.g. laser light-guides, high-voltage cables, gas contribution system etc. Tables 4.2 and 4.3 list the materials used for the structures of the walls and the cathode end-cap.

4.3.2 Radiation Length

With the baseline design, the contribution to the radiation length is less than 1% for a single side-wall in the direction perpendicular to the surface and about 1% for the layers forming the cathode end-cap. This is roughly twice the value achieved for the large prototype GEM-TPC (see Sec. 4.12.2), which is due to the fact that the 60 kV operation

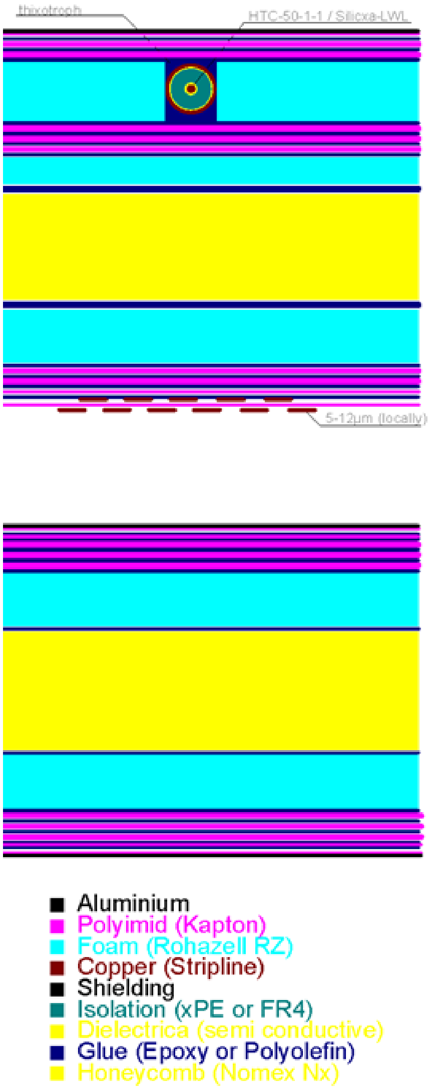

Figure 4.10: Cross section of the structural layout of the barrel walls (upper) and the cathode end-cap (lower). The layer stacking and the sequence of the materials used are shown not to scale.

voltage of the final $\overline{\mathrm{P}}$ANDA TPC is higher than the one for the prototype detector (30 kV).

The radiation length has been evaluated within the PandaRoot analysis framework [23]. A detailed geometry of the GEM-TPC was created and the radiation length was evaluated along tracks with different emission angles. In this way, one obtains the polar angle dependency of the radiation length. Figure 4.11 shows this dependency for angles up to about 130 °, where the material at the backward end-cap (GEM foils and pad plane) is not traversed by the particles. The radiation length for particles going through this part of the TPC is shown in Fig. 4.12.

Table 4.2: Materials and corresponding thicknesses for the barrel walls. The items are ordered from the outside to the inside of the field cage.

Material	Thickness	
	(μm)	(% X_0)
Aluminum	0.2	0.00022
Kapton	275	0.09679
Glue	60	0.01209
Rohacell	2000	0.02587
Glue	80	0.01611
Kapton	375	0.13199
Rohacell	1000	0.01294
Glue	100	0.02014
Nomex honeycomb	5000	0.06762
Glue	50	0.01007
Rohacell	1000	0.02587
Glue	80	0.01611
Kapton	275	0.09679
Copper	12	0.08362
Kapton	50	0.01759
Copper	12	0.08362

Table 4.3: Materials and corresponding thicknesses for the cathode end-cap. The items are ordered from the outside to the inside of the field cage.

Material	Thickness	
	(μm)	(% X_0)
Aluminum	0.2	0.00022
Kapton	400	0.14079
Glue	80	0.01611
Rohacell	2000	0.02587
Glue	50	0.01007
Nomex honeycomb	10000	0.13525
Glue	50	0.01007
Rohacell	2000	0.02587
Glue	100	0.02014
Kapton	425	0.14959
Aluminum	0.2	0.00022

4.3.3 Strip Foil and Voltage Divider

The innermost layer of the field cage vessel is composed of a polyimide (Kapton) foil coated with metal on both sides. The metal surfaces are patterned in two sets of parallel strips aligned transversely to the beam axis, and step-wise degrading the potential from the cathode voltage to the one close to the first GEM. In order to improve the homogeneity of the field close to the field cage walls, the two sets of strips on both sides of the foil are shifted by half a pitch between strips, a design that has proved to be superior to a single set

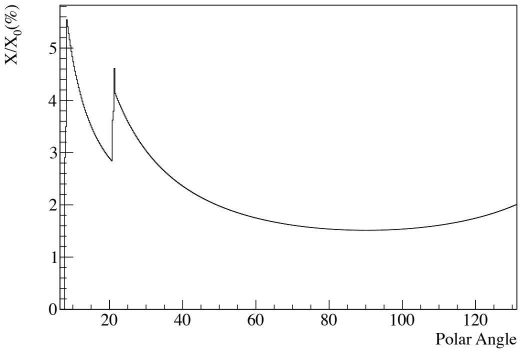

Figure 4.11: Radiation length of the GEM-TPC plotted versus the polar angle.

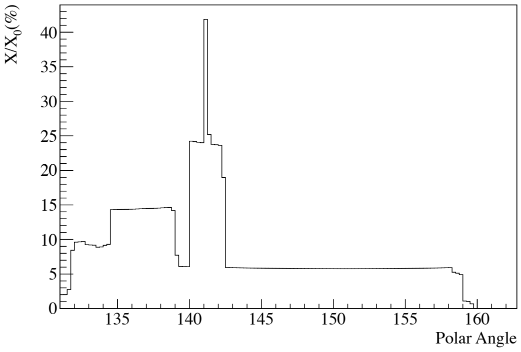

Figure 4.12: Radiation length of the GEM-TPC plotted versus the polar angle for the backward part of the chamber.

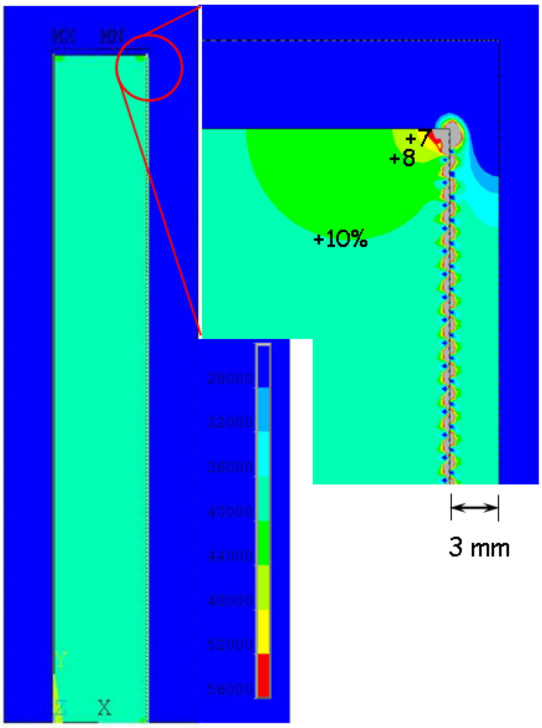

Figure 4.13: Results from a 2-D simulation of the electric field inside the drift volume and at its borders. The color code displays the field inhomogeneities. The width of the strips staggered at the inner and outer surface is 1 mm, the pitch is 1.5 mm. Most of the inhomogeneities occur within 1 mm from the innermost surfaces except for the corners where a 10% variation is reached at a distance of 10 mm from the surface.

of metallic strips with insulator in between. The thickness of the electrodes in the baseline design is 12 μm. We are investigating the possibility to adopt a minimum thickness of the copper layers of 2 μm, which is technically feasible, or switch to aluminum-based electrode structures; both measures would decrease the material budget with respect to the values quoted in Table 4.2.

Due to limitations in the availability of the base material and imposed by the production machinery which limits the width of the foils to about 600 mm, the field cage has to be assembled from stitched foils. At least three sections of equal width alongside the beam axis will be realized. This technique was already successfully applied for the large prototype (cf. Sec. 4.12.1.1).

Calculations of the electrostatic field using finite element methods (FEM) have been employed to evaluate the field inhomogeneity for different strip-line layouts. The obtained results lead to the choice of 1 mm wide electrodes separated by a pitch of 1.5 mm. Figure 4.13 shows the resulting electric field. The outreach of noticeable field inhomogeneities into the drift field region is of the order of 10% of the structural sizes which translates into a distance of 1 mm from the inner surface. This holds true alongside the field cage surface except for the corner regions. There, a 10% variation of the field reaches approximately a distance of 10 mm into the active detector volume. These static deformations of the field bend the drift path of the ionization electrons and thus spoil the resolution. These effects can be calibrated out by recording cosmic tracks or by a laser calibration system (see e.g. Sec. 4.6.1).

Figure 4.14 shows an enlarged view of the strip-line foil implemented in the large prototype TPC which will also be employed for the $\overline{\mathsf{P}}$ANDA TPC. The base-material is Kapton with a thickness of 50 μm, the electrodes are made of copper forming layers of 2×25 μm thickness including the gold-plating and the cover-lay.

In order to achieve a sufficient uniformity of the

Figure 4.14: Photograph of the strip-line field-defining electrodes. The surface facing the drift volume is shown. The strips of copper metal of $2\,\mu$m thickness have a width of 1 mm and a gap of 0.5 mm. The holes show the location of the bores used for the gas-distribution system integrated into the walls of the gas-tight vessel of the field cages. On the upper part the picture one clearly recognized the staggered structure of the strip-line electrodes between the front and backside of the foil.

field, the variations of the inter-strip resistivity should be of the order of 0.1 %. Unfortunately, such high-precision resistors are not available in the MΩ regime and for the small required dimensions (SMD 0805 or even SMD 0603). A lower-precision specimen was chosen (typically 1 %) and the resistors were grouped in parallel networks composing split chains with paired tolerances.

Figure 4.16 shows the sketch of the resistor network to be realized for the $\overline{\text{P}}$ANDA GEM-TPC.

We foresee to make use of the same resistor types (SMD 0805) and individual values (4.2 MΩ) that have been already employed for the large prototype TPC. This results in a total resistance of the strip-line field cage of $\approx 2.15\,G\Omega$. Given a drift field of 400 V/cm and thus applying a drift voltage of 62 kV to the cathode, a current of approximately $30\,\mu$A flows through the resistor network.

4.3.4 Temperature Stabilization

The heat dissipation produced by the persistent currents flowing through the resistor chains should be minimized. Direct cooling of the resistors is not favorable because it would require a metallic or ceramic contact introducing a quite large amount of material. Moreover, the electrical insulation would be quite challenging. To cope with this problem we will install multiple rows of resistors of the same value in parallel connection on the surface of the strip-line foil spreading the heat generated.

In order to monitor the temperature gradient inside the field-cage vessel, SMD-mounted 1-wire sensors will be integrated inside the walls. This allows for respective measurements with a precision of $\approx 0.2\,^{\circ}$C. This concept has been proven helpful and reliable in the framework of the tests done with the large prototype GEM-TPC detector (see Fig. 4.96).

4.4 GEM Stage

4.4.1 Mechanical Layout

The mechanical layout of the GEM stage follows the general design rules as presented in Sec. 4.2.1. Especially with respect to the acceptance of the detector, we maximize the active volume and avoid the introduction of zones with reduced detection efficiency. The GEM foils will be pre-stretched and glued to frames made of glass-fiber reinforced plastics (GRP). The width of the frames is chosen to be 11 mm to match the thickness of the drift volume walls. The total thickness of the frames for one GEM layer is constrained by the distance between the layers in the stack of 1 mm. The so-dimensioned frames can sustain the in-plane stretching forces of 18 N/cm.

Mechanical FEM simulations have been carried out to determine the deformation of the GEM frames. Figure 4.17 shows the results obtained assuming a 1 mm thick frame made from glass-fiber reinforced plastics (GRP) with isotropic E-modulus. A huge deformation of more than 10 mm is expected if the the original half-circular 'kidney' shaped design is assumed, as proposed in [24]. The GEM foil stretched with circumferential forces of 1 N/mm is assumed to be sandwiched between two frames of equal thickness of 0.5 mm in a way that the resulting forces in the direction perpendicular to the foils surface cancel out.

The situation changes drastically by adopting a design symmetric in the plane perpendicular to the beam axis as shown in Fig. 4.18. The respective simulations exhibit a reduction of the deformations to values around 1 mm horizontally and even below 1 mm vertically. These deformations are acceptable and can be treated assuming a proper suspension of the single framed GEM-foils.

This design will allow a modular GEM section which is favorable for maintenance purposes and in terms of the risk assessment.

The size of the TPC would allow for the instal-

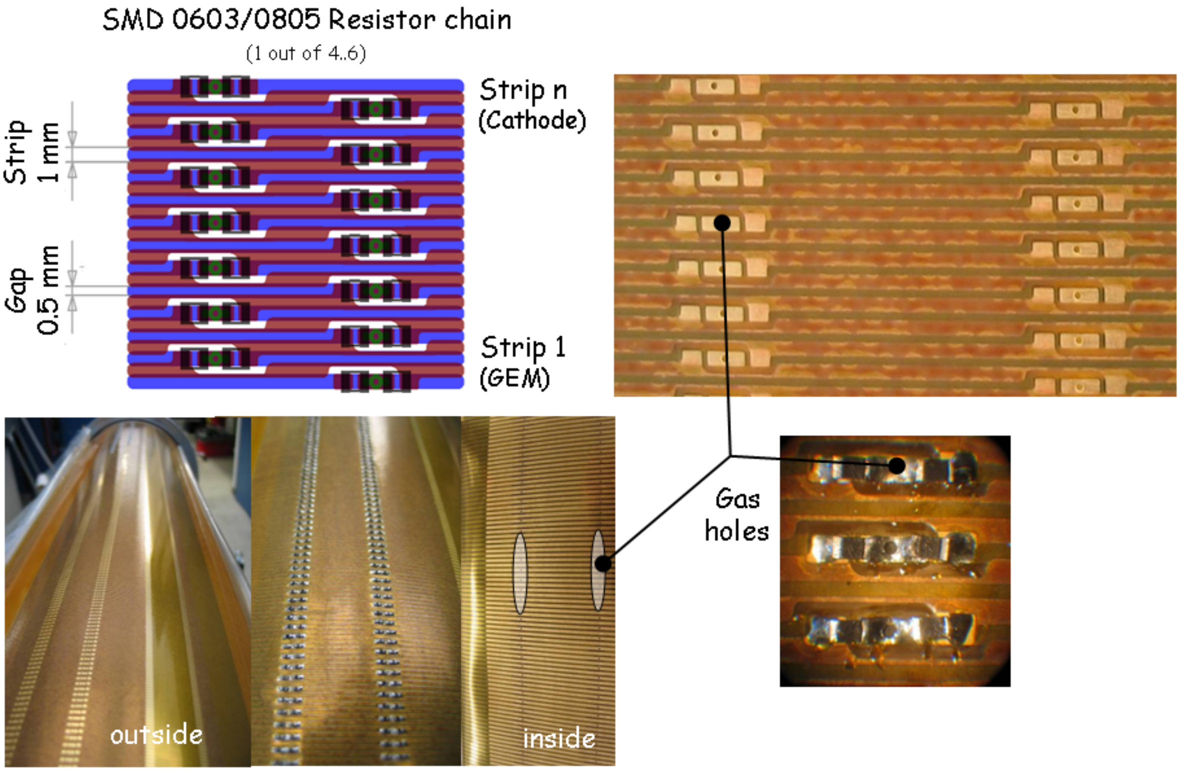

Figure 4.15: Photograph of the strip-line field-defining electrodes of the large prototype GEM-TPC with SMD 0805 resistors mounted on its surface. The layer oriented towards the outer circumference of the field cage vessels shown except for the part labeled 'inside' which shows the lines of holes of the gas distribution system integrated into the vessel-wall structure. The upper left part gives the sketch on details of the principle layout, the upper right part the realization. The lower right shows a photograph of an enlarged view on the SMD 0805 resistors soldered to their respective pads.

lation of GEM foils with a maximum diameter of 900 mm, which, however, is above the limits of today's technologies. The obvious solution is to follow the symmetries of the detector and cut the foils in half along the vertical direction ending up with $900 \times 450\,\mathrm{mm}^2$ foil sizes. This is well in accordance with what has already been achieved at the CERN production site in recent developments for other experiments [20, 21].

The technology applied for the production of these large-size foils is different from the standard GEM production technique used for most of the existing GEM detectors, including the large prototype GEM-TPC described in Sec. 4.12.1. The conventional method of GEM foil patterning requires photo-lithographic processes based on two masks with identical hole patterns, placed on the two sides of the copper-coated base foil, and aligned with a precision of $1\,\mu$m with respect to each other in order for the holes to be perpendicular to the surface. The maximum size of the mask sets one of the limitations to the process due to the extreme requirements on their relative positioning of $1\,\mu$m over ~ 1 m. Another important constraint is the size of the industrially available base material and the machinery required for the processing, both being basically limited to a width of 600 mm.

These limitations can be bypassed by employing a single-mask technique [25]. Indeed, this technique has been shown to deliver similarly good results with respect to homogeneity and gain performance of the GEM-foils Areas of $350 \times 700\,\mathrm{mm}^2$ for the single mask GEM have been achieved in the framework of R&D for the KLOE-2 by the RD51 collaboration [?]. A small decrease in gain by 25 % has been observed in comparison with a standard GEM at the same operation conditions, which can easily be compensated for by a slight increase of the operation voltage by 20 V. No discharges were observed up to a gain of $4 \cdot 10^4$. Similar results were obtained in the framework of developments for the CMS muon system with foils of an active area of $990 \times (220\text{-}455)\mathrm{mm}^2$ [21]. This already corresponds to the size needed to cover the active area of each of

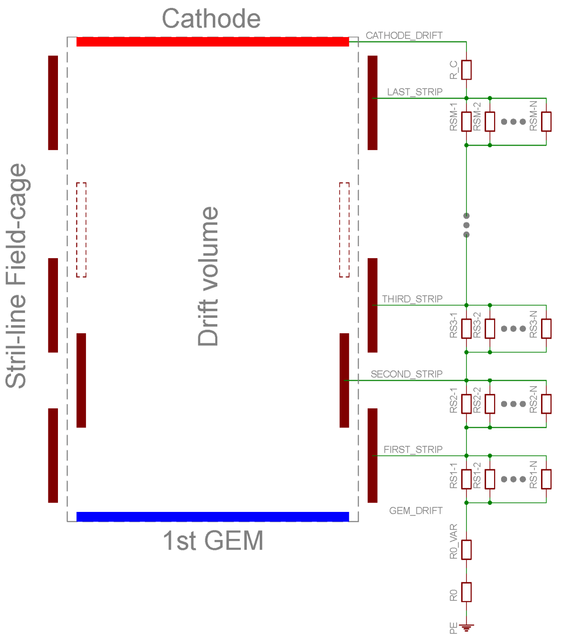

Figure 4.16: Sketch of the resistor network to be realized for the $\overline{\text{P}}$ANDA GEM-TPC. The field-defining electrodes on the strip-line foils as well as the cathode and the surface of the GEM-stack facing the Drift volume are visualized to the left. The right part shows the scheme of the various resistors to be installed. Please note that the GEM-stack itself is supplied by a separate circuit (see Fig. 4.21).

Maximum deformation (mm)			
U_x	U_y	U_z	U_{res}
-700	± 220	± 8	733

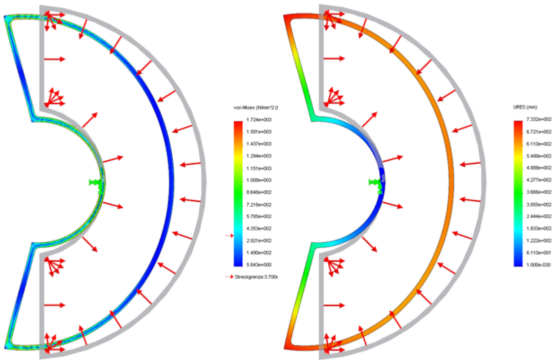

Figure 4.17: FEM simulation of the shape deformation of the GEM carrier frames made of glass-fiber reinforced plastic with a half-circular shape. The maximum bending exceeds several centimeters. The off-plane deformation emerging from the asymmetric boundary conditions applied is irrelevant because it will level out using double framing keeping the overall thickness of the set.

Maximum deformation (mm)			
U_x	U_y	U_z	U_{res}
±1,0	± 0,16	± 0,05	1,3

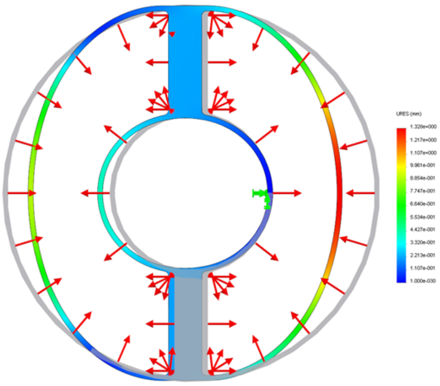

Figure 4.18: FEM simulation of the shape deformation of the GEM carrier frames composed of glass-fiber reinforced plastic in case of symmetrical layout. The maximum bending is kept at a bearable level of 1.5 mm in x-direction.

the two half-cylinders of the $\overline{\text{P}}$ANDA TPC. The gap of 50 mm between the two halve cylinders leaves sufficient space to stitch together two single foils without introducing any inefficient regions.

4.4.2 Electrical layout

Extensive studies have shown that reducing the capacitance between the two metal surfaces of a GEM foil significantly reduces the probability of discharges in a GEM detector [12]. To this end, one side of the GEM foil is segmented into individually powered sectors with a surface of $\sim 100\,\text{cm}^2$. This restriction limits the amount of charge which is involved in case of occasional sparks. The inter-sector distances are reduced down to $100\,\mu\text{m}$. As a result, approximately 36 sectors are required to cover the active cross-section of the GEM-TPC drift volume.

The optimization of the structuring shows that sectioning the surface into 1/4 - circular rings or vertical strips of equal area as shown in Fig. 4.19, respectively, allows to make electrical contact in the middle bar. In this way, also the contact problem for stacked foils is minimized.

In contrast to the design chosen for the large prototype, where the space limitations were not as stringent as for the final TPC and contact to the high voltage (HV) supplies is done via flaps to a common distribution structure embracing the GEM frame, we choose to contact via the middle section of the GEM frame here.

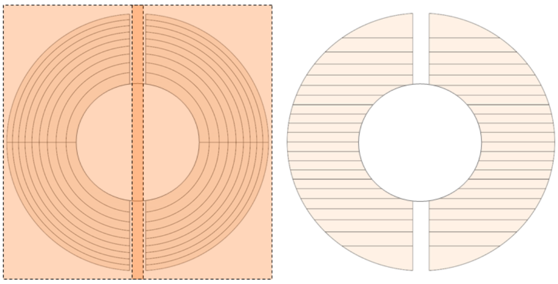

Figure 4.19: Sectioning of the GEM-foils. According to the design recommendations each sector has a surface of $\approx 100\,\text{cm}^2$. Two different schemes of adjacent foils in a GEM stack are proposed which avoid the generation of potentially less efficient zones due to an overlap of the section borders. The backside electrode remains unstructured in both cases. We will either use one single foil large enough to cover the whole surface or stitch two foils together (see left) at the vertical symmetry line.

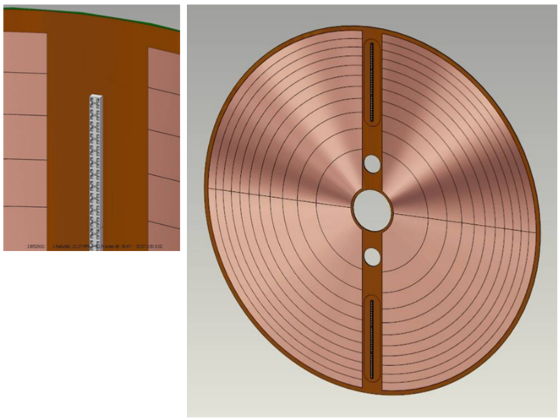

Figure 4.20: Framing and contact scheme of the GEM sectors shown for the circular design.

The potentials on the GEM electrodes are defined by individual external HV supplies. Figure 4.21 shows the schematics of the HV supply scheme.

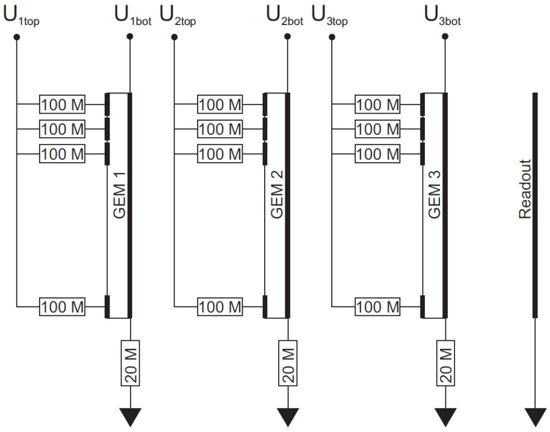

Figure 4.21: Schematics of the HV distribution scheme for the GEM detectors.

The potential on the sectored side of the GEM foil, which is facing the drift electrode, is defined through large $100\,\text{M}\Omega$ loading resistors. The potential on the unsectorized side, facing the readout plane, is supplied directly, and has a high-ohmic connection to ground. This scheme has the following features:

- In case of a discharge between the two sides of a GEM foil, a voltage drop occurs only on the top side, whereas the bottom side remains at its nominal potential. This prevents the propagation of the discharge to the next GEM foil or to the readout circuit.
- In case of a temporary or permanent short across a GEM foil in one or several sectors, the remaining sectors still remain fully operational. The resistor to ground for the bottom side of the GEM foil is necessary in order to avoid reverse currents into the HV supply.

4.4.3 Ion Backflow

In order to minimize the backflow of ions produced in the amplification region, the electric field configuration of the GEM stack as well as the sharing of the gain among the three amplification stages has been optimized. Measurements on small test detectors, reported in Sec. 4.11.2, indicate a minimum ion backflow at the voltage settings shown in table 4.4, which correspond to an effective gain of about 2000 in the GEM stack for the envisaged Ne/CO$_2$ (90/10) mixture. With an ion backflow of of 0.25%, this corresponds to four back drifting ions per electron reaching the GEM stack.

Drift Field	0.4 kV/cm
ΔU_{GEM1}	244 V
Transfer Field 1	4.5 kV/cm
ΔU_{GEM2}	278 V
Transfer Field 2	0.16 kV/cm
ΔU_{GEM3}	333 V
Collection/Induction Field	5.0 kV/cm

Table 4.4: High voltage settings for a minimal ion backflow at an effective gain of about $2 \cdot 10^3$.

A further reduction of the ion backflow to the level of 10^{-5} can be achieved using additional pattering on one side of a GEM foil, as will be discussed in Sec. 4.13.5. This very promising strategy will be

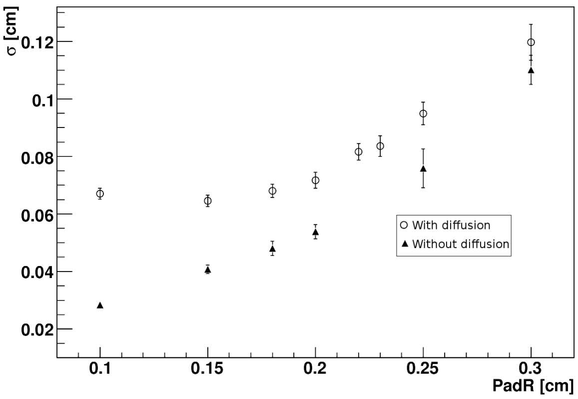

Figure 4.22: Cluster residual width along x versus pad outer radius, with diffusion in a 2 T solenoid field (open circles) and without diffusion (full triangles).

investigated using the large prototype. If successful, it essentially eliminates the problem of ion backflow for the TPC.

4.4.4 Pad Plane

The electrons emerging from the last GEM stage induce a fast signal on the readout pads. In order to achieve a more uniform distribution of the signal on neighboring pads, a hexagonal symmetry is foreseen. In this way, the distance to all neighboring pads is constant, in contrast to non-uniform distances for a rectangular pattern.

The optimum pad size was determined by Monte Carlo simulations of pions with 0.5 GeV/c momentum traversing the $\overline{\text{P}}$ANDA TPC at a polar angle of 40° in a magnetic field of 2 T. Figure 4.22 shows the r.m.s. width of the residual distribution of clusters along x, i.e. perpendicular to the drift direction, as a function of the circumscribed circle radius of the hexagonal pads, both with and without diffusion in the drift region. Below a pad outer radius of 1.5 mm, the diffusion starts to dominate the resolution, while the pad size dominates for larger values. A pad outer radius of 1.5 mm was chosen accordingly. It should be noted here that these simulations have been performed using slightly different parameters for the gas mixture[1]. Therefore, the absolute value of the r.m.s. width is to be taken with a grain of salt, but the conclusions towards the saturation remain valid. The total number of pads in the active area of the two halves of the TPC is about 80000. As for the large prototype (cf. Sec. 4.12), it is foreseen to measure the temperature at various positions on the pad plane inside the gas volume. Since the pad plane also encloses the gas volume of the detector at the backward end-cap, it is designed as a multi-layer PCB, thus avoiding through-going vias for the signal lines. Signals from different pads are routed to the connectors in way to minimize cross talk. The capacitance of the pads and the signal lines corresponds to 10 pF. The signals are read out by 320 front-end cards, mounted perpendicularly to the readout plane to minimize heat transfer to the readout plane, and each reading 256 electronic channels.

4.5 Gas System

4.5.1 Key Issues

For the design and operation of the gas system the following points are important and will be further discussed in the following sections.

- As chamber gas a Ne/CO_2 mixture (with a mole ratio 90:10) will be used.
- The TPC volume amounts to 0.7 m^3.
- A gas exchange rate to replace the TPC volume once every two hours is foreseen, the average gas flow amounts to 0.15 m^3/h.
- A closed cycle gas system with a purification unit is needed.
- O_2 and H_2O contamination will be controlled and monitored to be kept below a level of 5 ppm.
- The chamber pressure will be controlled to a value of 5±1 mbar above atmospheric pressure, to avoid a distortion of the chamber wall.

4.5.2 Choice of Gas Mixture

The choice of detector gas is crucial to the design of the TPC [?]. It not only influences the performance of the detector, but has impact on the design and electrical properties of the field cage, the amplification region, and the readout electronics. The requirements to the gas mixture for a TPC are manifold, and partly contradictory:

- high electron drift velocity: fast clearing of the gas volume,
- low electron diffusion: spatial resolution,

---

[1] for the large prototype TPC at a field of 2.5 T

Table 4.5: Properties of gases commonly used in TPCs at normal temperature and pressure (20°C, 1013.25 mbar). Density ρ, radiation length X_0, total number of electron-ion pairs for MIPs N_T.

Gas	ρ	X_0	X_0	N_T
	[g/l]	[g/cm^2]	[m]	[1/cm]
He	0.1785	94.32	5280	8
Ne	0.89990	28.94	322	40
Ar	1.784	19.55	110	97
CH_4	0.717	46.22	645	54
CO_2	1.977	36.2	183	100
C_2H_6	1.356	45.47	335	112
CF_4	3.93	36	90	120

- constant gain: variations of T, p, material,
- low electron attachment,
- high ion mobility: accumulation of space charge controllable,
- specific ionization: dE/dx vs. space charge,
- low density, high radiation length: multiple scattering,
- no aging.

Only the noble gases Argon and Neon qualify as the main component. Helium is difficult to contain and hence has a high leak rate, Krypton and Xenon are rare and hence not affordable in larger quantities. In addition, their high density leads to significant multiple scattering. Due to its lower abundance, Neon is about a factor of 8 more expensive than Argon, making a closed gas system indispensable. Table 4.5 summarizes the important parameters of some noble gases and common admixtures.

The radiation length is about a factor of three larger for Ne than for Ar, leading to reduced photon conversion and multiple scattering in Ne. The primary ionization rate is about a factor of two smaller for Ne ($n_\mathrm{mp} = 16$) than for Ar ($n_\mathrm{mp} = 38$), requiring a higher gain in the case of Ne. On the other hand, space charge effects will be significantly lower for Ne than for Ar, supplemented by mobility of Ne ions which is a factor of 2-3 larger than that for Ar ($\mu_\mathrm{Ne} \sim 4\,\mathrm{cm}^2/\mathrm{Vs}$ for $E < 10^4\,\mathrm{V/cm}$). Following these arguments, the preferred main gas component for the $\overline{\mathrm{P}}$ANDA TPC will be Ne.

As quenchers, either organic gases such as Methane (CH_4), Ethane (C_2H_6), Isobutane (iC_4H_{10}), freons such as CF_4, or CO_2 are most widely used. CH_4, used in e.g. P10 (Ar/CH_4 90/10) is a very convenient quencher, since it has a maximum drift velocity of 5 cm/μs at an electric field of only 125 V/cm, greatly simplifying the design of the field cage. A strong longitudinal magnetic field is necessary, however, in order to reduce transverse diffusion. The drawback of organic mixtures is that they may cause aging by forming polymeric deposits on the electrodes of the chamber when the accumulated charge is large. CF_4 is in principle interesting as quencher, since it provides a high drift velocity at low electric fields in mixtures with Ar or Ne. In addition, it is sometimes used in attempts to etch polymer deposits from electrodes. Its high reactivity, however, makes its use very dangerous to other components of the gas system, like glass joints, or Aluminum parts. In addition, fluorine is electronegative and attaches electrons. CO_2 remains as an uncritical quencher, with the advantage of low diffusion, and the disadvantage of lower drift velocities. Hence, CO_2 will be used as quencher for the $\overline{\mathrm{P}}$ANDA TPC.

Table 4.6: Gas parameters for the $\overline{\mathrm{P}}$ANDA TPC at a magnetic solenoid field of 2 T.

Gas mixture	Ne/CO_2 (90/10)
Drift field	400 V/cm
Electron drift velocity	2.731 cm/µs
Transverse diffusion	130 µm/$\sqrt{\mathrm{cm}}$
Longitudinal diffusion	230 µm/$\sqrt{\mathrm{cm}}$
Ne^+ ion drift velocity in Ne	1.767 cm/ms

The mixture ratio is Ne/CO_2 90/10 (by weight). This mixture, which is also used in the NA49 and ALICE TPCs, features attractive charge transport properties at reasonable drift fields, and is non-flammable. Figure 4.23 shows the drift velocity, Fig. 4.24 the transverse and longitudinal diffusion constant of Ne/CO_2 (90/10) in a 2 T longitudinal magnetic field as a function of the electric drift field, calculated with MAGBOLTZ [?, ?].

Table 4.6 summarizes important parameters of this mixture for the $\overline{\mathrm{P}}$ANDA TPC.

4.5.3 Operational Requirements

One of the main requirements to the gas system, including the detector vessel itself, is the limitation of oxygen and water vapor concentration. In the case of Ne/CO_2 mixtures for example the electron attachment is of the order of 1% per ppm oxygen concentration and per meter drift length. This has severe implications on the particle identification power, because it degrades the dE/dx-measurement. The contamination mainly originates from bad sealing joints and/or permeation of

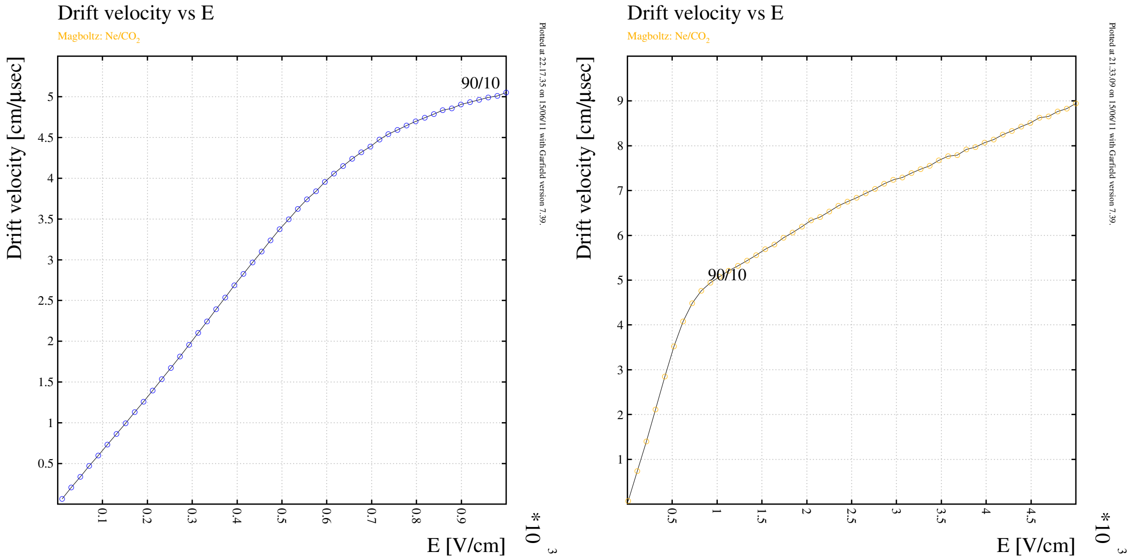

Figure 4.23: Drift velocity as a function of the electric drift field for a Ne/CO$_2$ (90/10) gas mixture. Low-field drift region (left) and region extended to fields in the GEM stack (right).

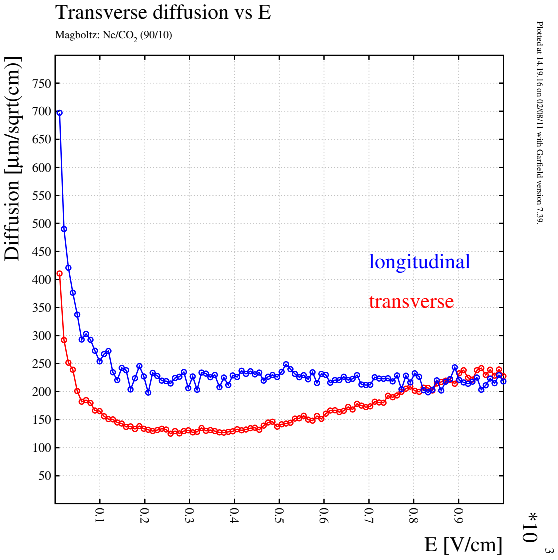

Figure 4.24: Transverse (red) and longitudinal (blue) diffusion as a function of the electric drift field for a Ne/CO$_2$ (90/10) mixture.

water and oxygen through the TPC wall material. The volume-to-surface ratio of the $\overline{\text{P}}$ANDA TPC is only about 0.1 m, compared to existing large TPCs, such the ALICE TPC (0.70 m), where an oxygen contamination lower than 5 ppm was achieved. This value is therefore regarded as the upper limit for the $\overline{\text{P}}$ANDA TPC.

In addition to the gas purity, the accuracy and stability of the Ne/CO$_2$ gas mixture is crucial, as it determines important parameters like the drift velocity or diffusion within the gas.

4.5.4 Design and Layout

The large detector volume of about 0.7 m^3 as well as the usage of a high-cost gas mixture leads to a closed circulation gas system as the natural choice. Figure 4.25 presents the basic layout of such a system. It is built up of the gas supply unit, the purification system and the gas analyzing devices (oxygen and water vapor monitors and a residual gas analyzer), which will be located outside of the experimental area in the gas supply building. For simplicity the TPC is drawn as one gas volume instead of two. While full lines mark the gas pipelines, the dashed lines correspond to control connections. For normal running the gas will be recycled through a purifier and go back to the main loop with a moderate ‘fresh’ gas injection of only a few percent. Therefore the return gas from the detector has to be compressed and pumped back to the gas supply building. The detector is planned to be operated constantly at 5 mbar over atmospheric pressure. This is achieved by an independent control loop consisting of a pressure transducer, an adjustable electro-magnetic valve and a stand-alone control unit, which is installed at the output line of the TPC. The transducer measures the pressure close to the TPC volume, submits the value to the control unit which then regulates the valve. In addition, to check the resulting pressure regulation, pressure measurements are done permanently at three different positions by transducers. In addition, the total gas flow is controlled by a flow meter and adjusted by an electro-magnetic valve. The main TPC gas monitor system collects all this information and also checks the gas quality at different points within the circulation system. Like the stand-alone pressure control system, it should be easily accessible inside a general control area close to the experiment.

4.5.4.1 Purification Unit

Closed loop gas circulation systems require gas purification in order to achieve high regeneration rates of the “old” gas and low requirement of “fresh” gas. The main impurities of concern, which accumulate in the system, are oxygen and water vapor. These pollutants infiltrate the system through the detector sealing and due to the under-pressure at the compressor entrance. A set of two purifier cartridges (see Fig.4.26) are filled with two cleaning agents: molecular sieve (3 Å) to remove the water vapor and activated copper to remove the oxygen content in the gas stream. The advantage of having two parallel cylinders in each cleaning stage is to run the gas mixture through one, while the other one is regenerated. Both agents in the same cylinder can be regenerated at the same time by heating the columns to 220 °C while purged with a Ne-H_2 gas mixture with a mixing ratio of 9:1. The operating cycle to clean the purifiers will be controlled by the slow control unit, which will follow exactly the same protocol each time.

4.5.4.2 Gas Mixing Unit

The design of the gas mixing unit is shown in Fig.4.27. It will mix the gas components in the desired proportions with the help of mass flow controllers. The device will have the possibility to run in two different modes: the “Fill”-mode with higher gas flow rates up to 350 l/h and the continuous “Run” mode with a lower rate of about 10 l/h, corresponding to the injection rate of fresh gas during normal operation. Additionally a separated purging line using N_2 will be installed. The contents of the gas mixture components are continuously monitored with a mass spectrometer (RGA) and the process parameters are recorded by the slow control system.

4.5.4.3 Emergency Devices

Very close to the TPC an emergency system has to be installed (at the input line of the system to avoid under pressure and at the output line and hence over pressure in the TPC). If for any reason the main system stops working (e.g. because of a power cut), this backup system keeps the pressure inside the TPC constant.

In case of over pressure gas is relieved through a security bubbler which is adjusted to 5 mbar over atmospheric pressure. In case of under pressure premixed Ne/CO_2 is injected from a bottle.

4.5.4.4 Filling, Purging and Calibration

Filling of the detector with operating gas will be done without recirculation and with a high inlet gas flow, compared to normal running conditions, from the mixing unit (see Fig. 4.25). For this a three way valve, positioned before the purifier input, can be set to “exhaust”. At the same time the second set of flow meters (“fill” condition, see Fig. 4.27) within the mixing unit is used to increase the flow. By this a gas exchange of at least one whole TPC volume should be possible every two hours.

For purging the TPC, a separate input gas line is connected. From there for example N_2 is injected into the gas system, flushed through the detector and exhausted through a bubbler. In case of a longer shutdown one can fill the two TPC vessels with N_2 and then use the purge system to keep them at a constant pressure.

For gain calibrations of the TPC and its readout channels a radioactive noble gas isotope could be admixed to the operating gas. A bypass arrangement will serve to implement this feature.

4.6 Calibration

4.6.1 Laser System

The drift velocity of charge carriers is a key parameter in the operation of a gaseous TPC. The knowledge of its absolute value within a relative precision of $5 \cdot 10^{-4}$ is crucial for a trigger-less system. Variations of the drift velocity can be introduced by imperfections and non-uniformities in the gas, temperature and the electric and magnetic fields.

Another source of deviations from the ideal homogeneous drift field are space charge effects arising from the ion backflow to the cathode. This can cause distortions in the drift path of the electrons (as described in Section 4.11.2) traveling to the anode. The effect is severe as its influence may vary with the beam intensity and time. It is also subject to

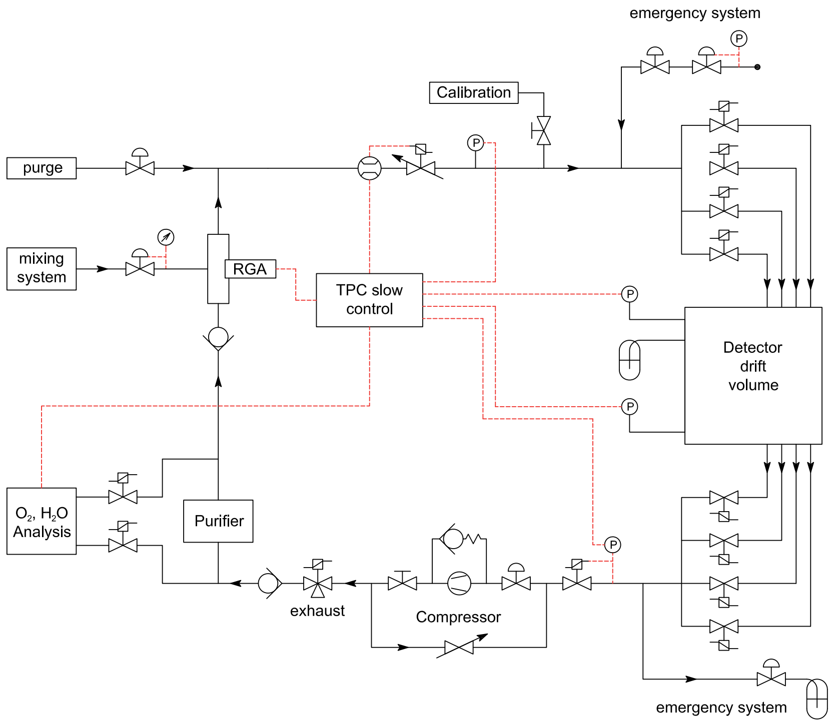

Figure 4.25: Basic layout of the cycle TPC gas system.

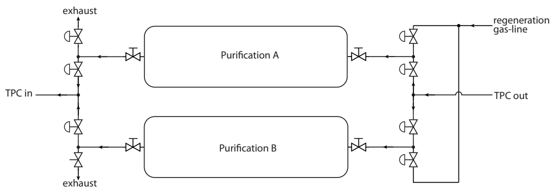

Figure 4.26: Gas purification twin-unit for the removal of oxygen and water vapor contamination in the TPC gas mixture.

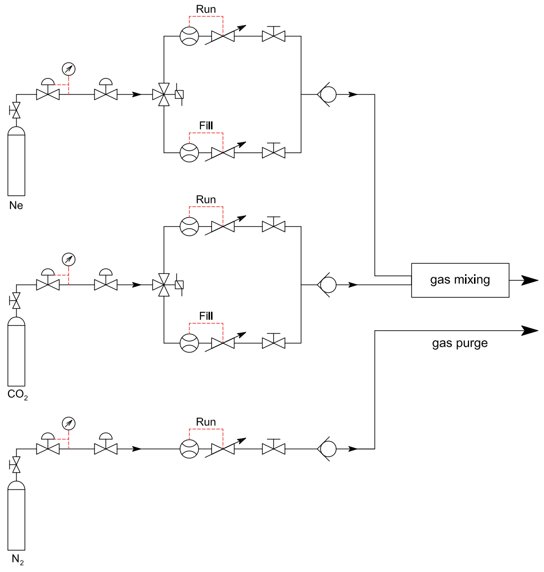

Figure 4.27: The gas mixing system with the possibility to switch between filling and continuous running application.

changes in the operation conditions of the detector, especially the settings of the GEM-voltages. There is also a non-negligible static contribution originating from mechanical and electrical imperfections of the field cage itself (see Sec. 4.3).

All these effects need to be corrected in order to achieve good spatial and momentum resolution. The goal is to obtain a uniformity within a relative error of about 10^{-4} corresponding to a point resolution of $150\,\mu$m and a z-resolution of $200\,\mu$m for a total drift length of 1.5 m. A calibration system has to fulfill all of these requirements. It has to be usable for calibration of intrinsic non-uniformities as well as time dependent non-uniformities. Due to the continuous operation of the $\overline{\mathsf{P}}\mathsf{ANDA}$ experiment, those calibrations will be performed in special calibration runs without beam and if possible during the beam operation.

There are various methods possible to achieve information on both quantities, drift velocity and field distortions, with different grades of feasibility and date of application.

- Reconstruction of cosmic tracks. Any deviation from a straight line of the reconstructed path may be attributed to local fields. Obviously this method is applicable only without the presence of a magnetic field limiting it to times without beam on target. The particles may probe the whole active volume basically in vertical direction. This method is very common and applied to all experiments of today.
- Generation of artificial tracks perpendicular to the electrical field lines in the drift volume probing the active volume in full 3-D. One method to obtain such a calibration is by a number of narrow ultraviolet rays at well known predefined positions.
- Generation of point- and/or strip-like 2-D patterns at the cathode end-cap surface. This method allows probing the active volume in an integral way.

For the last two methods a laser system [**?**] will be the best choice. Laser systems have been used in many TPCs as an essential tool for calibration. The main tasks of a laser calibration in a TPC are:

- determination of the drift velocity;
- alignment of different modules and sectors to each other;
- correction of spatial distortions.

Ideally, several of the above-mentioned calibration methods should be used in parallel for reasons of redundancy and systematic error minimization. For instance the drift velocity can be determined with reconstructed cosmic muons and the laser system. The combination of these two methods will help to reduce the systematic uncertainties and therefore allow a much higher precision on this critical parameter. As the drift velocity will not be in a plateau for the $\overline{\mathsf{P}}$ANDA TPC, the redundancy in the calibration methods will be of highest importance.

In the following, two possible laser calibration systems will be discussed. The 3-D laser system, on the one hand, would be the preferable choice as it would offer the maximum amount of information needed to perfectly calibrate the TPC. It will, however, require a high level of complexity in the mechanical implementation. A system like employed for the T2K TPC, on the other hand, requires less complexity, but might provide less information than the 3-D system. Therefore it can be seen as a potential fallback solution.

4.6.1.1 3-D Laser Calibration

Numerous systems based on the reconstruction of laser-generated tracks have been implemented and successfully operated in the past years, e.g. for the STAR TPC [**?**, **?**], and for the ALICE TPC [9]. It is the aim of such a setup to measure several hundred simultaneously generated laser tracks throughout the TPC drift volume.

While the molecules of the Ne/CO$_2$ gas mixture have ionization potentials above 10 eV, organic impurities have values in the range of 5–8 eV. A monochromatic laser beam with a wavelength of 266 nm ($E = 4.66$ eV) will ionize the gas impurities by a two-photon absorption process, which proceeds via a virtual state with a very short lifetime of $\tau \approx 10^{-16}$ s. The number of electrons n_e created per unit length of the laser track varies quadratically with the total number of photons N_γ: given by Eq. 4.1 [**?**]:

$$n_e = \frac{\sigma^2 n_0 N_\gamma^2 \tau}{sT} \qquad (4.1)$$

Here, $\sigma_1 = \sigma_2 = \sigma \approx 10^{-16} - 10^{-17}\,\mathrm{cm}^2$ are the cross sections for the excitation of the virtual state and the ionization from the virtual state, respectively, n_0 is the number of impurity molecules per cm^3, T the laser pulse width and s its area. Energy densities of about $20\mu\mathrm{J/mm}^2$ for a 5 ns pulse are sufficient to obtain an ionization, which corresponds to several minimum ionizing particles [9].

The implementation of such a system for the $\overline{\mathsf{P}}$ANDA TPC is at the cutting-edge of today's technology. The major constraints are given by the available installation space. Whereas the above-mentioned laser systems for TPCs are implemented on cm/m scales, one has to deal with a mm window in case of the $\overline{\mathsf{P}}$ANDA TPC. For this purpose the laser light is generated outside the TPC and distributed through light-guide fibers, which are incorporated in the wall of the FC vessels. Afterward it enters the gas volume under 90 ° to the beam axis at different z positions and providing tracks of constant drift time. Figure 4.28 illustrates the conceptual design of such a laser system.

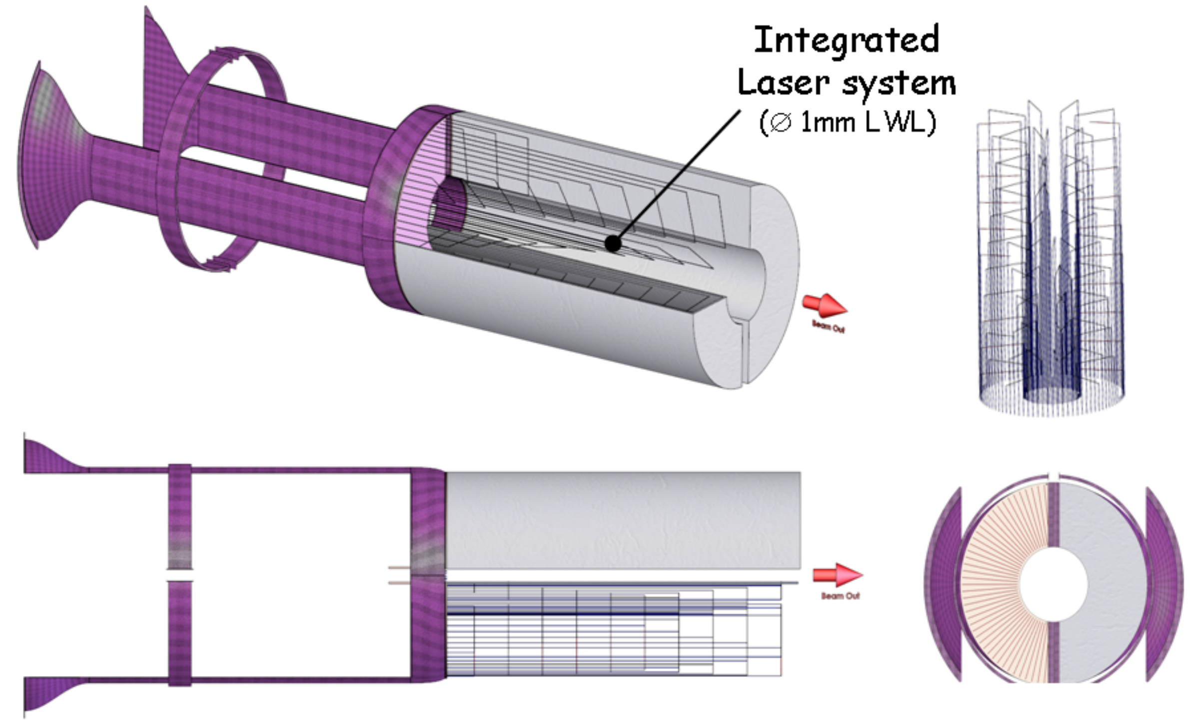

Figure 4.28: Conceptual design of the integration of the fiber light guide-based laser calibration system into the $\overline{\text{P}}$ANDA GEM-TPC is shown. The fibers are integrated into the walls of the field cage vessels. The lines traversing the drift volume visualize the laser beams and are shown to guide the eye only. Currently we foresee a granularity in z of 100–150 mm and 40° which allows for a total of 900 generated tracks, 45 per drift volume. The difference in angle between adjacent z layers is chosen to be 4°.

It is important to minimize the extraction of electrons within the chamber by the photoelectric effect which takes place on metals that release electrons at energies below 4.66 eV. A considerable amount of low-energy electrons has to be expected from diffusely scattered UV light hitting metallic surfaces. In the current setup these are mainly formed by the GEM layers (Cu: 4.3–4.5 eV) and the aluminum coating (Al: 3.0–4.2 eV) of the cathode end-cap and the copper (aluminum) strips of the electrode forming the field defining system of the field cage. Since the strip-lines currently are coated by a thin layer of Ni/Au with bigger values (Ni: 5.0 eV, Au: 4.8–5.4 eV), the emission from the cathode remains the main contribution.

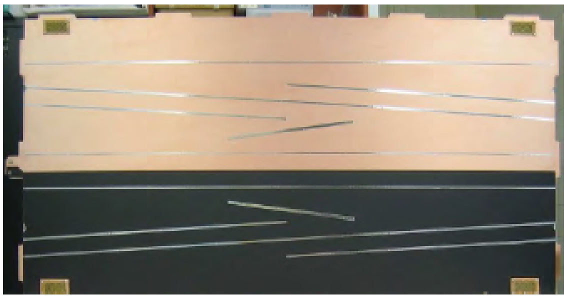

Figure 4.29: The picture shows the central cathode of the T2K TPC with aluminum strips [26].

4.6.1.2 2-D Laser Calibration

The other potential laser system, which is an option for the $\overline{\text{P}}$ANDA TPC is based on the laser calibration systems developed for the HARP TPC [27] and further optimized for the T2K [26] TPC. The benefit of this concept is that it is comparatively simple and easy to implement. The basic concept consists of a fiber system coupled in at the anode side of the TPC. The fiber system will follow basically the same implementation as shown in Fig. 4.28. The fibers however will not enter the drift volume, but instead produce a homogeneous light distribution at the beginning of the drift volume. The UV light distribution will illuminate a pattern of aluminum strips and dots imprinted on the copper cathode using photo-lithographic methods. The aluminum has a low extraction energy of 3.0–4.2 eV, so that charges comparable to MIPs would be produced.

The strip and dot structure forms a specific pattern, that after reconstruction can be used for a precise determination of absolute spatial distortions along the full drift length of TPC. As the laser pulse length is short (∼ 5 ns) compared to the total drift time variations of extracted electrons, it can be used to monitor the drift velocity.

Also for this system the fibers will have to penetrate through the GEM frame to have a direct connection the gas volume. For the T2K system, SILICA solar resistant fibers with diameters of 600 and 800μm have been tested. They have a damage threshold of 2.7 resp. 4.9 mJ for 5 ns pulses of 266 nm wavelength. This damage threshold is far above the total energy density needed for the illumination of the total cathode plane. To have a similar ionization like a MIP, roughly 10 e^- per mm must be produced. The strips should have a width of about 2 mm, so that the width of the charge cloud is dominated by diffusion and not by the strip width. The photon efficiency of aluminum is about $3 \cdot 10^{-8}\,e^-/\gamma$, and with an energy of 4.6 eV for each γ an energy density of 12.446 nJ/cm^2 is needed to produce a MIP-like charge deposition. With a total area of 789.75 cm^2 an integrated energy of about 30 µJ is needed to illuminate the whole cathode. There are several companies, that can provide Nd:YAG laser with an energy of several mJ per pulse.

4.6.2 Krypton Calibration

Absolute and relative gain calibration of a GEM-TPC is an important factor to improve the overall energy, dE/dx and spatial resolution. Spatial fluctuations in the gain factors for each channel can arise e.g. from different circuit lengths, gain variations in the ADCs and front-end electronics or sector borders of the GEM foils. Furthermore systematic GEM profile studies have shown that the spatial gain distribution of double and triple GEM detectors can have high variations. Gain variations up to 20% due to stresses on the GEM frame and bending of the foils could be observed. The bending does not change the gain of the GEM itself. However it modifies the effective transfer and induction fields between the GEMs. This leads to different attachment and extraction coefficients thus modifying locally the effective gain [28]. These effects need to be corrected in order to reach an optimal energy resolution.

One method to perform such an energy calibration is by introducing radioactive ^{83m}Kr into the drift volume. This technique has already been used in various large TPCs (e.g. ALEPH [29], HARP, NA49, ALICE [30], STAR [31]).

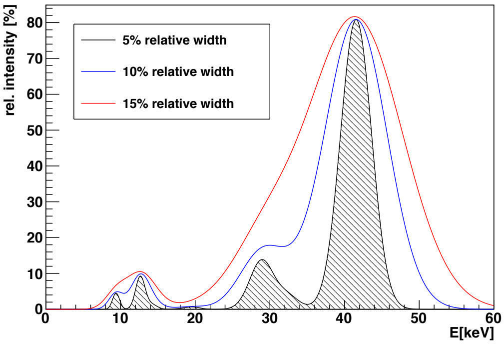

Figure 4.30: Charge spectrum from ^{83}Kr decays calculated combining the transition probabilities and fluorescence yields given in [32]. The photon conversion coefficients for the large TPC prototype with ArC0$_2$ 90/10 [?] were taken into account. The four main peaks between 9.4 keV and 41.6 keV are shown for different possible energy resolutions.

A ^{83}Rb source is mounted in a bypass of the TPC gas system. It decays with a half-life of 86.2 d into an isomeric 41.6 keV state of ^{83}Kr, which decays into the stable ground state with a half-life of 1.83 h via a short-lived excited state at 9.4 keV. The decay spectrum has 4 main peaks between 9.4 keV and 41.6 keV, originating from conversion electrons, that can be used for gain equalization and calibration (see Fig. 4.30). A detailed discussion of the decay spectrum can be found in [32].

For calibration of the prototype TPC (first results see 4.12.2.3) a ^{83}Rb source with an activity of 2.5 MBq has been produced at the HISKP cyclotron[2] in Mar 2011 using an $^{81}\mathrm{Br}(\alpha, 2n)^{83}\mathrm{Rb}$ reaction with $\sigma = 1300$ mb at an energy of 26 MeV. This production process has already been used before for a calibration source of the KATRIN experiment and is described in [33].

The container for the rubidium source can be seen in Fig. 4.31. The inner steel tube holding the radioactive material can be connected easily via two flanges to the gas system of the TPC. In case the system is not connected to the gas system it can be easily sealed with a dummy flange for transport. An outer shielding consisting of 13 cm of lead absorbs higher energetic decay photons that are emitted during the decay.

After connecting the container to the gas system the filling of the krypton-enriched gas is done by

---

[2] Helmholtz-Institut für Strahlen- und Kernphysik, Nussallee 14-16, D-53115 Bonn

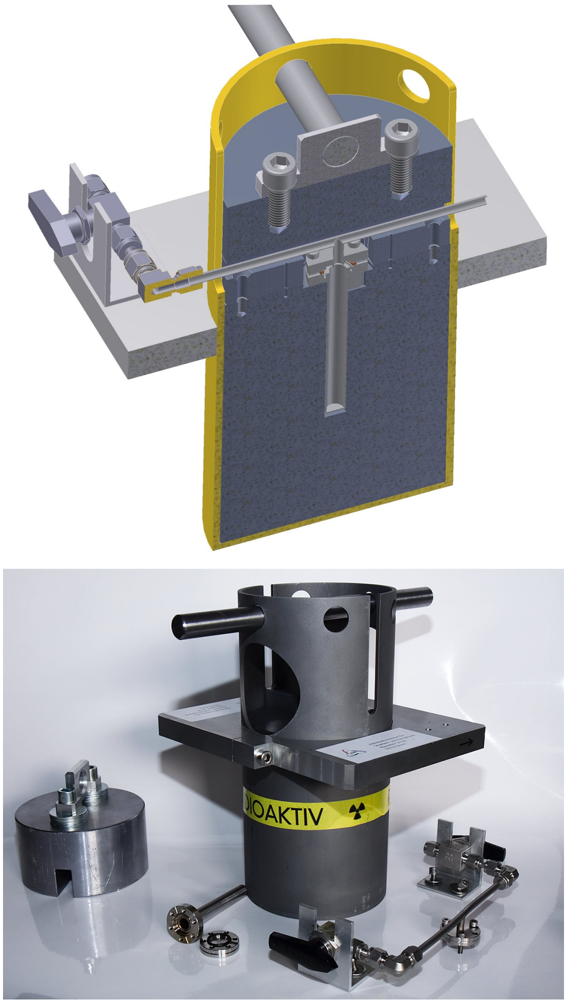

Figure 4.31: Lead-shielded container housing the ^{83}Rb source. The source is contained in a steel finger that can be attached to the gas inlet via a bypass system. The outer shielding absorbs higher energetic decay photons that are emitted during the decay.

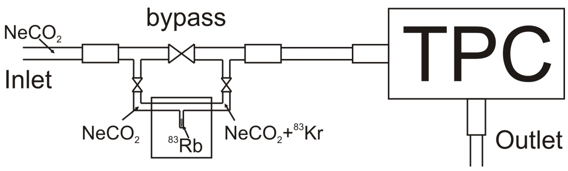

Figure 4.32: Sketch of the ^{83}Kr container connected to the TPC gas system.

a three valve system as shown in Fig. 4.32. In the normal operation of the gas system the krypton container is bypassed from the system by two valves. In phases of krypton calibration runs the gas is circulated through the krypton container releasing ^{83}Kr in the TPC volume. After finishing the calibration runs the container is bypassed again while the remaining amount of krypton decays within a couple of tens of minutes.

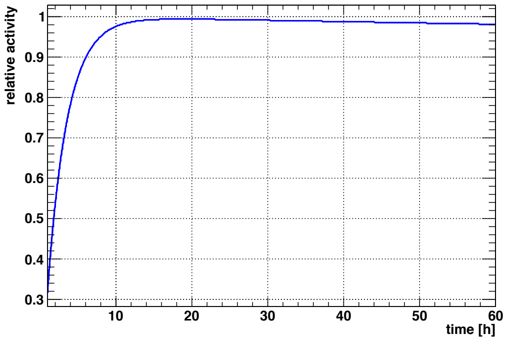

Figure 4.33: Reactivation time needed to recover a 100% ^{83}Kr activity after a complete exhaustion of the krypton container.

Figure 4.33 shows the reactivation time needed to recover a 100 % ^{83}Kr activity after a complete exhaustion of the krypton container.

4.6.3 Electronics Calibration

The readout plane of the final TPC detector is segmented into eighty thousand pads each one connected with the corresponding electronic channel. The readout system measures the charge induced on the readout pads and the absolute time when it occurs.

The charge value is very important for a precise determination of the x-y cluster coordinate as well as for dE/dx measurements. From our experience with the APV25 front-end chip the variations of charge sensitivity from channel to channel and from chip to chip are very small and do not require additional corrections. The ^{83}Kr calibration takes into account small remaining channel-to-channel variations of the charge sensitivity. The absolute value of the sensitivity has to be determined during production of the front-end electronics and used for the full period of chamber operation.

The absolute arrival times of detector signals are measured with respect to a clock, common to all $\overline{\text{P}}$ANDA detectors and distributed by SODA (Time Distribution System of $\overline{\text{P}}$ANDA experiment) [?]. The distributed clock has a very small time jitter but due to the difference in cable lengths and propagation characteristics of electronic components there is an unknown relation between clock phases between different front-end cards. For the time calibration of the TPC front-end electronics one may use straight tracks of the laser calibration system or high energy cosmic tracks. In order to time in the TPC timing information with other detectors one has to use physics events or cosmics.

4.7 Slow Control

To ensure a safe and stable operation of the TPC, there are several parameters that have to be controlled, monitored and stored. Besides the temperature distribution in- and outside the detector and the parameters of the gas system, primarily the settings of the high voltages for the drift and the GEM amplification stack are essential. Also, the low voltages for the readout electronics have to be supervised.

4.7.1 High Voltage System

The operation of the TPC demands on the one hand a separate supervision of every high voltage that is applied to the GEM foils and the drift cathode and, on the other hand, the possibility to operate all channels simultaneously, especially during ramping up and down the chamber. To avoid any damages to the chamber, a fast emergency shutdown of the high voltage system is indispensable. Furthermore the system should allow the configuration of this emergency behavior.

The high voltage system for the GEM stack requires good voltage stability (ripple and noise $<$ 50 mV), high precision current measurement (resolution 1 nA), adjustable ramp speeds, full remote controllability and output voltages up to 6 kV. For the drift cathode a high voltage system with a voltage of up to 70 kV and currents up to 1 mA is needed. Since both systems need to be connected for a synchronous operation and trip behavior an ISEG EHS 8060n HV module and an ISEG HPn700, controlled by a W-Ie-Ne-R MPOD Crate, would be a suitable choice. Both systems have a fast hardware current trip with a channel-wise adjustable current trip limit and can be controlled via SNMP commands over Ethernet or directly over CAN bus. For the large prototype a similar system is in use (30 kV module ISEG HPn300 instead of HPn700) and shows good functionality and reliability.

At these high voltages the security systems and the emergency behavior are important issues. The current architecture of an emergency high voltage shutdown system offers two solutions. A purely hardware based approach and a hardware plus software approach.

The hardware approach couples the HV system of the cathode plus field cage with the HV system of the GEM stack by an interlock cable. In case of a trip in one of the two systems the combined system is shutdown immediately and has to be ramped up from zero again. Since a trip in the GEM stack in this scenario also causes the drift voltage to trip, the ramping of which takes several hours, this introduces a significant dead time of the detectors, which is clearly disfavored during the time of operation.

The hardware plus software approach decouples the HV systems for the GEM stack and the drift cathode from each other. In case of a trip of one of the systems only the tripping system is shut down by hardware. To minimize the the potential danger of sustained discharges between the first GEM layer and the last field strip in case of a trip of the GEM stack, a software adjustment of the drift cathode voltage to a level of 60% has been implemented. This system has shown a good performance and has minimized the dead time significantly.

Besides the trip behavior, two security functions have been implemented purely on the software side: if the measured voltages rise above the set point voltage or if the current steps up unexpectedly the TPC should be ramped down within a short time to prevent severe damages. For the large prototype the voltage set point is compared with the moving average of the last measured values to detect these over-voltages. To detect any over-currents the average of the last ten measured values is compared with the average from ten seconds earlier.

Especially the currents are good indicators for a possible failure of the detector, because any shortcut between the GEM foils or at the field cage will result in a higher current. Therefore they have to be measured frequently and with high precision and be visible all the time.

To calculate the desired voltages from given values for the fields, distances and GEM foil potentials and to configure a ramp automation a GUI should be used (see Fig. 4.34). When ramping up the chamber, it is important to do this synchronously for all voltages (see Fig. 4.35) and with a slow ramp speed to avoid unwanted and dangerously high potentials between the GEM foils.

From the physical point of view it is necessary to monitor and save all voltages since the electron drift velocity arises from the applied drift field and the gain of GEM detectors is clearly linked to the adjusted settings. Furthermore it would be good to

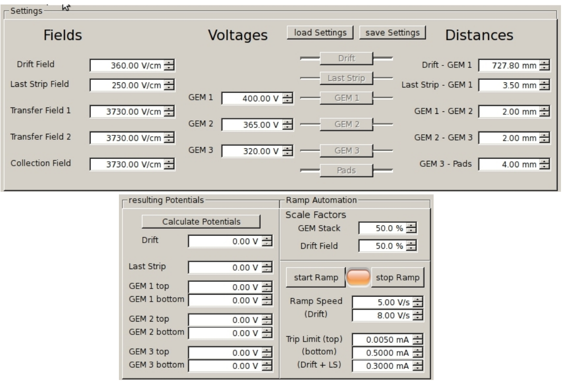

Drift Field 360.00 V/cm
Last Strip Field 250.00 V/cm
Transfer Field 1 3730.00 V/cm
Transfer Field 2 3730.00 V/cm
Collection Field 3730.00 V/cm
GEM 1 400.00 V
GEM 2 365.00 V
GEM 3 320.00 V
Drift - GEM 1 727.80 mm
Last Strip - GEM 1 3.50 mm
GEM 1 - GEM 2 2.00 mm
GEM 2 - GEM 3 2.00 mm
GEM 3 - Pads 4.00 mm

Drift 0.00 V
Last Strip 0.00 V
GEM 1 top 0.00 V
GEM 1 bottom 0.00 V
GEM 2 top 0.00 V
GEM 2 bottom 0.00 V
GEM 3 top 0.00 V
GEM 3 bottom 0.00 V

GEM Stack 50.0 %
Drift Field 50.0 %
Ramp Speed 5.00 V/s
(Drift) 8.00 V/s
Trip Limit (top) 0.0050 mA
(bottom) 0.5000 mA
(Drift + LS) 0.3000 mA

Figure 4.34: Graphical interface to set up the TPC high voltage for the large prototype. In the upper field the different settings can be adjusted. The lower box shows the calculated potentials and the settings for the ramp automation.

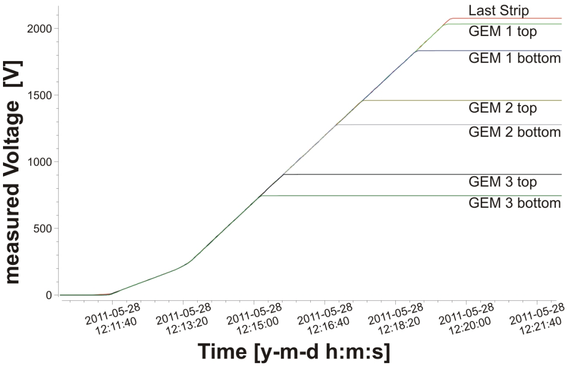

Figure 4.35: View of the voltages applied to the GEM foils when ramping up the chamber.

store these main parameters together with the taken data for the later analysis.

4.7.2 Low Voltage System

The low voltage for the Front-end electronics (FEE) will be provided by the $\overline{\mathrm{P}}$ANDA central low voltage supplies with a voltage of 48 V. Two or four such channels will be used, nevertheless each card can be switched on/off individually.

Three different powering schemes are being discussed at the moment.

- The first scheme is using air coils for DC-DC converters on the FEE. One has to investigate the influence of the high operating frequencies of the order of MHz on the noise of the FEE.
- The second solution is to put regular DC-DC converters just outside of the solenoid. The cable length from the DC-DC converters to the FEE will not exceed 2–3 m and the voltage drop over the cables will be sensed at destination.
- The last option is to power the FEE directly over long cables without voltage regulators at the FEE. This has been implemented successfully by the CMS tracker [34, 35].

For all options we foresee a maximum power consumption of 25 mW per channel, giving a maximal total power consumption of 2 kW. The power supplies will be floating with their ground being defined by the detector to avoid ground loops.

4.7.3 Front-end Electronics

Monitoring operation conditions and remote actions on all 320 front-end cards is important for stable data taking. It is foreseen to equip each front-end card with PT100 temperature sensors, voltage and current monitors. The slow control master will access these information with regular time intervals via optical interfaces. If one of the parameters exceeds its boundary conditions then the front-end card will be switched off by pulling down the voltage level of the safety wire.

Configuration of front-end electronics, reading status registers of front-end ASIC chips and injection of test pulses are also performed via the slow control interface.

4.7.4 Temperature Sensors

The temperature fluctuations of the detector gas have a major impact on the electron drift velocity. As the drift velocity is not on the plateau but on the slope region, monitoring of the gas temperature is crucial. Therefore several uniformly distributed temperature sensors are foreseen to get a precise distribution of the temperatures inside the TPC. Most of the sensors will be integrated into the walls of the field cage, since they should be as near to the active volume as possible but cannot be mounted inside the detector to preserve field homogeneity. More sensors will be installed on the pad plane to control the heat dissipation of the electronics. Also the temperature of the gas at the inlet and outlet will be monitored.

Due to the high number of needed sensors the use of PT100 or other analog temperature sensors would add many additional wires and material. Therefore digital readout sensors are advisable. For the proposed SMD mounted 1-wire sensors one can reduce

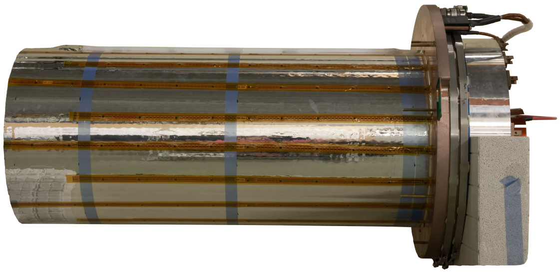

Figure 4.36: View of the TPC with the attached temperature sensors on the field cage. The sensors are placed every 5 cm on the yellow stripes.

the number to only two wires (ground and combined voltage/signal wire). Since the TPC is planned to be stabilized in the order of $\pm 0.2\,K$ the precision of the used sensors have be in the same order of magnitude.

At the large prototype 210 Dallas 1-Wire sensors (18B20U, see Fig. 4.36) with a USB readout are mounted on the outer field cage. Twelve analog PT100 sensors are attached to the pad plane. Unfortunately the 1-wire sensors induced too much noise during the prototype tests in the TPC FEE and the neighboring detectors due to the USB communication, which therefore had to be reduced to 9-bit and less frequent readout. For the $\overline{\text{P}}$ANDA TPC the usage of thin shielded twisted wires will be investigated to overcome crosstalk between adjacent detectors.

4.7.5 Gas

The gas control will follow the general layout of the PANDA slow control. In particular, it will be similar to the internal target slow control system.

The main hardware of the gas control equipment consists of a Compact Reconfigurable I/O (cRIO) made by National Instruments as a front-end real-time embedded controller. This system consists of a real-time controller, a chassis with an integrated FPGA and several easily exchangeable I/O modules (see Fig.4.37). This allows a secure, standalone solution, which is independent from generally used computer networks. Signals from sensors and actuators (e.g. pressure sensors) will be read out by input modules and control signals (e.g. mass flow controllers) are sent to the correct devices via output modules.

On a higher level, users will be able to interact with the gas control system via a Graphical User Interface (using LabVIEW). This will ensure an easy integration of the gas control system into the general PANDA Control System.

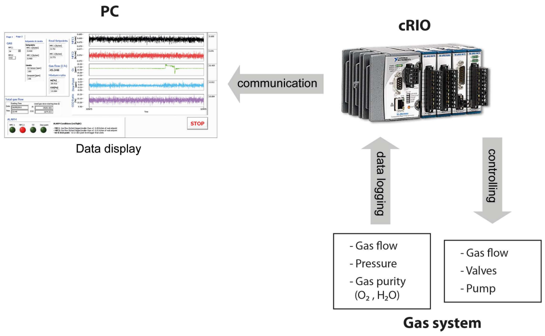

Figure 4.37: Block diagram of the main principle of the gas slow control.

4.7.6 Calibration

Any laser system as described in Sec. 4.6.1 requires remote control at least while it is active, which is basically realized by a simple trigger signal. In order to be able to deduce an intensity information, the stability of the laser has to be monitored either at the source or at the detectors place, e.g. by suitable photo diodes or something equivalent and the appropriate read-out electronics.

With respect to the calibration system based on Krypton gas as described in Sec. 4.6.2 simple remote controllable valves are sufficient to switch on and off this feature. In order to monitor the status of such a apparatus a few DC-level signal lines and a very simple electronic is needed.

4.8 Readout Electronics

4.8.1 Overview

The full TPC readout chain is shown in Fig. 4.38. It consists of the following components:

- 320 front-end cards, equipped with charge sensitive amplifiers, hit detection and digitization circuits,
- optical links,
- 40 data concentrator modules, performing feature extraction (time, amplitude) and cluster finding,
- high-speed serial links,
- data acquisition network,

- compute nodes for online reconstruction.

The front-end cards are mounted directly on the back side of the readout plane to minimize input capacitance to the CSAs. Since the electronic density is relatively low, the front-end cards are mounted perpendicularly to the readout plane (as it has been done on the large prototype chamber, cf. Sec. 4.12.1.3). Each front-end card reads 256 detector channels. According to the data-driven readout architecture of the $\overline{\mathsf{P}}$ANDA experiment, hits have to be detected autonomously, i.e. without requiring an external trigger signal. The analog signals are digitized and marked by a time stamp. A single optical link connects each front-end card to a data concentrator module. The link is shared between three independent interfaces: timing distribution (SODA), slow control and data taking. Each data concentrator module reads data from 8 front-end cards. It extracts time and amplitude of a signal on a pad by pulse shape analysis (PSA) of the samples received from the front-end cards ("feature extraction"). These pad hits are then combined in time and space to clusters ("cluster finding"). From the data concentrator modules the data are sent through high-speed serial links to the $\overline{\mathsf{P}}$ANDA data acquisition system, consisting of a large-bandwidth network fabric, which distributes the data from all sub-detectors to so-called compute nodes. These perform online processing of information combined in so-called super-bursts, corresponding to data from a time period of 0.5 ms, i.e. 10 full TPC drift frames with an overlap of 10% in order not to suffer from split tracks.

4.8.2 Front-end Electronics

The TPC measures three dimensional coordinates of charged particle trajectories. While the x and y coordinates are determined by processing charge information induced on a pad or group of pads of the readout plane, the z coordinate is obtained from the electron drift time between the primary ionization position towards the gas amplification stage and eventually the readout plane. The signal induced on the pads by the electrons emerging from the last GEM foil has a fast rise time (less than 1 ns) and a duration of about 50 ns, which is given by the drift time of electrons between the last GEM and the readout plane.

The readout plane has a shape of a ring with inner and outer radius of 15.5 cm and 41 cm, respectively. It is segmented into 80000 hexagonal pads of 1.5 mm outer radius each. The pads are read out by a Charge Sensitive Amplifier (CSA) followed by a shaper. The parameters of these analogue circuits are optimized for low noise and fast shaping time. The noise performance of the electronics uniquely determines the minimum needed gas amplification of the GEM stack, which in turn defines the ion backflow and the performance of the TPC as tracking detector: the lower the noise the lower the ion backflow and consequently the lower the distortion of measured primary cluster coordinates. Thus it is very important to develop front-end electronics with a noise performance as low as possibly achievable. The minimum shaper peaking time for the TPC is about 120 ns, which is defined by the duration of the electron signal of $\sim$ 50 ns and the average width in time of a charge cluster after 150 cm of drift due to longitudinal diffusion of $\sim$ 100 ns. Shaping times longer than about 150 ns lead to excessive occupancies, especially for pads on the inner circumference of the chamber. The design of modern analogue circuits usually allows adjusting of the peaking time within this range and optimizing detector performance for particular operational conditions. A value of the ENC of 600–630 e^- at 13–16 pF of input capacitance has been reached with the front-end electronics for the large prototype (cf. Sec. 4.12), including the digitization noise of $\sim$ 150 e^-. Subtracting the digitization noise quadratically, the ENC of the front-end electronics is in the range 580–600 e^-. For the prototype, the main contribution to the input capacitance comes from the packaging of the ASIC itself (10 pF), and the traces on the PCB between the connector and the ASIC (3–5 pF). The pad contribution is only 0.2 pF and thus negligible. Optimizing the input capacitance to values between 3 and 5 pF, a noise of 400–450 e^- can be reached. This value is thus defined as the maximum acceptable for the TPC detector.

Another important requirement parameter is the average hit rate per pad. The $\overline{\mathsf{P}}$ANDA experiment will run at $2 \cdot 10^7\,\mathrm{s}^{-1}$ annihilations per second. The hit rate per pad for the inner pads is expected to be 200 kHz while for the outer pads it will be below 100 kHz. The PANDA experiment will operate in continuous, trigger-less mode requiring the development of a new type of data driven front-end electronics, which autonomously identifies detector signals and marks them with temporal information.

Table 4.7 lists the main requirements for the front-end electronics.

At the moment of writing there are three ASICs which are being developed for trigger-less experiments and which are thus considered for the $\overline{\mathsf{P}}$ANDA TPC :

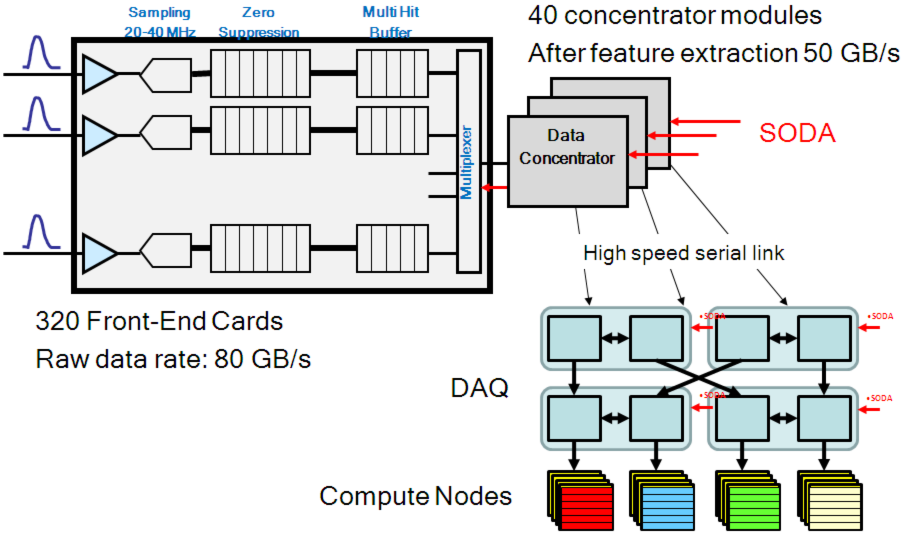

Figure 4.38: Schematic view of the TPC readout chain, including the $\overline{\text{P}}$ANDA data acquisition system (lower right corner).

Parameter	Value
Number of channels	80000
Signal polarity	negative
SNR (for MIP)	25
Dynamic range	10 bits
Noise (ENC)	400 e^- at 3 pF
Sensitivity	400 e^- per ADC bit
Shaping time	120–150 ns
Sampling rate	20–30 MHz
Power consumption	15 mW/channel

Table 4.7: Requirements for front-end electronics.

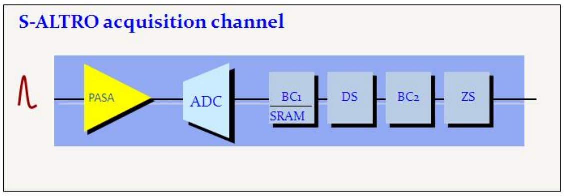

Figure 4.39: S-ALTRO ASIC architecture.

- S-ALTRO,
- Transient Recorder,
- SPADIC.

All those chips are mixed analogue-digital integrated circuits dedicated to run in continuous, data driven mode. The chip parameters are summarized in Table 4.8.

4.8.2.1 S-ALTRO

The S-ALTRO chip [36] is being developed by the CERN microelectronic group for the TPC at the International Linear Collider. Every channel of the chip includes an amplification stage with CSA and fourth order CR-RC^4 shaper, 40 MHz 10 bit pipelined ADC and advanced digital signal processing logic as shown in Fig. 4.39. The micro-electronic group recently received a first demonstrator chip with 16 channels and a total power consumption of 750 mW. 80% of the power consumption goes to ADCs. The main goal of this version of the chip is to demonstrate the feasibility and performance of the chip architecture.

The power consumption of the chip can be drastically reduced by using modern ADC designs which are able to achieve 4 mW/channel with similar resolution and sampling rate. If the development of the S-ALTRO chip is continued then the next generation of the chip will use low power consumption ADCs reducing the power to 12–15 mW/channel and increasing the integration level to 64 or even 128 channels per die.

4.8.2.2 Transient Recorder

The Transient Recorder ASIC is being developed by the GSI ASIC group. It is an alternative to the S-ALTRO approach, where zero suppression is done before digitization. After zero suppression the amount of information is significantly reduced allowing multiplexing of the detected samples from 32 channels into a single ADC. The architecture of the chip is shown in Figure 4.40; it consists of a Switched Capacitor Array, a zero suppression circuit and a pipelined ADC. The digitized information is transmitted to the next readout level via a serial link. The Transient Recorder requires a detector specific preamplifier-shaper chip for amplification and signal conditioning. It is foreseen to use the PCA16 ASIC, the front side of the S-ALTRO which includes a preamplifier and a shaper. The first prototype will be submitted for production in summer 2011.

4.8.2.3 SPADIC

The SPADIC ASIC is being developed at the University of Heidelberg for the Transition Radiation Detector of the CBM experiment at FAIR [37]. The chip has a similar architecture as the S-ALTRO, where every channel includes an amplification stage, a pipelined ADC and digital logic for signal processing. The chip is fabricated in UMC 0.18 μm technology and serves 32 detector channels. The dynamic range of the chip is 40 fC which is smaller than the charge created by low momentum particles on a pad by about a factor of two. Knowing the signal shape, however, it is possible to recover the amplitude information at a stage of feature extraction even with some channels in saturation. The advantage of the SPADIC chip is its low power consumption of 5 mW per ADC. The first prototype has been tested at the end 2010.

4.8.3 Feature Extraction

The data from a front-end card are transferred to so-called data concentrator modules. Here the following operations are performed:

- pulse shape analysis on the pad level to obtain the signal time and amplitude,
- sorting of data according to time slices,
- optionally cluster finding in order to further reduce the data rate at the output.

A first prototype of the data concentrator module is in development now at TU München. Figure 4.41 shows its functional diagram and a 3-D model. The module is based on Lattice FPGA featuring 16 high speed serial links. Up to 8 of such modules can be mounted on a single carrier card following the ATCA (Advanced Telecommunications Computing Architecture) standard. The optical transceivers are mounted on a separate module in the ATCA crate. The expected bandwidth of the module is 1.6 GB/s.

4.8.4 Data rates

The raw hit information is encoded into a 40 bit data word which includes 8 bits of channel number, 24 bits of three sample amplitudes and 7 bits of time tag. The raw data rate is about 80 GB/s at the output of the front-end cards. The first data reduction is done in a concentrator module by analyzing three amplitude values and extracting hit amplitude and time information. After feature extraction the data rate is reduced to about 50 GB/s. The next step in the data processing is clustering which is done after merging time correlated information into single data block. Clustering reduces the data rate down to 25 GB/s.

4.8.5 Online Reconstruction

After digitization, feature extraction and cluster finding, the data of all $\overline{\text{P}}$ANDA detectors are sent via high-speed serial links to the data acquisition network (FPGA-based or Infiniband, about 500 GB/s total bandwidth), which distributes them in a time-sorted manner to the Compute Nodes. These are custom-made ATCA modules, which form the platform to run online reconstruction and event selection algorithms. For online track reconstruction, two options are currently being pursued inside $\overline{\text{P}}$ANDA:

- FPGA-based algorithms [38, ?, 39],
- GPU-based algorithms [?, 40].

Figure 4.42 illustrates the logic steps foreseen for the reconstruction of data from the TPC as well as the merging with the information from other detectors and the selection of interesting events.

The pattern recognition and piece-wise reconstruction of tracks (tracklets) first proceeds in parallel and completely independent in eight geographic sectors of the TPC. Here, local pattern recognition is

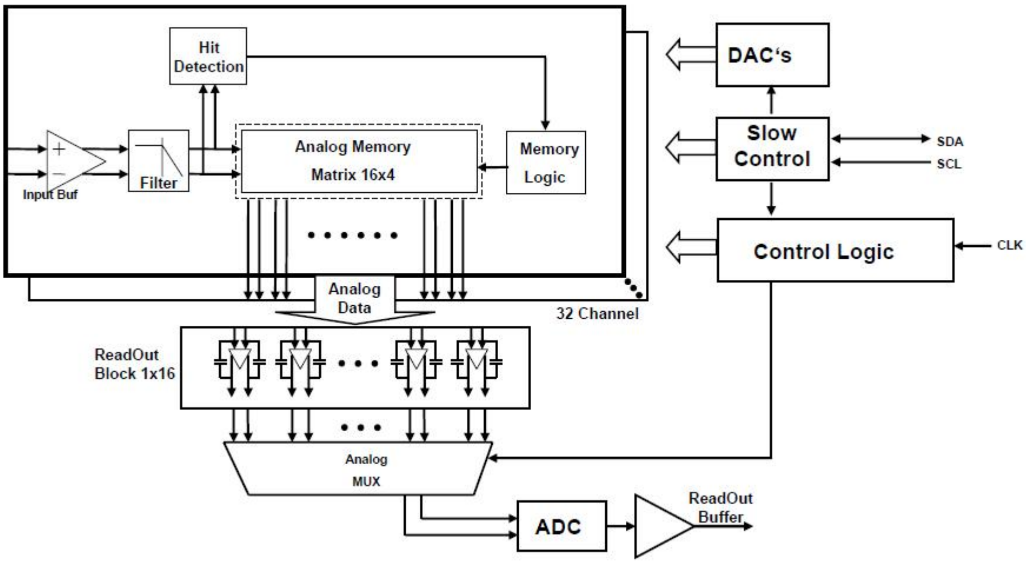

Figure 4.40: Transient Recorder ASIC functional diagram.

	S-ALTRO	PCA16 + TR	SPADIC
Process	IBM 0.13 μm	IBM 0.13 μm + UMC 0.18 μm	UMC 0.18 μm
Sensitivity	12 mV/fC	12 mV/fC	0.08 fC/ADCch.
Noise(ENC)	500 e^- at 5 pF	500 e^- at 5 pF	800 e^- at 30 pF
Dynamic range	10 bits	10 bits	8(9) bits
Peaking time	30–120 ns	30–120 ns	90 ns
Sampling rate	20–40 MHz	20–100 MHz	25 MHz
Power consumption	46 mW/ch	10 mW/ch	12 mW/ch

Table 4.8: Parameters of ASICs considered for the $\overline{\text{P}}$ANDA TPC.

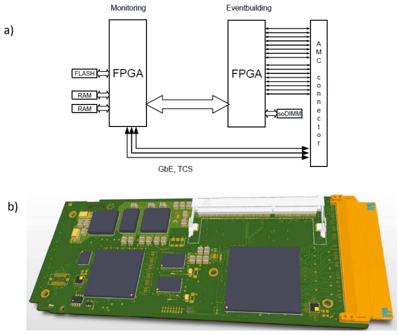

Figure 4.41: The TPC data concentrator module functional diagram and 3-D model.

performed by using advanced algorithms such as conformal mapping and Fast Hough Transform (cf. Sec 4.10.7.8 for details).

In the next stage, the tracklets from the individual sectors are merged making use of the preliminary helix parameters determined in the first step. At this step, first raw distortion corrections in the $r\phi$-plane will be applied to the tracks. A preliminary sorting of tracks is done based on the assumption that the tracks originate from the target ("target pointing"). At this stage, also more demanding algorithms selecting interesting event signatures in the TPC can be applied. These include

- decays of neutral particles, e.g. Λs,
- kinks in charged particle tracks, e.g. from Ξ decays,
- detection of $\pi \rightarrow \mu$ decays (important for background rejection in the muon range system of $\overline{\text{P}}$ANDA).

In the next stage, the information from the TPC will be combined with that from other detectors, e.g. the Micro-Vertex Detector or the Barrel ToF

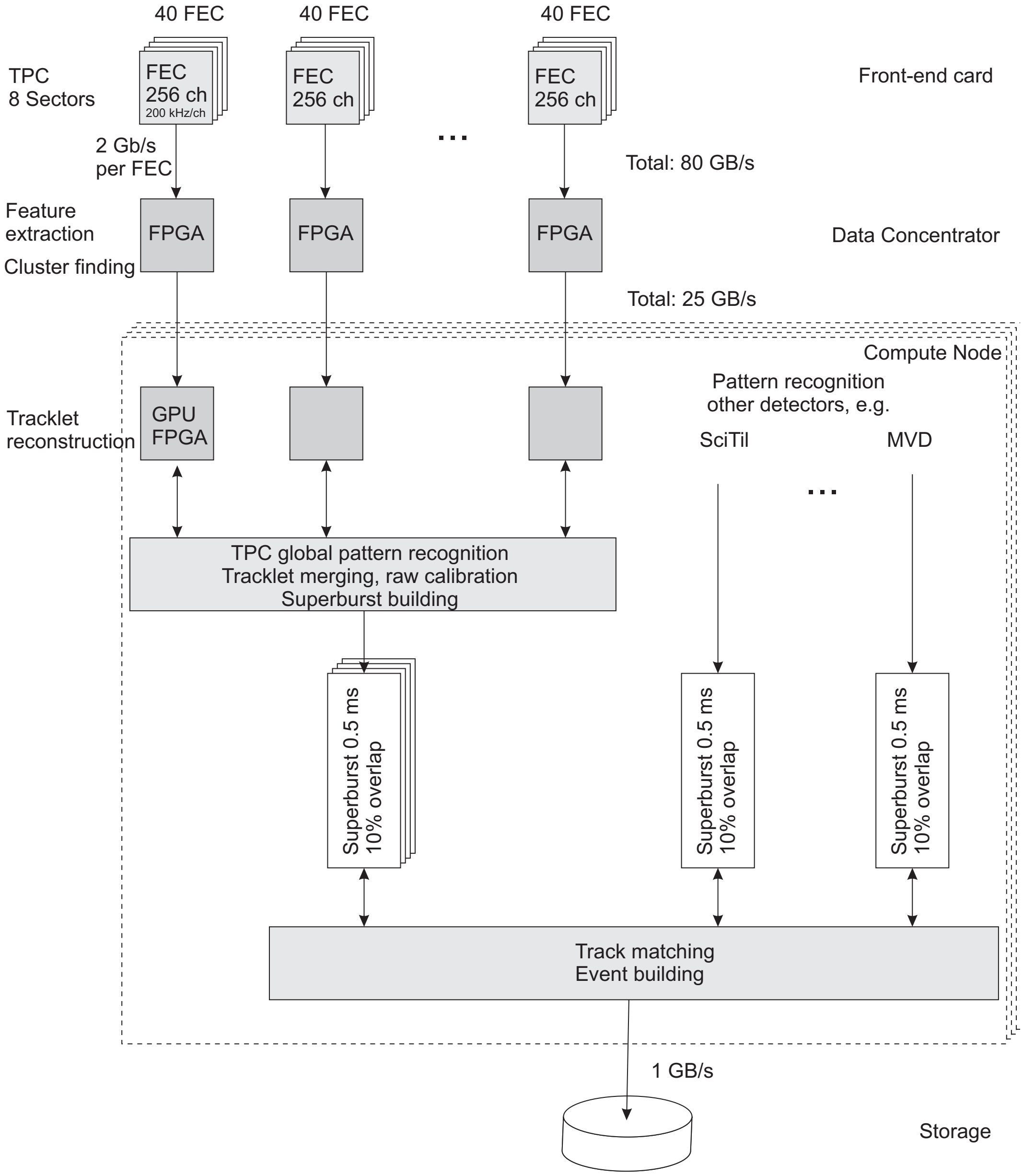

Figure 4.42: Flow diagram of the logic steps for online data reconstruction in the TPC, merging of data and event selection.

Detector. For the MVD, this will be done following the same scheme which has already been applied on simulation level (cf. Sec. 4.10.13):

- selection of TPC tracks (after target pointing) within a given time window (e.g. $\pm 200\,\mathrm{ns}$) around the time determined by the MVD (e.g. a displaced vertex),
- extrapolating the TPC track to the MVD and picking up MVD hits within a coarse roadwidth ($\mathcal{O}(1\,\mathrm{mm})$).

In this way, events with tracks originating from the primary vertex were shown to be identified with an efficiency of $> 95\%$ in Monte Carlo simulations. In a similar way, information from the Barrel ToF with its fine granularity of $3 \times 3\,\mathrm{cm}^2$ will also be used to assign an absolute time to tracks in the TPC.

Groups of tracks and signals which have been identified to bear a common physics signature are then stored or transferred for further analysis. In order to be able to apply full distortion corrections and advanced fitting algorithms, the preliminary track information determined in the global pattern recognition stage as well as the raw cluster data will be stored.

4.9 Cooling System

4.9.1 Requirements

The basic paradigm in operating the detector is to take away all heat introduced by the electronics into the detector and its surrounding in order to avoid that even a small percentage of it is transferred to the Pad-Plane and fed into the gas volume. This would cause a density gradient in the gas which is a source of inhomogeneities in drift velocity of the charge carriers.

The front-end electronics of the TPC is confined in a small volume where radiative or convection cooling is not effective enough nor applicable due to the high spatial density of the modules. Thus a closed loop cooling-system based on the liquid coolant HFE7100 has been set up. It fully exploits passive heat transfer processes from the electronics to a coolant circulating through a helix of canals with small cross-sections optimized for low-material budget. The flow of the low-viscosity medium is strictly turbulent throughout the structure to support optimal heat-exchange. The design of the light-weight heat exchange structure is facilitating the easy exchange of the front-end cards due to its key and slot geometry. The walls are made from aluminium and are providing the shielding characteristics of a Faraday cage. No tubing is required from card to card and only two joints equipped with self-closing and dead-volume free valves are necessary on the detector, one at the input and one at the output. This is minimizing the risks taken by introducing liquid coolants in the vicinity of electronics and neighboring detector systems. The coolant itself is nontoxic, noncorrosive, electrically nonconducting and has a vapor pressure which is low enough that it is vaporizing residue-free at room temperature.

For simplicity a central chiller with cooling, heating and reservoir option which can digest a 10 kW heat load is working in a 1-step closed circuit without a separate heat-exchanger. The system is operating in overpressure mode in order to avoid problems which often occur in under-pressure systems arising from differences in height-levels within the experimental set up (as faced by other experiments).

The system is remote controllable within a wide range of operation conditions. The operation point is chosen in a way that at any position inside the PANDA magnet the local temperature at the surface of the cooling structures does not reach the dew point. This way only a small amount of thermal isolation is needed and no perspiration water is to be expected at surfaces.

4.9.2 Layout

A cooling system envisaged to be used with the PANDA-TPC has been set up for the Large Prototype TPC. It is designed to work with overpressure and can digest up to 5 kW of thermal energy. Flow is kept strictly turbulent inside the detector-near structures in order to optimize heat transfer from the cooled surfaces to the coolant. With a media input temperature of 12 °C the output temperature does not exceed 25 °C.

The coolant is of type HFE7100 and has the following advantages over a conventional water cooling medium:

- low viscosity (lower than water), best suited for low-profile channels
- low vapor pressure at the operation condition given, thus it would vanish without remains even if there is a leakage incident
- electrically isolating, non corrosive, best suited to be used in the vicinity of electronics

For the chiller we use a very compact module type Huber Unichiller UCHT operating with ambient air.

The main unit and several sensors measuring the temperatures and pressures in the system at various places is included into the detector control system to ease remote control and setting of operation conditions (see Sec. 4.7).

4.10 Simulation of Detector Performance

An important tool to assess the general feasibility and estimate the actual performance of a complex detector system like the GEM-TPC for $\overline{\mathsf{P}}$ANDA are computer simulations. During R&D of the GEM-TPC detector, behavior has been modeled and studied in great detail using the tools provided by Pan-

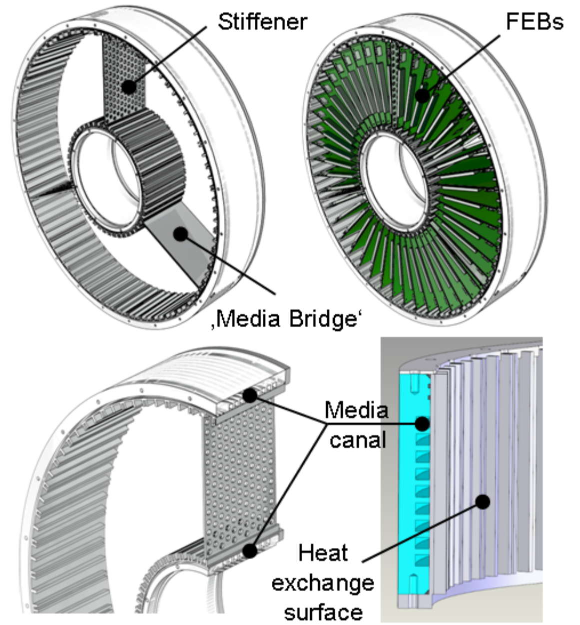

Figure 4.43: Design of the cooling structures without (upper left) and with (upper right) front-end boards (FEBs) installed. The lower part of the picture shows cutouts visualizing the helix of the media channels milled into the plastics part of the structure. The part facing the FEBs is made from chromatized Aluminium of 0.5 mm thickness of the heat-exchanger walls.

daRoot, the common `C++` computing framework developed within the $\overline{\text{P}}$ANDA community.

In Secs. 4.10.1 to 4.10.4, we give an overview of the simulation chain as it is implemented in the PandaRoot framework. Various algorithms for the reconstruction of tracks have been developed and are described in Sec. 4.10.4 and following. Results from simulations are reported in Sec. 4.10.9.

4.10.1 Simulation Chain Overview

We shall briefly describe the general structure of simulations, as implemented in the PandaRoot software framework [23]. Logically, the full simulation chain can be divided into three steps:

1. *“Monte Carlo”* simulations: particle generation and transportation,

2. *Digitization*: simulation of detector response,

3. *Reconstruction*: extraction of track parameters.

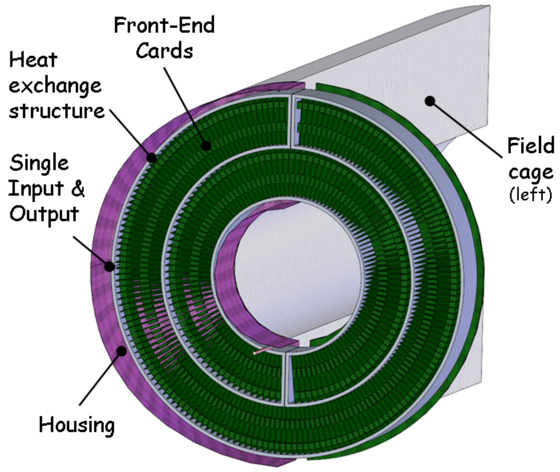

Figure 4.44: Conceptional design of the cooling structures envisaged for the PANTA-TPC. The structures give room for 320 Front-end Electronic Boards (FEB) each serving to read out 256 channels. Each card is assumed to introduce a heat load of up to 6.5 W on a surface of approximately 70 cm^2. The arrangement of the cards makes maximal use of available space exploiting the symmetry of the layout and the high-density plug currently used as input connector in the Large-Prototype TPC (see Sec. 4.12.1). Until now there is no higher pin-out available on the market meeting our requirements. This poses limitations in the shape and max. number in the arrangement of the FEBs which currently would serve for the readout of approx 76k channels.

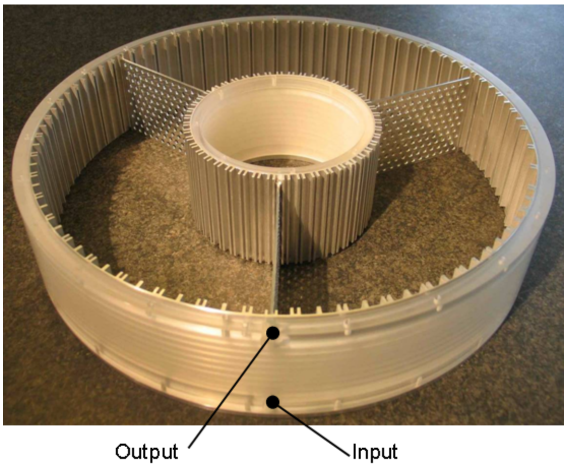

Figure 4.45: Photo of the realization of the system done for the Large Prototype TPC. Only two joints are required for the whole assembly which are labeled as ’Input’ and ’Output’, respectively.

4.10.2 Monte Carlo Simulations

In the first step of the chain starting values for physical particles traveling inside the detector volumes

Figure 4.46: Photo of the heater/chiller module Unichiller UHCT with a cooling capability of ≈ 10 kW.

are sampled from distributions from various models basically by “throwing the dice” (hence the term *“Monte Carlo simulations”*). These models range from simple “particle guns” simulating just one sort of particle at given momenta/angles to full-scale $\bar{p}p$-physics generators. The obtained generated particles (e.g. the starting values of their physical properties) are then extrapolated (*“transported”*) through the different layers of materials, based on a detailed geometrical model of the full $\overline{\mathrm{P}}$ANDA spectrometer. Figure 4.47 shows the geometrical model of the TPC as it is currently implemented in the simulation. The final result of this first step in the simulation chain is a set of space-points with attached information of associated momentum and energy loss, so-called *Monte Carlo (MC) Points.*

The piece of software responsible for this transportation is a widely-used community standard called *GEANT* [?]. GEANT has initially been developed at CERN as a package of FORTRAN routines and has been supported by CERN as a quasi-standard for many years up to its release version GEANT3. More recently, it has been ported to `C++` and extended by many features. The latest version available at CERN is GEANT 4 9.4.

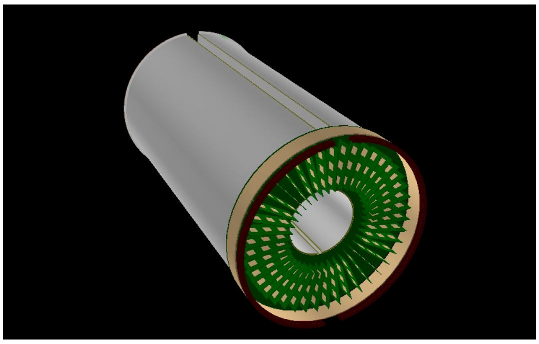

Figure 4.47: TPC geometry model as currently present in the Monte Carlo simulations. Placeholder volumes have been put where the final design is unclear (e.g. front-end electronics, cooling).

GEANT4 has a number of advantages over its older FORTRAN-based predecessor. The one with the most impact for TPC simulations is a more realistic set of algorithms to treat energy loss due to ionization processes (Photo Absorption Ionization (PAI) model). Unfortunately, until very recently, there have been known problems involving these algorithms when working inside gaseous media, visible e.g. as un-physical energy loss distributions inside the TPC simulations. These problems have led us to work with GEANT in the previous version 3 for many years, however adapting an improved and more transparent method of calculating the energy loss inside the drift gas that was originally developed by the ALICE TPC collaboration [?], referred to as the *“ALICE model”* from here on. This model basically uses known gas properties to sample the step length between collisions (Poisson-statistics), using the Bethe-Bloch-Formula to construct the momentum-dependence. The energy loss for each collision is calculated using a modified Rutherford cross section: to mimic the atomic binding of the electrons, the energy dependence of the cross section has been set to

$$\left(\frac{\mathrm{d}\sigma(E)}{\mathrm{d}E}\right)_{\mathrm{ALICE}} \propto E^{-2.2}. \qquad (4.2)$$

[?, 41]. This choice has been found to reproduce the collision cross-section obtained with a PAI simulation reasonably well (c.f. Fig. 4.48). However, the resulting energy loss distributions (*“straggling functions”*) tend to peak at slightly lower values for the ALICE model when compared to PAI results [?], possibly decreasing energy deposition and hence the obtained energy loss resolution of the detector in the simulation.

More detailed comparisons between GEANT3 and

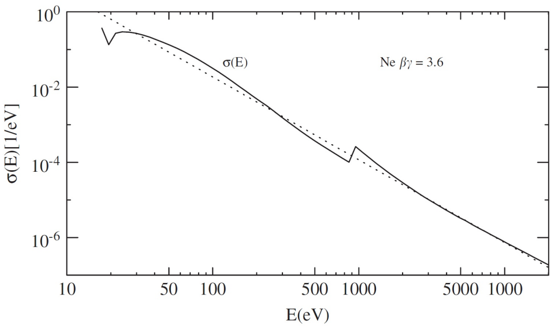

Figure 4.48: Comparison of inelastic collision cross-section $\sigma(E\,|\,\beta\gamma = 3.6)$ in Neon gas as obtained from the PAI method (solid line) and modified Rutherford cross-section of the ALICE MC model (Eq. 4.2). The ALICE coefficients have been chosen to match λ of the PAI model at $\beta\gamma = 3.6$ [?].

GEANT4 will have to be made in the near future. The very recent update of GEANT4 in the simulation framework has unfortunately made it impossible to do full simulations with the superior ionization models already in the course of this work.

4.10.3 Digitization

The second step (*"digitization"*) comprises the modeling of all physical and conceptual processes taking place in the sub-detectors of $\overline{\text{P}}$ANDA, from the initial deposition of charge up to the signal creation in the readout electronics. The responsible simulation code from here on is organized in a modular fashion in so-called *tasks* to allow easy enabling/disabling or replacing of single steps or algorithms. In the case of the GEM-TPC, the procedure can be summarized by only a few essential building blocks as shown in 4.49:

- Conversion of deposited energy in the detector gas into primary electron clusters
- Drifting of the primary clusters towards the readout, taking into account attachment, diffusion and field effects.
- Charge amplification in the GEM-stack
- Response of the pickup pads to the arriving electron avalanches (pad-response-function)
- Signal creation
- ADC sampling

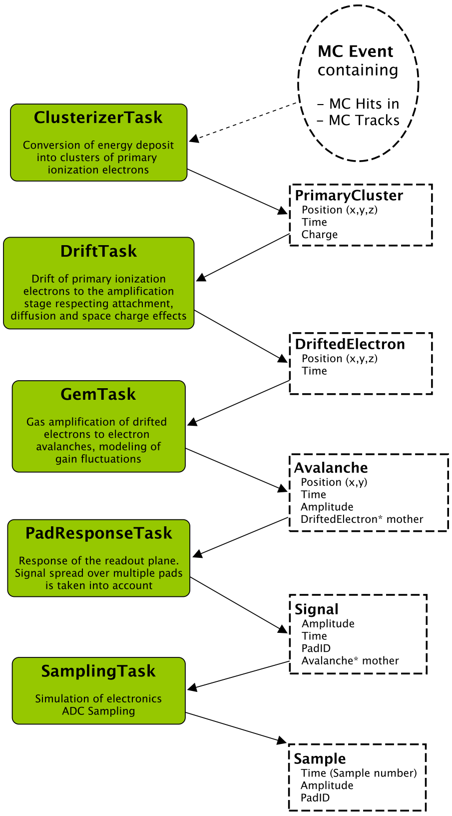

Figure 4.49: Standard work flow scheme of the $\overline{\text{P}}$ANDA TPC digitization. The output objects of each task are listed on the right. The simulation expert can chose individually, if they should be persistent, e.g. written to file.

4.10.4 Reconstruction

After the digitization stage of the simulation chain the obtained data resembles the digitized front-end electronics output of a fully equipped $\overline{\text{P}}$ANDA GEM-TPC, i.e. amplitude information for pad-time bins ("samples"). Ideally, all code developed for the *reconstruction* stage will be able to directly run on the data of the actual detector, once it has been built. As we will demonstrate in Sec. 4.12, this goal has already been achieved for the data recently taken with the large GEM-TPC prototype. The reconstruction stage comprises the following steps:

- Pulse Shape Analysis (PSA): adjacent samples in time on each pad are combined to pulse signals ("digits"), assigning to them a time and an amplitude.
- Cluster Finding: these digits are then grouped in space and time by the Cluster Finding task. The clusters, 3-D space points with a given amplitude, are the input to the

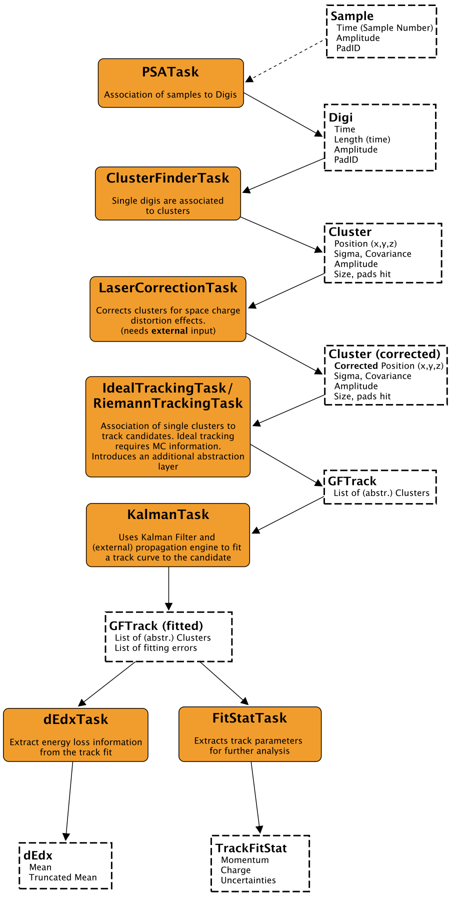

Figure 4.50: Standard work flow scheme of the $\overline{\text{P}}$ANDA TPC reconstruction. The output objects of each task are listed on the right. The simulation expert can chose individually, if they should be persistent, e.g. written to file.

- Pattern Recognition algorithm and the
- Track Fitting algorithm, which finally extracts the physical properties of the track.

Figure 4.50 sketches the most important tasks of the reconstruction stage. All of these algorithms will have to run in close-to real-time during data taking with $\overline{\text{P}}$ANDA, as their results are needed as input for the online trigger system. In the following sections, the individual steps will be described in detail.

4.10.5 Pulse Shape Analysis

The first step is thus to combine single “samples” from the ADC to signals of a given time and amplitude. For the simulations and the analysis of the TPC Prototype data a simple PSA algorithm has been implemented. It starts a pulse if two consecutive samples are above a given threshold. Further samples are added to the pulse until a local minimum or a sample below threshold is found. The maximum amplitude is then assigned to be the amplitude of the signal (as opposed to a integration over the full signal width). Due to the symmetrical shape of the pulse, the time of the signal is calculated as the mean of the peak time and the center of the pulse. An example of this PSA algorithm used on real data taken with the TPC prototype can be seen in Fig. 4.51.

4.10.6 Cluster Finding

An important tool for data reduction in the TPC readout scheme is clustering, e.g. combining the digis origination from some spatially well-defined accumulation of charge in the chamber to one single object - a so-called *cluster*.

A cluster in this sense is fully defined by

- the position (charge center of gravity) with error, and
- the total amplitude.

The standard implementation of the cluster finding algorithm starts by presorting all available digis by decreasing amplitude. It then loops over all digis, checking if a digi is

- an immediate neighbor (pad-wise) to an already existing cluster,
- and it is close enough in z-direction, e.g. it lies within a certain *time slice* around an existing cluster.

Consequently, the algorithm will start clustering around local maxima of deposited charge. If no matching cluster is found, a new cluster is created. If more than one cluster matches the digi, it is split, e.g. its amplitude is divided by the number of matching clusters and the digi is assigned to each of them. A threshold on cluster amplitude prevents isolated low-amplitude hits to form individual clusters, serving as an effective way of suppressing electronic noise.

As every digi needs to be checked against every cluster, the algorithm gets quite costly for large numbers of digis. To overcome this limitation, the digis are processed independently for each sector of the pad-plane and, additionally, a sectorization in z is performed. This sectorization is subject to further optimization.

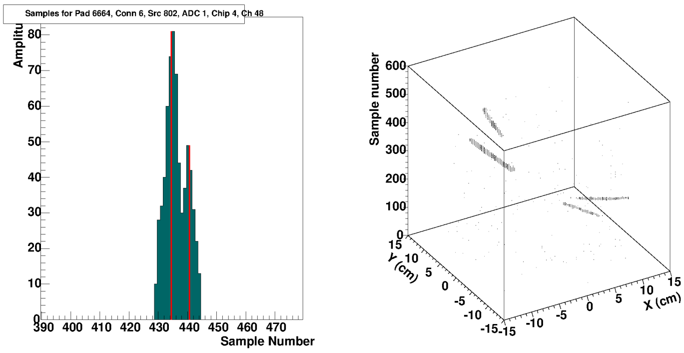

Figure 4.51: Example of the PSA on real data taken taken with the TPC-Prototype. On the left side one can see the time evolution of one pad with a signal from the steepest going track in the left figure. The red strips are the recognized pulses where the height is representing the amplitude. The data was taken with a peaking time of 116 ns sampling at 16 MHz.

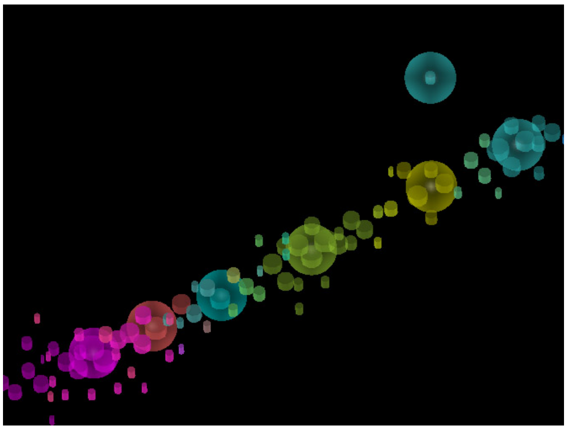

Figure 4.52: TPC cluster finding algorithm at work. The digitized single-pad hits (*digis* - output of the PSA algorithm, shown as coin-like shapes) are combined to larger *clusters*. Their amplitudes are summed up, the cluster position is calculated as the amplitude-weighted mean of the single digi positions.

Figure 4.52 shows a 3D view of the clustering algorithm working on a track piece measured with the large prototype detector at FOPI, GSI, Germany (cf. Sec 4.12.2). The coin-shaped entities are digitized single pad hits (*digis*), different sizes corresponding to different amplitudes. All digis of the same color are assigned to one cluster (depicted as bubble of the same color). Digis that are split between adjacent clusters are shown in mixed color.

The described cluster finding algorithm is robust and works reliably for simulated as well as real data from our beam tests. As an alternative, a cluster finding algorithm based on a Cellular Automaton (CA) algorithm has been developed. The advantage of this algorithm is its high parallelism, making it very well suited for a close-to-the-metal implementation in the final $\overline{\text{P}}$ANDA DAQ scheme. Both algorithms have been used over the years of software development can be considered final.

4.10.7 Pattern Recognition

One of the biggest advantages of the TPC as central tracker in the purely time-based trigger and DAQ paradigm that we are facing in $\overline{\text{P}}$ANDA, is its independence on other detectors when it comes to pattern (track) recognition. Typical non-curling tracks from primary particles consist of $\sim$ 30-50 clusters forming consistent 3-dimensional helical arcs in the chamber. While the data rates remain challenging, the pattern recognition problem as such can be solved without relying on any information from other detectors.

We have developed two conceptually different methods for pattern recognition during development of the TPC reconstruction software. The standard pattern recognition algorithm is a track follower based on a conformal mapping method involving the so-called Riemann Sphere [?, ?], a well-known entity from complex analysis.

4.10.7.1 The Riemann Transformation

Common to both methods is the employment of the so-called Riemann Transformation. It is a *stereographic projection* of points from a plane - in this case $\mathbb{R}^2$ - onto the Riemann Sphere, a sphere of diameter one sitting *on top* of the origin of the complex plane. In our application for pattern recognition, the complex plane is replaced by $\mathbb{R}^2$.

The stereographic projection is defined on the entire sphere except one point (here: the north pole).

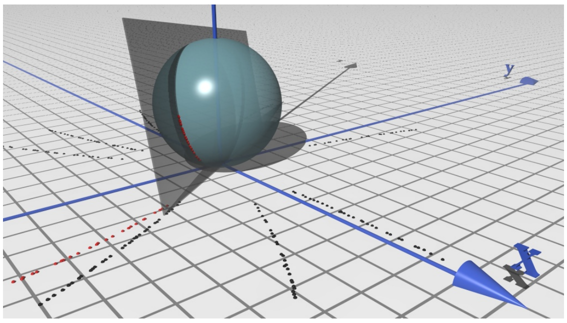

Figure 4.53: Example of the Riemann Transformation of a circular particle track (π^+). The tracks have been scaled by a constant factor to better match the scale of the unit Riemann Sphere. The plane defined by the transformed set of points is also shown.

It is smooth, bijective and conformal, but not isometric, thus preserving angles but not distances. The transformation rule for a point on the plane $\mathbf{x}_\mathrm{i} = (x_\mathrm{i}, y_\mathrm{i}, z_\mathrm{i})$ reads:

$$\begin{aligned} x_\mathrm{i} &= R_\mathrm{i} \cdot \cos\phi_\mathrm{i} \,/\, (1 + R_\mathrm{i}^2), \\ y_\mathrm{i} &= R_\mathrm{i} \cdot \sin\phi_\mathrm{i} \,/\, (1 + R_\mathrm{i}^2), \\ z_\mathrm{i} &= R_\mathrm{i}^2 \,/\, (1 + R_\mathrm{i}^2). \end{aligned} \tag{4.3}$$

It is useful to note that the mapping of Eq. 4.3 does *not* increase the dimensionality of the problem, as a first glance might suggest. The most important feature of Eqs. (4.3) in the context of pattern recognition is that circles and lines *uniquely* map to circles on the sphere [?]. Since in turn a circle on a sphere uniquely defines a plane in space, there is a direct correspondence between a *circle* (on the plane) and a *plane* intersecting with the Riemann Sphere.

This fact has been exploited in the field of track fitting (e.g. [?, ?]), since it reduces the problem of fitting a set of points to a nonlinear mathematical entity (circle) to a linear one. In the scope of the helix pattern recognition problem it is used to gain additional criteria of hit proximity and track affiliation.

Figure 4.53 shows an example of such a transformation of a circular particle track (projections of helical tracks on the readout plane). The black dots in Fig. 4.53 correspond to reconstructed hits in the TPC (`Clusters`, Sec. 4.10.4) from simulated π^+-tracks. Thus they have been subject to effects like diffusion, readout clustering effects and electronics response (see Sec. 4.10.7.8). Figure 4.53 shows the transformed points of one of these tracks (marked red) as well as the associated best-fit plane.

4.10.7.2 Riemann Pattern Recognition - A Track Follower

The *Riemann Pattern* recognition as implemented for the $\overline{\mathrm{P}}$ANDA TPC is a track following algorithm, that basically associates three-dimensional space points to track candidates by using different proximity criteria, both in detector coordinates (x, y, z) as well as using the transformation described in Sec. 4.10.7.1.

Before *track building*, the clusters are presorted by z, radius or angle. The idea is that the pattern recognition goes from areas of low track density, where tracks can easily be separated by their proximity in space, to areas of high track density. The very first *track* is built and contains only one hit at this time, then the algorithm loops through the presorted clusters. Each hit is checked against each existing track. If one or several matching criteria (*"hit-track correlators"*) are fulfilled, the hit may then be assigned to the best matching track.

A hit-track correlator can be applicable or not, and if it is, it delivers a *matching quality.* Two correlators are applied:

- The *Proximity Correlator* checks proximity in space, by finding the nearest cluster in the track. It is always applicable, and the matching quality is the distance of the two cluster positions.
- The *Helix Correlator* checks the distance of the cluster to the prefitted *helix* that defines the track. If the track has not been fitted, the correlator is not applicable. The matching quality is the distance to the helix.

If the matching quality is smaller than a user-definable cut (*proximity-* and *helix-cut*), the track *survives* the correlator. These cuts are dynamically scaled, depending on a quality estimation of the so far existing tracklets. With better track quality, the *helix-cut* is narrowed, which gives better track separation power in areas of high cluster density, whereas the *proximity-cut* can be opened, which makes the process less prone to track splitting.

We call the number of applicable *and* survived correlators the *correlation level.* The hit is added to the track that reaches the highest level. If there is more than one track, the best matching quality decides to which track the hit is assigned. If no correlator is survived, a new track is built from the hit.

To avoid following the wrong track in an area where two or more tracks are crossing, clusters which match well to more than one tracklet can be excluded.

4.10.7.3 Helix Prefit

When a track has more than a user definable minimum number of hits, a helix fit [?] is performed in two steps:

- A plane fit on the Riemann sphere (see Sec. 4.10.7.1).
- A dip fit via the hit angles and z-positions.

A covariance ellipsoid is built from the residua of the hits to the average hit position in the Riemann space (weighted with 1/cluster error to be noise and outlier tolerant). This ellipsoid has three major axes, and the smallest axis (which is the eigenvector to the smallest eigenvalue of the covariance ellipsoid) is the normal vector to the plane the hits lie on.

With this simple method, problems arise especially for short tracks, which do not span a significant distance on the Riemann sphere and are therefore not curved sufficiently, and tracks where the clusters are not well aligned and show a wide spread on the measurement plane. Reasons for this can be delta electrons that broaden the track, noise hits which were assigned to the track and effects of the clustering.

In these cases often a plane is found that is almost perpendicular to the surface of the sphere. This is due to the fact that the plane fit minimizes distances of the hits to the plane, and not distances of the hits to the intersection of the plane with the sphere (i.e. the projection of the track). To prevent that, a check is performed which calculates the RMS of the distances of the hits to the intersection of the plane with the Riemann sphere for the planes corresponding to the two smallest eigenvectors. Then the plane with the minimum RMS is selected.

This plane fit, projected back onto the pad-plane, delivers a circle, which has no constraints in radius and position of its center. It is the projection of the true helical track onto the readout plane.

In a second step, the winding sense and dip of the helix are fitted: The position of each cluster along the helix can be defined by its angle. The clusters are presorted by z. Iterating over all hits in the track, the angle of each hit is defined by the difference of its angle to the previous hit. This method grants consistent angles also for curling tracks.

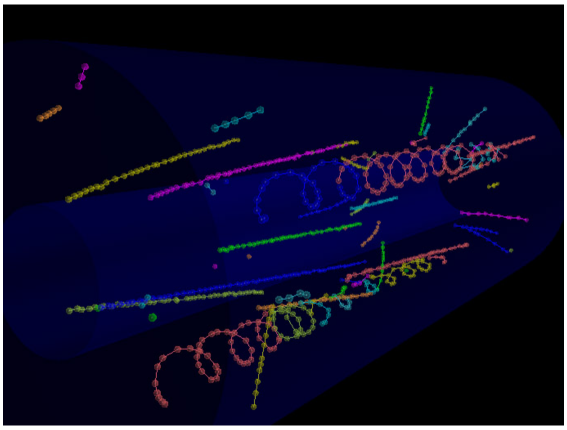

Figure 4.54: Performance of the Riemann pattern recognition for a real beam event taken with the prototype. Target tracks, curlers and steep tracks from interactions in the beam pipe are all recognized, merged and sorted properly.

A straight line fit of the hit angles versus the z positions of the clusters is then performed, which delivers the dip ϑ of the track. After that, the hits are again sorted, now by their angle. For steep tracks ($\vartheta < 30°$ or $\vartheta > 140°$) the angles are not a good sorting criterion anymore, so these tracks are left sorted by z. This technique makes sure that the hits of the track are well sorted along the track, which is quite important for the Kalman filter. The winding (± 1) can simply be calculated by checking if the angle of the last hit in track is greater ($+1$) or smaller (-1) than the angle of the first hit.

4.10.7.4 Track merging

In the process of track building, the actual tracks might not be found as a whole. Especially steep tracks and curlers are prone to be split into several track pieces or *tracklets*: As the track-building goes from big to small radii, curlers cannot be found as a single track in one step. The same is true for steep tracks, where the sorting in radial direction does not reflect the track topology properly anymore. Besides, particles with low energy loss can lead to fragmentary tracks, or the track may exit and re-enter the chamber one or more times. In the real chamber, dead channels or chips can also cause gaps.

Therefore, a second level *tracklet merging* is performed. Similar to the track building process, the tracklets are presorted, and then compared to each other. Again, there are several *track-track correlators* which all (in this point the merging is different to the track building) have to be applicable and survived.

- The *Proximity Correlator* compares the position of the first and last hits of the two tracks. If the smallest distance is smaller than a definable *proximity-cut*, the correlator is survived.
- The *Dip Correlator* compares the dip angles of the two tracks. Therefore, both tracks have to be fitted. But not only has the absolute difference of the dip angles to be smaller than a definable *angle-cut*, also the relative z positions of the track have to match. Thus, the distance to the helix (defined by the track with more hits) of the nearest point of the smaller track is calculated. It has to be smaller than an adjustable *helix-cut*.

  If only one of the tracks is fitted, the helix-distances of all hits of the smaller track are calculated and compared with the helix-cut. If none of the tracks is fitted, the correlator is not applicable and the tracklets cannot be merged.
- Finally, the tracklets have to pass the *Helix Correlator*. For tracks with few hits, the helix fit might not be very accurate, and for straight tracks, some parameters of the helix (i.e. radius, center) are not well defined. Thus it is not reasonable to directly compare the helix parameters.

  Instead, a new track is created temporarily, containing the hits of both tracks. A helix fit is performed and a *helix-cut* on the RMS of the distance of the hits to the helix is applied.

  If the two tracks together do not have enough hits to be fitted, this correlator is not applicable.

The algorithm has been substantially improved over the last months. Track finding and merging works satisfactory for simulated as well as for real data, up to very high track counts. Fig. 4.54 shows the result of the pattern recognition in the large prototype (cf. Sec. 4.12) for a rather complicated target event including tracks from the primary vertex (end of the chamber in Fig. 4.54, low-momentum curlers as well as “spray” tracks almost parallel to z from some event in the beam pipe.

4.10.7.5 Sectorization

The process of track building requires computational power in the order of $\mathcal{O}(n_{\text{clusters}} \cdot n_{\text{tracks}})$. In order to be performant also for large numbers of hits and tracks, the process is sectorized. The pad-plane is split into sectors. Track building and merging is done for each sector separately, and only then global merging is performed.

4.10.7.6 Multistep Approach

The pattern reconstruction efficiency for different track topologies depends strongly on the presorting of the clusters mentioned in 4.10.7.2. Performance is best for tracks in sorting direction (i.e. very steep tracks and very low momentum curlers for sorting along z, tracks with high transverse momentum from the interaction point for radial sorting, curling tracks for angular sorting). Thus, it is advantageous to run the pattern recognition more than once, and use a different presorting in each step. Tracks that reach certain quality criteria (i.e. a minimum number of hits and an RMS of distances of the hits to the helix smaller than a certain cut) are kept, the remaining clusters are sorted again, and the procedure is repeated.

This approach yields high efficiencies for all kinds of track topologies and a high track resolution power.

4.10.7.7 Track Seeding for the Fit

For track fitting, seed values for starting point, direction, momentum and charge have to be provided. These can easily be calculated from the helix prefit and the magnetic field. Moreover, tracks have to overcome a minimum number of hits in order to be passed to the Kalman filter, otherwise they are rejected.

4.10.7.8 Fast Hough Transform on the GPU

General purpose programming on Graphics Processing Units (GPUs) has been one of the hottest fields in parallel computing over the last years. Originating in the computer gaming industry, GPUs of today are versatile, conveniently programmable devices that offer massive *parallel* computing power.

Since the high level trigger of $\overline{\mathsf{P}}$ANDA is a performance critical system and the central tracker will play a decisive role as input, fast algorithms close to the hardware for pattern recognition are of great importance.

The Hough Transform [?] is a widely used, global method for pattern recognition. It is used for detection of a certain pattern in a given set of data points $\mathbf{X}_\mathrm{i}$. After choosing a fitting N-dimensional parameterization of a given pattern (e.g. a helix in the track finding problem at hand), every data point is transformed into the N-dimensional parameter space of that pattern parameterization. Consequently, every data point $\mathbf{X}_\mathrm{i}$ corresponds to an N-dimensional hyper-surface p_i in the parameter space.

By construction, the hyper-surface representations of a set of data points lying *perfectly* on the chosen pattern *intersect in one single point* in the parameter space. In the more realistic case of a distribution of the $\mathbf{X}_\mathrm{i}$ around the pattern (think of the hits from a detector system with a finite resolution forming a track) one instead observes a region of elevated density of the p_i in the parameter space. Consequently, the search for a pattern in the original data-set is transformed into a search for local maxima in an N-dimensional space.

A possible parameterization of a helix is

$$\begin{aligned} x &= r \cdot \cos(t) + x_0 \\ y &= r \cdot \sin(t) + y_0 \\ z &= c \cdot t + z_0, \end{aligned} \tag{4.4}$$

so in the case of helix detection $N = 5$. Here t is the path *along* the helix curve and c defines the pitch.

The search for maxima in a five-dimensional space is computationally non-trivial. A regular five-dimensional histogram in integer representation of moderate granularity would require memory allocation of the order of many terabytes. Alternatively, one can perform a tree-search in the parameter space instead, thus effectively trading memory load for computational cost. The recent developments in the field of massively parallel high-performance computing, however, make this kind of trade-off affordable.

The search implemented here works by iteratively dividing the parameter space into sub-spaces, so-called *nodes*, by bisection in each dimension [?]. In this way each node in the parameter space creates $2^5 = 32$ sub-nodes in every step of the algorithm. These nodes are then checked for intersection with the hyper-surfaces p_i. The number of hyper-surfaces p_i crossing a node gives the node's *vote*. An (adjustable) threshold of minimal votes is required for every node after each iteration step, deciding if the node qualifies for further subdivision or is discarded. In its current implementation the algorithm terminates when a fixed iteration depth is reached. In the future this threshold should be determined for each track individually.

The algorithm has been implemented in `C++` and tested on simple simulated events. However, the calculations required lead to computation times $\mathcal{O}(10\,\mathrm{s})$ for an example of five tracks on recent hardware (Intel Core2$^{\mathrm{TM}}$ 2.66 GHz). This is due to the still very high number of nodes present (up to $\mathcal{O}(10^5)$) before converging on the maxima.

Since all of the nodes, the hyper-surfaces p_i, and hence intersection checks are completely *independent* of each other, the high number of nodes makes a massively parallel implementation attractive. Therefore the algorithm has been implemented in `C` and `C++` on a NVIDIA GPU using CUDA.

The implementation on the GPU has proven to be significantly faster than the identical code on the CPU (GPU hardware used for development and testing: NVIDIA GTX 285$^{\mathrm{TM}}$). Currently, in a very early version of the implementation, a Speedup factors of $\sim$ 20 compared to single-thread performance on the CPU is observed. Without changes to the algorithm itself speed increases of another factor of $\sim$ 3-5 should be reachable. The pure GPU calculation time only accounts to $\sim 5\,\%$ of the total computation time in the examples shown. Moving more tasks from the CPU to the GPU will lead to significant performance improvements.

4.10.7.9 Closing Comments

A strong feature of such an implementation is its scaling behavior. More tracks (e.g. more hits) will not lead to an increase of combinatorics and thus an increase of computational cost following some power law, as it would be the case for any algorithm performing hit-to-hit comparisons. Instead, increasing the number of hits just increases parallelism (linearly), resulting in a much more shallow increase of execution time, of course depending on the actual hardware setup.

Exploiting the potential of massively parallel algorithms and hardware might prove to be crucial in order to keep computing times under control for the online trigger system of $\overline{\mathrm{P}}$ANDA (cf. discussion of Sec. 4.8.5). The final pattern recognition scheme for the TPC could be a combination of a massively parallel algorithms and more conventional methods, like the very successful track following algorithm described in Sec. 4.10.7.2.

4.10.8 Track Fitting - GENFIT

After the pattern recognition tools have determined sets of detector hits which comprise particle trajectories, the best estimates for the track parameters,

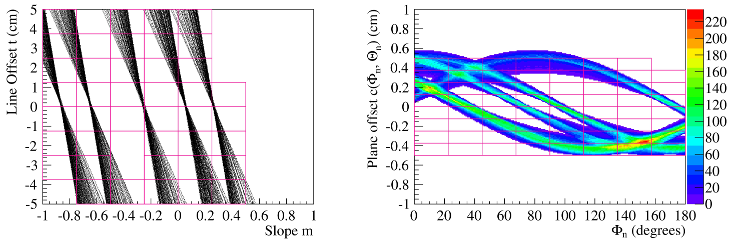

(a) Active nodes after 4 iterations

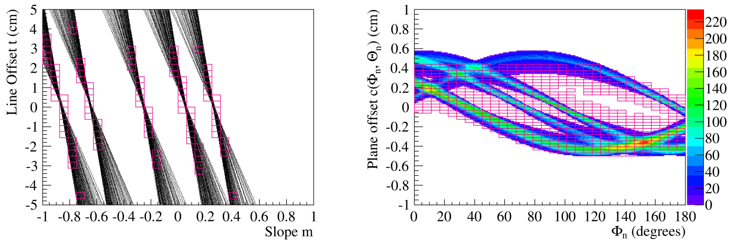

(b) Active nodes after 6 iterations

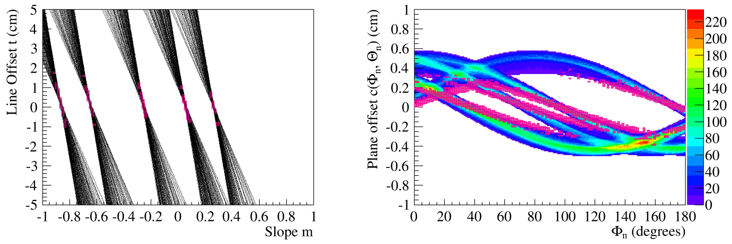

(c) Active nodes after 8 iterations

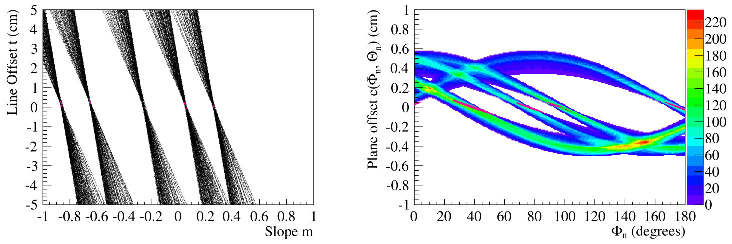

(d) Active nodes after 10 iterations

Figure 4.55: Tree search scheme of the FHT algorithm.

i.e. the particle positions and momenta with their covariances, have to be obtained. Space points measured by the TPC have to be fitted in combination with hits from other detectors with different geometries such as planar strip or pixel detectors in the Micro Vertex Detector of $\overline{\mathrm{P}}$ANDA. This has motivated the development of a generic toolkit for track fitting in complex detector systems, called GENFIT [42], which is now the standard track fitting tool in $\overline{\mathrm{P}}$ANDA as well as in the Belle-II project. Applications in other experiments like ILD are currently under consideration.

The fact that GENFIT is applicable to a very wide range of experiments, independent of the specific event topology, detector setup, or magnetic field arrangement, is due to its completely modular design. Fitting algorithms are implemented as interchangeable modules. At present, the framework contains a validated Kalman filter [43]. The implementation of another algorithm called Deterministic Annealing Filter (DAF) [44] is currently ongoing. The DAF is an iterated Kalman filter which has the virtue of being able to dynamically assign reduced weights to noise hits in planar detectors or to outlier hits in the TPC. Other algorithms like Gaussian Sum Filters [45] can be implemented easily in the GENFIT framework.

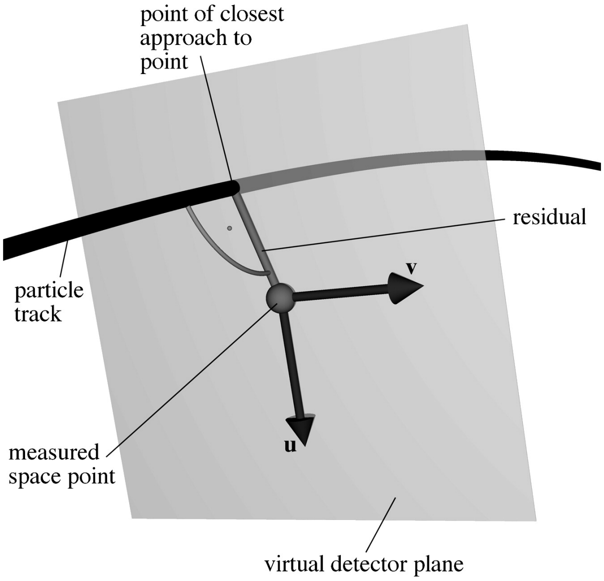

Figure 4.56:

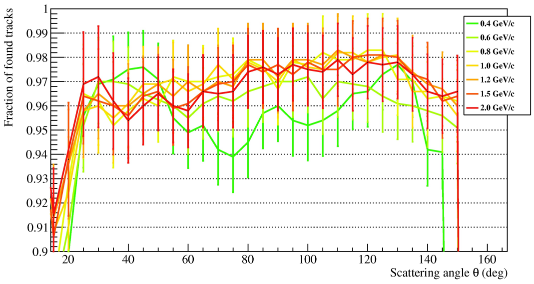

Figure 4.57: Fraction of found tracks (if a tracklet contains more than 50% of the clusters that belong to the track, it is found) vs. scattering angle θ for single track events. Regardless of the momentum, more than 94% of the tracks are found. Only for very steep tracks performance decreases significantly.

Track parameterizations and the routines required to extrapolate the track parameters and their covariance matrices through the experiment are also implemented as interchangeable modules. This allows the use of well established track extrapolation tools (e.g. GEANE [46]) as well as the development and evaluation of new track extrapolation tools. Different track parameterizations and extrapolation routines can be used simultaneously for fitting of the same physical tracks, which allows a direct comparison in terms of execution time, resolution, and efficiency.

Representations of detector hits are the third modular ingredient to the framework. The hit dimensionality and orientation of planar tracking detectors are not restricted in any way. Tracking information from detectors which do not measure the passage of particles in a fixed physical detector plane, e.g. drift chambers or TPCs, is used without any simplification. This goal is achieved via the concept of virtual detector planes, which are calculated dynamically each time a hit is to be used in a track fit. This allows to maintain complete modularity of GENFIT because the fitting-algorithm modules treat all hits in the same manner. In the case of space point hits in the TPC, the virtual detector plane is defined to be perpendicular to the track and to contain the point of closest approach of the track to the hit, as illustrated in Fig. 4.56. This allows the fitting algorithm to minimize the orthogonal distances of the track to the hits without projecting the hits onto predefined planes. The projection of hits onto planes defined by pad rows is common practice in TPC reconstruction.

GENFIT is implemented as a very light-weight C++ library, which is available as free software [47].

4.10.9 Tracking Performance

The following sections describe first results concerning the tracking performance of the $\overline{\text{P}}$ANDA TPC as evaluated with the present software framework:

- Reconstruction efficiency,
- Momentum resolution,
- Particle identification by dE/dx.

It is important to cross-check these results by experiment. For this purpose the large prototype has also been implemented in the simulation framework. A comparison of the resolution from experiment and simulation already shows very good agreement (cf. Sec. 4.12.2.1.

4.10.9.1 Single Track Reconstruction Efficiency

A detailed efficiency study of the Riemann pattern recognition has been performed for single-track events. A pad-plane with 16 segments was used. Tracking performance is excellent for tracks between 25° and 145°, as can be seen in figures 4.57 and 4.58.

Scalability to large track multiplicities up to 3000 in terms of tracking performance and computational cost still has to be evaluated in detail, but first preliminary tests look very promising.

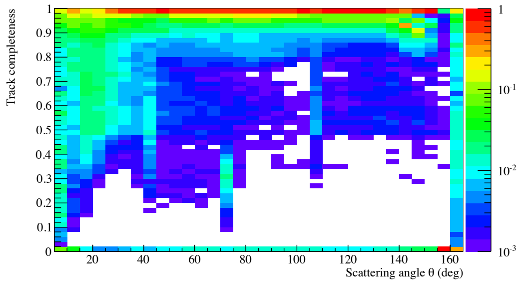

Figure 4.58: Track completeness (defined as the fraction of clusters of the track that are found in the biggest tracklet) vs. scattering angle θ. This plot combines single track events with momenta from 0.2 to 2.0 GeV.

4.10.9.2 Momentum Resolution

The $\overline{\text{P}}$ANDA Central Tracker (CT) has to be able to reconstruct momenta of charged tracks with a resolution in the low percent regime [24]. To project the momentum resolution performance of the final $\overline{\text{P}}$ANDA TPC, an extensive simulation study has been performed. For a range of momenta especially relevant for the CT, μ tracks have been simulated leaving the target at a set of fixed angles θ, undergoing the full simulation chain as described in Sec. 4.10.1.

Track extraction has been performed based on the available Riemann Pattern Recognition (c.f. Sec.4.10.7.2) without using any Monte Carlo information. The extracted tracks were fitted using GENFIT with Runge Kutta track representation (c.f. Sec. 4.10.8), immediately yielding the distribution of reconstructed momenta.

From the Central Tracker point of view, for charged particles originating from the primary interaction point in the target, track reconstruction and hence determination of the particle momentum will greatly benefit from the high-precision space points measured in the Micro Vertex Detector (MVD) of $\overline{\text{P}}$ANDA. However, for charged tracks from secondary vertices outside the MVD acceptance or tracks with insufficient number of hits in the MVD, the CT alone will have to be able to reconstruct tracks and their momentum sufficiently well. It is thus important to assess the momentum reconstruction capabilities of the TPC both with and without MVD (or GEM) hit data.

Figure 4.59 shows the momentum resolution obtained with reconstructing tracks in the TPC only without relying on any external detector information. In this study only primary μ tracks were considered. Secondary tracks, as well as all tracks not meeting the a required *completeness* of 50 % (c.f. Sec. 4.10.9.1).

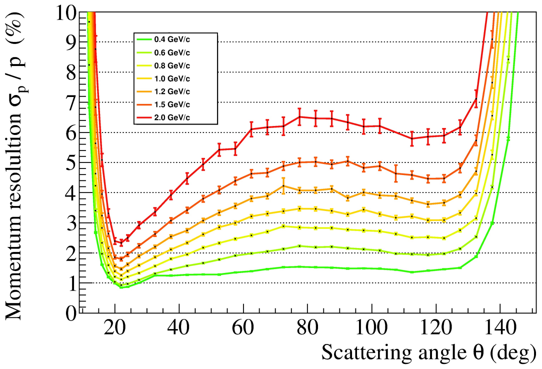

Figure 4.59: Momentum resolution σ_p/p obtained from μ-tracks reconstructed in the TPC alone. Each data point corresponds to a Gaussian fit to the momentum distribution as reconstructed from 5000 tracks. The error bars show the squared sum of the statistical uncertainties of sigma and mean of the final fit.

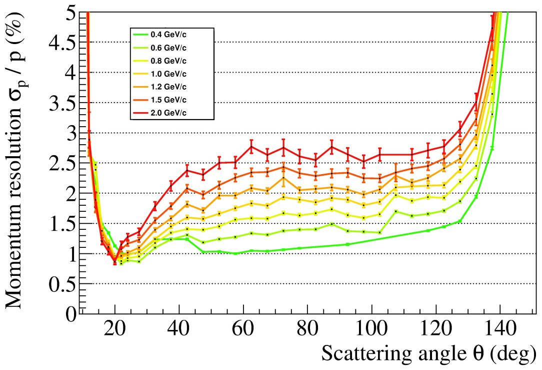

Figure 4.60: Momentum resolution σ_p/p obtained from μ-tracks reconstructed in the TPC and then merged with hits from the MVD and GEM detectors, using the same data sample as in Fig. 4.59. In each MVD (GEM) detector plane the closest hit inside a road width of 2 mm (5 mm) was added to the TPC track. No Monte Carlo information has been used for the matching.

It is important to note that Fig. 4.59 shows the reconstruction performance as a function of the *total momentum* p, not the transverse momentum p_t. The total momentum is reconstructed during fitting taking into account the measured curvature as well as the helix dip. This is possible because the TPC measures consistent three-dimensional tracks also without relying on any external references.

A second study has been conducted in order to project the performance of the TPC together with the MVD and the GEMs. The reconstruction scheme was the following:

- find tracks in the TPC only using real Riemann pattern recognition,
- fit the found tracks,
- extrapolate the tracks through the MVD,
- pick up MVD and GEM hits inside a certain road width around the track,
- re-fit the combined track.

The result of this method is shown in Fig. 4.60. The momentum resolution improves by a factor of ~ 2 when adding MVD hits to the TPC hits, as can be seen by comparing to Fig. 4.59.

4.10.10 Reconstruction of Λ Decays

The Central Tracker of $\overline{\mathrm{P}}$ANDA will have to be able to reconstruct events with complex topologies without the help of other detectors, e.g.

- decays of neutral particles, e.g. Λ hyperons,
- kinks in charged particle tracks, e.g. from Ξ decays,
- $\pi \rightarrow \mu$ decays (important for background rejection in the muon range system of $\overline{\mathrm{P}}$ANDA).

As an example for the reconstruction performance of the TPC for such topologies, e.g. the invariant mass resolution, the vertex resolution and the reconstruction efficiency of secondary vertices, we investigate here the reaction

$$p\overline{p} \rightarrow \Lambda\overline{\Lambda} \rightarrow p\pi^- + \overline{p}\pi^+ \quad . \tag{4.5}$$

To this end, 10000 events of this reaction were simulated at a $\overline{p}$-beam energy of 4 GeV. This was done using the EvtGen direct event generator with the $\Lambda\overline{\Lambda}$ generated over the whole phase space (PHSP flag). The present simulation does not take into account the real angular distribution of Λ and $\overline{\Lambda}$ from this reaction.

The kinematics of the reaction products of the simulation can be seen in Fig. 4.61. A strong forward boost is seen especially for the protons and antiprotons.

In Fig. 4.62 the number of primary particles leaving at least one MC point in the TPC is shown. This gives an upper limit for the geometrical acceptance of 52 %.

The number of reconstructed charged candidates can be found in Fig. 4.63; 30.5 % of the events have exactly two positive and two negative charged candidates.

For the analysis of this channel MC-based particle identification (PID) is used (e.g. the particle hypothesis is set to the one from the associated MC track). For each reconstructed event, lists are built of the track candidates for protons, π^-, antiprotons and π^+.

For further analysis, only events are considered which have at least one Λ and one $\overline{\Lambda}$ candidate. For all combinations of protons and π^- (antiprotons and π^+) the point of closest approach between the two tracks is calculated using a Newtonian method on only the available fits of the particle candidates. The center point of the line connecting the two points of closest approach on the tracks is taken as the vertex position. It should be stressed that no assumption on the vertex position is made for the reconstruction. In Fig. 4.64 one can see the distance from the calculated decay vertex to the MC vertex for all the different combinations where the MC vertex is taken as the creation vertex of the proton (antiproton). Resolutions of 0.4 mm and 1 mm are achieved for the x/y and z coordinate, respectively.

The tracks are then extrapolated to this vertex and the 4-momenta at this point are used to create a Λ candidate. The candidate where the distance between the two tracks is the smallest is chosen. One can see the invariant mass distribution of the Λ ($\overline{\Lambda}$) in Fig. 4.65. Within 3 σ of the mean fitted to the mass spectrum in total 3592 Λ ($\overline{\Lambda}$) were reconstructed with an invariant mass resolution of about 2 MeV. It should be noted that no kinematic vertex fit has been performed yet, which is expected to further improve these values.

The global reconstruction efficiency of this process is 18 %. Taking into account a detector acceptance of 52 % the final TPC reconstruction efficiency is given by 34 %.

4.10.11 Particle Identification by dE/dx

Charged particles can be identified with the help of their momenta and their specific energy loss. A TPC can measure both parameters and is therefore able to perform a complete particle identification (PID). The average specific energy loss of a particle crossing matter represented by the primary ionization is described by the Bethe-Bloch formula. It is

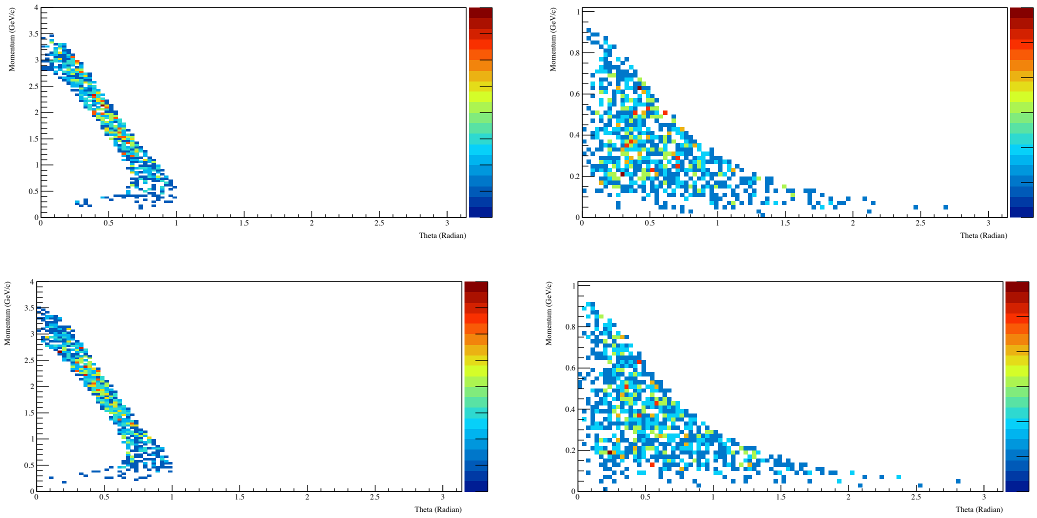

Figure 4.61: Kinematic distributions (momentum vs. laboratory polar angle) of the decay particles from $\Lambda/\overline{\Lambda}$ decays. Top left: protons, top right: π^-, bottom left: antiprotons, bottom right: π^+.

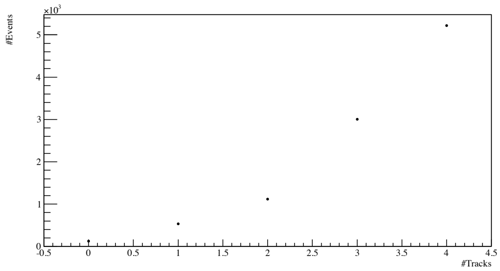

Figure 4.62: Number of primary tracks with at least one MC point in the TPC.

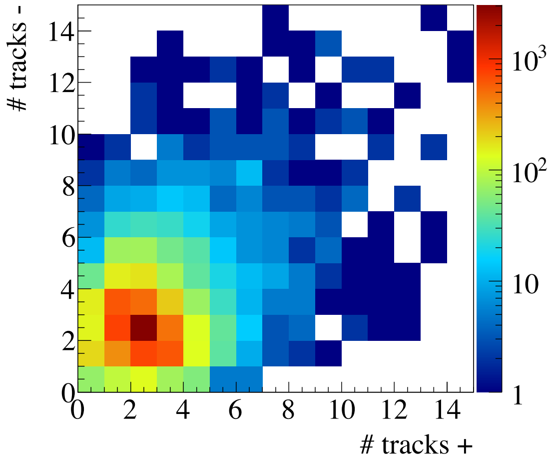

Figure 4.63: Number of reconstructed charged particle tracks.

based on three assumptions: First, the transfer of energy does not change the direction of flight of the ionizing particle, second, the gas molecules are at rest and third, the ionizing particle is much heavier than an electron. A modified version of the Bethe-Bloch formula, which makes the dE/dx behavior directly readable, can be written as a function of the particle velocity β and the charge number Q:

$$\frac{dE}{dx} = \xi \cdot \frac{1}{\beta^2} \cdot Q^2[K + \ln(Q^2) + \ln(\gamma^2) - \beta^2 - \delta(\beta\gamma)] \tag{4.6}$$

In this equation K is representing a constant and ξ the electron density of the gas, while $\delta(\beta\gamma)$ denotes the density function, first introduced by Fermi. This correction accounts for polarization effects due to the electrical field of the relativistic particle. The specific energy loss as function of the momentum can be subdivided in three regions. At low momenta and therefore non-relativistic velocities a decrease with $1/p^2$ is visible, which causes large ionization. For momenta corresponding to three to four times the mass of the particle, a minimum is reached, followed by the relativistic rise proportional to $\ln(p^2)$.The relativistic rise is an effect of the deformed electrical field of the ionizing particle, leading to an increase of the transverse component of the field. Saturation is reached for very large values of $\ln(\beta\gamma)$ at the Fermi plateau. There the relativistic rise ends and the energy loss becomes independent from $\beta\gamma$. The most interesting part in $\overline{\text{P}}$ANDA would be in the transition of the region from low momenta to the the relativistic

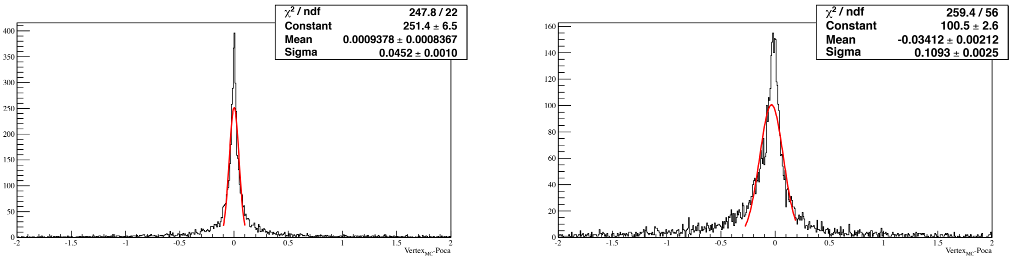

Figure 4.64: Vertex resolution for $\Lambda/\overline{\Lambda}$ decays in the $\overline{\text{P}}$ANDA TPC.

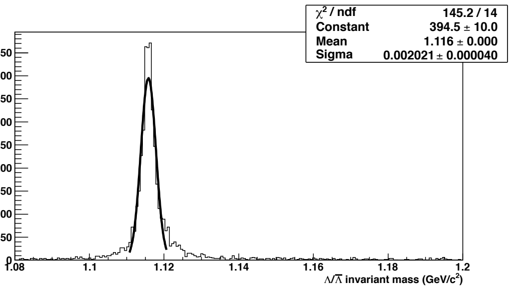

Figure 4.65: Reconstructed $\Lambda/\overline{\Lambda}$ mass.

rise. Therefore the resolution of dE/dx measurements has to be at the level of a few percent in order to give a handle for particle identification in this momentum regime. By measuring hit charges, using gain correction from the krypton calibration and applying the truncated mean method, the energy loss of a track can be determined. With the additional information of the momentum calculated from the track curvature the particle can be clearly identified.

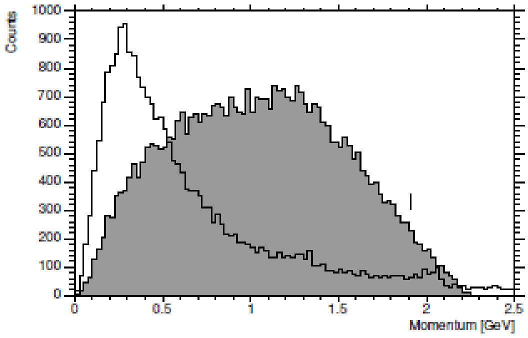

Figure 4.66: Momentum distribution of kaons from $\eta_c \Rightarrow$ 4K decay (dark plot) and background pions (transparent) [24].

Figure 4.66 shows the benefit of particle identification below 1 GeV/c for the $\overline{\text{P}}$ANDA central tracker. It shows the momentum distribution of kaons produced by the η_c decay. Within the same figure the momentum distribution of background pions is shown, generated at the η_c resonance. About half of the kaons have momenta below 1 GeV/c, where also most of the background pions are produced. Particle identification with with Cherenkov detectors can not be used at such low momentum values. The TPC would therefore add significant information for the PID.

A simulation study has been performed to study the motivated momentum region below 1 GeV/c in regard of the separability of kaons and pions [41]. Therefore three large samples (π^+, K^+, p) of 100.000 tracks have been produced each using the full $\overline{\text{P}}$ANDA root framework. A particle gun generator was used to distribute both scattering angle and momentum ($p \in [0.2, 1.2]$ GeV/c) homogeneously. The full digitization and reconstruction chain as outlined in the sections 4.10 has been used.

During reconstruction a track fit is performed using a Kalman filter (embedded in GENFIT), giving the reconstructed momenta. Energy loss is then extracted by a dEdx task. The track fit is used to "walk" along the particle's reconstructed trajectory in steps of fixed length Δx. At each step a plane is constructed perpendicular to the track and all TPC hits lying between this and the last plane are collected. These can either be the clusters obtained at the very end of the reconstruction or MC points.

In the first case the deposited energy ΔE over the length Δx has to be inferred from the `Cluster` signal amplitudes. When working on MC points, the energy loss can be directly obtained. Whatever the method, the single values will be distributed around the mean value given by the Bethe-Bloch Formula.

In the results presented here the hits are collected over track pieces of a fixed length $\Delta x = 3$ mm, resembling the pad size on the TPC readout plane. The single energy deposits associated to the hits of one such step will be distributed according to straggling functions, which have been optimized on ALICE TPC data. However, the number of points

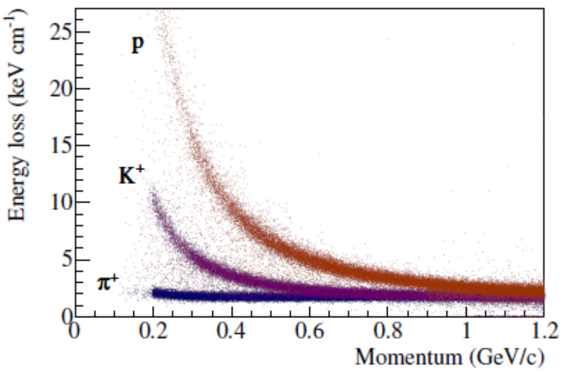

Figure 4.67: Scatter plot of dE/dx samples from Monte Carlo simulations of π^+, K^+ and protons at scattering angle $\Theta = 90°$. Each point consists of the reconstructed momentum from the Kalman tracker and the mean of the dE/dx distribution from 3 mm samples of the track. The truncated mean method has been used to suppress very high energy loss values (the highest 40 % are discarded). For each particle type $\sim 10^5$ tracks were included in the study [41].

will be small. Remembering the long tail of the straggling functions it is clear that this potentially leads to large fluctuations of the mean value.

A commonly used and robust approach to reduce the dependencies of these fluctuations is the truncated mean method: A certain fraction of the highest and/or lowest values is simply discarded. In this way one reduces statistics but on the other hand keeps the fluctuations of the mean values to a minimum, as the outliers from the underlying distribution's tail are likely to be completely omitted. Of course one has to take care of the systematic shift of the mean value that is introduced.

Figure 4.67 shows the results of the MC-based study. In the scatter plot three distinct bands $\frac{dE}{dx}(p)$ are visible, completely overlapping for $p \gtrsim 1200\,\mathrm{MeV}/c$. For lower momenta an efficient identification of either pion, kaon or proton seems possible.

Energy resolutions have found to be fairly good for low momenta. Example distributions and resolutions are given in Fig. 4.68 for a fixed momentum of $p = 400\,\mathrm{GeV}/c$, where contribution to PID of the TPC will be possible. When going to higher momenta (towards minimum ionization), the resolution decreases to $\sim$ 9-11 %.

An MC-based energy loss study was chosen in order to acquire a theoretical limit for the TPC subdetector. A similar study on reconstructed hits can in principle be done without modifications of the dE/dx-code itself.

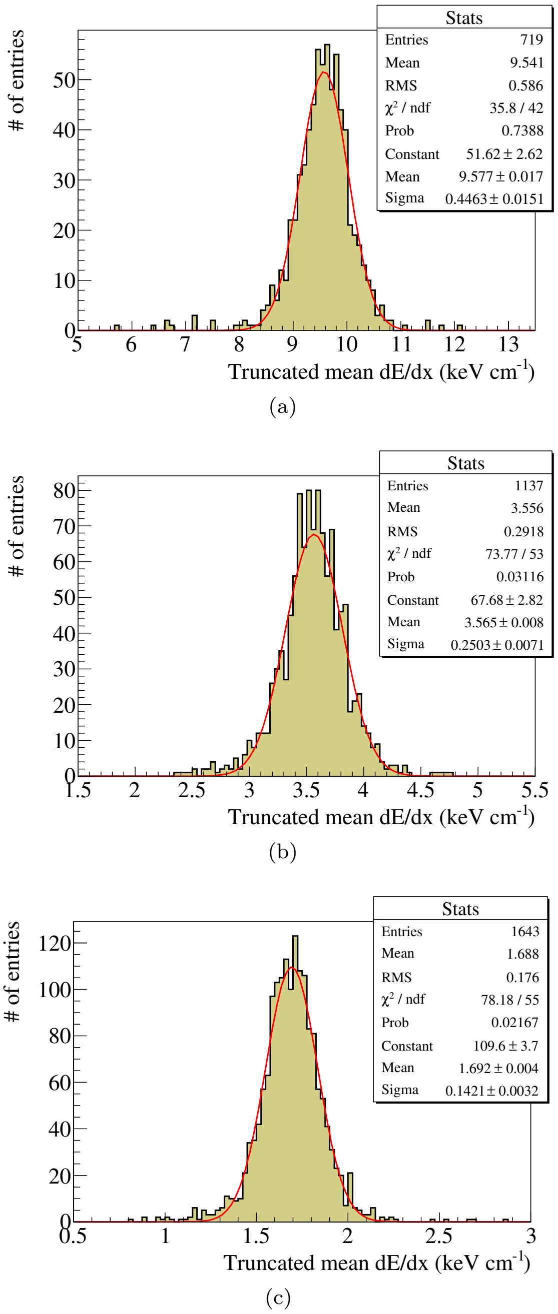

(a)

(b)

(c)

Figure 4.68: Distribution of mean dE/dx values obtained from analyzing 2000 tracks (truncated means, upper 40 % of values discarded) for pions (a), kaons (b) and protons (c) at $p = 400\,\mathrm{GeV}/c$ each. Scattering angle of the tracks has been restricted to $\Theta = 30°$, resulting in a close-to-optimal track length. Gaussian fits have been applied. The corresponding energy loss resolutions are 8.3 % (a), 7.0 % (b) and 4.7 % (c) [41].

However, the current implementation of the signal processing algorithms lacks an adequate pulse shape analysis: Only a local-minimum approach is currently available to disentangle pile-up signals on the readout pads. This is sufficient for tracking, where only the time and space information of a reconstructed hit is required. For dE/dx-analysis, however, one needs the signal height, which is proportional to the energy loss over the given pad. Therefore it is not only required to separate signal peaks in time, but also to subtract the signal's tail from the following/previous signal. Once these tail cancellation algorithms are in place, the same study can be repeated for fully reconstructed simulation data.

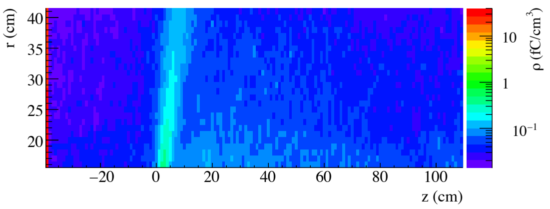

(a) Template distribution of ion space charge from 10000 DPM background events. The strong band leaving the interaction point (0,0,0) under $\sim 90°$ is due to slow, elastically scattered protons. The red band at the gas amplification at $z \sim -40$ models the amplification ions feeding back into the drift volume, assuming instantaneous electron drift.

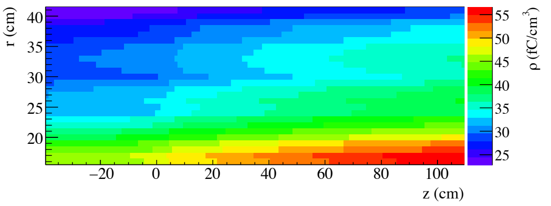

(b) Equilibrium space charge in the TPC chamber assuming azimuthal symmetry of the deposited primary charge.

Figure 4.69: Simulated initial space charge distribution from one time frame t_1 (a) and final equilibrium space charge after time integration (b).

4.10.12 Effect of Space Charge

Accumulations of space charge in the active volume of the TPC lead to distortions of the drift field and hence the drift paths of the electrons to be detected on the readout plane. In 4.1 we explained how the application of GEM foils as gas amplification devices can help to minimize the feedback of slow ions into the drift volume, and how this suppression can be characterized.

For simulating the effect of the remaining space charge we conveniently chose the *ion back-flow factor* ϵ as single input parameter, giving the number of back-drifting amplification ions per incoming primary electron. In the course of the studies presented here $\epsilon = 4$, which is equivalent to a *suppression factor* $\eta = 0.25\,\%$.

4.10.12.1 Simulation of Space Charge Buildup

For a realistic assertion of the projected space charge accumulation in the $\overline{\text{P}}$ANDA TPC we start with a sufficiently large set of events S with sample size s simulated using the Dual Parton Model (DPM) background generator for $\bar{p}p$-reactions. After passing this input data through GEANT (c.f. Sec. 4.10.1), we register the combined energy deposit of the full set of background events in the TPC active volume $\rho_i(r, z, \phi)$. Assuming instantaneous electron drift, we can regard this as the distribution of primary ion space charge.

In general, at time t_1 the charge density $\rho(t_1, r, z, \phi)$ in a volume element dV centered around a point (r, z, ϕ) is given by

$$\begin{aligned}\rho(t_1, r, z, \phi) = \frac{e}{dV} \cdot \int_0^{t_1} & N_p(t, r, z, \phi) \\ & + N_{in}(t, r, z, \phi) \\ & - N_{out}(t, r, z, \phi) dt\end{aligned} \tag{4.7}$$

where $N_p(t, r, z, \phi)$ is the rate of *primary* ions created in dV and $N_{in}(t, r, z, \phi)$ and $N_{out}(t, r, z, \phi)$ are the rate of ions drifting into and out of the volume element respectively.

In addition, the back-drifting ions from the amplification stage at the readout side of the chamber are modeled by adding a contribution proportional to the projection of the total amount of newly added primary charge onto the readout plane (assuming instantaneous electron drift):

$$N_{\text{in}}(t, r_i, z_0) = \epsilon \cdot \sum_j N_{\text{p}}(t, r_i, z_j). \tag{4.8}$$

Such a "template space charge distribution" from 10000 DPM background events is shown in Fig. 4.69a.

It has to be noted at this point that the shown simulations have been done using an old geometry model with insufficient detector wall thickness. In this light the following results should be regarded as an upper limit, as the correct wall material description can be expected to absorb some part of the incoming particles in the low momentum region. This might have a visible effect especially on the slow, elastically scattered protons which in turn dominate the energy deposition in Fig. 4.69a.

We choose the sample size s such that the associated accumulation time t_1 (given by s divided by the interaction rate $2 \cdot 10^7\,\mathrm{s}^{-1}$) is small compared to the ion drift time inside the TPC ($T_{\mathrm{ion}} \sim 85\,\mathrm{ms}$). Then we can regard the obtained initial space charge distribution $\rho_i(r, z, \phi)$ to be independent of the ion drift. In addition, the following assumptions are made to simplify the simulation of the space charge distribution in the TPC:

- Constant luminosity: We assume that N_p is constant on time scales of interest to us.
- Azimuthal symmetry: Owing to the typical cylindrical geometry of a TPC chamber we will treat the problem in cylindrical symmetry so that the resulting charge density map can be represented in the (r, z)-plane and we drop the dependency on ϕ: $\rho(r, z, \phi) = \rho(r, z)$
- For simplicity we neglect the electrostatic forces between the ions themselves. In this model ion drift proceeds along straight lines with constant velocity $\mathbf{u}^{I+}_{drift}$.

4.10.12.2 Modeling the Ion Drift

To represent the volume elements of 4.7 we choose a fixed binning in both coordinates (r, z). Each bin thus describes a ring-shaped volume in the TPC. The bin width Δz is chosen to correspond the accumulation time t_1 of the sample S. The actual time integration is then performed by repeated bin-wise shifting of the total charge distribution while adding the template charge distribution of Fig. 4.69a at the same time, until equilibrium is reached. The final equilibrium space charge map is shown in Fig. 4.69b.

4.10.12.3 Effect on the Drift Field

From the equilibrium space charge map in (r, z) (Fig. 4.69b) one can obtain the corresponding electrostatic distortion field. Figure 4.70 shows the result of a finite element calculation (DOLFIN), where the resulting field has already been superimposed with the ideal drift field of $400\,\mathrm{V\,cm^{-1}}$.

4.10.12.4 Resulting Electron Drift Distortions

The important question to answer is how these projected field distortions will affect the drift of electrons towards the readout plane. It can be answered by solving the equation of motion of electrons in the full **E** and **B** field configuration (c.f. [10]):

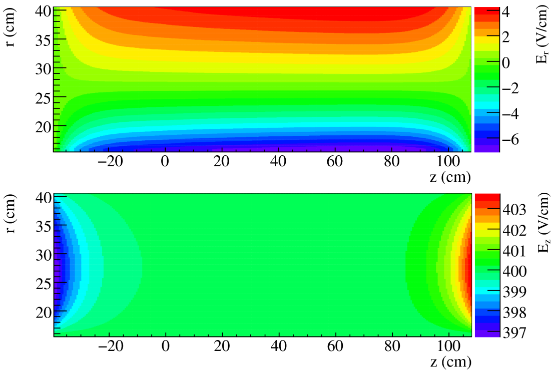

Figure 4.70: Distorted TPC drift field as calculated with a finite element software from the equilibrium space charge as shown in Fig. 4.69b. While effects in drift direction are small and localized at the drift cathode and readout plane respectively, there is a persistent field gradient along the radial direction.

$$m\frac{d\mathbf{u}}{dt} = e\mathbf{E} + e[\mathbf{u} \times \mathbf{B}] - K\mathbf{u} \tag{4.9}$$

Equation 4.9 is integrated with a fourth order Runge Kutta algorithm. The obtained drift paths for electrons of different starting positions are then compared to ideal straight line drifts as expected for an ideal drift field. Figure 4.71 shows a map of these deviations as a function of the starting position of the drift. Absolute offsets of up to 1 mm can be observed in certain regions of the chamber. Deviations along the drift axis are not shown, as they turn out to be negligible.

It should be noted that although both fields are assumed to exhibit cylindrical symmetry there are nevertheless drift distortions perpendicular to the (r, z)-plane. This is due to the well known $\mathbf{E} \times \mathbf{B}$ term in the solution to Eq. 4.9.

4.10.12.5 Recovery of Drift Distortions

In order to recover the distortions discussed in Sec. 4.10.12.4, they have to be measured directly during the operation of the TPC. A possible solution would be to artificially create a well defined pattern of tracks in the TPC and analyze its image as measured by the detector. A comparison with the expected image directly yields the distortions.

Straight line ionization tracks from UV-lasers can provide such a pattern and have already been used for calibration in other drift chambers (e.g. in STAR [?]). To assess the potential of this method

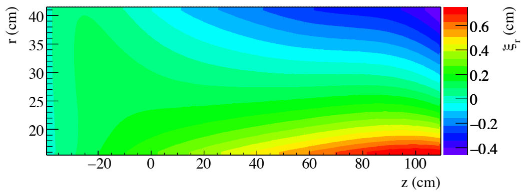

(a) Total drift distortions in radial direction (cm)

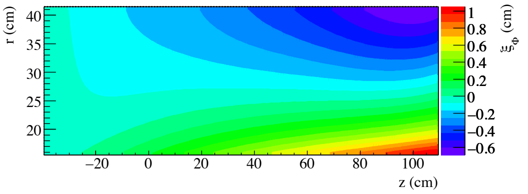

(b) Total drift distortions in azimuthal direction (cm)

Figure 4.71: Drift distortions of electrons in inhomogeneous **E** × **B** field. The graphs show the deviations from a straight line drift experienced by an electron which start their drift at points (r, z) in the TPC.

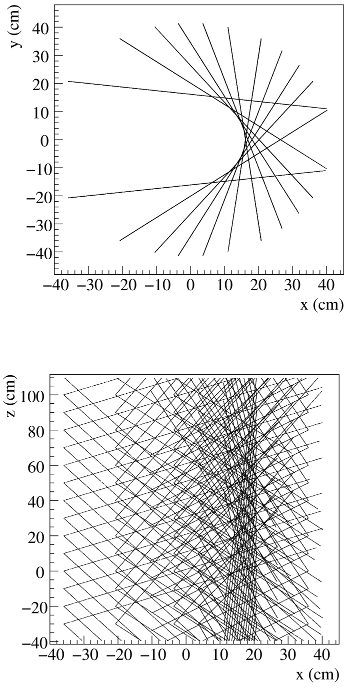

Figure 4.72: Primary ionization caused by laser tracks in the TPC volume as seen from the top of the chamber (a) and from the side (b).

we modeled a laser system in the simulation framework. The laser beams are parametrized as straight line tracks with constant ionization density and a Gaussian beam profile. Figure 4.72 shows an example of primary ionization along the laser rays in the simulation. This example laser grid geometry has been chosen under the requirements of complete chamber illumination and minimal number of track crossings, but is has not been optimized otherwise.

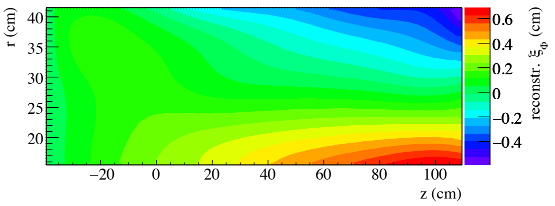

Figure 4.73: Reconstructed drift distortions in azimuthal direction based on one laser event (c.f. Fig. 4.71b).

The reconstruction of the laser tracks is greatly simplified by the knowledge of the geometry. For each laser-hit two residuals are obtained in the x-y-plane (assuming the point of closest approach to be exactly the true origin of the measured cluster): In radial direction and, perpendicular, in ϕ direction. Residuals in z are ignored. The introduced error is small due to the small variation of the distortion maps along the z-axis (c.f. Fig. 4.71). Always the nearest available track is chosen for residual calculation of a given detector hit.

4.10.12.6 Quality of Recovery

The obtained 2-dimensional raw data is then fitted and smoothed by a bi-cubic spline fit. Figure 4.73 shows an example of a reconstructed drift distortion map obtained from the laser-fitting algorithm in the spline representation. The grid of Fig. 4.72 has been used, with a Gaussian laser beam profile ($\sigma = 400\,\mu\mathrm{m}$) and an ionization density of 40 $\mathrm{e}^- \mathrm{cm}^{-1}$, which is a conservative setting.

To be able to judge the quality of the result shown in Fig. 4.73, we compared the reconstruction results to our original drift distortion input (Fig. 4.71), as shown in Fig. 4.74. This distribution does not directly give the principle reconstruction accuracy of the described method, but it also contains intrinsic offsets and uncertainties due to the different representations of the linearly interpolated input deviation make and the reconstructed spline fit. It therefore should be regarded as an upper limit.

Applying a Gaussian fit to the peak of the distribution (including the shoulder but neglecting the "background") lets us estimate the possible accuracy of the recovery method. It yields $\sigma_{\mathrm{Gauss}} \sim 180\,\mu$m and a mean of $\sim 80\mu$m, showing that the total systematic error of the laser correction method is

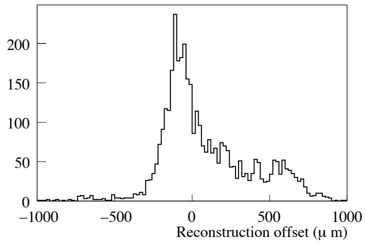

Figure 4.74: Distribution of total reconstruction offset compared to original distortion. **Mean:** 86.4 μm; **RMS:** 292.1.

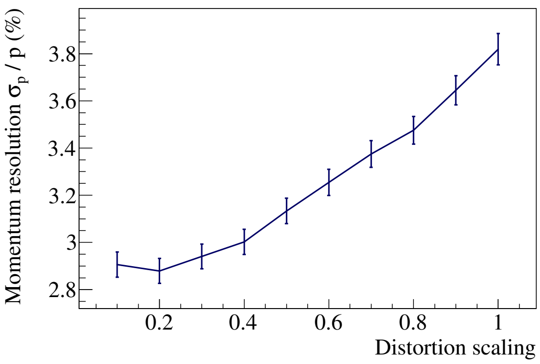

Figure 4.75: Effect of distortions with different scaling settings on momentum resolution.

small and the overall precision of the presented distortion reconstruction and fitting method is slightly better than the aspired spatial resolution of the $\overline{\text{P}}$ANDA TPC.

Such fit quality studies have been conducted for several scenarios (spline parameters, laser geometry), all yielding similar results. It is thus safe to say that we are able to reconstruct drift distortions with a precision better than $\mathcal{O}(300\,\mu\text{m})$, not taking into account mechanical distortions of the calibration system.

To estimate the momentum reconstruction and resolution as a function of the magnitude of present distortions, a sample of 1.0 GeV/c μ-tracks originating from the interaction point was simulated. The "scattering angle" θ was evenly distributed over the full CT acceptance. From the reconstructed tracks the momentum resolution as well as the resulting momentum offset due to the distortions can be studied (c.f. Fig. 4.75 and Fig. 4.76).

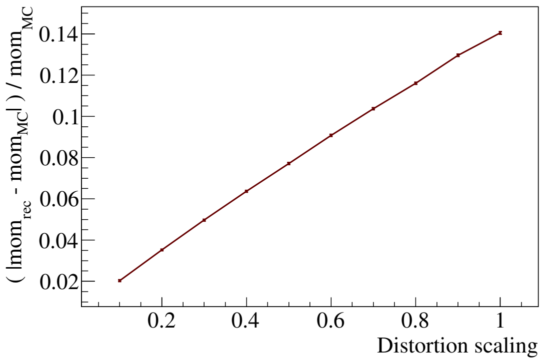

Figure 4.76: Relative error of reconstructed momentum compared to Monte Carlo value as a function of distortion scaling.

4.10.12.7 Application in the Simulation Framework to Correct Distortions

The results of the previous sections enable us to study both the impact of present space charge effect as well as their correction on track reconstruction within our simulation framework. The correction takes place directly inside the reconstruction part of the simulation chain, by applying shifts of the cluster coordinates in accordance with the obtained spline fit from the laser track data just before handing the tracks over to the fitting algorithms.

To study the effect of drift distortions on physics events, we simulated a test sample of 1000 pion tracks (π^+) at a momentum of 0.5 GeV/c and uniformly distributed scattering angle θ. Figure 4.77 visualizes the effect of uncorrected (red) and corrected (green) drift distortions compared to the ideal situation of completely homogeneous electrical field (black).

In Fig. 4.77a clusters in a small area of the TPC readout-plane for the three different scenarios are shown for a few selected events. Displacements of the order of several mm are clearly visible in the uncorrected case (as expected), while the correction moves them back on the ideal tracks nicely.

Figure 4.77b illustrates the large impact of drift distortions on momentum reconstruction. The initial distribution (black line) of reconstructed momenta is significantly deformed and shifted. Both effects can be understood within the scope of the preceding sections: Depending on the scattering angle of the individual track, it is more or less affected by drift distortions (compare to Fig. 4.71), leading to the broadening of the distribution. The asymmetric nature of the drift distortions with respect to the radial coordinate causes the measured curvature of

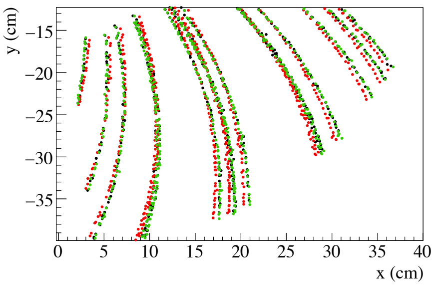

(a)

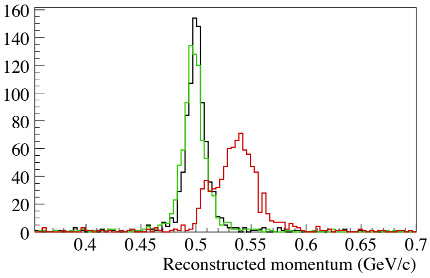

(b)

Figure 4.77: Effect of drift distortions and their correction for π^+- tracks at 0.5 GeV/c momentum. Black represents data from an ideal simulation with perfectly homogeneous drift field. The track data subjected to uncorrected space charge effects is shown in red, the corrected case is displayed in green. In (a) the effect on clusters as reconstructed on the readout plane is shown. Displacements of several mm are visible with the naked eye, as well as a tilting/stretching of tracks. The effect on momentum reconstruction is imaged in (b): Space charge effects distort and shift the spectrum of reconstructed momenta, the correction method is able to restore a close-to-ideal distribution.

the track to appear smaller than it actually was, leading to the shift to higher momenta. However, the correction method described in this section is able to fully recover the original position and shape of the distribution. A Gaussian fit of the ideal and corrected case reveals the difference of ideal and corrected case to be smaller than 1 % for both sigma and mean, respectively.

4.10.12.8 Final Remarks

We can conclude that we successfully showed the general principle of drift distortion correction using a grid of laser beams traversing the active gas volume of the TPC on simulation basis. Mechanical feasibility has to be studied, as well as the impact of structural uncertainties on the reconstruction quality and accuracy.

Alternatively, a simpler concept would be to just measure the *integrated* drift distortions over the full drift length and recover the z-dependence based on simulation models. As the distortions show a rather smooth structure along the drift direction (c.f. Fig. 4.71), this might prove to be a sufficient and mechanically much less challenging alternative.

As closing comment, a more detailed discussion of the presented simulation can be found in [41] and [**?**].

4.10.13 Event Deconvolution - Monte Carlo Studies

The time an electron needs to cover the complete drift distance in the TPC (a so called *drift frame*) is approximately 50 μs, depending on the gas mixture and the applied drift field. At an $\bar{p}p$ annihilation rate of $2 \cdot 10^7$ events per second, with an average time spacing of 50 ns between two events, thus approximately 1000 annihilations happen during one drift frame.

In order to reconstruct exclusive channels, it is essential to be able to assign the recorded signals in the central tracker to the correct physical event. To investigate this issue, a Monte Carlo simulation has been done. The individual events have been generated using the standard DPM $\bar{p}p$ background Monte Carlo event generator. In order to simulate the time distribution of the signals in the TPC these events have been mixed with an exponential distribution for the inter-event spacing, which corresponds to an annihilation rate of $2 \cdot 10^7\,\mathrm{s}^-1$. For each physics event 1000 background events have been added. For the physics events (only) also the information of the MVD has been retained in the simulation. Here we study the two cases where tracks originate from the primary vertex or where neutral particles (such as Λs) which decay into two charged tracks inside the central tracker are produced in the primary annihilation.

It should be noted that the criteria for event Deconvolution described below have deliberately been chosen as simple as possible, keeping in mind that all these operations will have to be done online. The strategy to disentangle the events is the following:

1. We assume stand-alone track reconstruction in the TPC, up to an unknown event-time-offset.
    - In the present study we assume this is possible with high efficiency and precision.
    - Note that the track reconstruction needs to be done online in order to implement a

trigger logic.

2. Under the assumption of tracks originating from the primary vertex we extrapolate to the beam axis. The offset along the beam from the target directly gives the event time of the track. If an event time is defined by outside detectors (as assumed in this study) the offset can be used to for a cleaning cut.

3. Remaining tracks are extrapolated to the Micro Vertex Detector and correlated with the hits in this detector. This yields additional selection criteria.

4. In a second sweep a V^0 hypothesis is tested to find candidates of neutral decays, for example Λs. If two tracks with opposite charge in the TPC appear close to each other a V^0 candidate is formed. Note that the reconstructed 3-momenta are sufficient to reconstruct the direction of flight of the neutral particle. With this direction we can extrapolate again to the beam axis and determine the offset with respect to the target region.

5. Detectors outside of the TPC, like the SciTil or the GEM detectors can also contribute to the timing information. This has not yet been taken into account in the simulations presented below.

4.10.13.1 $Y(4260) \to J/\psi\pi^+\pi^-$ Channel

In order to evaluate the event deconvolution performance for events where all tracks come from the primary vertex the decay of the charmonium-like $Y(4260)$ into $J/\psi\pi^+\pi^-$ where the J/ψ decays into two muons. So there are 4 charged tracks per physics event. To each physics event a background of 1000 DPM events has been added as described above. The physics event was given the time $t_0 = 0$, while the background events were distributed around this time. The track parameters have been taken from the Monte Carlo truth at the inner boundary of the TPC, assuming perfect track reconstruction and an external event time definition.

In order to suppress pile-up events the following cuts have been made:

- Remove all tracks with $p_t < 100\,\mathrm{MeV}/c$.
- Extrapolate track to the z-axis and cut around the target region in a time window ranging from 20 ns to 500 ns (see Fig. 4.78).
- Extrapolate the remaining tracks to the hits in the MVD and cut on the residuals. At least one hit surviving the cut is required in order to accept the track to the physics event.

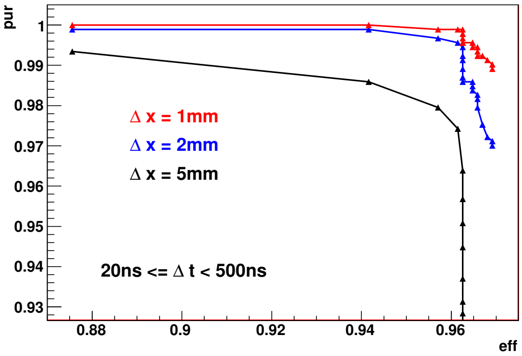

Figure 4.78: Event deconvolution performance for tracks from the primary target. Red: 1 mm cut on MVD residuals, blue 2 mm, black 5 mm. The points on the curve correspond to different event time cuts ranging from 20 ns to 500 ns.

Figure 4.78 shows the purity of this approach versus the achieved efficiency. Here we define the efficiency ϵ as the ratio of the number of recovered physics tracks N_{reco} divided by the number of total physics tracks simulated N_{phys}. The purity Φ is given by the expression

$$\Phi = 1 - \frac{N_{\mathrm{bkg}}}{N_{\mathrm{phys}} + N_{\mathrm{bkg}}}$$

Where N_{bkg} is the number of background tracks wrongly attributed to the physics event. A purity of 1 means that no pile-up track has been kept. If the number of physics tracks is equal to the number of falsely kept background tracks the purity would be $\frac{1}{2}$ and it goes to zero if there are much more background tracks kept than physics tracks were present in the actual event.

The red, blue and black lines correspond to MVD residual cuts of 1 mm, 2 mm or 5 mm, respectively. Note that even the 1 mm cut is comparably loose when compared to the expected resolution of the devices. The points on the curves correspond to different time cuts around the the target ranging from 20 to 500 ns.

With the tightest cut on the MVD residuals and a wide 500 ns cut on the event time still a single track event assignment efficiency of 97% with a purity of about 99% is achieved.

Of course in practice the stand-alone track reconstruction in the TPC will have some finite resolution. In Fig. 4.79 the corresponding efficiency plot

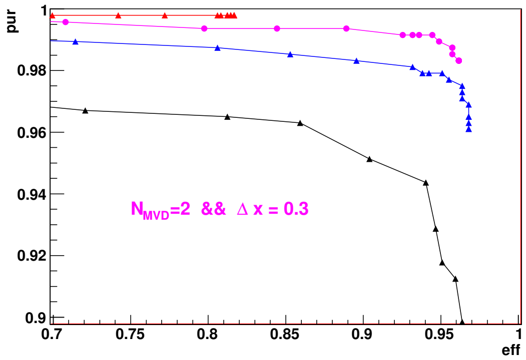

Figure 4.79: Event deconvolution performance for tracks from the primary target with smeared resolution: Red: 1 mm cut on MVD residuals, blue 2 mm, black 5 mm. Magenta: 3 mm residual cut but at least two hits found in the MVD. The points on the curve correspond to different event time cuts ranging from 20 to 500 ns.

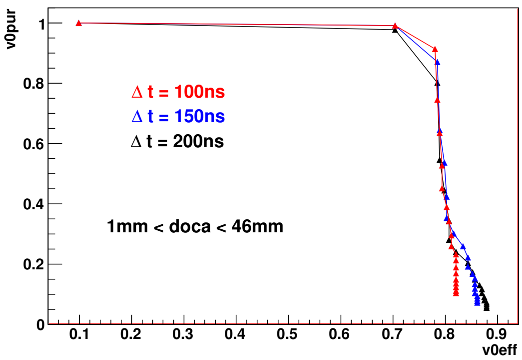

Figure 4.80: Event deconvolution performance for neutral Λ tracks from the primary target. Red 100 ns event time cut, blue 150 ns, black 200 ns. The points on the curve correspond to different cuts for the distance of closest approach of the two charged tracks originating from the decay of the Λ.

is shown for a simulation where the true track values were subjected to Gaussian smearing by 1% in the momentum and by 0.5 mm in the track position at the inner boundary of the TPC. One sees the drop in efficiency down to 80% for the 1 mm residual cut. The magenta colored curve shows a scenario where at least two hits in the MVD are required but with a relatively relaxed cut of 3 mm on the residual. In summary, even with these more realistic smeared track parameters the event deconvolution through target pointing criteria and correlation with the MVD data seems feasible for tracks originating from the primary vertex.

4.10.13.2 $\Lambda \rightarrow p\pi^-$ Channel

In order to study the case when no hits in the MVD are present because a neutral particle has decayed inside the TPC volume into two opposite charge tracks a sample of $\Lambda \rightarrow p\pi^-$ decays has been simulated with added background. In this case only the target pointing of a reconstructed V^0 has been used. Additional information from detectors outside the TPC would further improve the performance. Figure 4.80 shows the performance of the algorithm for different event time cuts: red 100 ns, blue 150 ns, black 200 ns. The points on the curve correspond to different cuts for the distance of closest approach of the two charged tracks originating from the decay of the Λ.

The crucial point here is the vertexing algorithm. As a crude approximation we have just cut on the distance between the endpoints of a track to define a V^0 vertex. It turns out that for V^0s decaying inside the TPC using a linear extrapolation to the beam axis and applying the event time cut all events were reconstructed background free. For Λs decaying closer to the z-axis a true vertexing algorithm is needed for higher efficiencies.

4.11 Detector Tests

In order to verify the design choices for the $\overline{\mathrm{P}}$ANDA TPC, several detectors with GEM amplification have been built and tested:

- a $10 \times 10\,\mathrm{cm}^2$ triple GEM detector for ion backflow studies,
- a small TPC with $10 \times 10\,\mathrm{cm}^2$ active area and 7.7 cm drift length for resolution studies and front-end tests,
- a large prototype TPC with 30 cm outer diameter and 73 cm drift length.

The following sections report key results obtained with the small detectors. The design of the large prototype and first results from beam tests are described in Sec. 4.12.

4.11.1 Gain Measurements

The effective gain of a GEM detector is determined by measuring the current at the readout anode I_{anode} for a given rate R of incident X-rays, each X-ray conversion producing N_{ion} ionization electrons:

$$G_{\mathrm{eff}} = \frac{I_{\mathrm{anode}}}{e N_{\mathrm{ion}} R} \quad . \tag{4.10}$$

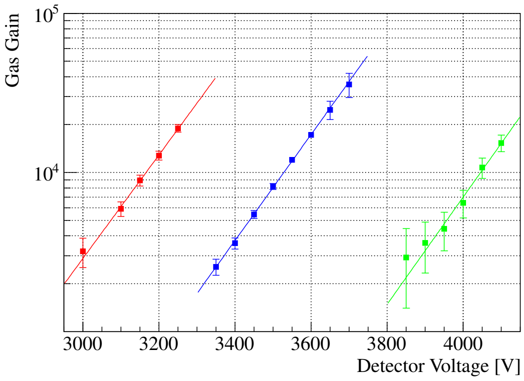

Figure 4.81: Effective gain of a triple GEM detector for three different gas mixtures as a function of the voltage applied to the drift cathode. Ne/CO$_2$ (90/10) in red, Ar/CO$_2$ (90/10) in blue and Ar/CO$_2$ (70/10) in green.

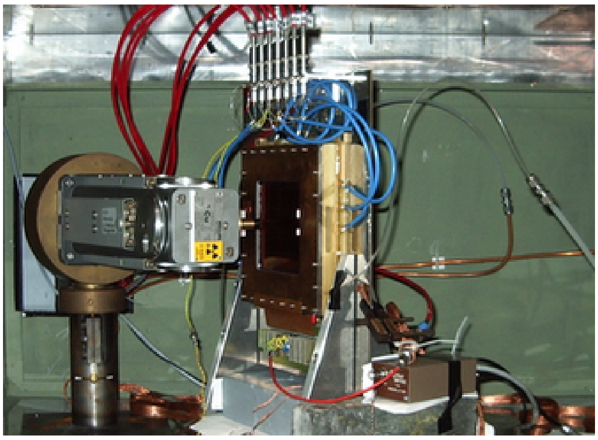

Figure 4.82: X-ray irradiation setup of a triple-GEM detector for ion backflow studies. The detector is mounted in vertical position.

Table 4.9: Electric potentials and fields for the gain measurements, defined by the cathode voltage through a resistive voltage divider. Here, the conversion gap between the drift cathode and the first GEM is 3 mm, the transfer gaps between GEMs and the induction gap are 2 mm, respectively.

Electrode	Potential (V)	Field (kV/cm)	ΔV (V)
Cathode	-4000	2.43	
GEM1 top	-3271		400
GEM1 bot	-2871	3.65	
GEM2 top	-2142		364
GEM2 bot	-1778	3.65	
GEM3 top	-1049		320
GEM3 bot	-729	3.65	
Anode	0		

Defined in this way, eq. 4.10 corresponds to the effective gain seen be the readout, and takes into account charge losses in the GEM structures. The effective gain curves for three different gas mixtures, Ar/CO$_2$ (70/30), Ar/CO$_2$ (90/10) and Ne/CO$_2$ (90/10), are shown as a function of the voltage applied to the drift cathode in Fig. 4.81.

During these measurements, the potentials of the GEM foils were defined by the cathode voltage via a resistor chain. Table 4.9 lists the voltage settings corresponding to a cathode voltage of 4000 V, which is also referred to as 100% standard settings.[3]

4.11.2 Ion Backflow Measurements

In order to prove the feasibility of the PANDA TPC, it is extremely important to study the accumulation of space charge in the drift volume and its effect on track reconstruction. In addition to the primary ionization, there is a backflow of slow ions ($v_{\mathrm{Ion}} \sim 1.7\,\mathrm{cm/ms}$) from the amplification stage, which has to be suppressed as much as possible in the GEM structures. To study this suppression, a $10 \times 10\,\mathrm{cm}^2$ dedicated triple-GEM test detector has been built, which allows an easy exchange of the GEM foils and an independent setting of all voltages. The single projection readout plane consists of strips with a pitch of 200 μm. A copper X-ray tube (8 keV K_α) is used for irradiation. Fig. 4.82 shows a picture of the whole setup.

The currents on all electrodes, including the GEM foils, are measured with custom-made high-voltage current meters with a resolution of a few tens of pA. Figure 4.83 presents a schematic view of the experimental setup.

With this setup different field configurations and foil geometries within the GEM stack have been tested. All measurements were carried out without magnetic field and in an Ar/CO$_2$ (70/30) gas mixture.

Figure 4.84 shows the value of the ion backflow, defined by the ratio between ion current on the cathode and electron current on the anode, as a function of the induction field, i.e. the field between the last GEM and the readout anode. A minimum ion backflow of 0.8% has been achieved. The corresponding settings comprise an induction field between the readout plane and the last GEM foil of 5 kV/cm and a transfer field between this and the

---

[3] These are the average settings for the COMPASS GEM detectors.

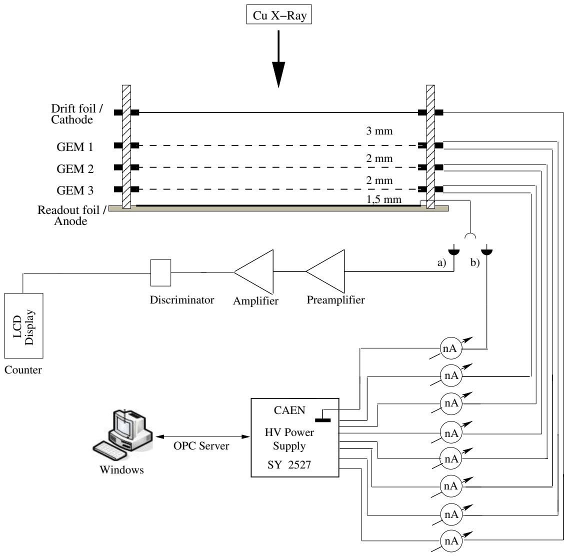

Figure 4.83: Schematic view of the experimental setup of the ion backflow studies: Via a), the rate of the Cu X-ray was determined and via b), the currents on all electrodes of the triple GEM were measured.

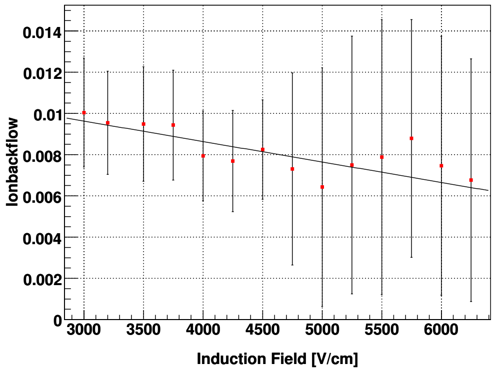

Figure 4.84: Ion backflow depending on the induction field value.

middle foil of 0.16 kV/cm. This asymmetry is essential for the ion suppression. A rather low drift field of 250 V/cm was used and the transfer field between the topmost and the middle foil was set to 4-6 kV/cm, which still ensures a stable and safe operation. Table 4.10 summarizes the settings of fields and GEM voltages. The chamber was operated at a rather high effective gain of $\sim 10^4$ during these measurements. Tests with the large prototype TPC (cf. 4.12) have shown that the TPC can be operated at a gain of $\sim 2 \cdot 10^3$, thus reducing the number of back drifting ions per electron arriving at the GEM stack.

Drift Field	0.25 kV/cm
ΔU_{GEM1}	330 V
Transfer Field 1	4.5 kV/cm
ΔU_{GEM2}	375 kV
Transfer Field 2	0.16 kV/cm
ΔU_{GEM3}	450 V
Collection/Induction Field	5.0 kV/cm

Table 4.10: Chamber settings for a minimal ion backflow at an effective gain of about 10^4.

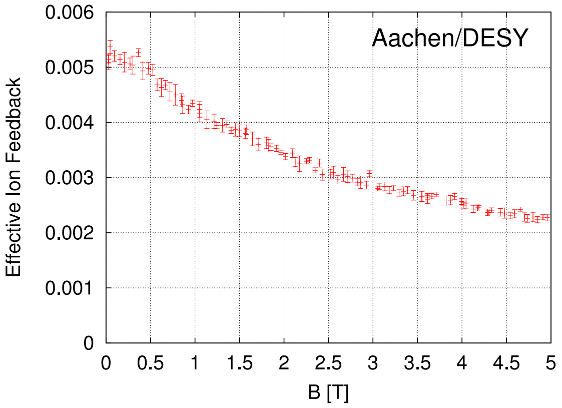

Figure 4.85: Ion backflow depending on the magnetic field.

The presence of a magnetic field helps to reduce the ion backflow even further [48]. An ion backflow value of 0.25% has been measured at a field of 4 T in a Ar/CH_4/CO_2 (93/5/2) gas mixture, as can be seen from Fig. 4.85. The reduction of ion backflow with increasing magnetic field can be explained by a reduced transverse diffusion in the GEM holes and therefore an increased electron transparency. For the $\overline{P}$ANDA TPC with its low diffusion gas mixture, a similar ion backflow can be achieved at a field of 2 T. At a gain of $2 \cdot 10^3$, this corresponds to four back drifting ions per electron reaching the GEM stack.

4.11.3 Test TPC

A small-size GEM-TPC detector ($10 \times 10\,\mathrm{cm}^2$ active area, 77 mm drift length) has been built and tested using cosmic muons [49]. Fig. 4.86 shows a picture of the fully assembled detector, which was operated with an Ar/CO_2 (70/30) gas mixture for the measurements presented here.

Several track topologies were studied by choosing different orientations of the TPC with respect to the incoming muons. For these tests, the readout plane consisted of rectangular pads with a pitch of $1.0 \times 6.2\,\mathrm{mm}^2$; the signals were read out with the PASA/ALTRO electronics [50] originally designed

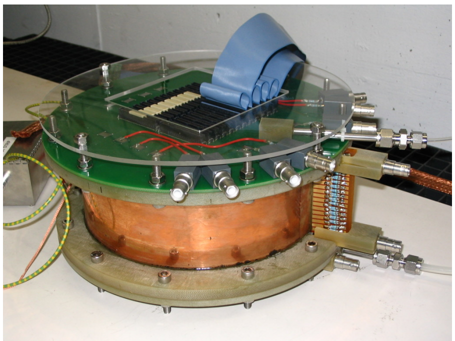

Figure 4.86: Picture of the TPC test chamber with the readout plane on top and the field-cage resistor chain on the right hand side. The GEM foils are mounted on the readout plane, the drift direction is from bottom to top.

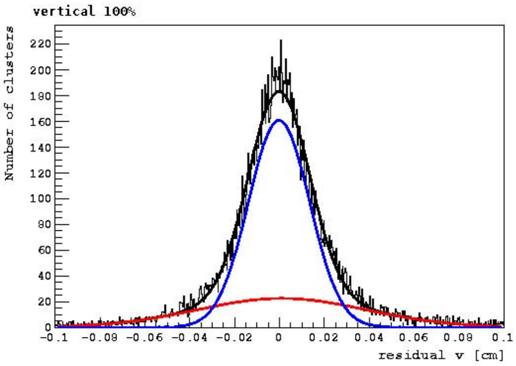

Figure 4.87: Residual distribution for tracks crossing the chamber parallel to the readout plane. The weighted mean of the standard deviations of the two Gaussians is 170 μm.

for the ALICE TPC. Figure 4.87 shows the residual distribution for the coordinate along the small side of the pads for tracks crossing the chamber approximately parallel to the readout plane. All clusters, which were selected by the pattern recognition algorithm to belong to the track, are considered. This introduces a small bias to the results, because these clusters are also used to define the track. This is in particular true for low multiplicity events; therefore a minimum of four clusters per track is required. The resolution is obtained by fitting the residual distribution with two gaussians and calculating the weighted mean of the standard deviations. Spatial resolutions of 170 μm and 200 μm, averaged over the full drift length, were achieved for tracks parallel and perpendicular to the readout plane, respectively.

The spatial resolution along the drift direction was found to be 240 μm.

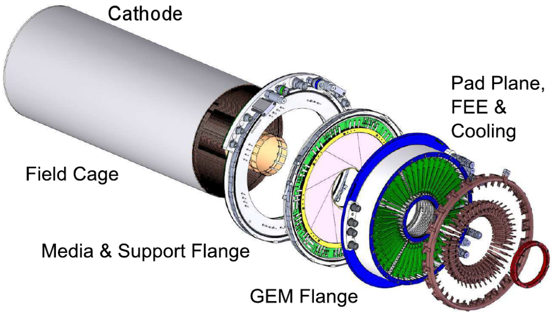

Figure 4.88: Explosion view of the GEM-TPC.

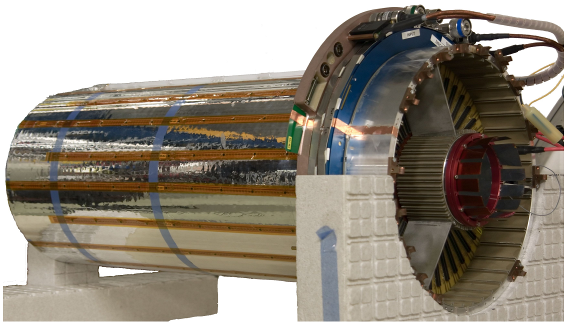

Figure 4.89: Photo of the large prototype.

4.12 Large Prototype

4.12.1 Design

A large GEM-TPC prototype was built to be employed in a physics run in hadron collisions at intermediate energies within the existing FOPI spectrometer at GSI. The size was chosen such to fit inside the Central Drift Chamber (CDC) of FOPI and to have the possibility to host different target types within the GEM-TPC detector. In addition design requirements for the usage of the same chamber within the Crystal Barrel experiment at ELSA in Bonn were taken into account.

The large prototype has a total drift length of 727.8 mm, an inner diameter of 104 mm and an outer diameter of 308 mm. The prototype mainly consists of three parts: the field-cage, the readout part and the media flange. Figure 4.88 shows an explosion view of the GEM-TPC prototype with the different detector parts, while Figure 4.89 shows a photo of the large prototype that was built.

4.12.1.1 The Fieldcage

The lightweight field-cage structure consists of a self-supporting sandwich made of a Rohacell core,

Material	Thickness
Aluminized mylar	200 nm
Kapton	25 μm
Kapton	125 μm
Rohacell	2 mm
Kapton	125 μm
Rohacell	2 mm
Kapton	125 μm
Kapton	25 μm

Table 4.11: Materials and their thickness listed from the outside of the fieldcage to the inside.

Kapton insulation layers and two skins of fiber glass material, arranged in two concentric cylinders. The materials of the fieldcage and their thickness is listed in table 4.11. The downstream end-cap is made of the same structure. Electrical shielding to the outside world is provided by an additional Kapton layer with aluminium coating. A homogeneous electric field in the drift direction is provided by the HV plane at the downstream end cap and precision concentric cylindrical field cage rings along the barrel that cover the inner and outer radius and are stepwise degrading the HV up to ground potential at the anode side. To improve the homogeneity, the cylindrical field cage consists of two sets of copper strips on both sides of the Kapton foil. The potential on each ring is defined by a resistor chain. The stripfoil is made out of a 25 μm thick kapton foil with over 700 copper strips with a pitch of 1.5 mm on each sides. The upstream side of the field cage is connected to the media flange made of fiber glass material, which provides mechanical stability and serves as the mounting structure of the GEM-TPC to the external support. The radiation length for a track perpendicular to the beam axis is 0.6 % and for a track in forward direction, crossing the drift cathode, it is 0.6 %.

4.12.1.2 The GEM Flange

The GEM-Flange is designed to hold up to four GEM foils for the gas amplification. The foils used for the prototype are standard foils produced at CERN with a thickness of 50 μm and a hole pitch of 140 μm. To keep the charge released in a discharge as low as possible each foil is segmented into 8 sectors on one side, each with its own loading resistor. A schematic of the employed GEM-stack is visible in Figure 4.90.

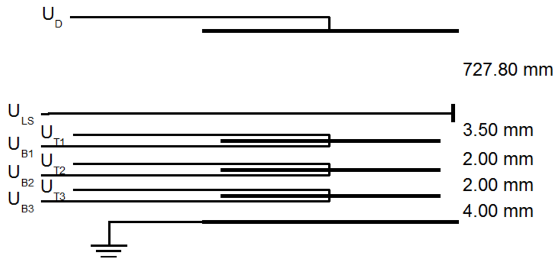

Figure 4.90: Scheme of the GEM-stack used for the large prototype where U_D is the drift voltage, U_{LS} is the voltage of the last strip before the GEM foils and U_T and U_B are the top and bottom voltages of the respective GEM foil.

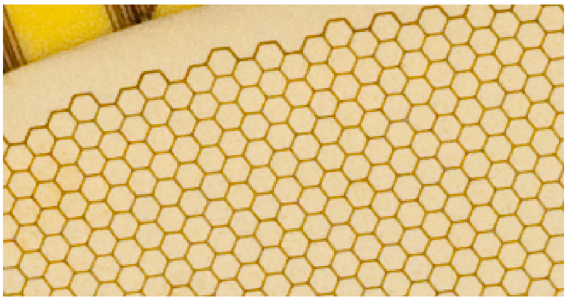

Figure 4.91: Closeup view of the pad-plane.

4.12.1.3 The Readout

For a more uniform charge distribution across the pads a new pad-plane with hexagonal pad shapes was designed. The optimum outer pad radius was determined to be 1.5 mm by Monte Carlo simulations of the $\overline{\text{P}}$ANDA TPC, taking into account a magnetic field of 2 T. These simulations show that the spatial resolution and hence the momentum resolution does not improve for outer radii of hexagonal pads below 1.5 mm, but is already dominated by diffusion in the chamber.

Since the pad-plane is used to close the gas volume it had to be designed in a gas tight way. This was done by using a four layer build-up with tracks on all layers and staggered connections only between neighboring layers. To avoid crosstalk between signals of different pads the connections from the pads to the connectors were designed to minimize crossing of tracks or narrow parallel tracks. In Fig. 4.91 a close-up of the pad-plane is shown. Field inhomogeneities on the outer part of the pad-plane were avoided by placing copper matching the shape of the pads.

For the readout the pad-plane is equipped with 42 front-end cards, each equipped with 4 T2K/AFTER chips [51]. The T2K/AFTER chip

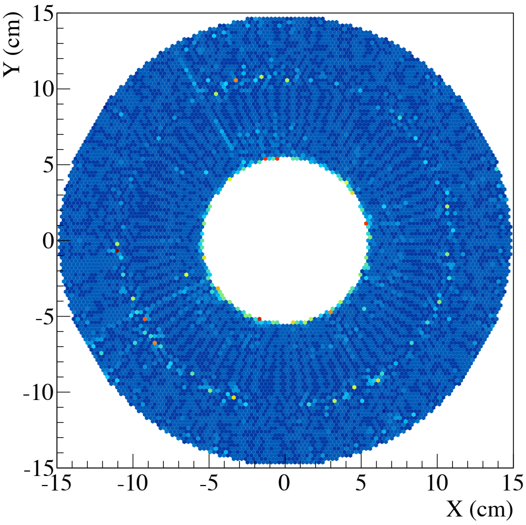

Figure 4.92: 2-Dimensional noise distribution on the pad-plane.

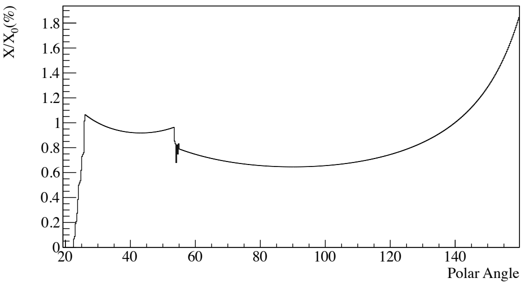

Figure 4.93: Radiation length plotted against the polar angle.

is an analog sampling chip with a 511-cell switched capacitor array per channel, a maximal sampling frequency of 50 MHz and a multiplexed output. The design value of the equivalent noise charge (ENC) is around 600 electrons at a 10 pF input capacitance. Figure 4.92 shows the 2-dimensional noise distribution on the pad-plane. One can see that the noise is rather uniformly distributed around a mean value of 1.6 *ADC* channels which corresponds to an ENC of 625 electrons. The visible ring structure is due to single high noise channels on each FE-chip.

Since the drift velocity depends strongly on the temperature, a cooling system for the front-end cards was installed to avoid heating the pad-plane (see 4.12.1.5)

4.12.1.4 Material Budget

The total radiation length seen by charged particles traversing the large prototype has been evaluated in the same fashion described in 4.3.2, employing a detailed geometry of the prototype within the PANDAROOT framework. To calculate the radiation length the origin of the tracks was set to the target position in the FOPI spectrometer (cf. Sec. 4.12), corresponding to a drift distance of about 65 cm in the large prototype. Figure 4.93 shows the obtained radiation length versus the polar angle of the track.

Starting from 20° to 55° the track goes through the drift cathode, therefore the radiation length is bigger than in the fieldcage in the area between 55° and 160°. After the fieldcage the radiation length increases significantly (not shown in Fig. 4.12) due to the material of the media and GEM flange. For experiments with FOPI this high material budget in backward direction is not an issue since no further detectors are located behind the prototype and in this region there is no overlap with the CDC.

4.12.1.5 The Cooling System

A water-driven cooling system was built to cool each front-end card, each ADC and the voltage regulators independently. A mixture of water and glysantin G48/BASF (Glycol & Ethandiol) is circulating in a closed pipe system and flowing through heat exchangers coupled to copper plates. The copper plates are put in contact with the elements that have to be cooled. The water temperature is kept to a constant value of 20° by a UC080T-H chiller system and distributed through flexible polyurethane pipes. Each front end card is sandwiched between 2 copper plates put in direct contact through heat conducting pads to the 4 FE chips. Figure 4.94 shows the copper plates and the heat exchangers attached to one FE card. Figure 4.95 shows the complete cooling ring connected to the readout electronics. The length of the pipes was chosen such to guarantee the same impedance for all the attached FE cards. The same system provides the cooling of the ADC and the voltage regulators through a serial connection of the pipes following the cooling ring for the FE cards.

Temperature sensors were applied on the pad plane and along the external surface of the field-cage in order to monitor the thermal fluctuations. The envisaged temperature stability, necessary in order to maintain a constant drift velocity, yields 0.1 K. 12 PT100 sensors were placed on the pad-plane along the outer radius, while 210 Dallas Semiconductor DS18B20U 1-wire temperature sensors were distributed along the field cage cylinder.

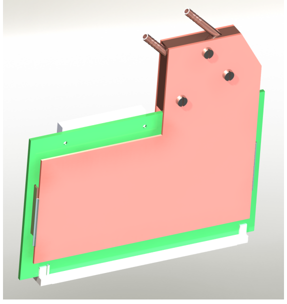

Figure 4.94: Copper plates utilized to cool the FE chips.

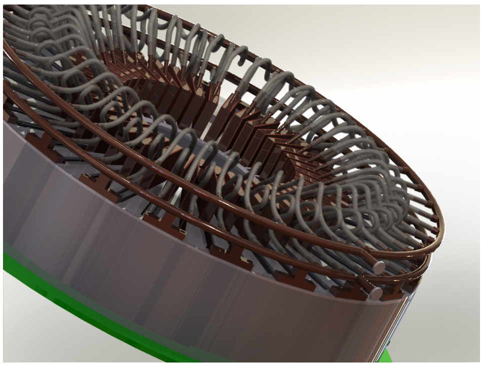

Figure 4.95: Complete cooling ring for connected to the the FE cards.

The region inside the FOPI spectrometer is characterized by rather large temperature fluctuations, mainly due to the heat dissipated by the RPC detectors. In order to stabilize the temperature along the field cage, compressed air was blown inside the 5 mm gap that separates the internal hole of the CDC from the external walls of the TPC barrel.

Figure 4.96 shows the temperature distribution as a function of the azimuthal angle ϕ and the z coordinate measured along the field cage. One can see that temperature fluctuations up to 1.5 K appear along the field cage. The same fluctuations are measured on the pad-plane surface which shows that the temperature gradient surrounding the chamber is responsible for the measured variations.

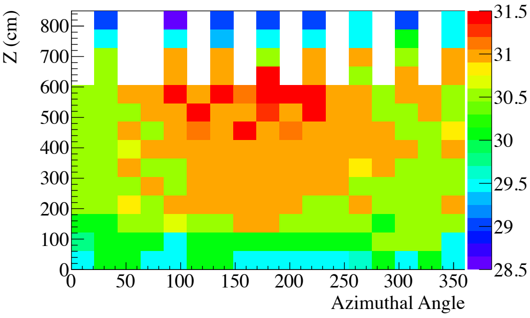

Figure 4.96: Measured temperature along the field cage as a function of the azimuthal angle ϕ and the z coordinate.

4.12.1.6 The Gas System

An open gas circulation system was employed for the large prototype. The system is composed by a supply unit and analyzing devices that monitor the gas mixture and flow, the Oxygen content, the dew-point and the pressure. The total volume of the large prototype is about 45 l and a flow rate of 45 l/h was used for both $ArCO_2$ and $NeCO_2$ gas mixtures. A Brooks model 0254 was used to control the mass flow. This and the other parameters were monitored on a labview-based slow control system. A quadrupole mass spectrometer (QMS) was used to measure the Ar-CO_2 and $NeCO_2$ gas mixture during run time. A special measuring scheme was developed, where the TPC gas sample is measured in-between two calibration samples. This allowed a suppression of long-term drifts of the mass spectrometer and therefore the determination of the CO_2 concentration with an accuracy of less than 1 % was possible. Figure 4.97 shows an example of this measurement for a time interval of 2.5 days. The ratio Ar to CO_2 is shown for the analyzed gas sample and the calibration sample, the extracted CO_2 concentration is shown as well. The error band corresponds to 1 % fluctuations. A constant overpressure of 18 mbar was kept inside the chamber and an Oxygen content between 6 and 8 ppm was reached.

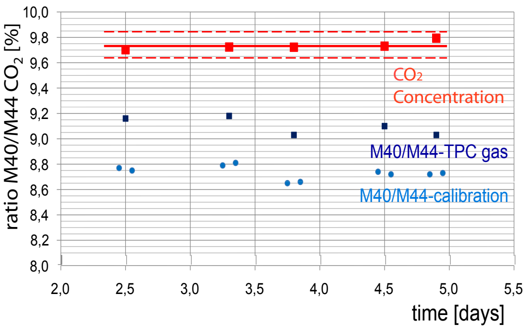

Figure 4.97: QMS analysis of the CO_2 content in a $ArC0_2$ 90/10 gas mixture along 2.5 days of data taking.

4.12.2 Results

To test its operation, the large prototype was installed inside the FOPI [52] spectrometer at GSI (Darmstadt, Germany). FOPI is a large acceptance, fixed-target heavy ion experiment. It has been designed to study the properties of compressed nuclear matter formed by collisions of heavy ions at energies from 0.1 *A*GeV to 2.0 *AGeV*. The detector consists of sub-detector systems which nearly have a complete azimuthal symmetry. This nearly 4π coverage of the solid angle, allows for an almost complete event characterization. FOPI is able to identify light charged particles (pions, kaons, protons ...) and intermediate mass fragments. Hadron resonances and neutral hadrons can also be reconstructed from their decay products.

In Fig. 4.98 FOPI (grey color) as well as the GEM-TPC (violet color) are shown. The FOPI spectrometer consists of a central drift chamber (CDC) which is surrounded by a scintillator barrel (Barrel) and a RPC barrel (RPC) with an intrinsic time of flight resolution of 200 ps and 80 ps respectively. In forward direction another drift chamber (Helitron) and a scintillator time of flight wall (PLAWA) with a time of flight resolution of 120 ps - 150 ps are installed. The CDC, Helitron and the two barrels are surrounded by a 0.6 T solenoid magnet (not shown in Figure 4.98).

The FOPI spectrometer delivers a vertex resolution of few millimeters in the $x - y$ plane and a resolution along the beam axis of around 5 cm. The reached momentum resolution for particles traversing the CDC is $4 - 10\,\%$. Vertex and especially secondary vertex resolutions can be significantly improved by using the GEM-TPC prototype as an additional tracker.

The TPC was mounted in the inner hole of the central drift chamber of FOPI. With this configuration it is possible to use the tracking and time-of-flight detectors of FOPI as a reference. All detectors of FOPI have a 2π acceptance in the azimuthal angle. The acceptance in the polar angles are listed in table 4.12.

The data acquisition (DAQ) of FOPI is based on the Multi Branch System (MBS) and designed for a trigger-rate of around 600 Hz. The DAQ of the GEM-TPC is based on a different system since the VME readout like in FOPI would be too slow to handle the large amount of data coming from the TPC ($\sim$ 40 MB/s). This system is a slightly modified version of the COMPASS readout [53]. The Trigger Control System module (TCS) of the GEM-TPC gets control signals from the FOPI main trigger and sends out triggers to the GEM-TPC readout modules (GeSiCA) accordingly. TCS also sends out to the FOPI system its dead-time signal, which amounts to 2.5 ms. Additionally the time-stamps from the MBS event header are communicated to the GeSiCa, in order to achieve the synchronization of the data word of the different sub-detectors. Optical fibers are used to send the data of the prototype via the S-Link protocol [53] to the event builder were it is merged with the FOPI data stream.

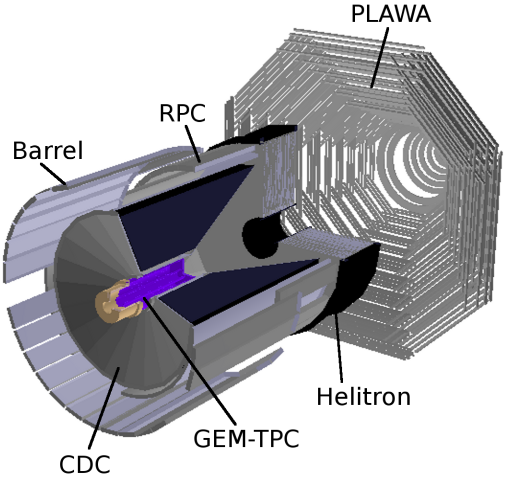

Figure 4.98: The FOPI spectrometer (gray color) with the GEM-TPC (violet color) prototype mounted in the inner bore of the central drift chamber (CDC).

Detector	Acceptance
CDC	30° - 140°
RPC	36° - 67°
Helitron	10° - 30°
Barrel	60° - 110°
PLAWA	10° - 35°
GEM-TPC	5° - 175°

Table 4.12: Acceptances of the FOPI detectors and the GEM-TPC.

Furthermore a lot of different programs to monitor and control the high voltage, low voltage, temperatures, gas mixture, DAQ and data were developed and improved.

Several different settings of the large prototype have been tested during the measurement within FOPI.

- Several drift fields: $150, 200, 300, 360\,\mathrm{V/cm}$ with the corresponding drift velocities: $0.9, 1.4, 2.2, 2.9\,\mathrm{cm}/\mu\mathrm{s}$ [54].
- Different settings for the gain for the GEM-

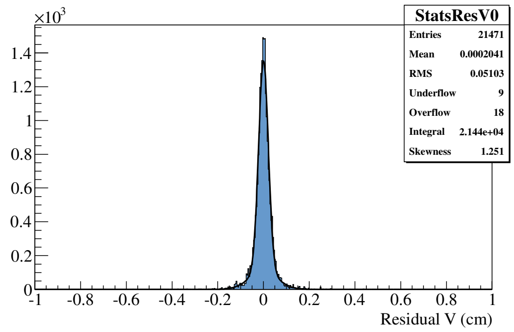

(a) Residual measured with cosmic tracks. The experimental distribution is fitted with two Gaussian functions. The weighted mean of the sigmas of the two Gaussian curves is 230 µm.

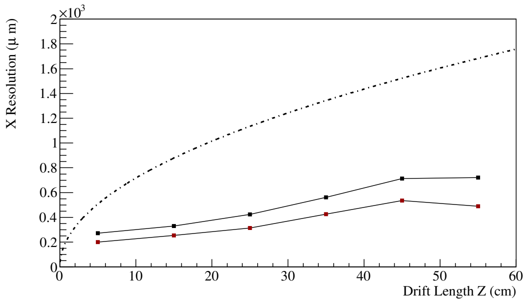

(b) Chamber resolution (along x) as a function of drift length. The dashed line is the transverse diffusion for single electron drift as calculated with GARFIELD. The dots show the results from residual distributions for tracks in 10 cm bins along the drift direction (cf. (a)). The red dots are the sigmas of the narrow Gaussian, while the black dots above correspond to the weighted mean of both Gaussian curves. Statistical error bars are included, but smaller than the data points.

Figure 4.99: Figure (a) shows the residuals of one slice in z. Figure (b) shows the z-dependence of the residuals. The results were obtained from cosmic date.

stack. The nominal setting of the high voltage, referred to as 100 %, are given in Table 4.9.

- Two gas mixtures, namely Ar/CO_2 and Ne/CO_2 both in a 90/10 mixture by weight.

4.12.2.1 Results with Cosmics

As a first test, tracks from cosmic rays were measured, using the Barrel as a trigger. The TPC was operated at a drift field of 360 V/cm with an Ar/CO_2 (90/10) mixture, which translates into a drift velocity of ~ 2.9 cm/µs. The high voltage settings for the GEM corresponded to 85 % of the reference values.

The track reconstruction in the GEM-TPC was done by first finding the track points with the standard three-dimensional clustering algorithm (cf. Sec. 4.10.6). The obtained clusters were then used in a four-dimensional Hough transformation for linear straight line pattern recognition, a modification of the algorithm described in Sec. 4.10.7.8. The obtained residuals are shown in Fig. 4.99. According to the definition of U and V given in 4.10.8 and considering that most of the analyzed cosmic tracks are vertical, the V residuals represent the resolution in the x-coordinate. A spatial resolution of 230 µm for the first slice along the z-axis was obtained. It should be noted at this point that the transverse diffusion for an electron at the end of the large prototype (z = 70 cm, cf. Fig. 4.99) in Ar/CO_2 (90/10) and no magnetic field is roughly 1.5 times *larger* than the maximum transverse diffusion in the final TPC with full PANDA field configuration. The same procedure has been tested with simulation. The full-scale simulation (cf. Sec. 4.10.1) of the large prototype has been used with events containing mono-energetic muons with a kinetic energy between 10 and 100 GeV. A total statistics of $1 \cdot 10^6$ vertical muon tracks has been simulated. After the Monte Carlo and digitization procedures the full analysis chain has been utilized and the residuals extracted in the same way used for the real data. Figure 4.100 shows the chamber resolution calculated for simulated tracks for the first 10 cm drift (panel a)) and as a function of the drift length (panel b)). The same comparison with the Garfield calculation shown in Fig. 4.99 is shown also in Fig. 4.100 together with the results of the Gaussian fits. The red dots are the sigmas of the narrow Gaussian, while the black dots above are from the weighted mean of both Gaussian curves. The agreement between simulations and experimental data is satisfactory but small differences remain for large drift length slices that should be systematically studied.

The simulated cosmic tracks have also been analyzed in terms of completeness and splitting. The completeness of the track is defined as the percentage of clusters that belong to a certain track and are also associated to this track. An average completeness of 91.4% has been obtained for the simulated cosmic tracks. The splitting defines the number of segments one track is split into by the pattern recognition algorithm. About 5 % of all the cosmic tracks are split and mainly (84 %) into two segments.

Cosmic events have been collected also utilizing a NeCO_2 mixture (90/10) as drift gas and the drift field was set to 360 V/cm. Several settings of the GEM high voltage have been tested, ranging from 70 % to 74 % in steps of 1 %. This data sample has

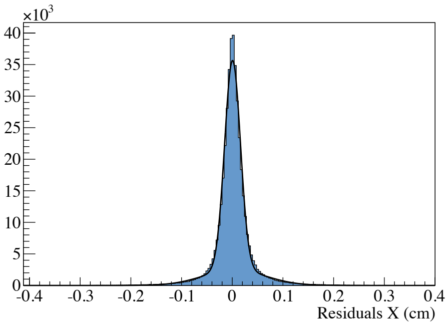

(a) Residuals in V direction (approx. parallel to the $x-$axis for cosmics) for the first 10 cm of drift. The resolution obtained from the weighted mean of two fitted gaussian curves is 259 µm

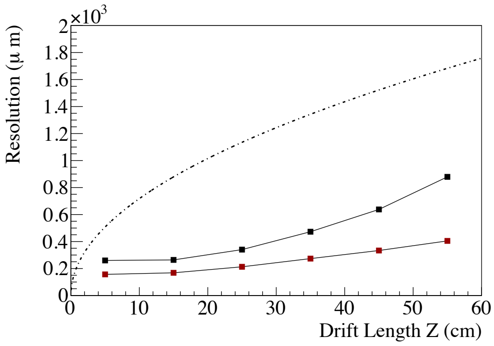

(b) Chamber resolution (along x) as a function of drift lenghth. The dashed line is the transverse diffusion for single electron drift as calculated with GARFIELD. The dots show the results from residual distributions for tracks in 10 cm bins along the drift direction. The red dots are the sigmas of the narrow Gaussian, while the black dots above are from the weighted mean of both Gaussian curves. Statistical error bars are included, but smaller than the data points.

Figure 4.100: Figure (a) shows the residuals of one slice in z. Figure (b) shows the z-dependence of the residuals. These results are extracted from simulations (see text for details).

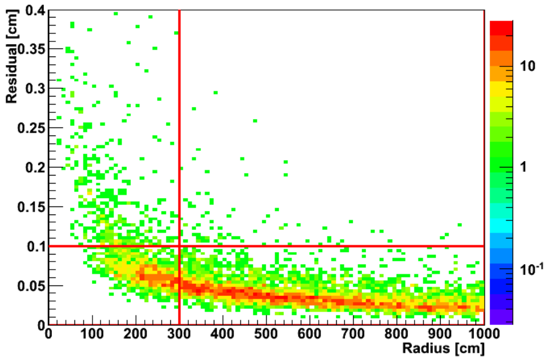

Figure 4.101: χ^2 for the straight line fit as a function of the track radius reconstructed in the CDC. The full lines identify the cuts applied to select straight tracks.

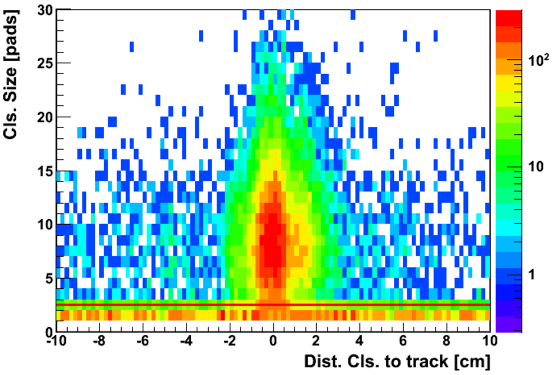

Figure 4.102: Cluster size as a function of the cluster distance from the CDC reference track.

been utilized to check the efficiency of the GEM-TPC chamber and the total efficiency of the track reconstruction algorithms. The cosmic tracks reconstructed in the CDC detector have been used as an external reference to evaluate the efficiency. Events containing a single track have been selected and the curvature radius of the identified particles in the CDC has been determined. Applying an additional straight line fit and evaluating the respective reduced χ^2 for each track, its degree of straightness was evaluated. Figure 4.101 shows the residual (defined as $\frac{\sqrt{\chi^2}}{Ndf-2}$ for the straight line fit as a function of the track radius. Straight tracks are selected applying the following cuts on these variables: Residual$<$ 0.1 and Radius $>$ 300 cm. A fiducial volume is defined in the GEM-TPC, to exclude the detector edges and account for the scarce position resolution of the CDC along the beam axis (about 5 cm). The first and last 5 cm of the chamber (Z direction) are excluded and a maximal radius of 13 cm is defined. The selected straight tracks in the CDC are extrapolated to the GEM-TPC within the fiducial volume defined above and used as a reference to evaluate the efficiencies.

First, the efficiency of the GEM-TPC chamber is extracted counting the number of extrapolated segments in the fiducial volume that are correlated with identified clusters in the GEM-TPC. Clusters have been selected which lay within a maximal distance of 2 cm in both the X and Y coordinates respect to the extrapolated CDC track in the GEM-TPC fiducial volume. No matching in the Z coordinate is required due to the insufficient spatial resolution of the CDC. In order to reduce the contribution of the electronic noise arising in the GEM-TPC a minimal cluster amplitude ($\geq$ 30 ADC channels)

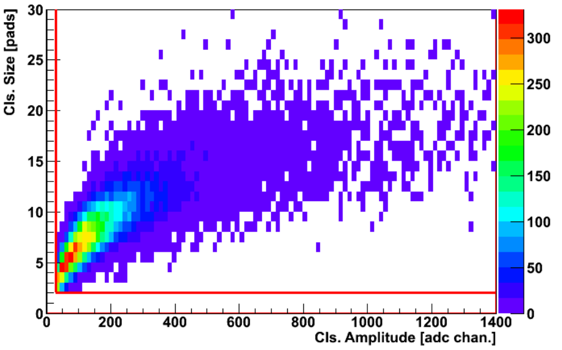

Figure 4.103: Cluster size versus cluster amplitude.

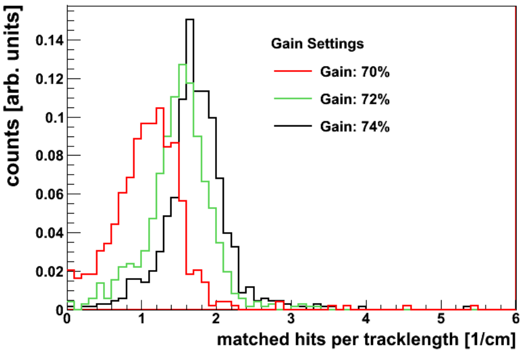

Figure 4.104: Distribution of the number of matched clusters normalized to the track length in the GEM-TPC (see text for details). The different curves refer to different settings of the GEM gain.

and size ($\geq$ 2 pads) have been requested. Figure 4.102 shows the cluster size as a function of the distance between the clusters and the reference CDC track. Figure 4.103 shows the size of all the clusters as a function of the cluster amplitude after the selections mentioned above have been applied. These two histograms demonstrate that after the applied selection most of the clusters do not stem from electronic noise and hence are suited for the calculation of the efficiencies.

Figure 4.104 shows the number of clusters matched to the extrapolated CDC track divided by the length of the extrapolated track segment in the GEM-TPC. This quantity is referred hereafter as the parameter P. The different curves refer to 3 different gain settings for the GEM stack. A minimal length of 12 cm is required for the extrapolated segment in the GEM-TPC volume. One can see how decreasing the GEM gain the average number of clusters normalized to the track length shifts as expected to lower values. The efficiency of the chamber for the different GEM gain settings can be extracted varying the threshold value of the parameter P. Table 4.13 shows the obtained efficiency for the three different gain settings and applying either no cut on P and or selecting two threshold values: $P = 0.3 - 0.5$. These extracted efficiencies include the pulse shape analysis and cluster finding procedure described in 4.10.5 and 4.10.6.

Table 4.13: Chamber efficiency for different GEM gains and different cuts on the parameter P, see text for details.

	Efficiency		
Gain	All	$P \geq 0.3$	$P \geq 0.5$
74 %	96.2 %	95.9 %	95.5 %
72 %	91.6 %	90.9 %	89.2 %
70 %	79.5 %	75.2 %	71.5 %

Given the identified clusters matched to the external reference track in the CDC, the full reconstruction chain based on the PandaRoot framework [23] has been applied to the data. This analysis chain includes additionally to the clustering algorithm the pattern recognition (cf. Sec 4.10.7.2) and the track fitting algorithms. The efficiency is defined as the probability of obtaining a fitted track candidate in the GEM-TPC if a matching between the clusters in the GEM-TPC and the reconstructed track in the CDC is available.

When applying the full reconstruction chain to this sample, the combined efficiency of the pattern recognition and track fitting is found to be 100 % for all the gain settings and selections of the cut on the P variable.

4.12.2.2 Results with Beam Data

Several beam species have been utilized to collect data for the joint GEM-TPC/FOPI system at GSI. Two test experiments have taken place in November 2010 and April 2011 and ^{84}Kr, ^{197}Au and ^{22}Ne beams at 1.2 AGeV, 1.0 AGeV and 1.7 AGeV kinetic energies respectively have been colliding on an Al target of 2 % interaction length inside the GEM-TPC. The beam parameters were set to an average particle rate of $5 \cdot 10^6$ particles/spill with a total spill length of about 10 sec and a duty cycle factor of 50 %. One physics run employing a π^- beam at 1.7 GeV/c colliding on different solid target has taken place in June 2011. For this secondary beam a lower rate of 25.000 π^-/spill with a total spill length of 3.5 sec and a duty cycle factor of 42 % was available. The major aim of this experiment was to measure charged and neutral kaons produced almost at rest in a nuclear medium and the employment of the GEM-TPC together with the other FOPI sub-detectors can increase sensibly the momentum resolution and the secondary vertex identification.

Figure 4.105 shows two typical events in the GEM-TPC when particles are produced from reactions happening upstream (panel a)) and on the Al target (panel b)) employing a ^{22}Ne beam. On the left panel the three-dimensional view of the hit points is shown where the vertical axis corresponds to the beam axis. On the left panel the projection of the event on the pad-plane is depicted, the color-code is proportional to the cluster amplitude. The chamber settings corresponded to 360 V/cm drift and 86% of the GEM gain. The ArCO$_2$ mixture was used as drift gas. The noisy pads have been rejected on-line by applying a threshold of 4.5 times the σ value of the amplitude distribution stemming from electronic noise only. This threshold values are the same for all the data presented hereafter.

The curled tracks shown in panel a) refer to low energy electrons strongly bent in the 0.6 T magnetic field. Even if the 3D representation on the right hand side of the panel shows the raw hits, the excellent tomographic capability of the device is evident. Panel b) shows the particle tracks detected in the TPC after a collision of the ^{22}Ne beam with the Al target. An average length of 14 cm characterizes the tracks reconstructed in the GEM-TPC and due to the fact that the average particle momentum exceeds 1 GeV/c, the tracks are rather straight. The momentum of each track candidate can be reconstructed in the CDC, where the path length of each particle yield in average 80 cm. The additional space points in the GEM-TPC can be combined to the CDC points to improve the accuracy of the determination of the bending and hence of the particle momentum.

The track reconstruction in the GEM-TPC was done according to Sec. 4.10.7.2 with the Riemann track follower. The procedure is exactly the same described for the PANDA TPC except for the fact that the pad-plane of the large prototype is not sectorized. The distribution of the number of reconstructed tracks for ^{22}Ne+Al collisions at 1.7 AGeV is shown in Fig.4.106. A maximal multiplicity of 100 particles per event was reached, on average 19 tracks per ^{22}Ne collision, with an average number of 23 hits per track have been reconstructed in the GEM-TPC.

The resulting residuals expressed along the two coordinates U and V (see Figure 4.56 in Sec.4.10.8) that define a plane perpendicular to the track and that contains the hit are shown in Figure4.107. The residual width for the U and V coordinates is extracted fitting the residual distributions obtained for the different slices in the z-coordinate with a double Gaussian, like it was done for the cosmic data. In Fig.4.107 the residual distribution for the first 10 cm drift is shown in panel a) together with the result from a fit with 3 Gaussian function. Panel b) in Fig. 4.107 shows the sigma of the narrow Gaussian fits as a function of the drift length. It should be pointed out that in the case of particle tracks stemming from beam reactions, U and V do not correspond univocally to cartesian coordinates. This preliminary result agrees rather well with the resolution obtained for cosmic tracks. The residual distribution obtained for the beam data displays a larger background in respect to the cosmic residuals. This is probably due to the fact that the rather high GEM gain leads to overflow and this effect is more present for beam data where the particle energy loss is about 5 times larger than for cosmic tracks. The overflow spoils the determination of the cluster barycenter and hence the resolution. Further studies will exclude such tracks.

The homogeneity of the tracks distribution has been checked displaying the chamber occupancy for reactions with the π^- beam. Figure 4.108 shows the track occupancy as a function of the radial and z coordinates of the GEM-TPC chamber. The scale is linear in z. This distribution has been obtained with a reduced drift field of 235 V/cm drift, 80% of the GEM gain and a sampling frequency of 16 MHz, corresponding to a drift window of 31.93 µs. The resulting active length with these settings is 55 cm, shifted to the end of the chamber. The location of the target set in the middle of the GEM-TPC chamber, can be recognized in Figure4.108 and the resulting acceptance is well suited to measure low momentum kaons produced in the π^--induced reactions. One can see that a good homogeneity is guaranteed for a minimum distance of 0.5 cm from the field-cage walls. Further distortion effects of the electric field are currently under study.

A similar matching procedure like the one used to correlate the cosmic tracks identified in the CDC with the hits recorded in the GEM-TPC has been used for the heavy ion collisions data. Figure 4.109 shows the projection on the X-Y plane of the recorded tracks in one ^{22}Ne +Al collision. The pink lines shows the circle fits applied to the tracks in the CDC, in the insert the GEM-TPC fiducial area is magnified and the blue points represent the reconstructed clusters. The correspondence between the tracks measured in the two detectors is evident but a relative mis-alignment between the detector

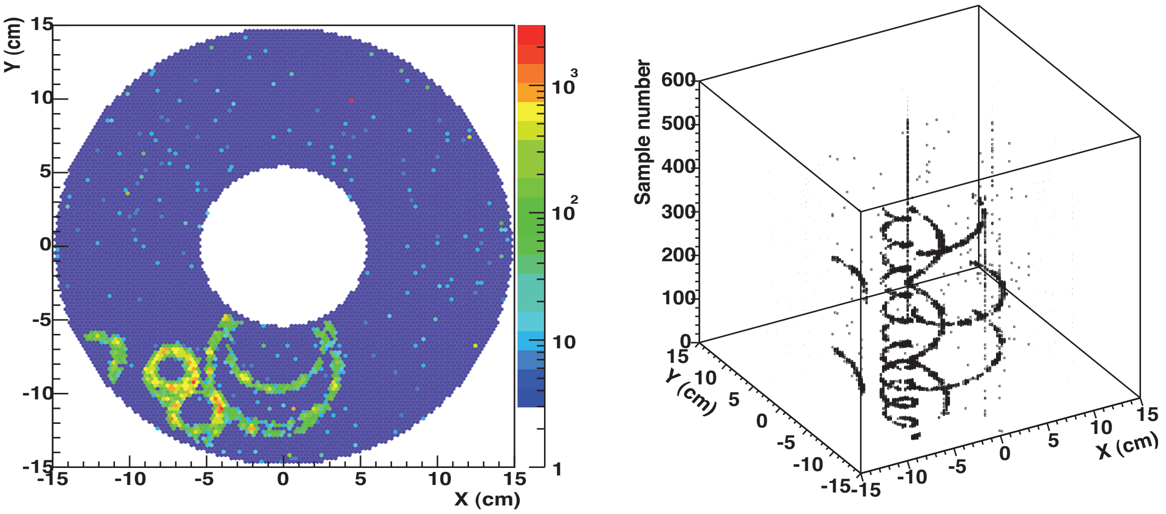

(a) Typical event characterized by an interaction of the ^{22}Ne beam upstream the target region. The curled tracks represent the tracked electrons in the chamber.

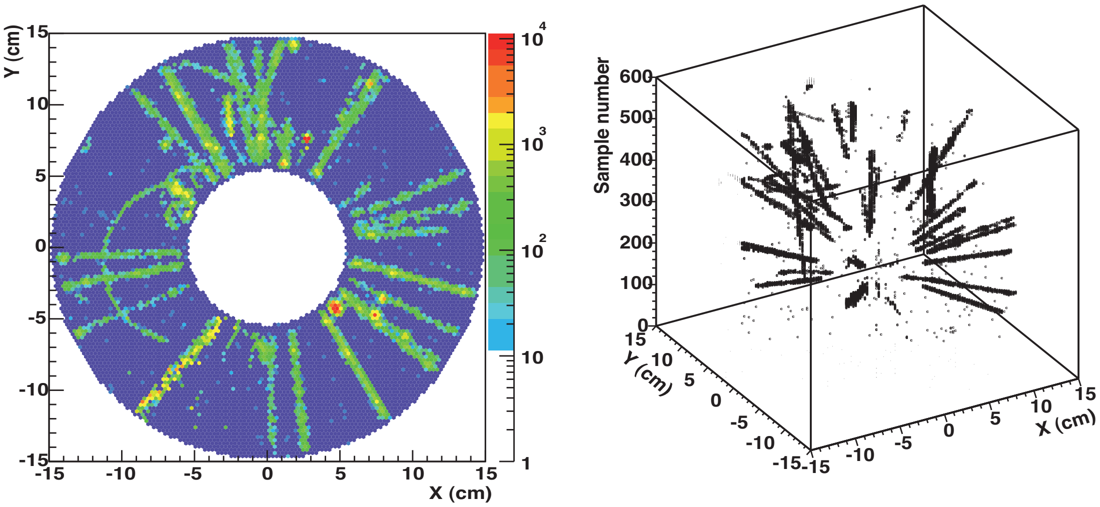

(b) Typical event characterized by an interaction of the ^{22}Ne beam with the Al target.

Figure 4.105: Picture (a) and b) show two typical events in the GEM-TPC. The left panel shows the samples from the ADC in both pad-plane position and sample time while the right picture shows the projection onto the pad-plane. The color code corresponds to the amplitude of a signal.

is visible as well. Currently the alignment of the GEM-TPC chamber is being studied using cosmic and beam data. Figure4.110 shows an event which might be identified with the decay of a Λ hyperon ($\Lambda \rightarrow p + \pi^-$) This event was also selected from the ^{22}Ne data sample and this qualitative picture shows clearly how the particle identification and momentum determination capability of the CDC detector can be combined with the secondary vertex information delivered by the GEM-TPC to improve the reconstruction of hadron decays. As already mentioned, the simultaneous fit of the CDC and GEM-TPC hits is currently being implemented to achieve a global track representation in the combined detection system.

4.12.2.3 Calibration Results with Krypton

During the beam time in Apr 2011 the source containment could be integrated into the gas system and first data from Krypton decays could be taken with Ar/CO$_2$ (90/10), Ne/CO$_2$ (90/10) for different GEM gain settings during the April beam time and in the beginning of June. A typical event with clusters from ^{83m}Kr decays is shown in Fig.4.111. The size and overall charge of the clusters is much

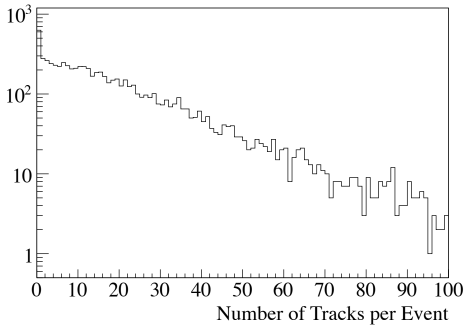

Figure 4.106: Multiplicity distribution of the reconstructed tracks in the GEM-TPC detector for ^{22}Ne+Al collisions at 1.7 AGeV.

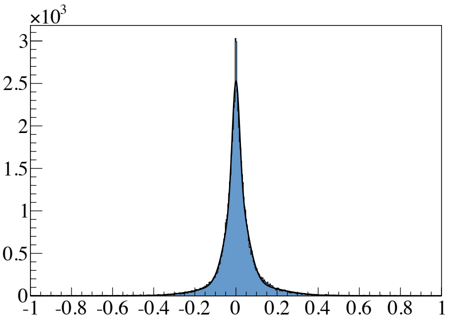

(a) Residuals in V and U direction for the first 10 cm of drift. The data are fitted with 3 Gaussian function. The line shows the sum of the resulting fitted curves.

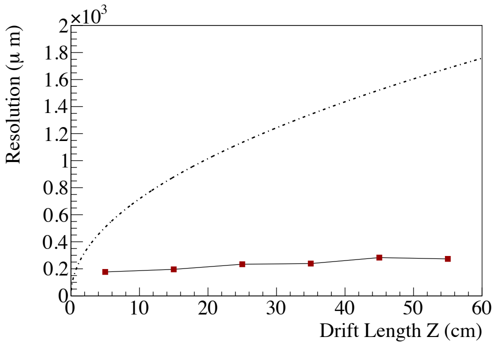

(b) Residual distributions for tracks reconstructed from ^{22}Ne+Al at 1.7 AGeV collisions as a function of the drift length. The dashed line shows the transverse diffusion for single electron drift calculated with GARFIELD, the red dots represent the sigmas of the narrow Gaussian fits.

Figure 4.107: Picture (a) shows the residuals of one slice in z. Picture (b) shows the z-dependency of the residuals. These results are extracted from experimental ^{22}Ne+Al at 1.7 AGeV collisions (see text for details).

higher as for cosmic tracks and thus can be clearly separated from background events or noise. As a first approach for a relative gain-calibration of the readout-pads a modification of the so-called

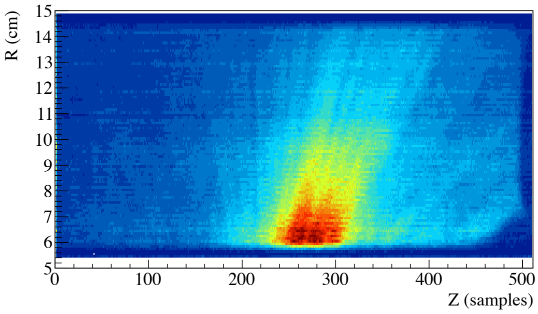

Figure 4.108: Occupancy plot of the GEM-TPC detector obtained with tracks produced in π^-+C at 1.7 GeV/c reactions (see text for details). The z-axis is displayed with a linear scale, units are arbitrary.

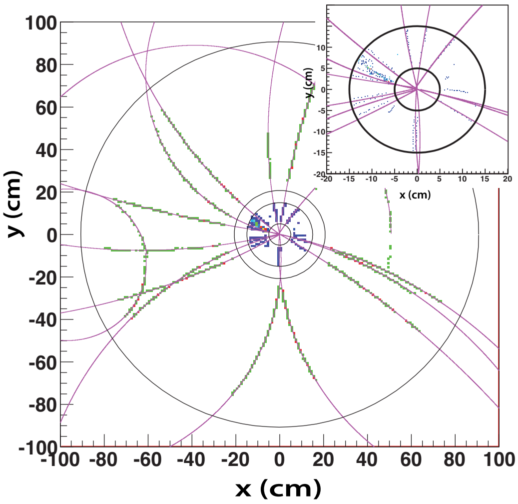

Figure 4.109: A matched event in TPC (two inner circles) and CDC (two outer circles) in a x-y projection. The pink lines indicate the reconstructed tracks of the CDC while the green point are CDC hit points and the blue points are hits in the TPC

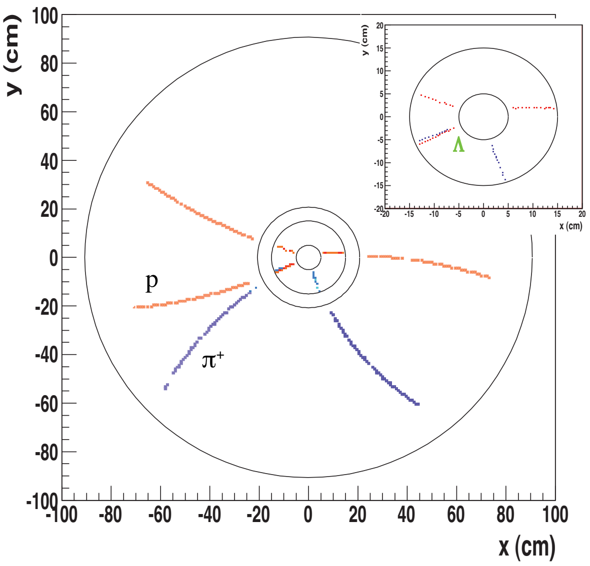

Figure 4.110: Λ candidate.

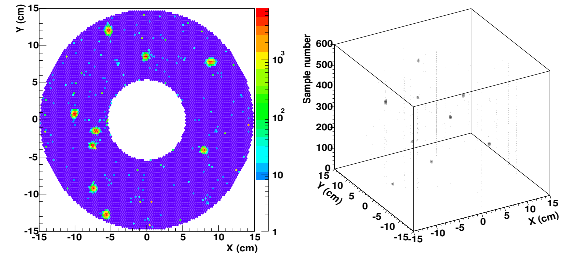

Figure 4.111: A typical krypton calibration event with several decays inside the TPC volume

"leader-pad method" was chosen. In its original form it has been developed and successfully tested for the HARP TPC and is described in [55]. Clusters associated with the highest energetic decay of 41.6 keV are selected by cuts on total ADC charge and pads per cluster. The accumulated charge of each pad in a selected cluster is calculated and the energy entries of the highest 3 pads (so-called "leader-pads") that carry the main charge are filled into a histogram for each pad. The parameters and pad size of the HARP TPC are different, i.e. the main charge was deposited on only one single pad. Regarding the pad size of the prototype TPC and the width of the observed clusters the number of 3 pads for this method was found to be optimal. Less pads introduce a bigger error on the estimation of the central peak position in each bin while more pads introduce a higher background by lower energetic hits. Normalized gain equalisation factors for the whole pad plane are calculated from the peak positions and applied as a correction factor to the raw data hits. A plot of the equalisation factors for each pad can be seen in Fig. 4.112. The sector borders of the GEM detector responsible for the higher gain can be clearly seen as these lines are almost blind and subjacent pads have to register a lower overall charge. The same effect is true for pads close to the field cage as they do not register the full cluster charge. Thus the position of the leader-pad cannot be determined clearly and the gain of such pads would be over-corrected. Such pads have been left out in this map and are shown with a correction factor of 0. Different methods have to be applied for such cases as it was already shown in [55] where a truncated-means method had been shown to be suitable. For the GEM-TPC prototype a suitable method to treat such pads still had to be tested or developed.

One damaged GEM sector in the upper region can be clearly seen in the gain map. This sector showed a very noisy spectrum during the krypton runs and no usable clusters were observed. As a consequence the gain equalisation constants could not be determined and were set to 0 in this plot to show this effect.

Several iterations of the leader-pad method running the full cluster reconstruction have been used to correct for possibly wrongly reconstructed clusters in a previous iteration. After 3 iterations the relative change in the equalisation constants is about 1-2%, the resulting leader-pad peaks before and after correction are shown in 4.113. Gain variations show a periodic structure that has a dependence on the FE chip channels as well as on geometrical properties and the GEM foils as discussed above.

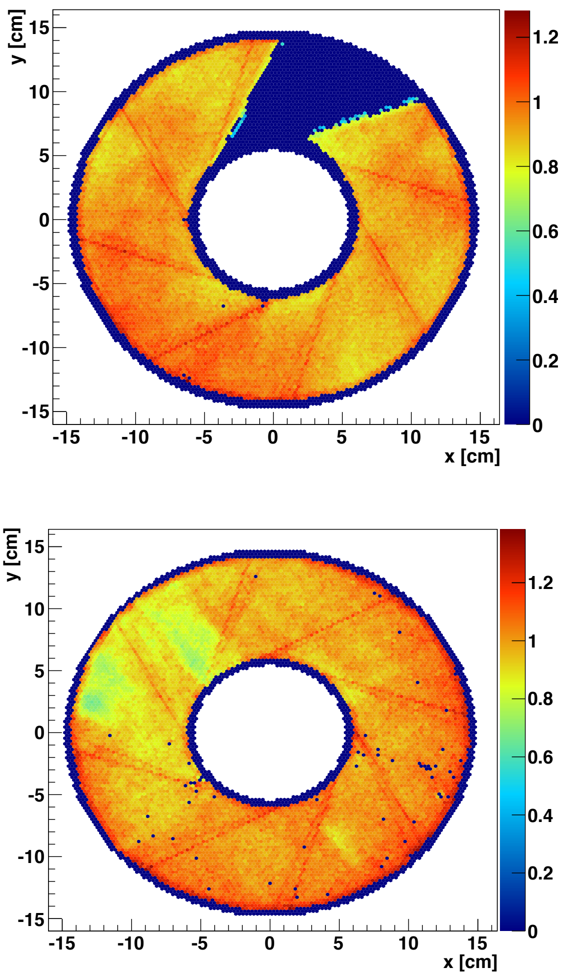

Figure 4.112: Gain equalisation constants plotted for each channel over the pad plane. The overall gain shows small spatial fluctuations while the pads below a gem sector boundaries need to be corrected as the deposited charge on the central pad below such borders is lower. At the inner and outer field cage no central energy deposition of krypton clusters was observed, different methods have to be applied here. One damaged GEM sector was found during the krypton calibration. Even though this sector cannot be calibrated a quick check for damaged sector is possible with the krypton method.

4.13 Quality Control and Risk Assessment

4.13.1 Field Cage

Building gaseous detectors, cleanliness, especially the absence of dust and lints and low humidity is a prerequisite for good quality especially if gluing with epoxy glues is involved. Dealing with high voltages of several 10 kV as involved in the development of the $\overline{\text{P}}$ANDA TPC gives even harder constraints to a proper surrounding. Thus building and handling of the field cage will be done in a clean-room surrounding of class ISO 4. All materials especially the ones involved in the production of the sandwich walls of the field-cage vessels will be stored in zero-humidity compartments and processed solely in the clean room.

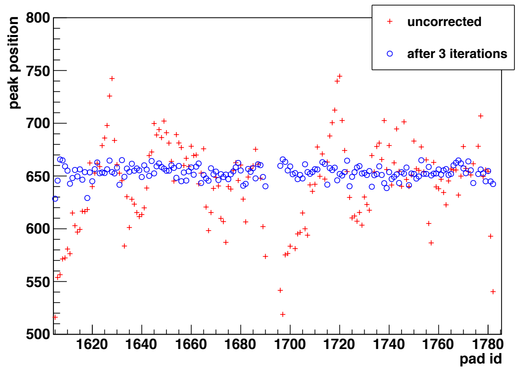

Figure 4.113: Peak positions of leader-pads uncorrected (red) and after 3 iterations of corrections. The corrected distribution is compatible with a flat distribution within the error bounds (not shown here for better visibility of the data points). The periodic structure can be seen on all pads and it repeats for each new FE chip while additional effects due to pads at sector borders or next to the field cage can be observed.

All base materials will be quality checked before their application in production. Especially their electrical properties concerning resistivity and HV-stability will be subject to tests. Their properties in terms of detector aging will be investigated in a dedicated setup (cf. Sec. 4.13.4).

All parts of the field defining system, especially the foils carrying the strip-line electrodes will be checked optically and electrically for any deviations of resistivity, quality of the surface and deviation from their ideal shape on small and large-area scale. The field homogeneity, which has to be expected from the field-cage foils will be checked by measuring individual resistivity values for every adjacent strip. The final specimen produced will be quality checked with respect to the major characteristics, e.g. the high-voltage stability for representative time period.

The test procedures, tools, process descriptions which will be applied for the production of the final detectors have already been developed and successfully applied during the development and construction of the Large-Prototype TPC.

4.13.2 GEM Detectors

COMPASS was the first large-scale experiment to use GEM-based detectors. A lot of experience has been gained during the construction of these detectors. Quality assurance procedures for all detector components have been established in order to guarantee a uniform and stable operation of the chambers [13]. These have successfully been applied to the large prototype, and will be adopted to a large extent for the $\overline{\text{P}}$ANDA TPC.

Since the active detector surface required for the $\overline{\text{P}}$ANDA TPC is relatively small compared to other experiments which use the GEM technology (it is e.g. only about a quarter of the total active area of GEM detectors in COMPASS), the production of the required number of GEM foils at CERN-TS/DEM does not require any additional resources in this laboratory. Nevertheless, first contacts with external companies have been established in order to explore alternative providers. Test samples of GEM foils have been provided by one company and are currently being tested.

The testing and handling of GEM foils and the construction of GEM detectors will be done under clean-room conditions (class 10 000 or better). The foils and all mechanical parts in contact with high voltage (HV) will be tested for HV stability and leakage currents before being mounted, and after each mounting step. For use in a TPC, a good uniformity of gain over all GEM foils is essential in order to achieve the desired dE/dx resolution. This will be tested using optical methods to verify uniform hole shapes and thus transparency, and will be measured on control samples in a dedicated test setup. The final detectors will be subjected to extensive tests using X-rays, radioactive sources and cosmics, before they are mounted to the TPC.

4.13.3 Pad plane

The proper reconstruction of tracks inside the drift volume of the TPC relies on the constant drift velocity without distortions as well as on the knowledge of the shape and layout of the pad-electrodes on the pad-plane where these charges are projected and collected.

The design of the hexagonal pads and their relative positioning among each other and with respect to the optical axis of the detector has to be known within an accuracy of below 0.1 mm. To check the quality of these configurations, a system for optical inspection has been used for quality control. It consists of a large-area planar scanning table with 3D axis motion and a digital optical microscope.

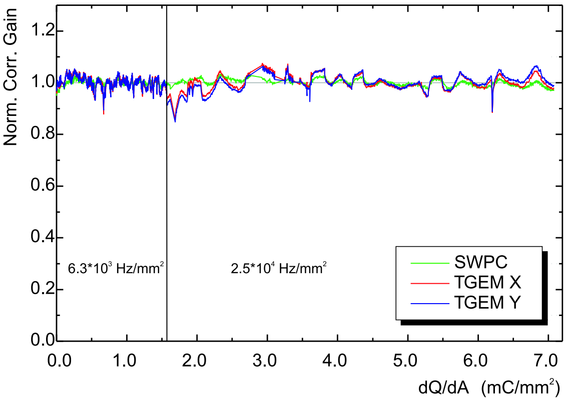

Figure 4.114: Normalized gain as a function of the integrated charge for a COMPASS triple GEM detector in a mixture of Ar/CO$_2$ (70/30).

The measurements of the geometries, e.g. of the mounting holes of the pad-plane reveal small deviations from its perfect circular shape which are well within the design values.

4.13.4 Aging

In COMPASS, the GEM detectors, operated at a gain of $\sim$ 8000 in an Ar/CO$_2$ (70/30) gas mixture, are exposed to extremely high particle fluxes of charged particles ($> 1 \cdot 10^5\,\text{mm}^{-2}\text{s}^{-1}$ close to the beam axis), imposing considerable requirements to the radiation tolerance of their performance. During aging tests, more than $7\,\text{mC/mm}^2$ were collected on the readout strips using an intensive X-ray beam without loss of gain or energy resolution [56]. This corresponds to the total charge collected in more than 7 years of operation in COMPASS. Figure 4.114 shows the variation of the effective gain of a triple GEM detector with 2-D readout under irradiation, compared to a single-wire proportional counter irradiated in parallel.

No degradation of performance was observed in nine years of operation, both with μ and hadron beams, with local charge accumulation exceeding $10\,\text{mC/mm}^2$ in some areas.

In aging studies performed for the LHCb triple GEM tracker, operating with an Ar/CO$_2$/CF$_4$ (60/20/20) gas mixture, the total integrated charge was as high as $200\,\text{mC/mm}^2$ without degradation of the performance [57], as shown in Fig. 4.115.

Owing to the facts that the anti-proton beam does not cross the GEM detectors in $\overline{\text{P}}$ANDA, and that the detectors are located in the backward hemi-

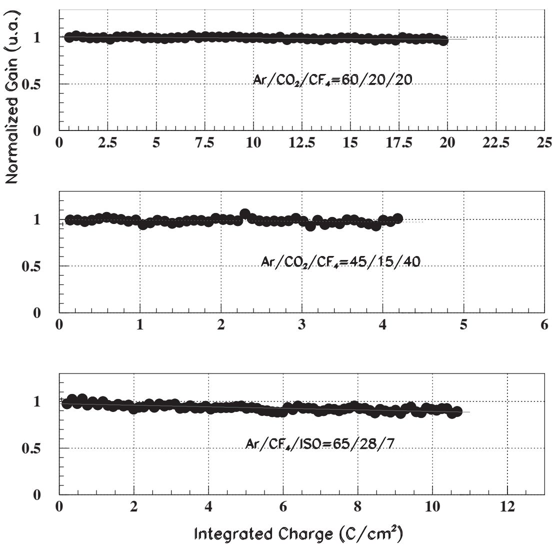

Figure 4.115: Normalized gain as a function of the integrated charge for a triple GEM detector of the LHCb experiment in various gas mixture containing CF$_4$.

sphere of the target, the operating conditions for the GEM detectors in $\overline{\mathrm{P}}$ANDA are expected to be less harsh. At the foreseen gain of 2000, and assuming half a year of running at 80% duty cycle, the total integrated charge is estimated to be about $0.1\,\mathrm{mC/mm^2}$, much below the numbers quoted for other experiments. The fact that the $\overline{\mathrm{P}}$ANDA TPC will operate with the noble gas Ne instead of Ar is not expected to make any difference concerning aging, as it is either the quench gas or impurities introduced into the gas volume which cause aging. All materials in contact with the detector gas will be subject to aging tests using a dedicated setup consisting of a reference detector, a heatable sample box, which contains the material under investigation and is flushed with detector gas, and a second detector downstream of the sample box.

4.13.5 Ion Backflow

As mentioned already in chapter 4.11 the ion backflow is one of the main parameters, that has to be controlled for a continuously operating TPC. Two contradicting requirements have to be kept in mind. On the one hand large gas avalanches, especially in the first GEM foil, are favored for optimal resolution. Ionization charges lost in the very beginning of the charge avalanche process contribute to a deterioration of point and energy resolution. However in regard of ion backflow a very small amplification in the first GEM stage is favored to minimize the backflow of ions where the ions can directly escape into the drift volume. The triple GEM amplification with the electric field settings indicated in Sec. 4.4.3, which is the current baseline solution for the $\overline{\mathrm{P}}$ANDA TPC, provides an ion backflow of 0.25%, corresponding to four back drifting ions per electron reaching the GEM stack at a gain of $2\cdot10^3$. We have shown that corrections based on a conventional laser system restore the required point resolution of the detector even at the maximum luminosity of $2\cdot10^{32}\,\mathrm{cm^{-2}s^{-1}}$.

Currently, there are two different strategies of further reducing the ion backflow, which will be pursued in the future, and which potentially eliminate the problem completely. The first strategy will be the further optimization of the MPGD devices. There are promising new results using GEM foils with additional patterning on one side, which are already available and will be investigated in the near future. The second strategy will be to investigate an alternative amplification concept of the primary electrons, that does not produce ions in the first place. However, as the alternative concept has so far never been applied to the field of tracking detectors some R&D effort have to carried out. Therefore this alternative concept certainly requires a longer time perspective.

4.13.5.1 Strategy 1: Reduction of IB by Optimization of Amplification System

The next logical attempt to improve the performance after monitoring and calibrating the TPC will be to minimize the IB by optimizing the TPC by modifications of the gas amplification methods. One promising technique, which has to be evaluated for the specific need of the PANDA TPC is the application of a Cobra/2GEM device as it has been proposed by [**?**]. The new patterned microhole electrode named Cobra (see Figure 4.116) was developed with a geometry that is expected to improve the ion divergence away from the holes. It has thin anode electrodes surrounding the top side of the holes and creating strong electric field inside the holes (required for charge amplification). The more negatively biased cathode electrodes cover a large fraction of the area for a dramatic improvement of the ion-collection efficiency on the top side of the Cobra device. It was found, that when introduced as a first element (with the patterned area pointing towards the drift volume), preceding two GEMs in the cascade (Figure 4.116), it drastically improves the ion trapping capability. The ion backflow (IB) as a function of the total gain for drift fields of 0.2

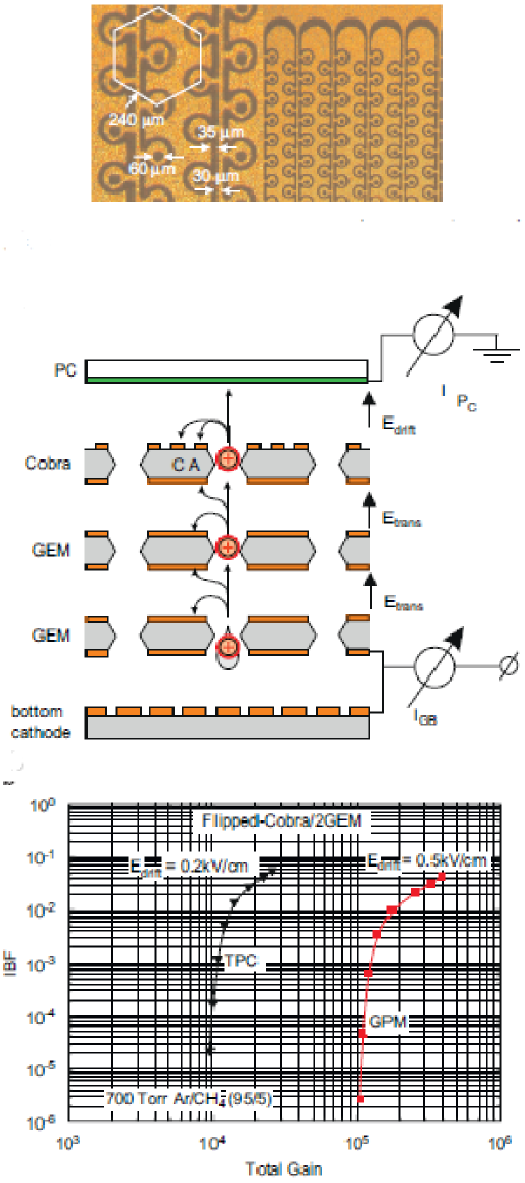

Figure 4.116: Figure (a) shows a microscopic photograph of a Cobra micro hole electrode with the dimensions given in the figure. Figure (b) shows the scheme of a COBRA/2GEM amplification. Possible avalanche ion paths are shown. Figure (c) gives the IBF as a function of the total gain for drift fields of 0.2 and 0.5 kV/cm [?]

and 0.5 kV/cm is shown in Figure 4.116. With a drift field of 0.5 kV/cm in an Ar/CH_4 gas mixture the IB was 3 x 10^{-6} and with a drift field of 0.2 kV an IB of 2.7 x 10^{-5} was reached. These values are so far the best values ever achieved for IB measurements. It has to be investigated if this setup is applicable for the PANDA TPC without deteriorating other key parameters such as the momentum resolution. Especially the large scale application for tracking purposes has to be demonstrated to establish this as an alternative technique to an conventional amplification system with GEMs alone.

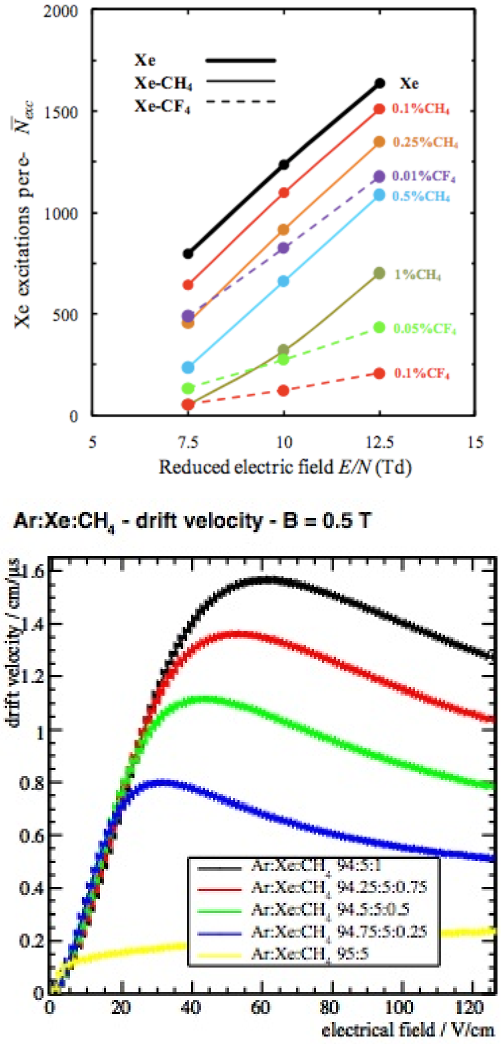

Figure 4.117: Figure (a) shows the light yield as function of the electric field for pure xenon and with a small percentage of CH_4 resp- CF_4 quencher [?]. Figure (b) shows the development of the drift velocity for a Ar/Xe gas as function of the electric field for small contributions of CH_4.

4.13.5.2 Strategy 2: Prevention of IB by an Alternative Concept

An alternative approach would be to employ a completely new concept, which reduces the ion backflow to zero. Instead of amplifying the primary charges by charge avalanche of the gas in an amplification stage such as a GEM, Micromega, Cobra or MHSP it is possible to only excite a noble gas by electroluminescence (EL). This process produces vuv photons. The wavelength of the photons depends on the composition of dimers of the specific gas. In xenon the vuv photons of about 178 nm are produced. The number of photons depends on the number of collisions of the primary charges with the gas atoms. This process is linear to the length of the scintillation gap, where a specific electric field is applied. The following empirical formula [?] is given to describe the EL gain:

$$\eta_{Xe} = 140(E/p - 0.83)p\Delta x \text{ (UV photons /e cm}^{-1}\text{)}, \quad (4.11)$$

where E denotes the electric field, p the pressure and Δx the length of the scintillation gap. As the photons leave the amplification region without further interacting with the gas atoms, no secondary interaction will take place, so that also the gain fluctuations are linear. Therefore EL also improves significantly the energy resolution of a TPC detector.

The EL process will reduce the IB to zero. The drawback of a detector operating in EL mode is that it works best in pure noble gases like argon or xenon. Pure noble gases have a very low drift velocity, which limits the readout speed of the detector. The key optimization, which has to be performed is to find the right gas mixture of a noble gas plus a minimal amount of quencher, which speeds up the drift velocity (and therefore the readout speed) and at the same time allows still an sufficient light yield. In conventional TPCs a quencher is added exactly for the reason to reduce the vuv photon to zero and to increase the drift velocity. In [?] a study to find a suitable quencher has been performed. In Figure 4.117 the quencher CH_4 and CF_4 have been investigated. It is shown, that if the CH_4 contribution is below 1%, still a sufficient light yield can be reached. In the case of CF_4 even a minimal contribution of 0.1% will practically kill the whole EL light production. Figure 4.117 shows the increase of drift-velocity as a function of the applied electric field for gases with CH_4 contributions from 0.25 to 1%. A 1% contribution of CH_4 would increase the drift velocity significantly (see Figure 4.117), so that the drift velocity becomes comparable to the ones used in current TPC detectors.

Also the readout plane would have to follow the different concept of light readout. Instead of a passive readout by pads, which is non amplifying, photosensors like Avalanche Photo Diodes (APD) or Silicon Photomultiplier (SiPM) have to be used, which would convert the photons back into an linear or exponentially amplified electric signal. The size of these devices would have to be in the order of the current pad size, which is about 3x3 mm^2. APDs as well as SiPMs can be built in these sizes (see [58]). With APDs or SiPM one has readout pixels, which are amplifying devices so that an additional pre-amplifier might not be needed.

In the scope of neutrinoless double beta gaseous TPCs ([58]) first preliminary results for such a readout are shown. However the proof of principle still has to be given that such a technique can be applied for a tracking TPC of the PANDA type. Therefore strategy 1 will be the short to mid term solution as strategy 2 would be a more fundamental study, which would also require a long term perspective.

4.14 Organization

4.14.1 Work Packages

Table 4.14 lists the work packages which have been identified for the construction of the $\overline{\mathsf{P}}$ANDA TPC, together with the foreseen responsible institutions.

Table 4.14: Work packages and foreseen responsible institutions.

Item	Institution
Mechanical support	INFN
Field cage	HGF
High voltage system	HGF
GEM detectors	TUM, HGF
Readout plane	TUM
Front-end electronics	TUM
Gas system, Kr calibration	OeAW, HISKP
Laser calibration	HGF, TUM
Slow control	HISKP, OeAW
General infrastructure	FAIR

4.14.2 Schedule

Figure 4.118 shows the time-lines for the construction of the $\overline{\mathsf{P}}$ANDA TPC.

The design of the field cage of the $\overline{\mathsf{P}}$ANDA TPC has started a and the GEM detectors of the $\overline{\mathsf{P}}$ANDA TPC has started at the beginning of 2011. The preparatory work for the construction of the field cage, i.e. tooling and testing of materials, will start in the first quarter of 2012 and last until the second

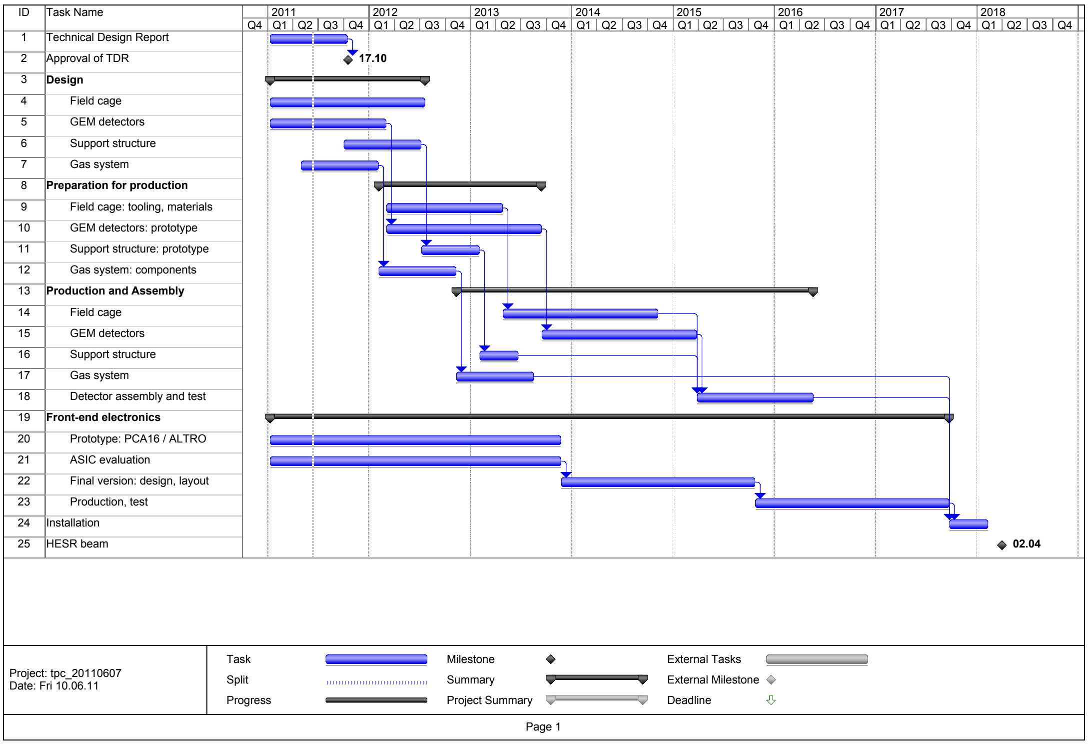

Figure 4.118: Time-lines for the construction of the $\overline{\rm P}$ANDA TPC.

quarter of 2013. The construction of the field cage is expected to be finished in the second half of 2014.

A full-size prototype of a GEM detector based on the single-mask technique will be constructed and tested in 2012. After validation of the prototype, the production of the final readout chambers will commence at the end of 2012 and is expected to finish in the first half of 2015.

The closed-loop gas system is currently being designed and it is foreseen to start ordering the components in early 2012. The assembly and commissioning will take place in 2013, such that it is ready for first tests in 2014.

The assembly of the final detector will take place in 2015. Using the existing front-end electronics based on the AFTER ASIC, a large-scale test of the full TPC can already be performed at this time.

Concerning the front-end electronics, a prototype version of a data-driven front-end PCB based on the PCA16 / S-ALTRO chip will be developed and tested on the large prototype detector until the end of 2012. In parallel, the other two ASIC options, and possible new developments will be evaluated concerning their suitability. The design and layout of the final front-end electronics is expected to begin in 2014 and finish at the end of 2015. The production of the required number of boards including a sufficient amount of spares will start at the end of 2015, and end in mid-2017, including testing and system integration.

The installation of the TPC in $\overline{\rm P}$ANDA is currently foreseen for the beginning of 2018.

4.14.3 Cost Estimate

The total cost of the TPC has been estimated, where applicable, taking into account the experience from the large prototype detector. Table 4.15 gives an estimate of the total cost of the TPC in units of 1 000 €. The cost of the online reconstruction farm is not included in this table, as it constitutes a general $\overline{\rm P}$ANDA item and will be included in the cost of the data acquisition system.

Item	Cost [k€]
Mechanical support	400
Field cage	450
High voltage system	200
GEM detectors	300
Readout plane	150
Front-end electronics	1000
Gas system, Kr calibration	250
Laser calibration	250
Slow control	200
General infrastructure	200
Total	3400

Table 4.15: Cost estimate for the $\overline{\text{P}}$ANDA TPC.

References

[1] D. R. Nygren and J. N. Marx, Phys. Today **31N10**, 46 (1978).

[2] R. J. Madaras et al., IEEE Trans. Nucl. Sci. **30**, 76 (1983).

[3] W. B. Atwood et al., Nucl. Instrum. Meth. **A306**, 446 (1991).

[4] C. Brand et al., Nucl. Instrum. Meth. **A283**, 567 (1989).

[5] S. Wenig, Nucl. Instrum. Meth. **A409**, 100 (1998).

[6] S. Afanasev et al., Nucl. Instrum. Meth. **A430**, 210 (1999).

[7] K. H. Ackermann et al., Nucl. Phys. **A661**, 681 (1999).

[8] K. H. Ackermann et al., Nucl. Instrum. Meth. **A499**, 713 (2003).

[9] J. Alme et al., Nucl. Instrum. Meth. **A622**, 316 (2010).

[10] W. Blum, W. Riegler, and L. Rolandi, *Particle Detection with Drift Chambers*, Springer-Verlag, Berlin, 2 edition, 2008.

[11] F. Sauli, Nucl. Instr. Meth. A **386**, 531 (1997).

[12] S. Bachmann et al., Nucl. Instr. Meth. A **479**, 294 (2002), CERN-EP-2000-151.

[13] C. Altunbas et al., Nucl. Instr. Meth. A **490**, 177 (2002).

[14] B. Ketzer, Q. Weitzel, S. Paul, F. Sauli, and L. Ropelewski, Nucl. Instr. Meth. A **535**, 314 (2004).

[15] G. Baum et al., COMPASS: A proposal for a COmmon Muon and Proton Apparatus for Structure and Spectroscopy, CERN/SPSLC 96-14, SPSC/P 297, 1996.

[16] B. Ketzer et al., A triple-GEM detector with pixel readout for high-rate beam tracking in COMPASS, in *2007 IEEE Nuclear Science Symposium Conference Record*, Piscataway, NJ, 2007, IEEE.

[17] G. Bencivenni et al., Nucl. Instr. Meth. A **488**, 493 (2002).

[18] Z. Fraenkel et al., Nucl. Instr. Meth. A **546**, 466 (2005).

[19] M. G. Bagliesi et al., Nucl. Instr. Meth. A **617**, 134 (2010).

[20] G. Bencivenni and D. Domenici, Nucl. Instr. Meth. A **581**, 221 (2007).

[21] D. Abbaneo et al., (2010).

[22] K. Dehmelt, PoS **EPS-HEP2009**, 155 (2009).

[23] S. Spataro, J. Phys. Conf. Ser. **119**, 032035 (2008).

[24] M. Kotulla et al., Technical Progress Report for PANDA: Strong Interaction Studies with Antiprotons, FAIR-ESAC/Pbar/Technical Progress Report, 2005.

[25] S. Duarte Pinto et al., JINST **4**, P12009 (2009).

[26] C. Hearty et al., (2007), T2K Internal Note.

[27] G. Vidal-Sitjes, NIMA **518**, 132 (2004).

[28] L. Hallermann, *Analysis of GEM Properties and Development of a GEM Support Structure for the ILD Time Projection Chamber*, PhD thesis, DESY, 2010.

[29] D. Decamp et al., NIMA **294**, 121 (1990).

[30] S. Gaertner, Gain calibration of the ALICE Time Projection Chamber, Master's thesis, Techn. Univ. Darmstadt, 2008.

[31] T. Eggert, Star Note **424** (2000).

[32] B. Lasiuk and C. A. Whitten, Star Note **360** (1998).

[33] M. Rasulbaev et al., Applied Radiation and Isotopes **66**, 1838 (2008).

[34] S. Paoletti, A. Bocci, R. D'Alessandro, and G. Parrini, (2004).

[35] S. Paoletti, (2007).

[36] P. Aspell et al., S-ALTRO Specification, 2009.

[37] T. Armbruster, P. Fischer, and I. Peric, SPADIC - A Self-Triggered Pulse Amplification and Digitization ASIC, in *Nuclear Science Symposium Conference Record (NSS/MIC), 2010, IEEE*, 2010.

[38] W. Kühn et al., J. Phys. Conf. Ser. **119**, 022027 (2008).

[39] S. Lange and D. Münchow, FPGA Implementation of a Track Finder and Fitter for PANDA, 2011.

[40] M. Al-Turany, Track finding and fitting with GPUs, 2011.

[41] F. Böhmer, A High-Rate Time Projection Chamber for PANDA - Simulation Studies and GPU-based Track Finding, Master's thesis, Techn. Univ. München, 2009.

[42] C. Höppner, S. Neubert, B. Ketzer, and S. Paul, Nuclear Instruments and Methods in Physics Research A **620**, 518 (2010).

[43] R. Frühwirth, Nuclear Instruments and Methods in Physics Research Section A: Accelerators, Spectrometers, Detectors and Associated Equipment **262**, 444 (1987).

[44] R. Frühwirth and A. Strandlie, Computer Physics Communications **120**, 197 (1999).

[45] G. Kitagawa, Annals of the Institute of Statistical Mathematics **46**, 605 (1994), 10.1007/BF00773470.

[46] M. Innocente, V. Mairie, and E. Nagy, CERN Program Library **W5013-E** (1991).

[47] C. Höppner and S. Neubert, http://sourceforge.net/projects/genfit/.

[48] M. Killenberg et al., Nucl. Instr. Meth. A **530**, 251 (2004).

[49] Q. Weitzel et al., IEEE Nucl. Sci. Symp. Conf. Rec. **1**, 227 (2007).

[50] R. Esteve Bosch, A. Jimenez de Parga, B. Mota, and L. Musa, IEEE Trans. Nucl. Sci. **50**, 2460 (2003).

[51] P. Baron et al., IEEE Trans. Nucl. Sci. **55**, 1744 (2008).

[52] K. Hildenbrand, GSI Nachr. **91-02**, 6 (1992).

[53] L. Schmitt et al., IEEE Trans. Nucl. Sci. **51**, 439 (June 2004).

[54] F. Sauli, Principles of operation of multiwire proportional and drift chambers, page 92 p, Geneva, 1977, CERN, CERN, CERN, Geneva, 1975 - 1976.

[55] F. Dydak and A. De Min, HARP memo **04-103** (2004), submitted 28 April 2004 corrected 7 May 2004 updated 10 June 2004.

[56] M. Altunbas et al., Nucl. Instr. Meth. A **515**, 249 (2003).

[57] M. Alfonsi et al., Nucl. Instrum. Meth. **A518**, 106 (2004).

[58] NEXT, a HPGXe TPC for Neutrinoless Double Beta Decay Searches, Technical report.